Nouvelle génération de détecteurs d'ions sensible en position et en temps pour le développement de la sonde atomique tomographique

Christian Bacchi

Normandie Université

THESE

Pour obtenir le diplôme de doctorat

Spécialité Physique

Préparée au sein de
« Groupe de Physique des Matériaux, UMR 6634, CNRS, Normandie Université »

New Generation of Position-Sensitive Detectors for the Development of the Atom Probe Tomography

Présentée et soutenue par
Christian BACCHI

Thèse soutenue publiquement le 2 octobre 2020 devant le jury composé de		
Mme Oana COJOCARU-MIREDIN	Groupe Leader / RWTH (Université d'Aix-la-Chapelle)	Rapporteur
M. Philippe RONCIN	Directeur de recherche / ISMO (Université Paris Saclay)	Rapporteur
M. Benoit GERVAIS	Directeur de recherche / CIMAP (Normandie Université - Caen)	Examinateur
M. Thomas Kelly	Professeur / Directeur Général de Steam Instruments / Madison	Examinateur
M. Hermann ROTHARD	Directeur de recherche / CIMAP (Normandie Université - Caen)	Examinateur
M. François VURPILLOT	Professeur / Directeur de thèse / GPM (Normandie Université - Rouen)	Directeur de thèse

Thèse dirigée par François VURPILLOT, Groupe de Physique des Matériaux

UNIVERSITÉ DE ROUEN

ED PSIME

GPM Groupe de Physique des Matériaux

Normandie Université

THESE

Pour obtenir le diplôme de doctorat

Spécialité Physique

Préparée au sein de
« Groupe de Physique des Matériaux, UMR 6634, CNRS, Normandie Université »

Nouvelle génération de décteteurs d'ions sensible en position et en temps pour le développement de la sonde atomique tomographique

Présentée et soutenue par
Christian BACCHI

Thèse soutenue publiquement le 2 octobre 2020 devant le jury composé de		
Mme Oana COJOCARU-MIREDIN	Groupe Leader / RWTH (Université d'Aix-la-Chapelle)	Rapporteur
M. Philippe RONCIN	Directeur de recherche / ISMO (Université Paris Saclay)	Rapporteur
M. Benoit GERVAIS	Directeur de recherche / CIMAP (Normandie Université - Caen)	Examinateur
M. Thomas Kelly	Professeur / Directeur Général de Steam Instruments / Madison	Examinateur
M. Hermann ROTHARD	Directeur de recherche / CIMAP (Normandie Université - Caen)	Examinateur
M. François VURPILLOT	Professeur / Directeur de thèse / GPM (Normandie Université - Rouen)	Directeur de thèse

Thèse dirigée par François VURPILLOT, Groupe de Physique des Matériaux

UNIVERSITÉ DE ROUEN

ED PSIME

GPM Groupe de Physique des Matériaux

In memory of Alain Bostel (a.k.a. Monsieur du Lundi)

Aknowledgements

The contributions introduced in this manuscript would not have been possible without the guidance of my thesis supervisors, François Vurpillot and Gérald Da Costa. In addition to bringing me the essential knowledge in this field of research, which was new for me, François has been able to show me how to ask myself the right questions throughout my research studies. Like a flavor enhancer, François is for me a "curiosity enhancer" who can induce the desire to learn and experiment further and further. On the other side, these contributions would be quite impossible without the guidance, the assistance and the unfailing support of my other supervisor, Gérald Da Costa. To put it in simple terms, Gérald was clearly my reference during this thesis. I would never thank him enough for his significant contribution to my professional and personal development. Around those two great men, there is the instrumentation team of the GPM lab (ERIS), that I do not want to forget. Thank you all for your help, for our constructive discussions, for your sincerity and your kindness. Not forgetting the GPM lab, which was like my second home.
I would also like to thank the company CAMECA in Madison, Wisconsin, for their significant financial support and their keen interest in my research studies. Special thoughts for Tom Kelly, Dave Larson, Dan Lenz and Ed Oltman.
Concerning the main developments performed during this thesis, I would like to introduce my acknowledgments to Constance Stoner from Arizona Carbon Foil Inc. and Eric Forget from Cibel company, for their assistance, their patience and their understanding. I want to express special thanks to Hermann Rothard, who welcomed me in his laboratory (CIMAP laboratory – Caen), and who took his time to enlighten me on the first principles of the Ion Induced Electron Emission phenomenon.
And last, but not least, a big thank to my lovely wife who supported me from the beginning to the end this thesis.

Contents

List of Figures

List of Tables

Introduction

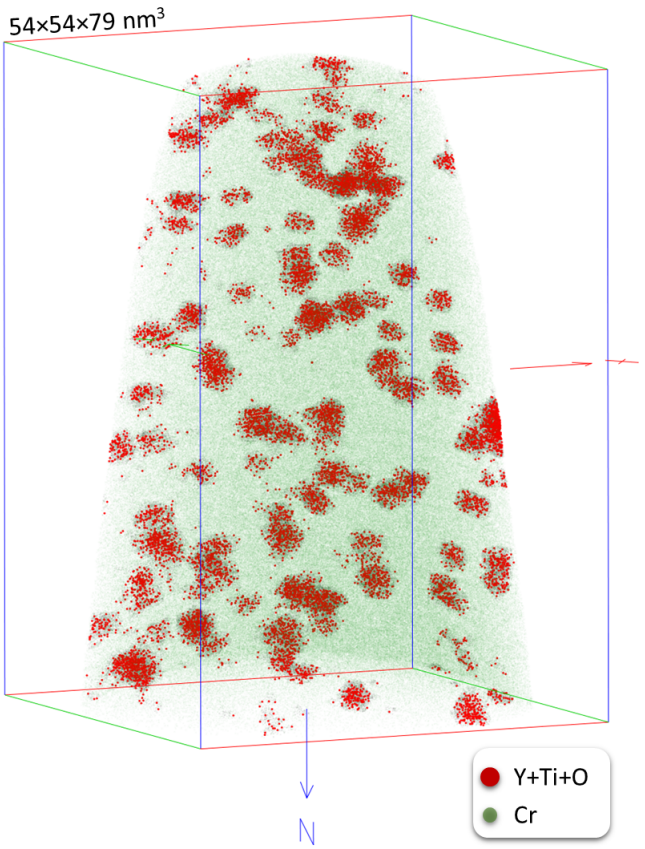

Figure 1: APT volume reconstruction of a ferritic ODS steel introducing nano-particles enriched in YTiO (Courtesy of Dr. Constantinos Hatzoglou)

Nanotechnology is one of the fastest growing areas of research in material sciences. The reason for that originates from the growing need to create new materials that would imply significant technological breakthroughs over the next decades [24]. Whether it is a question of increasing the efficiency of solar cells, developing carbon storage at large scale or finding alternative to

rare earth, it becomes essential to understand the internal nanostructures of materials relying on those future technologies. With the aim of correctly characterizing nano-features, it is sometimes necessary to both determine their shape and their composition at the atomic scale. It turns out that the only analytical tool that is able to combine those requirements is the Atom Probe Tomography (APT) [16, 22]. The APT has been primary developed for identifying, imaging and measuring compositional fluctuations in metals and more generally metallic alloys, and is currently used for almost all types of material [13]. Conversely to electron microscopes, APT instruments are able to both localize and identify elemental nature of individual atoms, not only from the sample surface, but also from internal atomic layers. APT datasets give access to true 3D information of elemental heterogeneities in materials at a sub-nanometer scale (Figure 1).

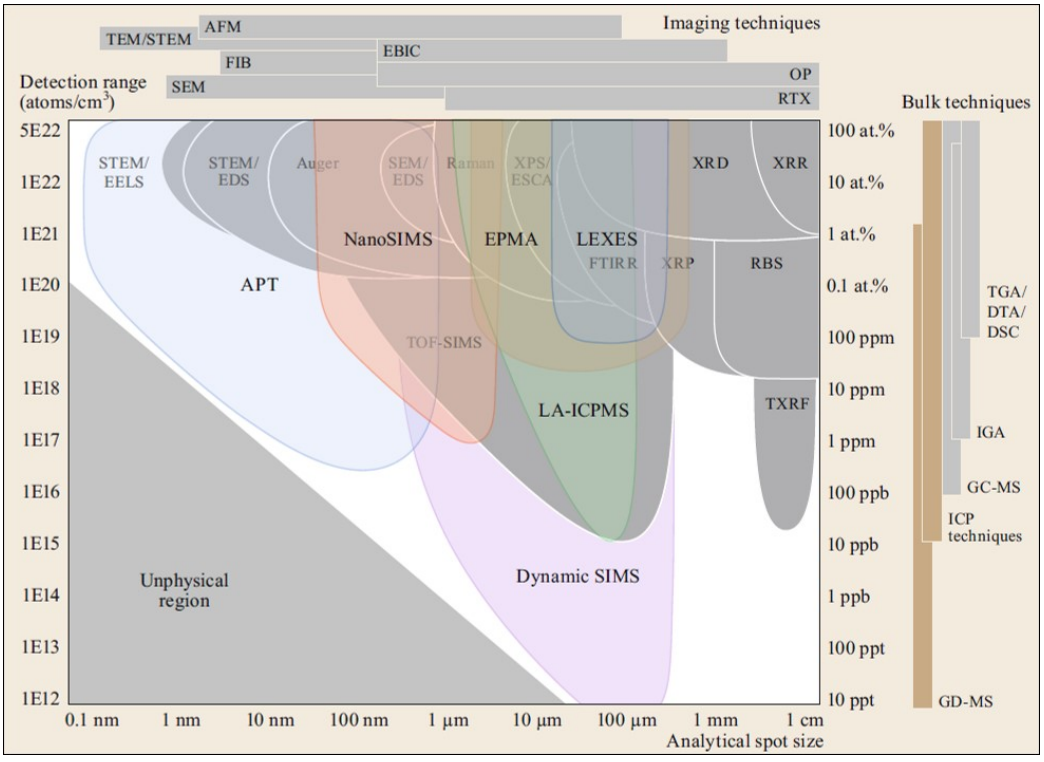

Figure 2: Chart comparing the detection range, the spatial resolution and detection limit between different microanalytical methods (from Springer Handbook of Microscopy [11]).

As shown in Figure 2, the identification and the localization of individual atoms, at tens of ppm level, make the APT one of the most powerful analytical tool in material sciences.

The basic principle of this technique relies on the field evaporation of atoms from the surface of material samples, and the detection of these emitted particles in the form of ions by a high-performance detector. The detector converts ion impacts into coordinates and flight times. The measurement of ions time-of-flight (TOF) enables to determine the elemental nature of each ion by a technique named the time of flight mass spectrometry (TOF-MS). Ions detected are then chemically identified through their mass-to-charge ratio. A 3D reconstruction of the analyzed material is then computed with a reverse-projection algorithm using both the order of arrival of each ion on the detector and the theoretical areal density of the sample surface [1, 9, 10]. Regarding the working process of the instrument, it may be thought that the APT could be the best mean for analyzing materials at the atomic scale. However, since the invention of the technique, more than 30 years ago [3], the instrument is still not fully recognized as a reliable tool perfectly suited for material analyses. About 100 instruments are in use in the world, compared to thousands electron microscopes. The first cause to this originates from the relative difficulty to prepare samples. However with the advent of focused ion beam (FIB-SEM) preparation technique [14, 15, 23], this difficulty gradually vanishes. The second point is the difficulty to get reliable 3D reconstructions which sometimes do not really correspond to the reality [7, 19, 28]. This point also is in constant improvement with a huge effort made by different research group to improve reconstruction algorithms [2,10,25]. The last main cause originates from biases brought by the APT detection system, which is the subject of this thesis. Indeed, it has been pointed out that spatial and compositional biases may occur when APT detection systems are stressed by simultaneous or quasi-simultaneous multi-hit impacts [4, 5]. This mainly concerns the inability of the detector to correctly treat high amounts of hits in a short period of time. Coupled with the fact that some elements tend to field evaporate in multi-hit events more than others [6, 21], it is highly probable that selective losses may occur because of this limitation. Another limitation related to the APT detection system concerns the difficulty to identify objects composed of very few atoms (nano-clusters), due to the non-perfect efficiency of the detector [12, 20, 26]. It turns out that APT detectors are intrinsically limited by their transparency inducing more than 20% of losses on the detection surface. Given that the identification of small clusters relies on density-based methods [7, 17], those losses have clearly the effect of reducing their detectability. The last important limitation on APT detectors concerns their inability to distinguish some elements from one another. Indeed, it can be noticed that the composition of some analyzed materials may involve the evaporation of elements having almost equal mass-to-charge ratios. That is the case, for instance for nitrogen and silicon in TiSiN systems [8], as

well as in field-effect transistors [18], or titanium and carbon in cemented carbide materials [27]. Thus, materials made of different elements having near or equal mass-to-charge ratios may be subjected to uncertainties on the estimation of their fraction in the analysed material. Based on the foregoing, this thesis is intended to answer to the following issue: How to outperform the limitations of APT detection systems? To do so, Chapter I will first introduce details about the APT working principle, as well as a state-of-the-art around the evolution of APT detectors. Next chapters will treat on the two main levers of improvement that have to be applied on APT detection systems; the enhancement of their multi-hit capacity (MHC) and their ability to distinguish all elements from one another. Studies have shown that the complexity of APT detection systems does not allow to draw firm conclusions on the origin of biases caused by multi-hit events, that is why Chapter II will be focused on a systematic study about the impact of the detection system on material analyses through the development of a simulation tool. This study is also intended to provide concrete arguments in favour of a promising detection system which still waits to be democratized to all APT instruments; the advanced Delay Line Detector (aDLD). Theoretical and experimental studies on the aDLD will be introduced in Chapter III, and more specifically, the development of a new design of position-sensitive detector ensuring its optimal running performance. Finally, Chapter IV will deal with the development of a new concept of position-energy-sensitive detector that would be able to resolve significant uncertainties related to the inability of APT detectors to distinguish some elements from one another.

Bibliography

[1] P. Bas, A. Bostel, B. Deconihout, and D. Blavette. A general protocol for the reconstruction of 3d atom probe data. *Applied Surface Science*, 87-88:298–304, 3 1995.

[2] Daniel Beinke and Guido Schmitz. Atom probe reconstruction with a locally varying emitter shape. *Microscopy and Microanalysis*, 25(2):280–287, 4 2019.

[3] A. Cerezo, T. J. Godfrey, and G. D. W. Smith. Application of a position-sensitive detector to atom probe microanalysis. *Review of Scientific Instruments*, 59(6):862–866, 6 1988.

[4] G. Da Costa, F. Vurpillot, A. Bostel, M. Bouet, and B. Deconihout. Design of a delay-line position-sensitive detector with improved performance. *Review of Scientific Instruments*, 76(1):013304, 1 2005.

[5] G. Da Costa, H. Wang, S. Duguay, A. Bostel, D. Blavette, and B. Deconihout. Advance in multi-hit detection and quantization in atom probe tomography. *Review of Scientific Instruments*, 83(12):123709, 12 2012.

[6] F Danoix, M.K Miller, and A Bigot. Analysis conditions of an industrial al–mg–si alloy by conventional and 3d atom probes. *Ultramicroscopy*, 89(1-3):177–188, 10 2001.

[7] Yan Dong, Auriane Etienne, Alex Frolov, Svetlana Fedotova, Katsuhiko Fujii, Koji Fukuya, Constantinos Hatzoglou, Evgenia Kuleshova, Kristina Lindgren, Andrew London, Anabelle Lopez, Sergio Lozano-Perez, Yuichi Miyahara, Yasuyoshi Nagai, Kenji Nishida, Bertrand Radiguet, Daniel K. Schreiber, Naoki Soneda, Mattias Thuvander, Takeshi Toyama, Jing Wang, Faiza Sefta, Peter Chou, and Emmanuelle A. Marquis. Atom probe tomography interlaboratory study on clustering analysis in experimental data using the maximum separation distance approach. *Microscopy and Microanalysis*, 25(2):356–366, 4 2019.

[8] David L.J. Engberg, Lars J.S. Johnson, Jens Jensen, Mattias Thuvander, and Lars Hultman. Resolving mass spectral overlaps in atom probe tomography by isotopic substitutions – case of tisi15n. *Ultramicroscopy*, 184:51–60, 1 2018.

[9] B. Gault, D. Haley, F. de Geuser, M.P. Moody, E.A. Marquis, D.J. Larson, and B.P. Geiser. Advances in the reconstruction of atom probe tomography data. *Ultramicroscopy*, 111(6):448–457, 5 2011.

[10] Constantinos Hatzoglou, Gérald Da Costa, and François Vurpillot. Enhanced dynamic reconstruction for atom probe tomography. *Ultramicroscopy*, 197:72–82, 2 2019.

[11] Peter W Hawkes and John CH Spence. *Springer Handbook of microscopy*. Springer Nature, 2019.

[12] D. Isheim, J. Coakley, A. Radecka, D. Dye, T. J. Prosa, Y. Chen, P. a. J. Bagot, and D. N. Seidman. Atom-probe tomography: Detection efficiency and resolution of nanometer-scale precipitates in a ti-5553 alloy. *Microscopy and Microanalysis*, 22(S3):702–703, 7 2016.

[13] Thomas F. Kelly and David J. Larson. Atom probe tomography 2012. *Annual Review of Materials Research*, 42(1):1–31, 8 2012.

[14] DJ Larson, DT Foord, AK Petford-Long, TC Anthony, IM Rozdilsky, A Cerezo, and GWD Smith. Focused ion-beam milling for field-ion specimen preparation:: preliminary investigations. *Ultramicroscopy*, 75(3):147–159, 1998.

[15] Ji Yeong Lee and Jae-Pyoung Ahn. Focused ion beam-based specimen preparation for atom probe tomography. *Applied Microscopy*, 46(1):14–19, 3 2016.

[16] Williams Lefebvre, Francois Vurpillot, and Xavier Sauvage. *Atom Probe Tomography: Put Theory Into Practice*. Academic Press, 5 2016. Google-Books-ID: YwNaCgAAQBAJ.

[17] Emmanuelle A Marquis, Vicente Araullo-Peters, Yan Dong, Auriane Etienne, Svetlana Fedotova, Katsuhiko Fujii, Koji Fukuya, Evgenia Kuleshova, Anabelle Lopez, Andrew London, et al. On the use of density-based algorithms for the analysis of solute clustering in atom probe tomography data. In *Proceedings of the 18th International Conference on Environmental Degradation of Materials in Nuclear Power Systems–Water Reactors*, pages 2097–2113. Springer, 2019.

[18] Andrew J. Martin, Yong Wei, and Andreas Scholze. Analyzing the channel dopant profile in next-generation finfets via atom probe tomography. *Ultramicroscopy*, 186:104–111, 3 2018.

[19] M. K. Miller. The effects of local magnification and trajectory aberrations on atom probe analysis. *Le Journal de Physique Colloques*, 48(C6):C6–565–C6–570, 11 1987.

[20] M. K. Miller, D. Reinhard, and D. J. Larson. Detection and quantification of solute clusters in a nanostructured ferritic alloy. *Journal of Nuclear Materials*, 462:428–432, 7 2015.

[21] M. K. Miller and G. D. W. Smith. An atom probe study of the anomalous field evaporation of alloys containing silicon. *Journal of Vacuum Science and Technology*, 19(1):57–62, 5 1981.

[22] Michael K. Miller and Richard G. Forbes. *Atom-Probe Tomography*. Springer US, Boston, MA, 2014. DOI: 10.1007/978-1-4899-7430-3.

[23] Michael K. Miller, Kaye F. Russell, Keith Thompson, Roger Alvis, and David J. Larson. Review of atom probe fib-based specimen preparation methods. *Microscopy and Microanalysis*, 13(6):428–436, 12 2007.

[24] Mark Miodownik. Materials for the 21st century: What will we dream up next? *MRS Bulletin*, 40(12):1188–1197, 12 2015.

[25] Nicolas Rolland, François Vurpillot, Sébastien Duguay, Baishakhi Mazumder, James S. Speck, and Didier Blavette. New atom probe tomography reconstruction algorithm for multilayered samples: Beyond the hemispherical constraint. *Microscopy and Microanalysis*, 23(2):247–254, 4 2017.

[26] L. T. Stephenson, M. P. Moody, B. Gault, and S. P. Ringer. Estimating the physical cluster-size distribution within materials using atom-probe. *Microscopy Research and Technique*, 74(9):799–803, 2011.

[27] M. Thuvander, J. Weidow, J. Angseryd, L.K.L. Falk, F. Liu, M. Sonestedt, K. Stiller, and H.-O. Andrén. Quantitative atom probe analysis of carbides. *Ultramicroscopy*, 111(6):604–608, 5 2011.

[28] F. Vurpillot, A. Bostel, and D. Blavette. Trajectory overlaps and local magnification in three-dimensional atom probe. *Applied Physics Letters*, 76(21):3127–3129, 5 2000.

Chapter I

The Atom Probe Tomography

Knowing that the goal of APT instruments is to obtain the internal atomic structure of materials and determine their composition both globally and locally [7], it is clear that priority should be given to the development of a detector with high spatial performances and equal sensitivity for each element. Position-sensitive detectors used in APT instruments generally perform well when the detector is subjected to individual ion hits, but significant technological bottlenecks have been pointed out when the device is stressed by simultaneous or quasi-simultaneous multi-hit impacts [14, 15]. The complexity of APT detection systems does not permit to draw firm conclusions on the origin of biases caused by multi-hit events [33, 44, 54]. Thus, it becomes obvious that a clear description of the APT operating process, and more specifically the APT detection process, has to be drawn. Therefore, this chapter is first aimed at introducing details about the APT working principles, from the field evaporation of atoms from the surface of material samples, to their identification and localization within 3D maps. Thereafter, it would not be appropriate to refer to just a single detection process but to more than one, covering the evolution of position-sensitive detectors used in APT instruments. It will be shown that the quest of an instrument provided with an atomic scale resolution, coupled with an ultimate sensitivity to all elements, is a story successive trade-off. The history of the APT shows that each step towards better spatial performances lead to difficulties for getting accurate compositions and vice versa. That is why; a state-of-the-art around the evolution of APT detectors will also be introduced, starting with the fluorescent screen used in the Field Ion Microscope, the ancestor of APT instruments, to the Delay-Line Detector used in current instruments, in order to get a clear understanding of current trade-offs.

I.1 APT working principles

I.1.1 Field evaporation mechanism

The APT working principle relies on the emission of atoms from the surface of an analyzed material by the fundamental process of Field Evaporation (FE) [52]. By applying a high electric potential, in the range 1 - 20 kV, on a material sample shaped as a sharp needle tip, it is possible to generate a strong electric field at the vicinity of the tip apex (Figure I.1). Assuming that the apex of the tip has a hemispherical shape with a radius of curvature R, in the range 10-100 nm, the theoretical electric field on its surface is given by

$$F = \frac{V}{k_F R} \tag{I.1}$$

Where k_F is a constant called the field factor, and V the electric potential applied on the tip. Under these several tens of V/nm, surface atoms can be expelled and directly ionized into cations.

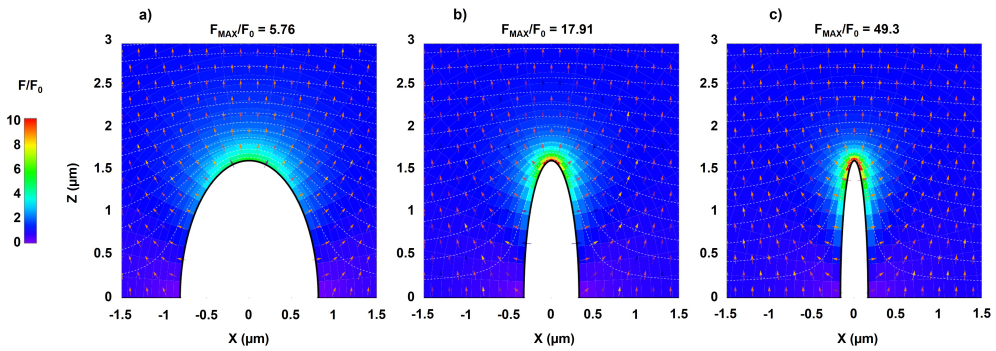

Figure I.1: 2D representations of electric field produced by a tip with different radius of curvature at the tip apex; (a) $R = 407$ nm, (b) $R = 163$ nm, (c) $R = 81$ nm. The electric field is shown by coloring and arrows, and the corresponding equipotential lines are drawn as white dashed lines. All field values are normalized to the applied uniform field F_0

At a very low temperature T, this phenomenon is considered spontaneous and occurs for an electric field exceeding a specific threshold F_e, that depends on the composition and the structure of the analyzed material [16, 37, 42]. Atoms from the tip surface are then ionized and expelled under the influence of an electrostatic repulsion. For moderate temperature (10 - 300 K), it is generally assumed that the field evaporation mechanism is a thermally

activated process, inducing an evaporation rate of atoms from the tip surface following an Arrhenius law $K(F)$;

$$K\left(F\right) = A\ \exp\left(-\frac{Q(F)}{k_B T}\right) \tag{I.2}$$

k_B is here the Boltzmann constant, and A is a constant proportional to the phonon vibration frequency. Atoms from the tip surface must undergo an energy barrier of height $Q(F)$ linearly dependent of the surface field F;

$$Q(F) \approx C\left(1 - \frac{F}{F_e}\right) \tag{I.3}$$

Where C is an energetic term proportional to the binding energy of atoms. It is then assumed that, a constant temperature T and an average field F above the tip surface, should induce a stochastic evaporation process. One may note that the surface field is strongly influenced by the surface roughness, determined by the atomic scale structure of the surface atoms. The evaporation order of surface atoms is therefore semi-deterministic at low T.

I.1.2 Pulsed field evaporation

In order to achieve material analyses at the atomic scale, the evaporation process has to be finely controlled. To do so, a DC voltage V_{DC} is coupled with electric pulses V_P (Voltage Pulse mode) applied directly on the sample or on a counter electrode placed ahead, or with temperature pulses (Laser Pulse mode), driven by a pulsed laser focused on the tip apex.

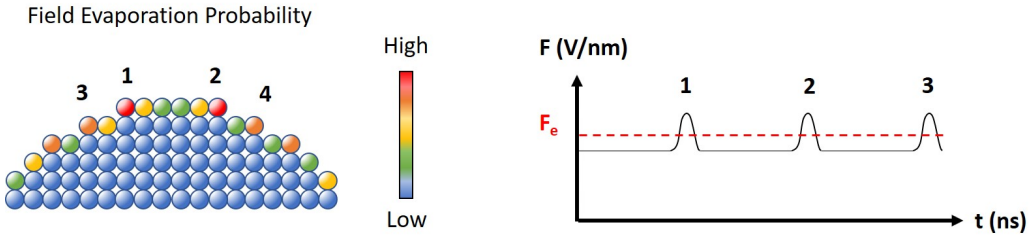

Figure I.2: Schematic of the field evaporation. The sequence of field evaporation at each voltage (or laser) pulse is a function of the probability to ionize atoms from the surface

In Voltage pulse mode, V_P is set to 15-20% of the DC voltage, ensuring negligible DC field evaporation. In laser mode, temperature pulses are in the

range 100-1000 K depending of the material of interest. By this way, the evaporation process is only triggered during a very short time (< 1 ns) and allows performing atom-by-atom analyses (Figure I.2).

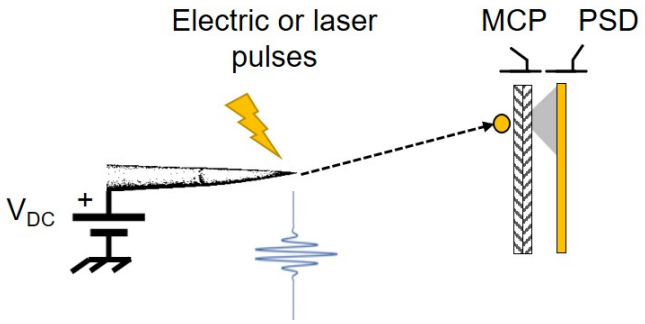

Figure I.3: Scheme of the APT detection process. After being field evaporated, cations are collected through an MCP assembly, transforming hits into exploitable electric signals, coupled with a position-sensitive detector allowing the recording of hit maps.

During the erosion of the analyzed material by the field evaporation process, the idea is to collect a part of the projected cations through a high-performance detector placed in front of the sample, in order to identify and localize them. Those two operations are mainly performed through two devices; the Microchannel Plates assembly (MCP) and the Position-Sensitive Detector (PSD) (Figure I.3), which will be described in details in *Evolution of APT detectors*.

I.1.3 Time-of-Flight Mass Spectrometry

During their projection, cations reach a kinetic energy E_K tending towards the value of the potential energy E_P generated on the tip apex;

$$E_K = \frac{mv^2}{2} \tag{I.4}$$

$$E_P = ne(V_{DC} + V_P) \tag{I.5}$$

With m the mass, v the velocity and n the charge state of projected ions, and e the elementary charge of the electron. This kinetic energy of cations is acquired in the first micrometers of their flight [52], due to the strong diverging nature of the electric field generated by the sample. Cations fly to the detector at constant velocity on a large part of their length of flight (LOF), in such a way that the acceleration stage close to the sample

can be neglected. Thus, ions velocity can be determined through a simple measurement of their time of flight (TOF). Assuming an energy conservation between E_K and E_P (Equations (I.4) and (I.5)), one can determine the mass-to-charge ratio of each detected ion though the following equations;

$$v = \frac{LOF}{TOF} \tag{I.6}$$

$$\frac{m}{n} = 2e\left(V_{DC} + V_P\right)\frac{TOF^2}{LOF^2} \tag{I.7}$$

The measurement of cations TOF is taken between a start pulse originating from the evaporation pulses (Figure I.2), and their arrival on the detector (stop time on the detector). Therefore, this technique called "Time-of-Flight Mass Spectrometry" (TOF-MS), can provide a straightforward information on the elemental nature of each detected cation.

One of the main parameters used for evaluating the ability of mass spectrometers to correctly separate elements with near mass-to-charge ratios is the mass resolution. By computing the width Δm of a mass peak, at a specific fraction of its height, it is possible to get an estimation of the mass resolution through the ratio $\frac{\Delta m}{m}$. Most of the time Δm is taken at half of the peak height (FWHM), with the value of m taken at the centroid of the peak. However, in the framework of the atom probe community, the quality of mass spectra is most commonly evaluated through the reciprocal of this ratio, known as the Mass Resolving Power (MRP). It is evident that the narrower are the mass peaks; the better will be the ability to distinguish elements with very near mass-to-charge ratios (Figure I.4).

$$MRP = \frac{m}{\Delta m} = \frac{1}{\sqrt{(\frac{\Delta V}{V})^2 + 4(\frac{\Delta TOF}{TOF})^2 + 4(\frac{\Delta LOF}{LOF})^2}} \tag{I.8}$$

Through the propagation of uncertainties on the calculation of mass-to-charge ratios (Equation (I.8)), it can be seen that the MRP is mainly dependent on the measurement of cations length-of-flight (LOF) and TOF.

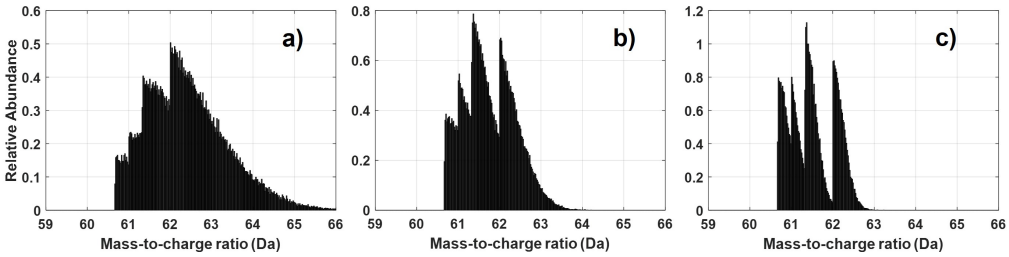

Figure I.4: Comparison of simulated tungsten (W^{3+}) mass spectra as a function of their MRP (computed at $\frac{m}{n} = 61.33$); (a) $MRP = 60$, (b) $MRP = 120$, (c) $MRP = 240$.

I.1.4 Quasi-stereographic projection

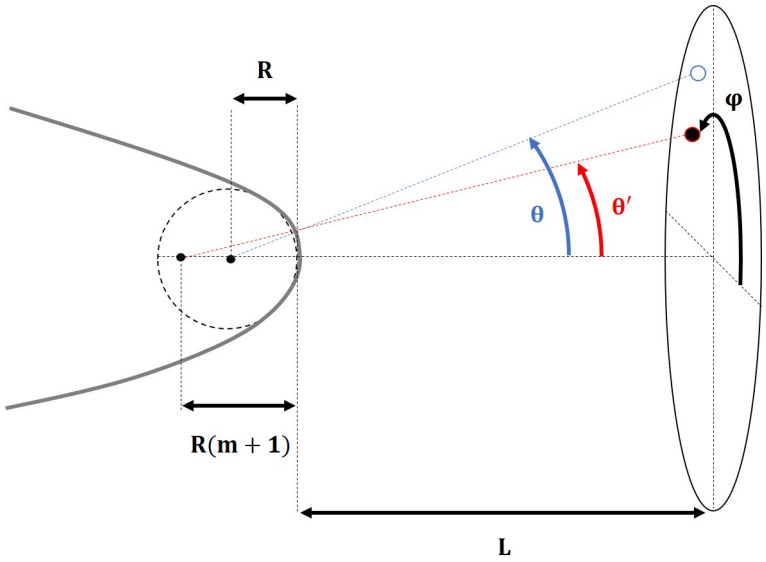

Figure I.5: Representation of the quasi-stereographic projection during the field evaporation. Electric field lines drawn by a perfect hemispherical model of the tip apex are found to be compressed by considering the shank angle of the tip. As a consequence, projections of cations on the detection surface are then characterized by a compression factor m.

Still considering a hemispherical shape of the tip apex, it can be assumed that the projection of cations towards the detector follows a simple angular projection. In the first steps of flight, cations leave the tip in a radial direction from the hemispherical apex. Due to the shank angle introduced by the tip shape, that slightly bend the electric field lines (Figure I.1), cation

trajectories deviate from the theoretical radial projection and trajectories are slightly compressed to the tip axis. The final projection is close to a stereographic projection [4, 22]. A point projection can be defined with a projection center situated at a distance mR from the tip apex center. The parameter m is an empirical compression factor (Figure I.5). As a consequence, cation trajectories are subjected to a compression that affect the theoretical projection angle θ, and in a first approach the compressed projection angle θ' is linearly dependent in such a way that

$$\theta \approx (m+1)\theta' \tag{I.9}$$

That means that 2D maps created from cation impacts represent magnified views of the tip surface.

$$M = \frac{L}{R(m+1)} \tag{I.10}$$

The magnification M of the instrument is a function of the distance L between the tip and the detector, and the radius of curvature of the tip apex (Equation (I.10)). Assuming a distance of 10 to 25 cm, $m \sim 0.6$, and $R \sim$ 10-100 nm, magnification can reach several millions.

I.1.5 Tomography

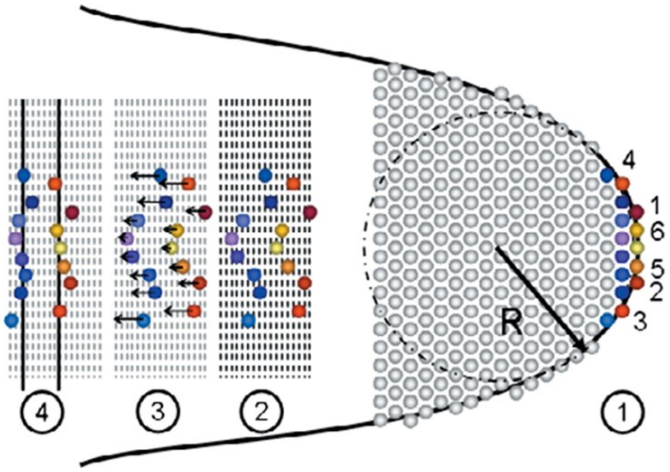

Figure I.6: (From Gault et al. [23]) Diagram of the sequential procedure used to build the tomographic volume: Step 1. The atoms are successively field evaporated from the specimen in a given order; Step 2. Each atom contributes to the depth by increment that directly relates to its atomic volume; Step 3. A correction term is computed for each atom to account for the curvature of the emitting surface; Step 4. Final reconstruction shows the atomic planes structure (not to scale in depth).

The next step of the detection process is the localization of the detected cations. Impacts on the detector surface are localized through the PSD (details in *Evolution of APT detectors*). 2D maps created from cation impacts on the detector generate tomographic cross-sections that constitute the baseline of samples 3D reconstruction. The previous assumptions on the quasi-stereographic projection make it possible to calculate the original position of each detected ion, through simple trigonometric equations;

$$x = R.\sin\theta.\sin\varphi \tag{I.11}$$

$$y = R.\sin\theta.\cos\varphi \tag{I.12}$$

$$z = R(1-\cos\theta) \tag{I.13}$$

Since the evaporation field F_e is constant, a good estimate of the radius of curvature R can be found using Equation (I.1) ($R \approx \frac{V}{k_F F_e}$), and the initial position of field evaporated atom are easily derived.
Since field evaporation is used to gradually erode the material, the position of the hemispherical surface gradually shifts along the tip axis

(the z coordinate). Through the computation of the magnification M (Equation (I.10)), the detector area S_D is back projected to the tip as a probed area S_A, that can be easily estimated ($S_A \sim \frac{S_D}{M^2}$). The detection of N atoms, indicates that a volume V_A was analyzed, that is equal to $S_A.\Delta z$, with Δz the probed depth. Assuming each atom with a constant atomic volume V_{at}, and taking into account the detector efficiency η (50-80%), the analyzed depth Δz is estimated through

$$\Delta z \approx \frac{N.V_{at}.M^2}{\eta.S_D} \tag{I.14}$$

As a result, the actual z coordinate is given by Equations (I.13) and (I.14). In practice the real volume of a truncated hemisphere shape is used, as well as, a refined expression for the reverse-projection law. In addition, a gradual atom by atom reconstruction process is used, considering the atom by atom evolution of the voltage applied during the analysis (Figure I.6).

I.2 Evolution of APT detectors

Based on the foregoing, it can be understood that the performances of APT instruments mainly result from the fine control of the field evaporation mechanism and the 3D reconstruction. However, it must be realized that between those two building blocks, most of the information allowing the localization and the identification of each ion comes from another important part; the APT detection system. Therefore, priority should also be given to the development of a detector with high spatial performances and with a precise and equal sensitivity for each element. Therefore, the following part is aimed at showing how important is the choice of the position-sensitive detector for getting both qualitative and quantitative APT results, by historically retracing the evolution of APT instruments.

I.2.1 Spatial performances of Position-Sensitive Detectors

Before retracing the evolution of APT instruments, it is important to clarify some common metrological terms that are generally used for PSDs, in order to correctly evaluate their performances.

Spatial Resolution

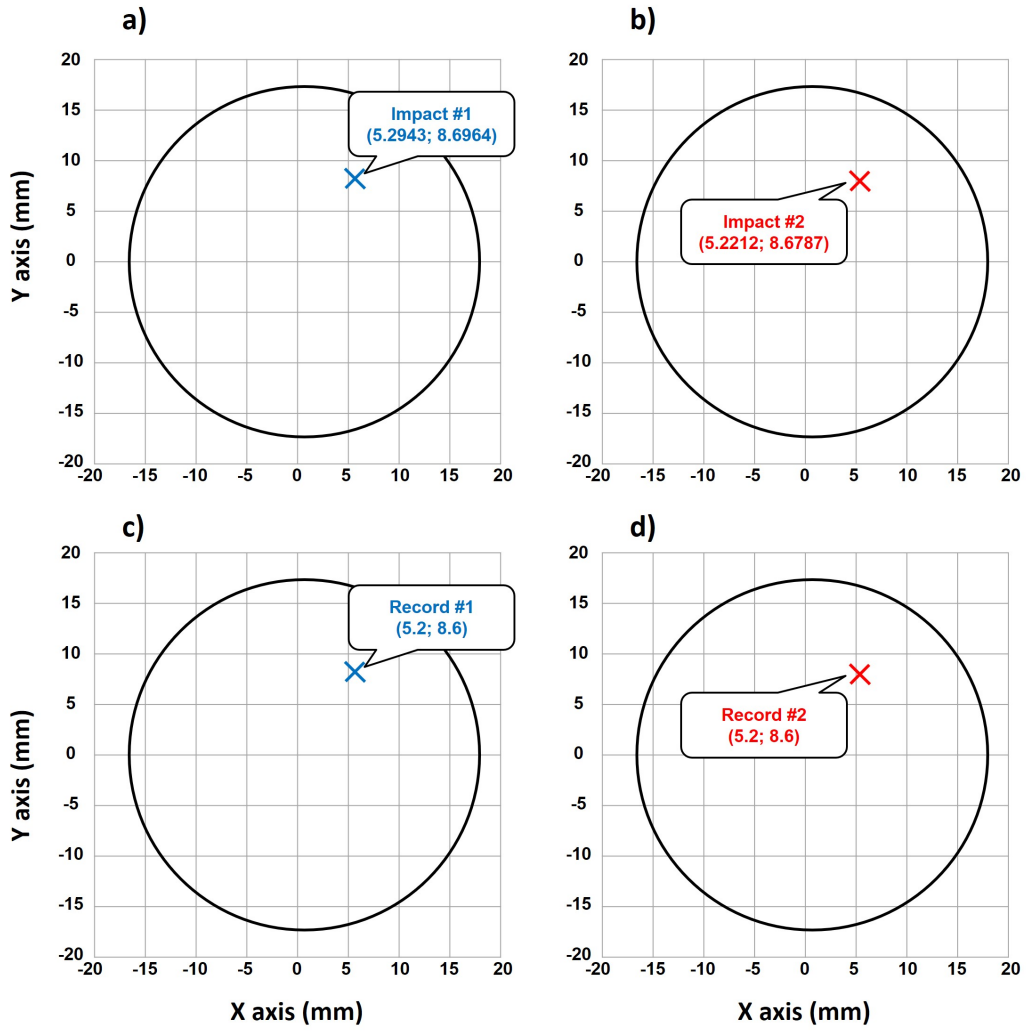

Figure I.7: Illustration of the biases that may occur with a poor spatial resolution. The two impact positions in (a) and (b) can potentially share the same recorded position because of the limited spatial resolution of the PSD.

It has to be known that extracted positions coming from PSDs are all subjected to a digitization that is performed by the electronic detection system. That means that every extracted position is intrinsically limited by the inability of the detection system to provide the strict analog value of every real position (Figure I.7). Therefore, it is possible that a specific single impact position can be measured with the same coordinates as for

another specific single impact position, if their respective coordinates are very close one another. Thus, the smallest perceptible change in position for individual measurements, also called spatial resolution, represents one of the key performance criteria allowing the evaluation of PSDs. By considering this performance criterion, it can be assumed that a PSD can be partly defined by a detection area covered by small pixels taking the dimension of the spatial resolution (Figure I.8). The less is the spatial resolution the finer will be this virtual grid covering the detection surface.

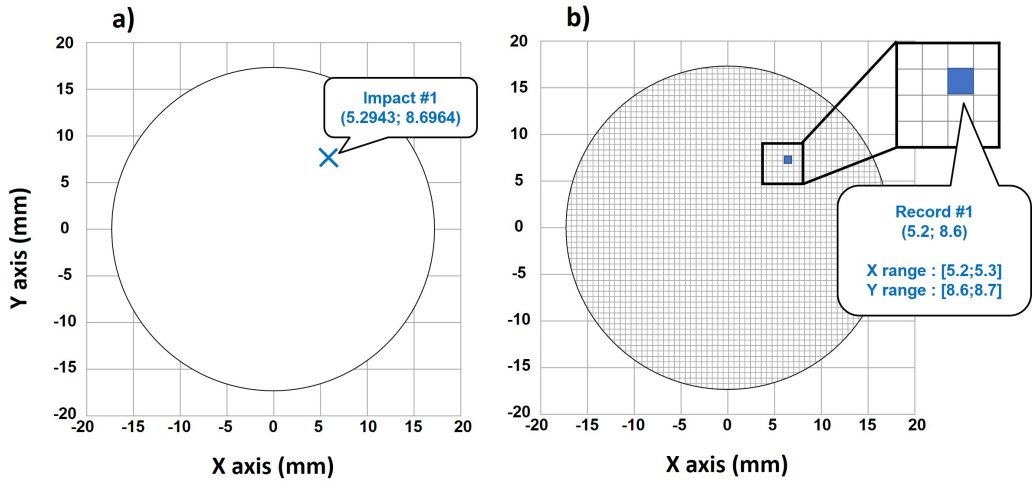

Figure I.8: Illustration of the discretization of an impact position (a) to a virtual pixel on the detection surface, having the dimension of the spatial resolution (b).

Position errors and spatial accuracy

In cases where the spatial resolution would be very small, one may ask whether it could be possible to detect impact positions that would be very close to their respective real impact positions. Theoretically, the distance between real impact positions and their associated detected positions, also called **position errors**, would give a quantitative answer to this last question (Figure I.9). The qualitative term associated to this criterion is called spatial accuracy. The lower are the position errors, the higher will be **spatial accuracy** of the PSD.

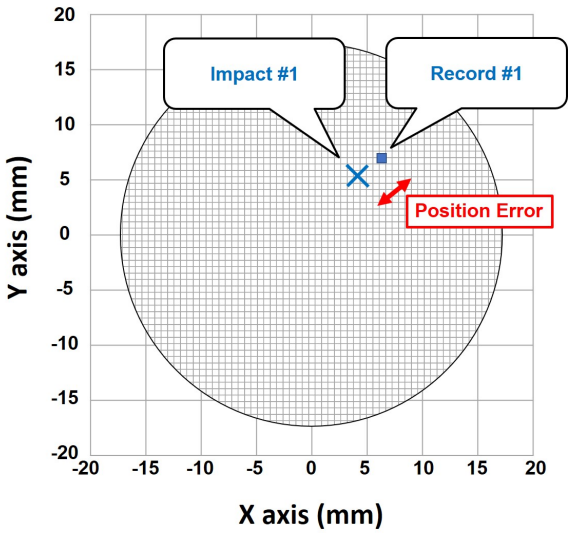

Figure I.9: Illustration of the position error between a recorded impact position and its associated real position.

However, experimentally, it is not possible to correctly estimate those position errors because of the obvious lack of information about real impact positions. One the means used for avoiding position errors is the use of constant parameters to calibrate the PSD, upstream or downstream of the measurements. An example can be found in the use of an in-situ calibration mask placed at the front-end of the detection surface, where the pattern of the mask is finely identified upstream (Figure I.10). A comparison between the reference pattern of the calibration mask and the pattern obtained with the detected positions, allows the application of corrections that will be able to increase the spatial accuracy of the PSD.

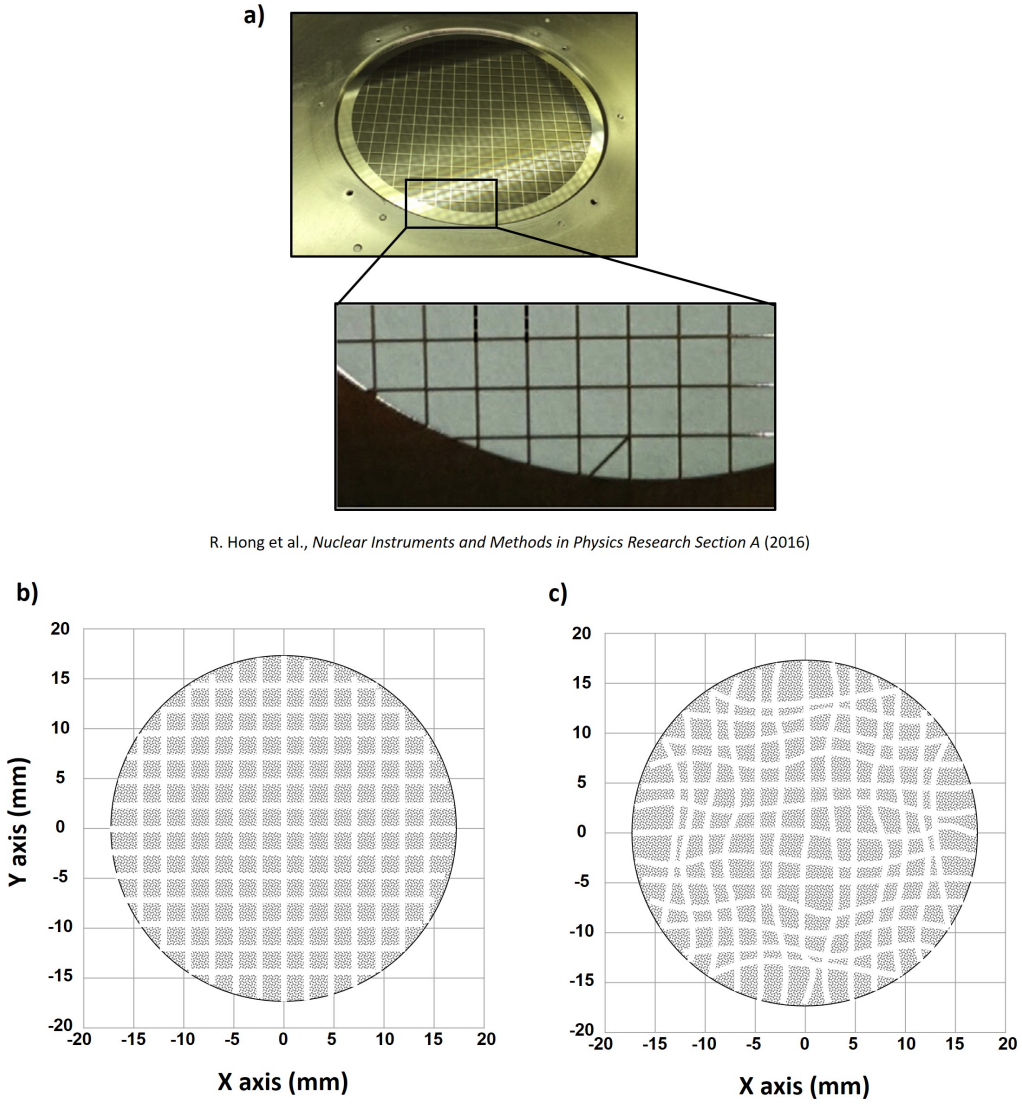

Figure I.10: (a) Photograph of a calibration mask, placed in front of a PSD detection surface, used for indirectly correcting position errors; (b) Perfect hit map that would be detected if there is no position error on the entire detection surface; (c) Distorted hit map caused by significant position errors of the detection surface. The spatial transfer function between (b) and (c) would allow the reduction of position errors and increase the spatial accuracy of the PSD.

Spatial precision

By minimizing the spatial resolution and maximizing the spatial accuracy of PSDs, it would be possible to provide impact positions that would be

very close to the real impact positions. However, assuming that individual particle impacts are respectively located at the same position on the PSD detection surface, one may ask if the recorded positions will always give the same coordinates, by relying solely on a high spatial resolution and a high spatial accuracy. It turns out that despite the significant efforts that could be applied for performing position measurements in repeatable conditions, it is almost impossible to record exactly the same position for individual particle impacts truly arriving at the same position. Therefore, it is most likely that each individual recorded position is surrounded by a position uncertainty (Figure I.11). This position uncertainty, also called the **spatial precision**, is usually expressed numerically by measures of imprecision, such as standard deviation, variance, or coefficient of variation under the specified conditions of measurement.

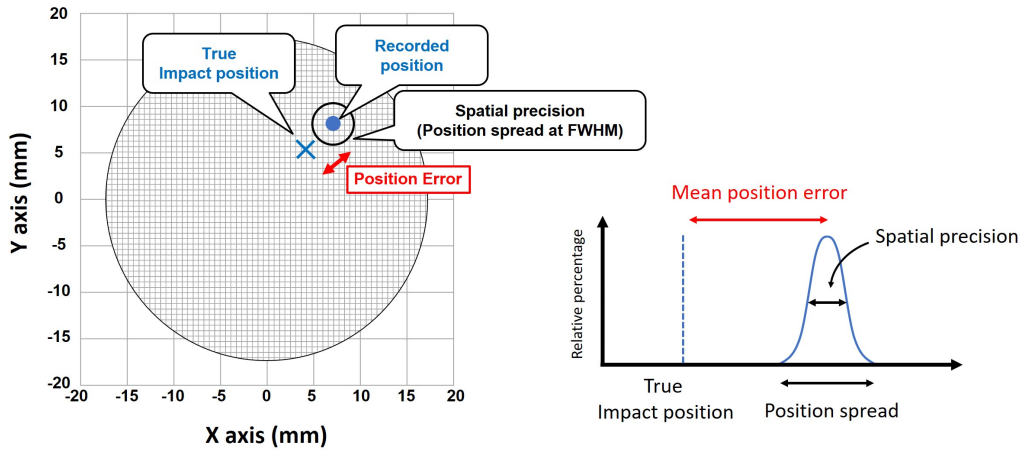

Figure I.11: Illustration of the main performance criteria allowing the evaluation of PSDs.

In most cases, the spatial precision can also be used for determining the spatial resolution. Indeed, the relative position spread induced by the spatial precision can be used for determining the smallest perceptible change in position for individual measurements (spatial resolution). In most cases the spatial resolution is determined through the full width at half maximum (FWHM) of this position spread (Figure I.11). Care must be taken to do not erroneously confuse "spatial precision" with "spatial accuracy". While the first one is a quantitative term that determine the relative spread of recorded positions, the other one is a qualitative term qualifying the level of position errors occurring during position measurements.

I.2.2 Field Ion Microscopy

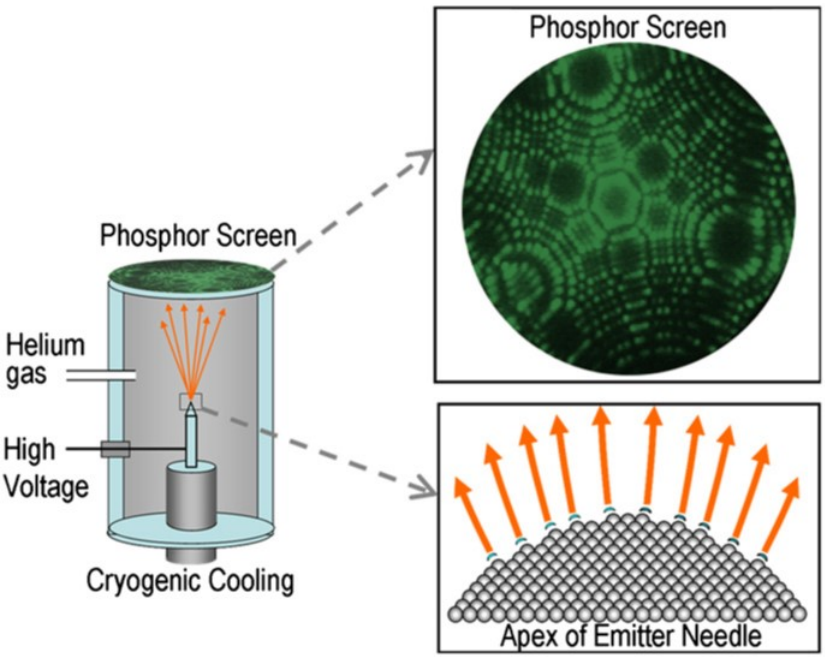

Figure I.12: Essential components of the FIM. Within the FIM (left) the atomic sites at the apex of a needle provide sufficient field strength to ionize any nearby helium gas atoms (lower inset). The resulting stream of ions emanates from the disc shaped regions above the atomic sites and creates a pattern on the phosphor screen (upper inset) [45].

The history of APT detectors began with an older-established technique called the Filed Ion Microscopy (FIM). The FIM is the ancestor of APT, and shares the same principles, with the exception that instead of directly evaporating atoms from tip surfaces, noble gas atoms, used in an imaging purpose, are introduced inside the analysis chamber. Under the high electric field existing in the vicinity of the tip (Figure I.12) these atoms are adsorbed, positively ionized and finally projected to an imaging screen, in such a way that each surface atom acts as an ionization site for the imaging gas. In 1955, E. W. Müller and his graduate student Kanwar Bahadur revealed the first observation of a material surface at the atomic scale through this technique [40]. At that time, the imaging screen was a simple fluorescent screen, performing an inefficient ion-to-photon conversion It is well known that the brightness of such a direct ion image is low because of the small ion-current density at the screen [51]. Furthermore, it is considered that each surface atom ionizes between 1,000 and 100,000 image gas atoms per second.

Long exposure times were then necessary to achieve direct visualization of atomic contrasts. Therefore, with sufficient exposure, the cumulative image of ions impacting the screen was able, for the first time, to reveal the atomic structure of a material surface on 2D maps.
In order to realize how far the instrument was able to resolve atomic structures, it could be useful to look after the smallest perceptible variation of position on FIM images, known as the spatial resolution [17]. At the early stages of the FIM, it has been reported that the spatial resolution could reach ∼3 Å (by taking into account the instrument magnification), which was sufficient for resolving the atomic lattice of low-index poles in pure materials [39]. The logical outcome to this development was to associate this high spatial resolution to a single particle sensitivity.

I.2.3 The Microchannel Plates

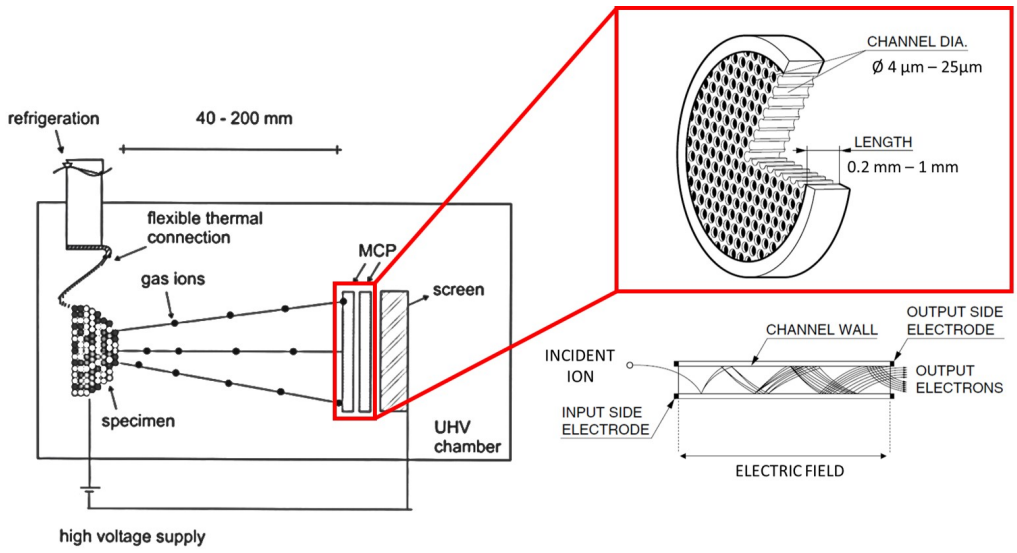

Figure I.13: Imaging system of the last version of the FIM instrument, consisting of a single or a chevron-type MCP coupled with a phosphor screen [1]

To offset the loss of brightness from the first FIM setup, other devices called Microchannel Plates (MCP) have been appended to the phosphorescent screen in order to increase the image brightness through an intermediate ion-to-electron conversion (Figure I.13). An MCP is essentially a two-dimensional array of millions of ultra-thin conductive glass capillaries, from 4 µm to 25 µm in diameter and 0.2 mm to 1 mm in length, fused

together and sliced in the shape of a thin plate [29]. The diameter of the active area can vary between 20 mm and 100 mm. By means of a coating made of special semiconducting material, having secondary electron emission characteristics [10, 24, 26], each of these capillaries (or channel) works as an independent secondary electron multiplier, and form together a two-dimensional secondary electron multiplier.
When an ion hits the internal surface of a channel, with sufficient energy to overcome the work function of the doped semiconducting glass, secondary electrons are generated [29, 30]. Through an accelerating voltage of ∼1000 V between the metallized input and output faces of the MCP (Figure I.13), these secondary electrons are accelerated down the channel and trigger a chain reaction implying successive secondary electron emissions all along the channel path at each new electron-matter interaction. A charge cloud made of 1,000 to 10,000 secondary electrons is finally generated at the channel output [3, 29]. One can infer that this gain could be increased by increasing the accelerating voltage applied on the MCP. However, it turns out that the gain of MCPs is strongly nonlinear. Indeed, it has been observed that the increase of the gain is limited by a maximum electron density at the end of each channel, having the effect of saturating every MCP output pulse to the same amount of electrons [3, 29]. This saturation effect turns out to be an advantage in atom probe experiments since all elements can be detected in the same way, without inducing selective losses. As illustrated in Figure I.14, under the saturation effect, lighter ions introduce higher detection efficiencies than heavier ions for a same MCP bias voltage.

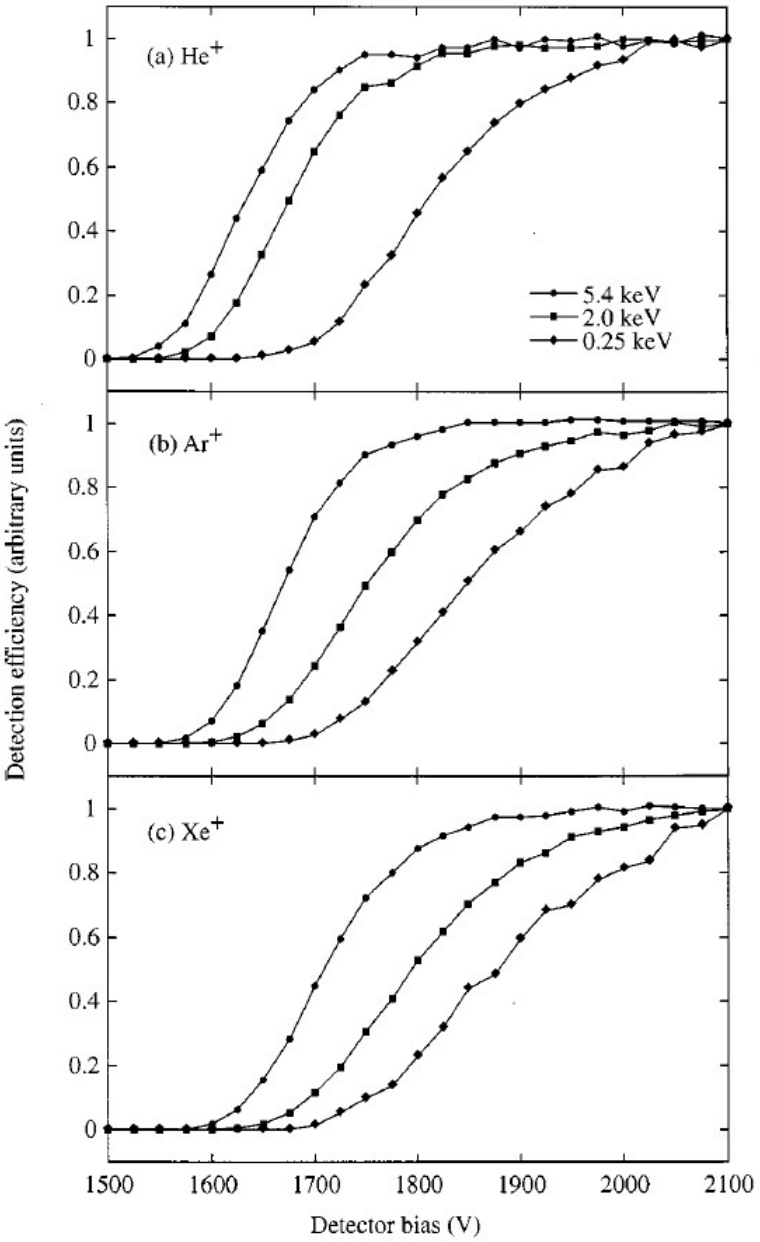

Figure I.14: (From [49]) Relative ion detection efficiency as a function of detector bias for for (a) He^+, (b) Ar^+, and (c) Xe^+ at impact energies of 0.25, 2, and 5.4 keV. Note that each of the nine curves has been normalized to unity at a detector bias of 2100 V (in a chevron configuration).

With the aim of increasing the gain of MCPs, it is required to stack them into assemblies. Therefore, MCPs are often mounted in two or three stacks

(chevron or Z-stack configuration), spaced at ∼100 microns apart from each other (Figure I.15). By this way, the gain of MCP assemblies can reach up to 10^8 secondary electrons.

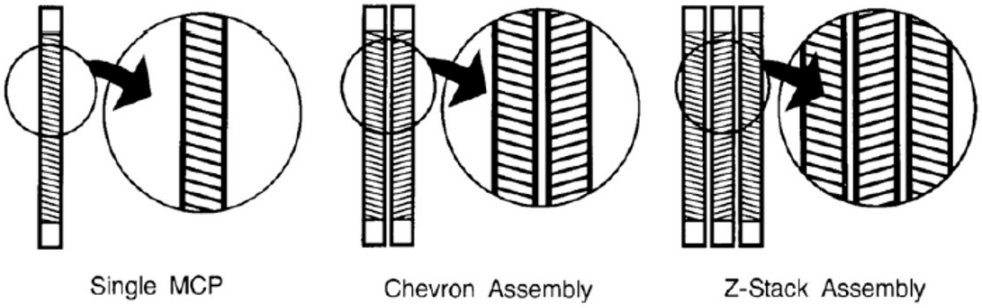

Figure I.15: MCP stack configurations (from [3])

It has been stated that the spatial resolution of this new setup is still comparable to a conventionally recorded field-ion image and have not been degraded through the ion-to-electron conversion applied by the MCP assembly [51]. Indeed, the bursts of electrons from MCP output are spatially localized in sub-millimeter zones centered on ion hits position [50], corresponding to few angstroms on the analyzed material, by taking into account standard magnifications exceeding the million.
Like all active components (devices having the ability to amplify a signal through an external DC supply), the MCP assembly is subjected to noises interfering with useful signals. It has been observed that this background noise mainly depends on the vacuum level of the analysis chamber, and also depends on the MCP bias voltage [29, 50, 55]. The background noise is generally limited to less than 1 hit/s/cm^2 at higher gain.
It may also be noted that electron bursts are also localized in time after ion hits. Indeed, with sufficient gain and voltage, the impact of an ion on the MCP surface can give a small electrical signal of 10 to 100 mV in amplitude, and 1 to 5 ns in width, for generating stop signals to a timer [14, 29].
Subsequently, due to their high performances in terms of single particle detection and spatial resolution MCP assemblies have, from that point, equipped all types of atom probe instrument.

I.2.4 The Atom Probe Field Ion Microscope

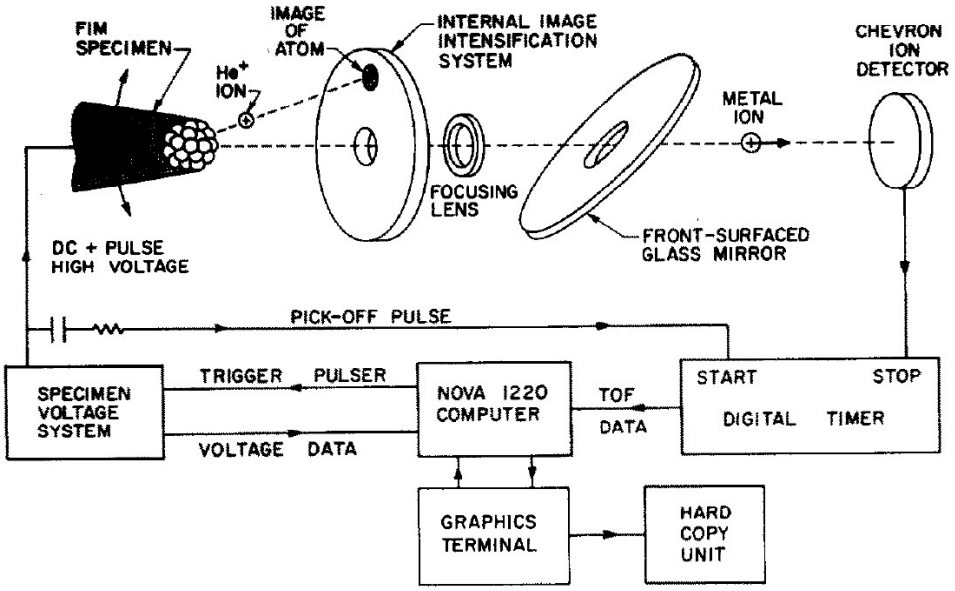

Figure I.16: Schematic diagram of the APFIM. While preserving the main setup of the FIM, a small aperture has been drilled at the center of the MCP phosphor screen detector for performing TOF measurements of individual ions. In addition to expelling gas ions for imaging the specimen surface on the phosphor screen, a further step consists of removing the "image gas" from the vacuum system in order to exclusively ionizing atoms from the specimen surface by combining the DC voltage with an additional electric pulse, and then identify them through a TOFMS technique [53]

Despite the impressive technical achievement of the FIM technique, its lack of chemical sensitivity has the effect of being limited to the analysis of pure materials, introducing only highly perfect FIM patterns. It turns out that most of researches in material sciences involve the study of materials containing impurities, different elements, and/or different phases. High amount of unregular FIM patterns are then expected with this technique [19, 46]. Therefore, it is quite clear that the development of an analytical tool, combining FIM analyses and single particle chemical sensitivity, would bring a clear added-value to concrete material analyses.
This additional dimension was brought by Müller and Panitz in 1968 [41] with the development of the Atom Probe Filed Ion Microscope (APFIM). The APFIM was developed with the aim of combining the FIM setup with a mass spectrometer. While preserving the main setup of the FIM, a small aperture

has been drilled at the center of the MCP phosphor screen detector for performing TOF measurements of individual ions, directly originating from the specimen, between the specimen and a single atom detector (Figure I.16). In addition to expelling gas ions for imaging the specimen surface on the phosphor screen, a further step consisted of removing the "image gas" from the vacuum system in order to exclusively ionize atoms from the specimen surface by combining the DC voltage with an additional electric pulse, and then identify them through a TOFMS technique (see "Time-of-Flight Mass Spectrometry"). Knowing the fixed distance between the specimen and the single atom detector, this new setup allowed for determining the mass-to-charge ratio of individual ions (Equation (I.7)). In order to keep an eye on FIM images, a front silvered mirror, oriented at an angle of 45° with respect to the phosphor screen [41,53], has been placed between the phosphor screen and the single atom detector (Figure I.16).

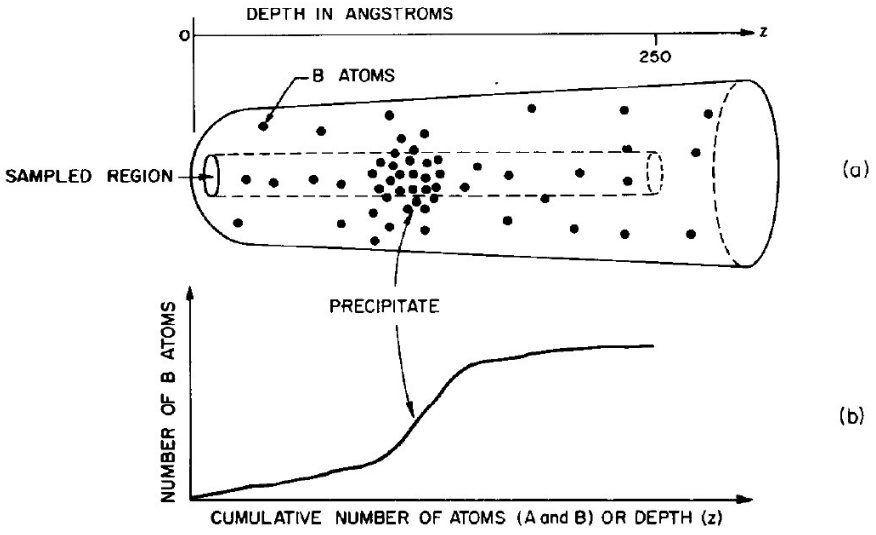

Figure I.17: During the course of an atom-by-atom dissection of a FIM specimen the atom probe determines the distribution of chemical species in an approximately cylindrical volume element of the specimen as shown in 2(a). A plot of the number of B atoms in the binary alloy consisting of A (solvent) and B (solute) atoms versus the total number of atoms (A plus B) detected yields a composition profile. The presence of a local composition variation produced by a precipitate rich in B results in a change of slope of the composition profile; this is illustrated in 2(b) [53]

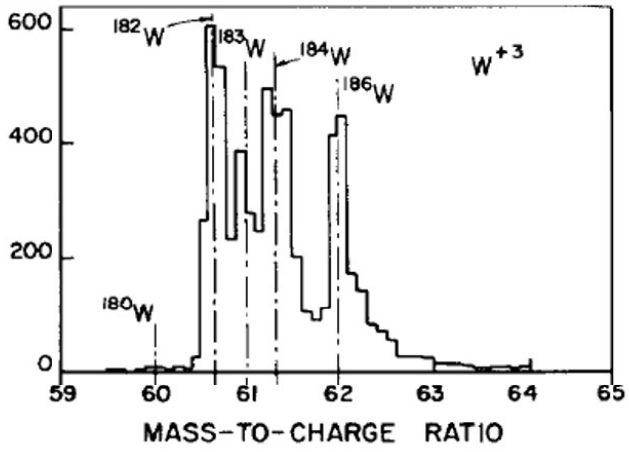

Figure I.18: Mass spectrum from the analysis of a tungsten tip, analyzed with an APFIM instrument and field evaporated with electric pulses varying from 13 to 15 kV, and a tip-to-detector distance of 1.6 m [53]. The total number of W^{3+} events in this histogram is 6045

Through this additional dimension, a fraction of a particular element in a small volume can be determined by simply counting the number of atoms of that element related to the total number of detected atoms (Figures I.17 and I.18). With the capability to select areas of interest, containing defects or impurities, the APFIM represented one of the best analytical tool for determining local compositions with a sensitivity that could reach parts per million [28, 36]. As illustrated in Figure I.18, it can be seen that the major isotopes of the tungsten (^{182}W, ^{183}W, ^{184}W and ^{186}W) can be resolved through an APFIM setup characterized by electric pulses varying from 13 to 15 kV, and a tip-to-detector distance of 1.6 m. The resulting MRP (see Time-of-Flight Mass Spectrometry) at the mass peak centered at 62 Da can be measured with a value of 345 (FWHM).

I.2.5 The 10 cm Atom Probe

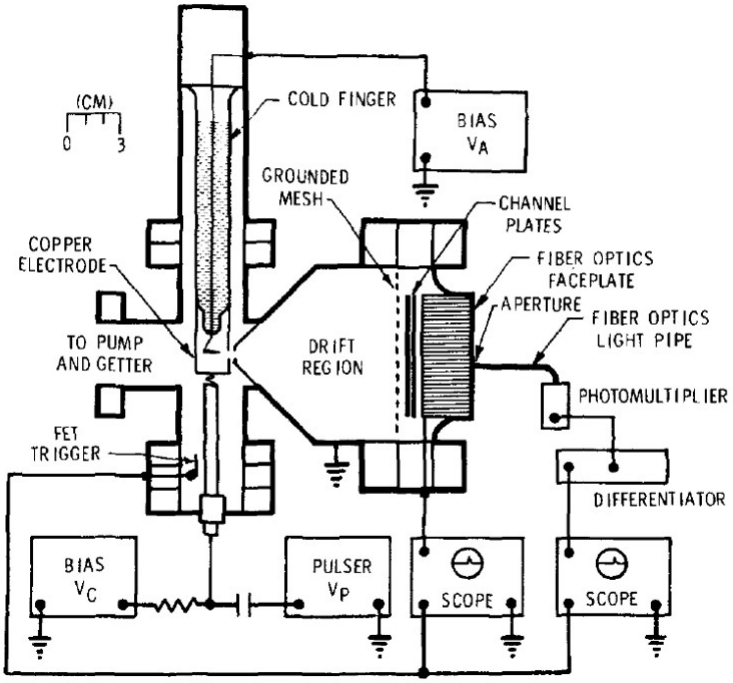

Figure I.19: Schematic of the 10 cm Atom Probe [43]. Imaging is done at the detector, eliminating the need for a probe hole or a mechanism to move the specimen. In order to preserve the benefits given by the TOFMS in terms of compositional analysis a photomultiplier aperture has been placed outside the vacuum system to record TOFs from preselected atomic sites.

The next breakthrough was brought by Panitz in 1973 with the "10 cm Atom Probe" [43], thereafter called the Imaging Atom Probe (IAP). The idea behind this instrument was to simplify former atom probe designs and, for the first time, record the precise position of each desorbed ion on the detection surface. To do so, the former MCP-phosphor screen detector, deprived of probe-hole, has been taken back for imaging the entire specimen surface, while continuing to perform TOFMS. This performance was reached through the use of a photomultiplier aperture, placed outside the vacuum system, recording TOFs from preselected atomic sites (Figure I.19).

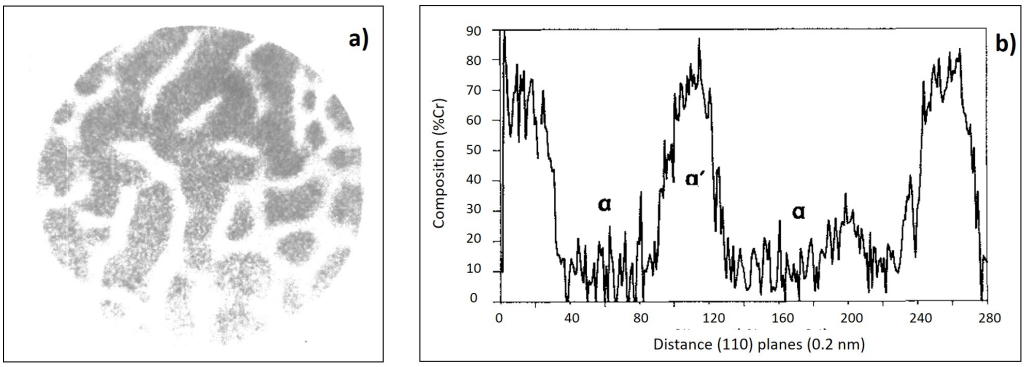

Figure I.20: Results from the analysis of a Fe-45 wt.% Cr alloy on the IAP instrument; a) Field desorption micrograph of the analyzed sample. Bright regions are chromium-enriched α' phase. b) One-dimensional composition profile across α-α' phase boundaries in the specimen

Therefore, conversely to the APFIM, the idea was not to acquire a refined mass spectrum during the analysis, but to accurately locate and characterize areas of interest, without changing the orientation of the sample . Moreover, this is through a controlled time-window, during TOF measurements, that single elements can be characterized in terms of composition and spatial distribution (Figure I.20).

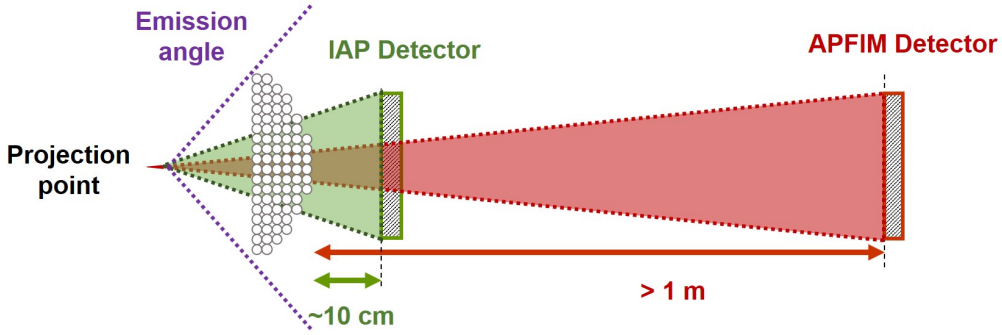

Figure I.21: Comparison between IAP and APFIM detection angles. The short distance between the sample and the detector on the IAP allows the collection of higher volumes of atoms.

By contrast with the APFIM, the IAP instrument is known as a wide-angle atom probe. Which mean that, due to the reduced distances between the sample and the detector, related to APFIM setup ($>$ 1 m), the IAP allows an increase of the analyzed volume (Figure I.21). However, despite this improvement, it has been observed that the reduction of the

tip-to-detector distance has a significant effect on the MRP [43]. By referring to the theoretical expression of the MRP (Equation (I.8)), one can note that the reduction of the tip-to-detector distance has the effect of degrading the ability of the instrument to distinguish elements with very near mass-to-charge ratios. It has been reported that the main parameter responsible to this performance loss, is the timing system. Panitz experiments showed that time spreads of only 3.5% on TOF measurements, can introduce significant downturns in the MRP. Given the major impact of the timing precision in atom probe experiments, Panitz shown that the MRP can be reduced to the following equation;

$$MRP \approx \frac{TOF}{2.\Delta TOF} \tag{I.15}$$

By this way, it has been reported that the MRP cannot exceed 15 (FWHM) for a mass peak centered at 62 Da (tungsten tip) on the IAP. As a comparison, the previous analysis of a tungsten tip on the APFIM (Figure I.18), introduced a MRP of 345 (FWHM). That is why, one the proposed solutions for keeping large analyzed volumes and high MRP, is the improvement of the timing system.

I.2.6 The Position Sensitive Atom Probe

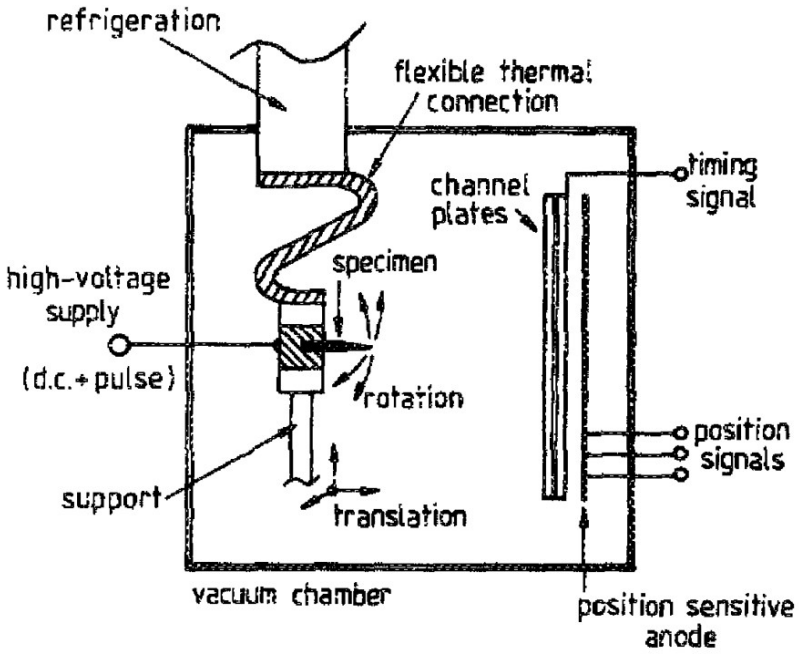

Figure I.22: Schematic design of the PoSAP [12]. The PSD consists of an MCP assembly mounted in chevron configuration coupled with a position-sensitive wedge-and-strip anode, which is mounted behind the MCP assembly at a distance of 10 mm and is held at -200 V with respect to the output of the MCP assembly. The tip-to-detector distance is held at a distance of 110 mm.

These great advances have finally conducted the atom probe community to think that future developments should lead to an ultimate instrument that would be able to detect all atoms from the volume of analyzed materials, by getting their original position with an atomic resolution, and uniquely determine their elemental identity [36]. Despite the breakthrough brought by Panitz, the IAP could only characterize a selection of mass-to-charge ratios located at restricted areas of the detection surface. To perform the detection of all elements during the same analysis, it was necessary to acquire both positions and mass-to-charge ratios on the same detector. This vision was unable to start without the emergence of the first position-sensitive atom probe, also known as the PoSAP, giving rise to the first three-dimensional atom probe (3DAP).

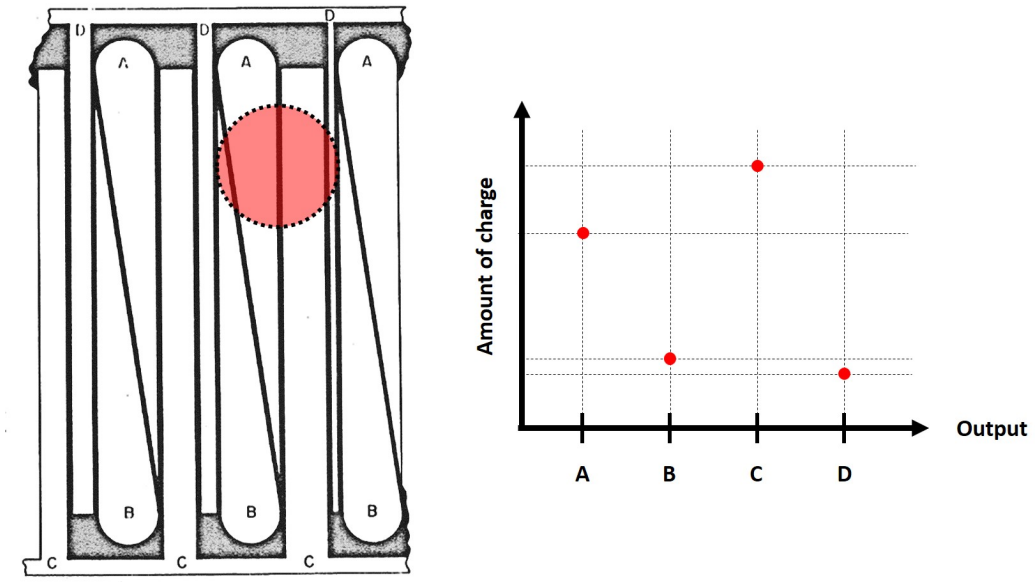

Figure I.23: Schematic of a WSA detector [32]. The X and Y coordinates of an electron cloud, originating from the MCP back-end, are determined by computing relative charge ratios between the different outputs (A, B, C and D).

In 1988, Cerezo and his coworkers substitute the conventional phosphor screen by a commercially available off-the-shelf PSD, called the Wedge-and-Strip Anode (WSA) [36]. The WSA is a PSD on which the working principle is based on charge measurements. Figure I.23 illustrates one of the first versions of WSA, firstly used for space programs [32]. The simplicity of this version permits to get a clear understanding of the working principle of this type of detector. The figure describes the detection surface covered by pseudo-periodic pattern made of wedges and strips. A, B, C and D electrodes are used for collecting and distributing the amount of charge coming from the MCP back-end.

$$X = \frac{C}{C + D} \tag{I.16}$$

$$Y = \frac{A}{A + B} \tag{I.17}$$

Components having the same shape are electrically connected each other, which makes the WSA detector a serial encoding system. On one side, all wedges (A and B electrodes) have the same shape and reveal charge collecting areas that vary linearly with the Y-coordinate. Their staggered

configuration enables the introduction of a charge ratio that is propotional to the Y coordinate of the charge centroid position (Equation (I.17)). On the other side, the strips (C and D electrodes) reveal charge collecting areas that vary linearly with the X-coordinate. Similarly, their inter-engaged comb-like pattern enables the introduction of a charge ratio that is propotional to the X coordinate of the charge centroid position (Equation (I.16)). This encoding system makes it possible to reach a lateral spatial resolution of $\sim$5Å and a depth resolution of one atomic layer after the 3D reconstruction (Figure I.24).

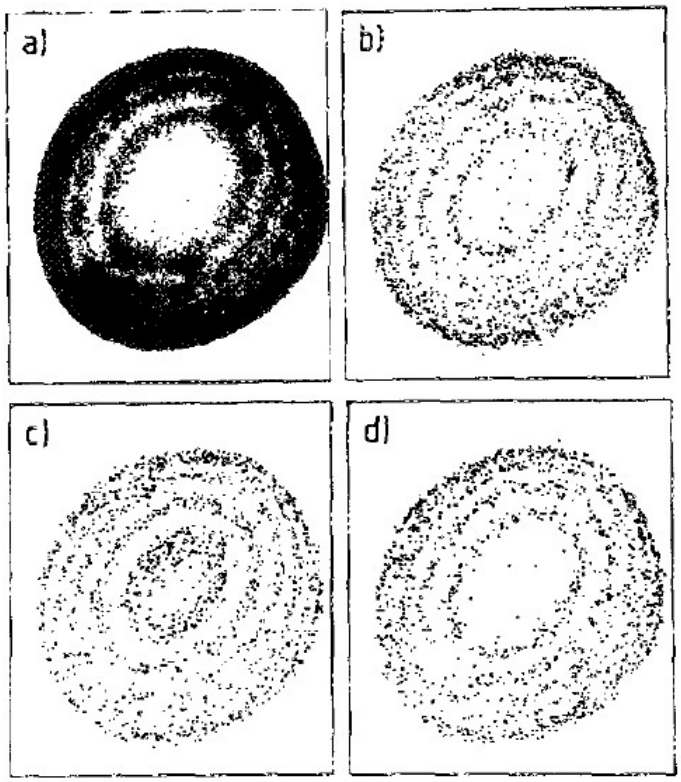

Figure I.24: First results published by Cerezo et al. with the PoSAP instrument [12]; (a) Digitized field-ion image of the (110) pole of a tungsten specimen; (b)-(d) Distributions of tungsten ions (W^{4+} and W^{3+}) obtained in consecutive analyses from the region shown in (a), showing the collapse of a (110) plane. Each image represents the analysis of about 2000 ions ($\sim$0.3 monolayer).

Despite the simplicity of the WSA working principle, a major limitation prevents its use in the framework of quantitative APT analyses. Regarding the serial processing used for determining impact positions, one can note that it is clearly impossible to treat impacts having very close TOFs during

a same evaporation event, also known as a multi-hit event. Indeed, it turns out that that the electronic detection system of the PoSAP was unable to record successive TOFs separated by a time duration under 300 ns, due to the time to collect and digitalize every impact. This duration is also known as the dead-time of the detection system. With a tip-to-detector distance of 110 mm, and an electric pulse reaching a potential of 10 kV, it can be calculated that Al^+ ions, having a mass-to-charge ratio of 27 Da, can only be followed by ions having mass-to-charge ratios exceeding approximately 80 Da. In order to avoid losses caused by this effect, known as the "pile-up effect", the detection rate had to be restricted to around 0.01 atoms per pulse, limiting the maximum data acquisition rate that could be achieved.

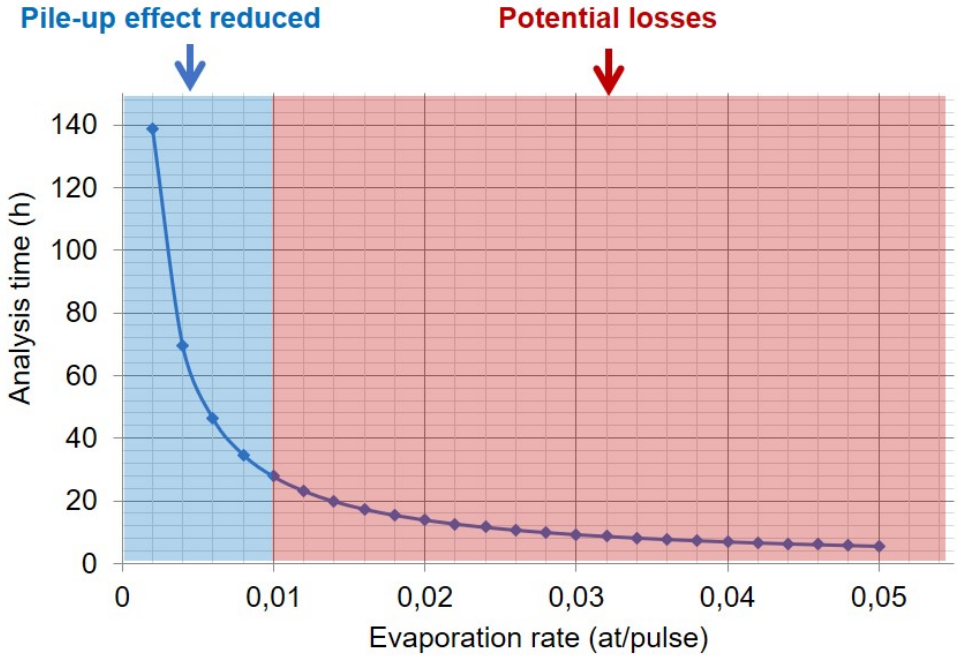

Figure I.25: Theoretical analysis time that can be achieved for detecting one million of atoms with the PosAP as a function of the evaporation rate. It has been assumed a pulse rate of 1 kHz.

Figure I.25 implicitly shows the importance of resolving multi-hit events both because of potential compositional biases that may occur during the dead-time, and because of the waste of time induced by the reduction of the evaporation rate. Indeed, it can be seen that the reduction of the pile-up effect through the reduction of the evaporation rate, involves the increase of the analysis time up to hundreds of hours.

I.2.7 The Tomographic Atom Probe

An alternative to the serial approach used by WSA detectors is the use of a parallel encoding system. This approach has already been studied few years before the emergence of the PoSAP [5], firstly designed by Bostel et al. in 1989 [8], and finally developed in 1993 under the name of Tomographic Atom Probe (TAP) [6]. This time, the idea was to improve the multi-hit capacity of APT instruments by using a multi-anode detector.

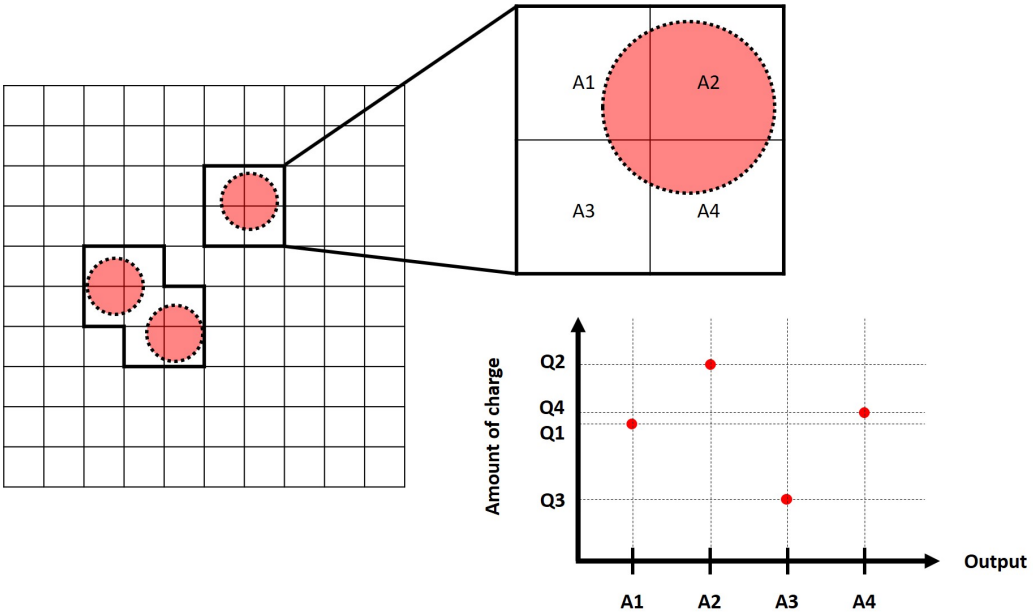

Figure I.26: Schematic of a multi-anode detector. The x and y local coordinates from a zone affected by an electron cloud, originating from the MCP back-end, are determined by computing relative charge ratios between the different concerned anodes (A1, A2, A3 and A4).

$$x = \frac{Q2 + Q4}{Q1 + Q2 + Q3 + Q4} \tag{I.18}$$

$$y = \frac{Q1 + Q2}{Q1 + Q2 + Q3 + Q4} \tag{I.19}$$

The multi-anode detector used in the TAP was a 10 X 10 array of individual cells (Figure I.26), using a parallel processing that was able to identify ions from simultaneous impacts. In the same way as WSA detectors, the working principle of multi-anode detectors was also based on charge measurements.

After collecting electron clouds coming from the MCP back-end, the first step consists of localizing the different cells that have been affected. To do so, a charge threshold is fixed on each cell to avoid the detection of noise. According to the size of electron spots, the number of cells affected and the spatial distribution of charge will determine the number ions detected. Then, precise positions are determined by the computation of charge centroids, which represents an approach that is very close to the WSA. Each separated zone, comprised of impacted adjacent cells, is labeled with x and y local coordinates (Equations (I.18) and (I.19)) that give the precise position of ion impacts. The illustrated example in Figure I.26 shows that x and y local coordinates from an impact zone can be obtained by computing charge ratios between the amount of charge collected on designated reference cells (Q2 and Q4 for the X-axis, and Q1 and Q2 for the Y-axis), and the total charge Q collected inside the zone. One can note that for avoiding artifacts during the detection process, the electron spot size has to be correctly defined in such a way that any scenario can be managed [5].
A similar parallel type system was also thought by Miller et al., under the name of Parallel Atom Probe (PAP) [34]. The PAP concept gathered two different designs; one similar to the multi-anode used in the TAP, and another one introducing an array of photodiodes. The latter will not be described regarding its proximity to the TAP detector.
The main disadvantage of multi-anode detectors is their limited spatial resolution caused by their limited number of individual cells that can be used [34]. In fact, using a high number of cells has the effect of increasing the complexity of the detection system. Essentially, the more the detection system has to treat information, the more the detection system itself will be busy to ensure information exchanges between parallel cells. The only way to increase the size of multi-anode array without overloading the detection system would be to reduce the acquisition rate by reducing the evaporation rate. However, it would highly increase the acquisition time (Figure I.25).
By referring back to WSA detectors, one can mention their superiority in spatial resolution compared to multi-anode detectors [12, 32]. Indeed, contrary to the discrete geometries of multi-anodes, the WSA introduces electrode geometries that give continuous variations all along the X and Y axes. As a result, WSA detectors can typically achieve a spatial resolution ten to one thousand times finer than the spatial structure of multi-anode detectors.
At this point, it is clear that a trade-off between high spatial resolution and multi-hit capacity has to be considered for ensuring the performances of APT instruments.

I.2.8 The Optical Atom Probe

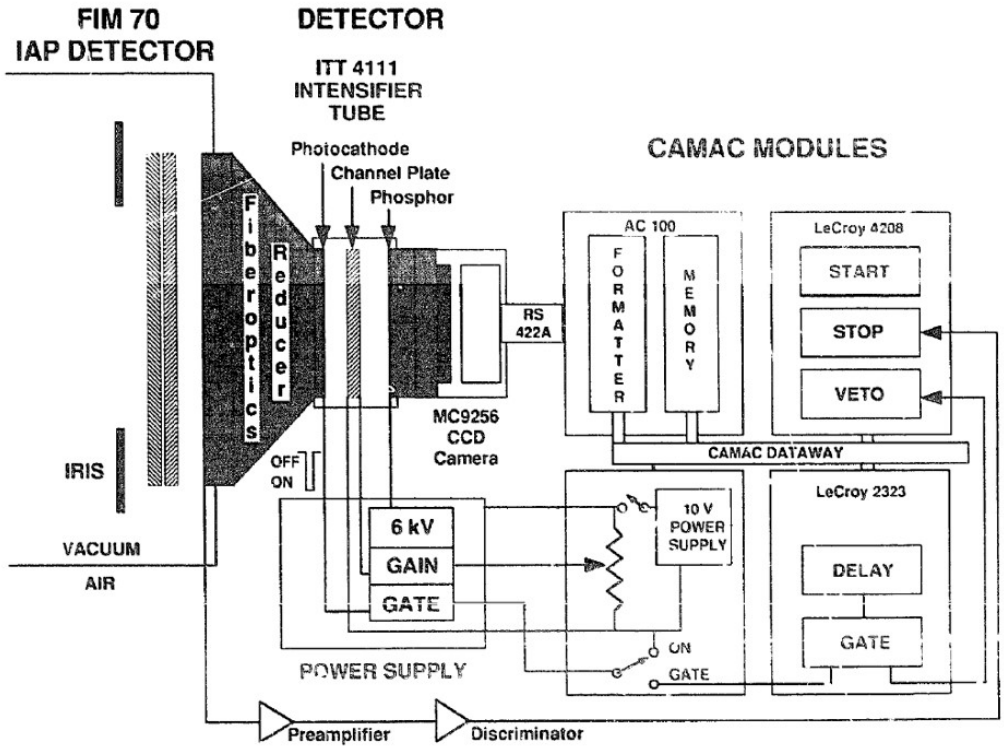

Figure I.27: Schematic diagram of the OAP [35]. This detector provides both visible and electrical signals of coming from ions impact. The PSD consists of an MCP assembly mounted in chevron configuration coupled a phosphor (P20) screen that is coated on the inside of the fiber-optics window that forms the vacuum seal. The tip-to-detector distance is held at a distance of 146 mm.

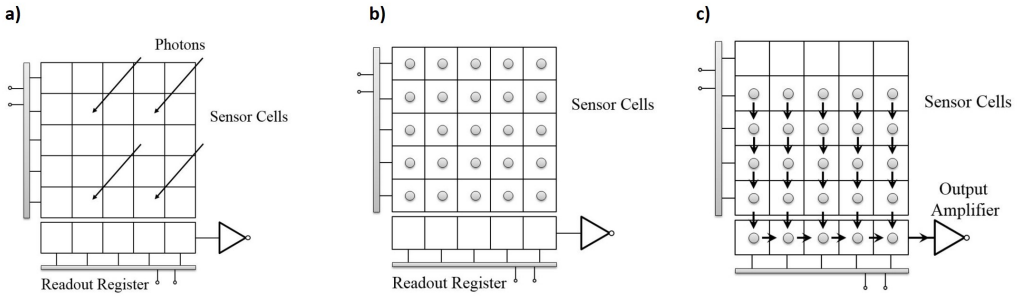

Figure I.28: Imaging process of a CCD camera [48]. a) The first step of the process is the acquisition phase, when incoming photons fall on the sensitive MOSFET cells. b) Then the cells convert incoming photons into electrical charges. c) Finally, the readout phase is in charge of handling charges row by row to generate the final image through the vertical transfer, horizontal transfer, voltage conversion and amplification processes.

During the same time as the TAP was developed, another instrument called the Optical Atom Probe (OAP) was aimed at maintaining the high spatial resolution obtained with the IAP by keeping the MCP-phosphor screen detector [35]. The idea was to record the coordinates and the TOF of each incident ion through the use of a CCD camera at the output of the phosphor screen (Figure I.27). Instead of determining ion impacts through charge centroids, the OAP detector was aimed at localizing ion impacts through the conversion of electron clouds into light spots. This idea was based on the potential performances of CCD cameras that introduce higher spatial resolution than previous multi-anode detectors from the TAP and the PAP. Indeed, the number of pixels available on CCD cameras is higher than the number of anodes on multi-anode detectors, making them excellent candidates for reaching high spatial resolution. Since the CCD array was made of 256 $\times$ 256 independent cells, this system was capable of deriving positions for many ions detected on the same evaporation pulse (multi-hit event).
The structure of the OAP detector is mainly composed of three parts; an MCP assembly, a phosphor screen and a CCD camera (Figure I.27). Electron clouds, coming from the MCP back-end, are converted into photons through the phosphor screen. Light spots generated are then converted into electric signals through the CCD camera, which is composed of Metal Oxide Semiconductor Field Effect Transistor (MOSFET) cells. As illustrated on Figure I.28, the photoelectric effect caused by photons on the gate of MOSFET cells, allows a discrete processing on the whole detection surface.

The processing of each voltage value extracted from MOSFET cells is performed by a serial data transfer.
During the OAP detection process, two kind on information are treated; TOF measurements and hit maps. At this time, one can state that difficulties may arise with the management of multi-hit events. Indeed, in the case of successive arrivals during a same event (successive TOF measurements), no additional information can indicate the order of arrival of detected ions. That means that only simultaneous ion impacts can be resolved. Therefore, the major limitation of the OAP is that, without a parallel timing scheme, it is not possible to directly correlate multiple TOFs with positions on the detector.

I.2.9 The Optical Position Sensitive Atom Probe

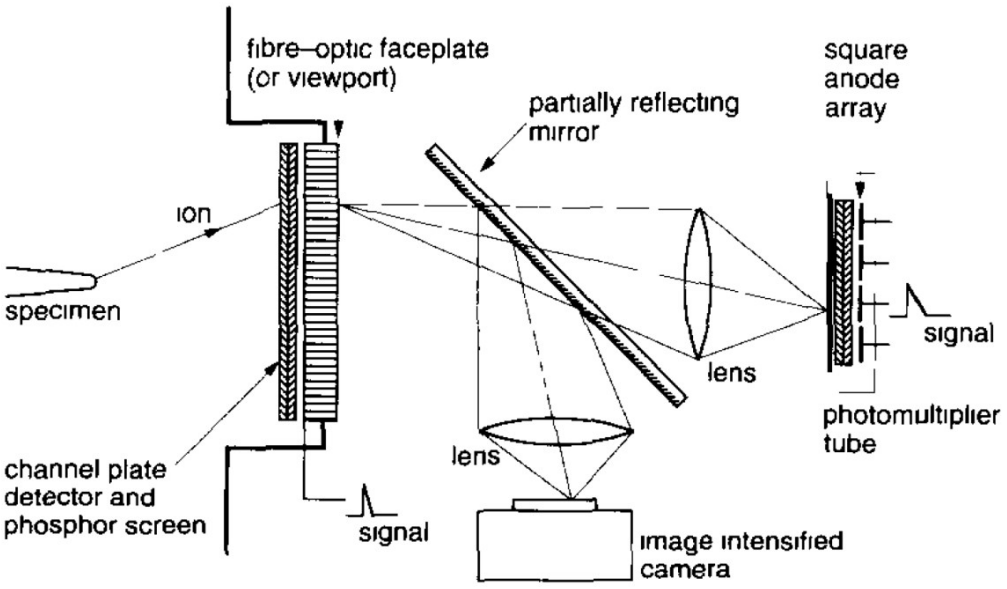

Figure I.29: Schematic of the Optical PoSAP [11]. As for the OAP, this detector provides both visible and electrical signals from ions impact. The PSD consists of an MCP assembly mounted in chevron configuration coupled with a phosphor screen. The light output from the phosphor screen is optically split and focused onto two separate closed-tube imaging systems; The image intensified camera and the photomultiplier array. The tip-to-detector distance is held at a distance of 280 mm.

To provide a pragmatic response to the strengths and weaknesses between

the OAP and the TAP instruments, having respectively a high spatial resolution and a high multi-hit capacity, the team behind the creation of the PoSAP proposed an instrument attempting to couple those respective performances. The Optical PoSAP (OPoSAP) [11] was an instrument combining in parallel the OAP setup, with an image intensified CCD camera, and a PAP detector, composed of a photodiode array (Figure I.29). In the same idea as the APFIM setup, a tilted semi-transparent mirror was used for both imaging and chemically identifying ions impinging the two orthogonally positioned detectors. Contrary to the APFIM, the TOFMS is applied over the whole detection surface. Moreover, contrary to the OAP, multi-hit events involving separate TOFs can be resolved by correlating spot light intensities, from the CCD camera, to signal amplitudes extracted on photodiodes. This operating mode makes the OPoSAP, theoretically, the best atom probe setup, gathering high multi-hit capacity and high spatial resolution. However, it must be recalled that, like the TAP instrument, the OPoSAP is basically a parallel-type system using an array of a hundred anodes. The high number of cells to manage makes the OPoSAP a complex system that cannot manage high detection rates without losing information.

I.2.10 The Optical Tomographic Atom Probe

In the quest for reducing the complexity of 3DAP instruments, a team from the University of Rouen decided to reduce the imaging and timing systems of the OPoSAP into a single system. The compact system was called the Optical Tomographic Atom Probe (OTAP) [18, 47]. The OTAP nearly relies on the same setup as the OAP, with the exception that a conductive strip array has been appended to the phosphor screen in order to reproduce the operating process of the TAP. As shown in Figure I.30, each conductive strip was connected to an individual timing system to perform a parallel processing, similar to multi-anode detectors. By this way, chances for detecting ions having different TOFs, during a same event, are increased through parallel timing measurements. However, due to the fact that conductive strips are only oriented on a single axis, the same problem as in the OAP still remain for ion impacts aligned on the same strip. It was not possible to directly correlate successive TOFs with positions coming from the same strip.

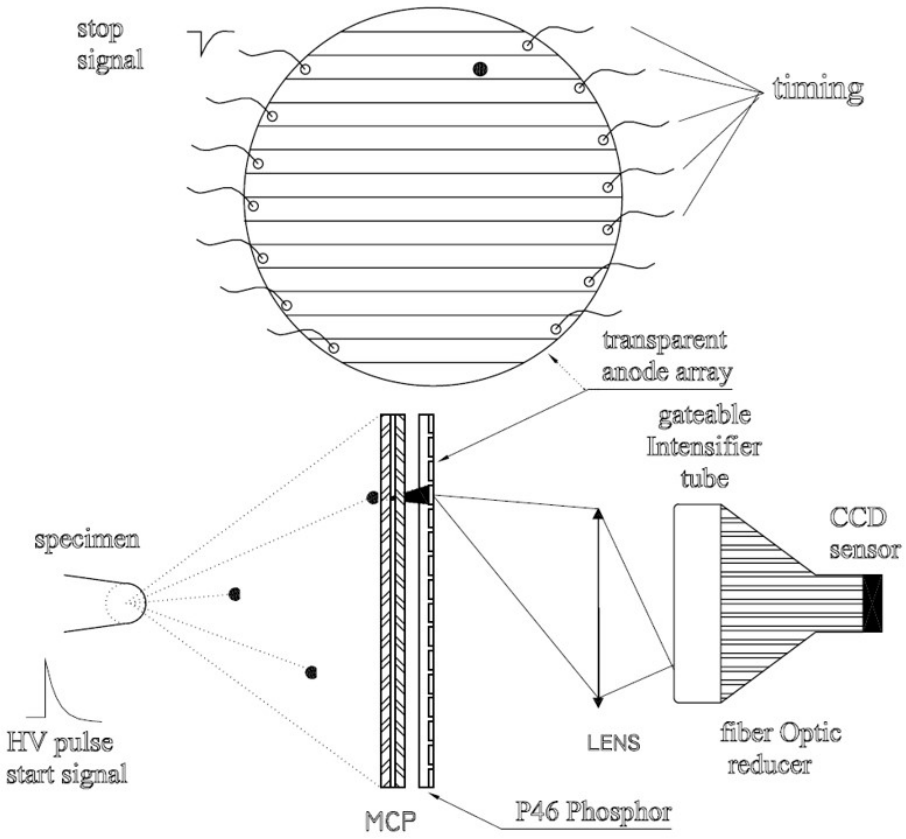

Figure I.30: Schematic diagram of the OTAP [18, 47]. The detector is basically an MCP–phosphor screen assembly in which the conductive coating of the phosphor screen is divided into 16 strip-like-shaped anodes. Electron clouds produced by ion impacts, generate light spots on the phosphor screen, and signal output from strips that are used as stop signals for timing. By comparing the image recorded by the CCD camera and the distribution of TOFs measured on the anode array, it is possible to assign a TOF to every light-spot.

Another limitation on the use CCD cameras is the limited acquisition rate. It should be understood that the acquisition of images on a CCD camera requires; an exposure time, a time to transfer data and a read-out time (Figure I.28). That means that CCD cameras, just like multi-anode detectors, have to be limited on their acquisition rate in order to prevent significant losses. Despite the existence of more recent image sensor technologies [20, 21] offering lower acquisition time, it is still not possible to get exploitable volumes in a working day without significant losses.
In the same way as the transition between charge detectors and optical

detectors, it was clear that another approach had to be adopted to get high spatial resolution, high multi-hit capacity and high detection rate capability.

I.2.11 Delay Line Detectors

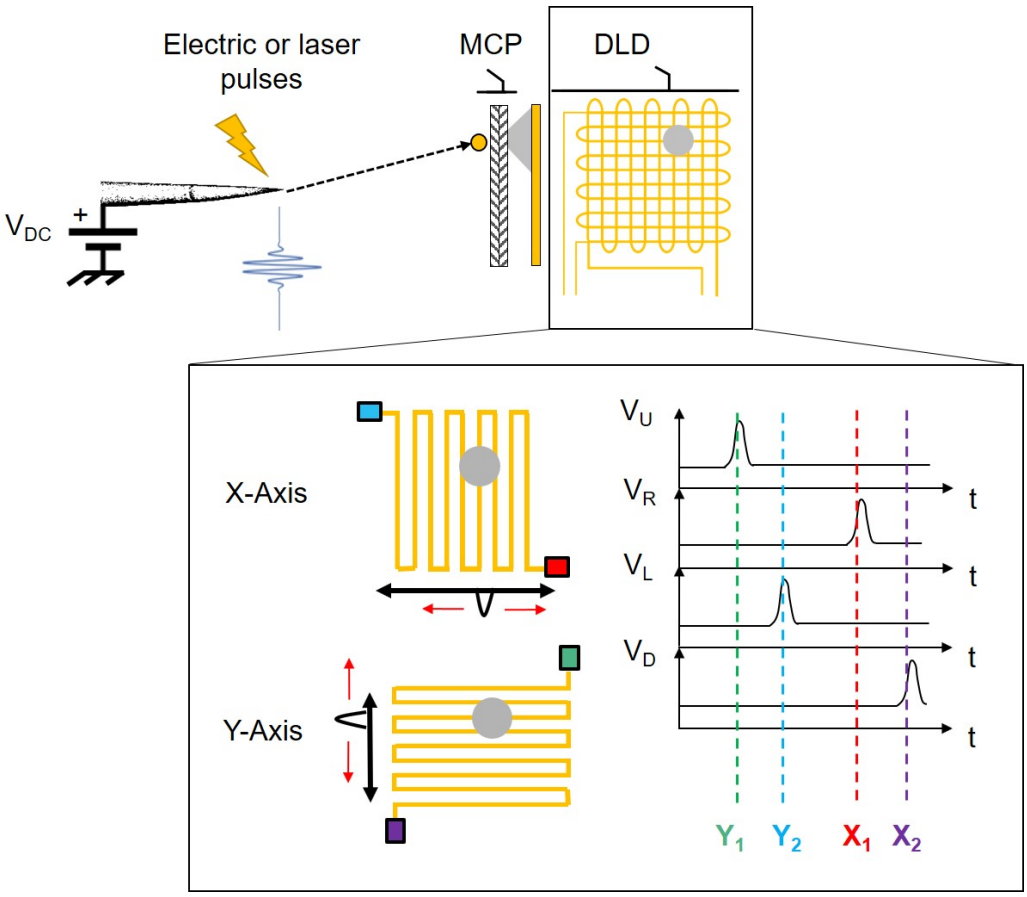

Figure I.31: Schematic of the operating process of a DLD.

The last answer to those requirements appears in current APT instruments (LEAP series [27], LaWATAP [9]). The third and last category of PSD used in APT instruments is the Delay Line Detector (DLD). DLDs are generally made of two (or three) independent conductive delay lines, superimposed and orthogonally oriented from each other (Figure I.31). Electron clouds, coming from the MCP back-end, induce electric signals that are transmitted towards each ending of the delay lines. From the start pulse applied on the tip to the arrival of electric signals on DLD outputs, time measurements are performed to determine the position of each detected ion.

Knowing the transversal length of the delay lines on both axes (l_X and l_Y) and the signal propagation times all along the lines (TPX and TPY), X and Y coordinates of ion impacts can be determined through the time differences between time stamps, respectively measured on each axis (T_{X1} and T_{X2} for the X axis, and T_{Y1} and T_{Y2} for the Y axis).

$$X = \frac{T_{X1} - T_{X2}}{2.TPX} l_X \tag{I.20}$$

$$Y = \frac{T_{Y1} - T_{Y2}}{2.TPY} l_Y \tag{I.21}$$

$$TPX = T_{X1} + T_{X2} - 2.TOF \tag{I.22}$$

$$TPY = T_{Y1} + T_{Y2} - 2.TOF \tag{I.23}$$

Contrary to multi-anode detectors, very few outputs are necessary to detect positions. For getting X and Y coordinates DLDs only need, at minimum, four outputs, reducing then the complexity of the detection system. However, this low amount of outputs may lead to ambiguous situations during multi-hit events, where successive outputs signals may be associated in different combinations (see Chapter II). Therefore, two types of MCP-DLD output configurations can be found in current APT instruments; a particle detection operated with the MCP output and four outputs coming from two delay lines (Figure I.31), and a particle detection which does not take into account the MCP output, but which resolves ambiguous particle detections with a third superimposed delay line, either oriented at 45° related to the two firsts orthogonally oriented delay lines [31], or three delay lines oriented at 60° from each other [25]. The first configuration has been adopted by the LaWATAP instrument [9], and the second one by the LEAP series [27].
At this point, it can be specified that through the use of DLDs, TOF measurements can be performed in two different ways:

- After the start time from the pulse event on the analyzed material (Section I.1.2), ions arrival time can be measured from an output signal originating from a capacitive sensor at the input or output ending of the MCP assembly (Figure I.13)

- On the other hand, ions arrival time can be calculated from time-stamps measured on DLD endings and from the theoretical signal propagation times on delay lines (TPX and TPY). Therefore, ions TOF can

also be deduced from Equations (I.22) and (I.23), giving the following equations;

$$TOF = \frac{T_{X1} + T_{X2} - TPX}{2} \tag{I.24}$$

$$TOF = \frac{T_{Y1} + T_{Y2} - TPY}{2} \tag{I.25}$$

Due to the time-to-position conversion performed by the DLD, it must be considered that the computation of ion impact coordinates might be subjected to position uncertainties originating from timing uncertainties for all DLD timing measurements. Thus, the point here is to find a relation between the spatial precision and the time precision of the DLD. This relation can be simply determined from Equations (I.20) and (I.21), where it can be considered that the spatial precisions in X and Y axes (ΔX and ΔY) can be determined through the timing precision of the signal propagation times (ΔTPX and ΔTPY).

$$\Delta X = \frac{\Delta TPX}{2.TPX} l_X \tag{I.26}$$

$$\Delta Y = \frac{\Delta TPY}{2.TPY} l_Y \tag{I.27}$$

As a consequence, it is through the experimental observation of the timing spread of TPX and TPY that the spatial precision of DLDs can be determined (Figures I.32 and I.33). Furthermore, as previously mentioned, the spatial precision can also be used for determining the spatial resolution of PSDs by considering the width at half maximum of the statistical spreads of ΔX and ΔY (Table I.1).

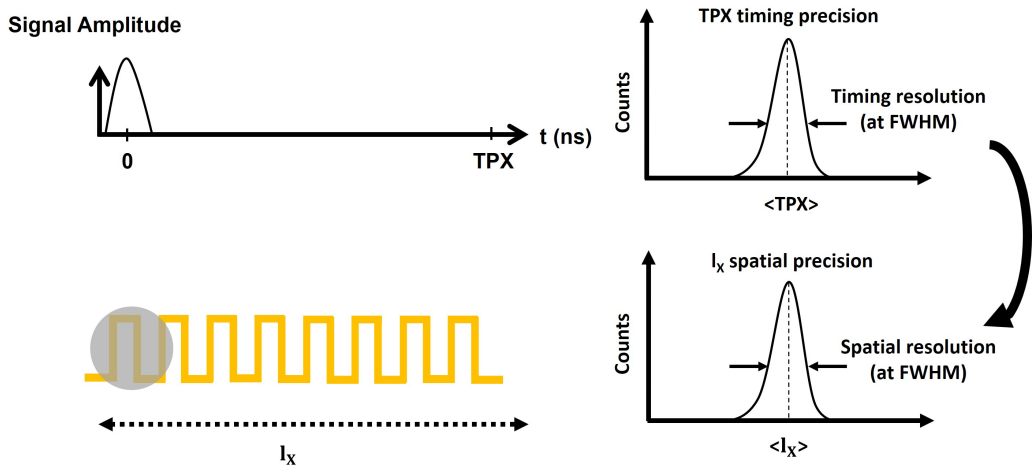

Figure I.32: Representation of the direct relation between the timing precision and the spatial precision on the X-axis delay line. The spatial resolution of the DLD can be determined by considering the width at half maximum of the statistical position spread.

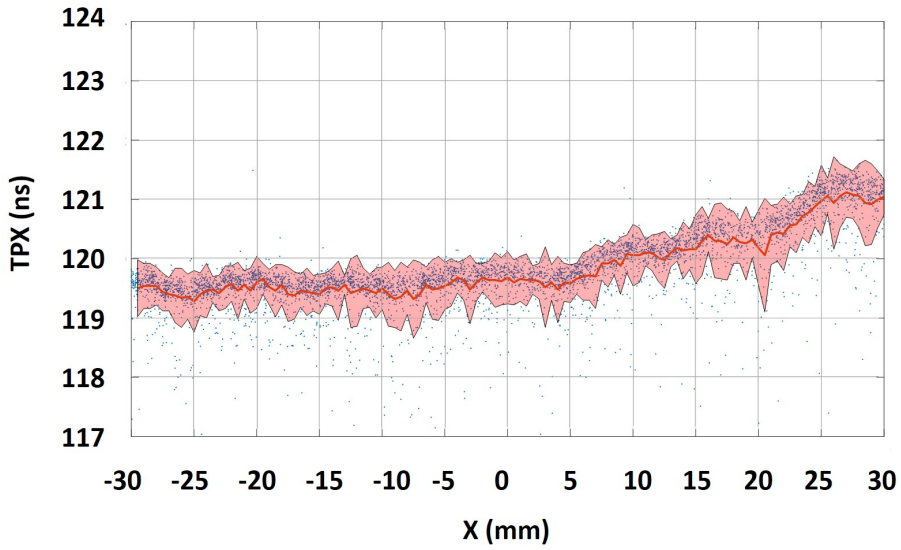

Figure I.33: Signal propagation time on the X-axis as a function of the impact position (Analysis from a LaWATAP). Blue dots represent the different propagation times calculated from the X-axis (Equation (I.22)), at different impact positions. The red line and the red zone respectively represent the moving average of TPX over the X-axis, associated with its timing spread at FWHM, which represent the timing resolution of the DLD.

<TPX> (ns)	<ΔTPX> (ns)	Spatial resolution (µm)
119.65	0.8375	279.98

Table I.1: Mean values obtained from Figure I.32.

The calculation of the DLD spatial resolution then lead to the calculation of the potential lateral spatial resolution that can be obtained on a 3D reconstruction. Assuming a tip-to-detector distance of 20 cm, a compression factor m ∼0.6 and a tip radius of curvature of 50 nm, it can be deduced that the lateral spatial resolution of an APT instrument can reach ∼1 Å by using a DLD (Table I.1 and eq. (I.10)).

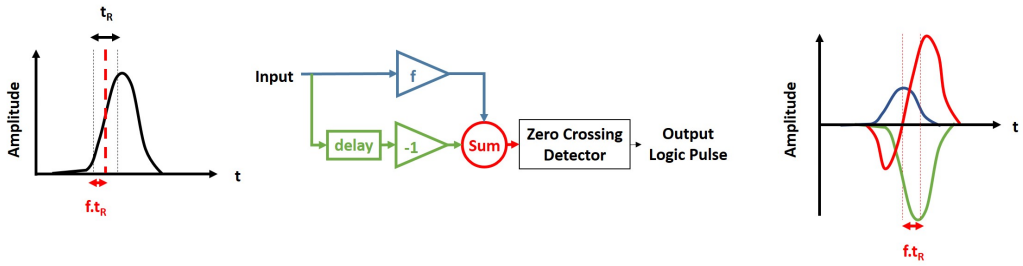

Figure I.34: Schematic of the operating process of the CFD. The subtraction between a replica of the output signal shifted by the time fraction $f.t_R$, and another replica whose amplitude is attenuated by the factor f, gives a resulting signal on which each zero crossing point corresponds to the overtaking of the time threshold $f.t_R$

Most of the timing systems used for DLDs are generally composed of Constant Fraction Discriminators (CFD), for triggering electric signals, and Time-to-Digital Converters (TDC), for providing digital values of time intervals measured between the start pulse applied on the tip and signal outputs, originating from the MCP assembly and the DLD (Figure I.31). Contrary to simple discriminators, which rely on the detection of electric signals exceeding an amplitude threshold, CFDs rely on time thresholds defined by a fraction of signals rise time.

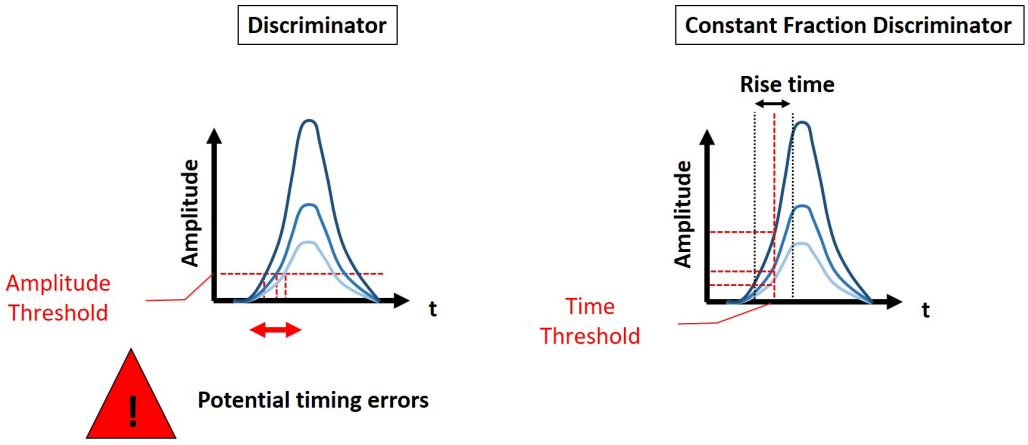

Figure I.35: Timing measurement comparison between discriminators and CFDs. The timing precision of discriminators is much lower than CFDs because of the different time-stamps that can be measured for distinct signals occurring at the same time, with similar shapes, but with different amplitudes.

Figure I.35 clearly illustrates the difference between discriminators and CFDs. Time measurements performed on distinct signals with the same shape, occurring at the same time and having different amplitudes, are differently triggered. The use of discriminators has the effect of getting different time-stamps for signals occurring at the same time, whereas CFDs provide almost the same time-stamps.
Thus, in accordance with the homothetic behavior of output signals [14], time measurements with CFDs can ensure a high timing precision. In order to trigger an output signal at a fraction f of its rise time t_R, a CFD uses a zero-crossing detector (Figure I.34). The subtraction between a replica of the output signal shifted by the time fraction $f.t_R$, and another replica whose amplitude is attenuated by the factor f, gives a resulting signal on which each zero crossing point corresponds to the exceeding of the time threshold $f.t_R$. Every zero crossing detection is followed by a logic signal going towards a TDC for triggering time measurements. The time duration of this logic signal represent a dead-time during which no successive signal can be detected (Figure I.36). Therefore, time and space information from DLDs might be subject to information losses.

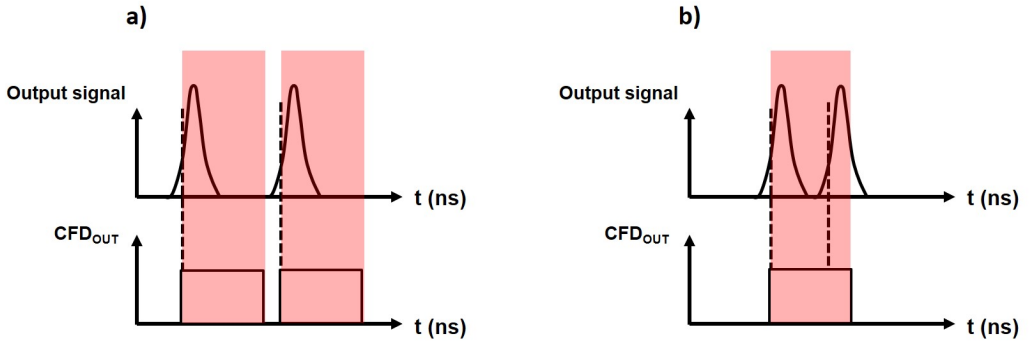

Figure I.36: Schematic representation of the signal loss mechanism through the use of CFD systems (Figure I.34). The time offset between the two output signals in a) is longer than the dead-time of the CFD system, contrary to the shorter time offset between the two signals in b). Therefore two timing measurements are not possible in cases similar to b).

By referring to the variability of the evaporation mechanism, it is known that some elements, and/or phases might tend to field evaporate more than others during multi-hit events [16, 37]. Which means that some elements and/or some phases might have higher probabilities to be subject to losses caused by the dead-time [2, 33]. As a consequence, selective losses might occur during APT experiments. Da Costa et al. illustrated this effect with the analysis of a boron-silicon alloy [15]; where the boron tends to field evaporate more than the silicon during multi-hit events. It has been demonstrated that the high amount of boron lost during multiple events induced an under-estimation of the boron in the analyzed material.
Regarding the working principle of DLDs, the instrument dead-time has two effects; the first one is a limitation on successive TOF measurements, which is simply called the "dead-time" (DT); the second one is a limitation on the distance between ion impacts, which is called the "dead-zone" (DZ).

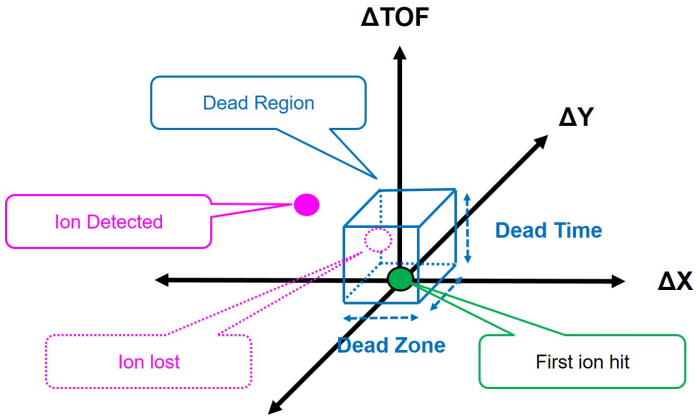

Figure I.37: Schematic representation of the DR around each first ion hit as defined in the literature [13, 38]. Any other ions arriving inside the DR are considered to be lost.

So far in the literature, it has been reported that the combination of the DT and the DZ represents a "dead-region" (DR) around each first ion hit [13, 38], where it is expected to lose any other ions arriving inside (Figure I.37). In other words, this assumption says that when two ions hit the detector very close in time and space, only one ion could be localized and identified (Figure I.38).

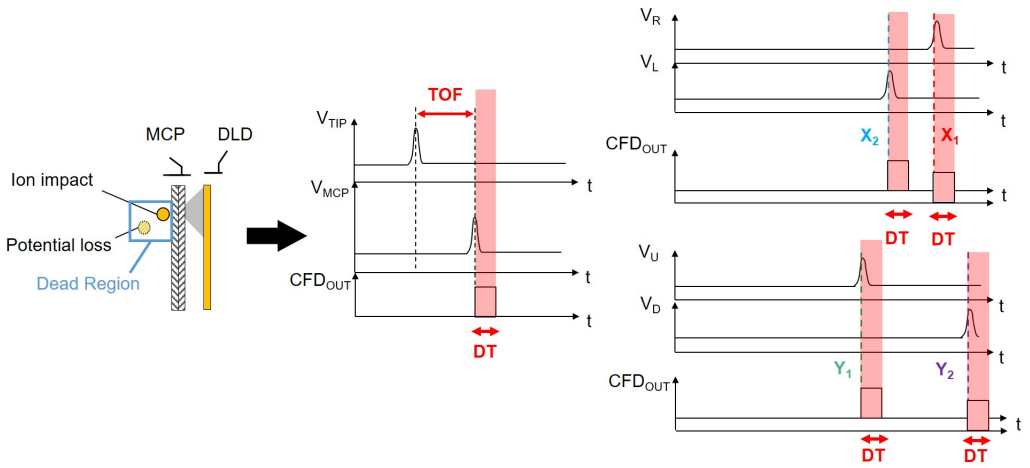

Figure I.38: Schematic representation of potential losses that may occur during multi-hit events through the theoretical DR of APT instruments.

This last assumption on theoretical DR can be directly verified through

experimental data by computing the relative time and space distribution of every second ion related to their associated first ion hit in multi-hit events. A depleted region should appear where TOF differences and relative positions do not exceed respectively the DT and the DZ around each first ion hit (Figure I.37). This phenomenon has been clearly highlighted by Z. Peng et al. [44] with the analysis of a tungsten carbide. A 3D map of relative positions and TOF differences between ion pairs, also called multi-hit 3D correlation map, was introduced to reveal the space and time limitation of the instrument during multi-hit events (Figure I.39).

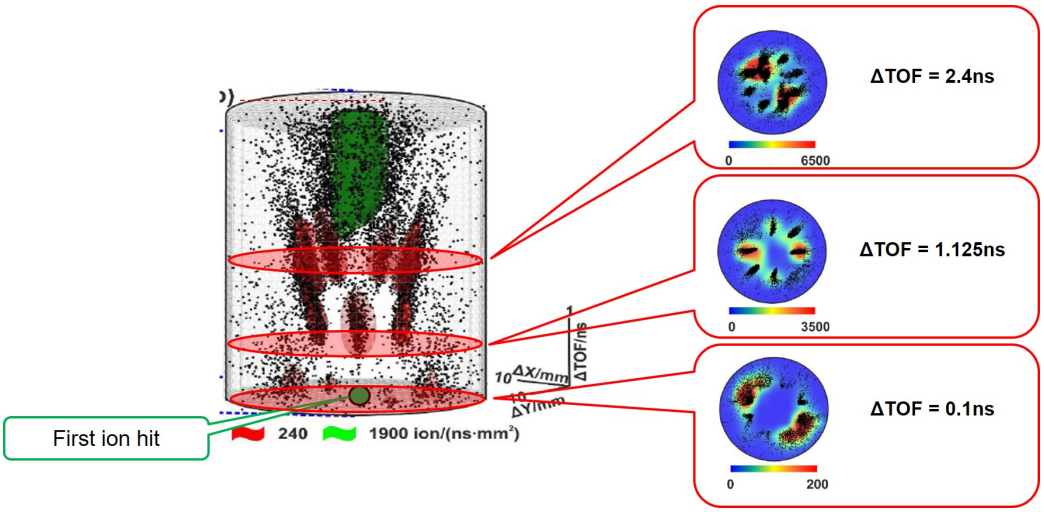

Figure I.39: Multi-hit 3D correlation map from the analysis of a tungsten carbide sample on a LEAP 5000 XS [44] This 3D map reveals the relative position and TOF differences between ion pairs during multi-hit events.

Conversely to expectations, the observed DR was found larger than expected. Both DT and DZ turned out to be extended beyond their theoretical boundaries. Other authors pointed out the same observation on 2D maps of relative distances between ion pairs [25, 33], but with fixed TOF differences. At this point, no clear explanations have been reported about this phenomenon. Thus, it can be said that spatial and compositional biases caused by the detection system are still not fully understood.

I.3 Conclusion

This is through this chapter that the APT working process has been introduced, from the field evaporation mechanism to the 3D reconstruction of material samples. The described state-of-the-art show that the APT technique is genuinely one of the most powerful analytical tools allowing the visualization of both the atomic structure and the elemental composition of material samples. On the other side, it has also been shown why APT instruments are still relatively confidential in the panel of techniques in material sciences. One of the main reasons concerns the potential spatial and compositional biases brought by APT detectors. That is why, it was also necessary to trace the evolution of APT detectors, in order to get a proper grasp on those potential biases. It has been demonstrated that the quest of an instrument provided with an atomic scale resolution, coupled with an ultimate sensitivity to all elements, is a story successive trade-off, reflected in the balancing between spatial and compositional performances.

Bibliography

[1] T. Al-Kassab, H. Wollenberger, G. Schmitz, and R. Kirchheim. Tomography by atom probe field ion microscopy. In Frank Ernst and Manfred Rühle, editors, *High-Resolution Imaging and Spectrometry of Materials*, Springer Series in Materials Science, pages 271–320. Springer, Berlin, Heidelberg, 2003. DOI: 10.1007/978-3-662-07766-5.

[2] C. Bacchi, G. Da Costa, and F. Vurpillot. Spatial and compositional biases introduced by position sensitive detection systems in apt: A simulation approach. *Microscopy and Microanalysis*, 25(2):418–424, 4 2019.

[3] Jürgen Barnstedt. Microchannel plate detectors, 2016.

[4] P. Bas, A. Bostel, B. Deconihout, and D. Blavette. A general protocol for the reconstruction of 3d atom probe data. *Applied Surface Science*, 87-88:298–304, 3 1995.

[5] D. Blavette, A. Bostel, and J. M. Sarrau. A new detection system for an atom probe fim. *Le Journal de Physique Colloques*, 47(C2):C2–473–C2–477, 3 1986.

[6] D. Blavette, B. Deconihout, A. Bostel, J. M. Sarrau, M. Bouet, and A. Menand. The tomographic atom probe: A quantitative three-dimensional nanoanalytical instrument on an atomic scale. *Review of Scientific Instruments*, 64(10):2911–2919, 10 1993.

[7] D. Blavette and X. Sauvage. Early developments and basic concepts. In *Atom Probe Tomography*, pages 1–15. Elsevier, 2016. DOI: 10.1016/B978-0-12-804647-0.00001-2.

[8] A. Bostel, D. Blavette, A. Menand, and J. M. Sarrau. Toward a tomographic atom-probe. *Le Journal de Physique Colloques*, 50(C8):C8–501–C8–506, 11 1989.

[9] Joseph H. Bunton, Jesse D. Olson, Daniel R. Lenz, and Thomas F. Kelly. Advances in pulsed-laser atom probe: Instrument and specimen design for optimum performance. *Microscopy and Microanalysis*, 13(6):418–427, 12 2007.

[10] Weiwei Cao, Bingli Zhu, Xiaohong Bai, Peng Xu, Bo Wang, Junjun Qin, Yongsheng Gou, Fanpu Lei, Baiyu Liu, Junjiang Guo, Jingping Zhu, and Yonglin Bai. High-sensitivity and long-life microchannel plate processed

by atomic layer deposition. *Nanoscale Research Letters*, 14(1):153, 5 2019.

[11] A. Cerezo, T. J. Godfrey, J. M. Hyde, S. J. Sijbrandij, and G. D. W. Smith. Improvements in three-dimensional atom probe design. *Applied Surface Science*, 76-77:374–381, 3 1994.

[12] A. Cerezo, T. J. Godfrey, and G. D. W. Smith. Application of a position-sensitive detector to atom probe microanalysis. *Review of Scientific Instruments*, 59(6):862–866, 6 1988.

[13] G. Da Costa. Atom probe tomography. In *Atom Probe Tomography*, pages 155–181. Elsevier, 2016. DOI: 10.1016/B978-0-12-804647-0.00006-1.

[14] G. Da Costa, F. Vurpillot, A. Bostel, M. Bouet, and B. Deconihout. Design of a delay-line position-sensitive detector with improved performance. *Review of Scientific Instruments*, 76(1):013304, 1 2005.

[15] G. Da Costa, H. Wang, S. Duguay, A. Bostel, D. Blavette, and B. Deconihout. Advance in multi-hit detection and quantization in atom probe tomography. *Review of Scientific Instruments*, 83(12):123709, 12 2012.

[16] F Danoix, M.K Miller, and A Bigot. Analysis conditions of an industrial al–mg–si alloy by conventional and 3d atom probes. *Ultramicroscopy*, 89(1-3):177–188, 10 2001.

[17] Paul De Bièvre. The 2012 international vocabulary of metrology: "vim". *Accreditation and Quality Assurance*, 17(2):231–232, 4 2012.

[18] B Deconihout, L Renaud, G Da Costa, M Bouet, A Bostel, and D Blavette. Implementation of an optical tap: preliminary results. *Ultramicroscopy*, 73(1):253–260, 6 1998.

[19] M. A Fortes and B Ralph. A field-ion microscope study of segregation to grain boundaries in iridium. *Acta Metallurgica*, 15(5):707–720, 5 1967.

[20] E.R. Fossum. Cmos image sensors: electronic camera-on-a-chip. *IEEE Transactions on Electron Devices*, 44(10):1689–1698, 10 1997.

[21] Eric R Fossum. Active pixel sensors: Are ccds dinosaurs? In *Charge-Coupled Devices and Solid State Optical Sensors III*, volume 1900, pages 2–14. International Society for Optics and Photonics, 1993.

[22] B. Gault, D. Haley, F. de Geuser, M.P. Moody, E.A. Marquis, D.J. Larson, and B.P. Geiser. Advances in the reconstruction of atom probe tomography data. *Ultramicroscopy*, 111(6):448–457, 5 2011.

[23] Baptiste Gault, Michael P. Moody, Frederic De Geuser, Alex La Fontaine, Leigh T. Stephenson, Daniel Haley, and Simon P. Ringer. Spatial resolution in atom probe tomography. *Microscopy and Microanalysis*, 16(1):99–110, 2 2010.

[24] Junjiang Guo, Dan Wang, Yantao Xu, Xiangping Zhu, Kaile Wen, Guanghui Miao, Weiwei Cao, JinHai Si, Min Lu, and Haitao Guo. Secondary electron emission characteristics of al2o3 coatings prepared by atomic layer deposition. *AIP Advances*, 9(9):095303, 9 2019.

[25] O Jagutzki, V Mergel, K Ullmann-Pfleger, L Spielberger, U Spillmann, R Dörner, and H Schmidt-Böcking. A broad-application microchannel-plate detector system for advanced particle or photon detection tasks: large area imaging, precise multi-hit timing information and high detection rate. *Nuclear Instruments and Methods in Physics Research Section A: Accelerators, Spectrometers, Detectors and Associated Equipment*, 477(1-3):244–249, 1 2002.

[26] Slade J. Jokela, Igor V. Veryovkin, Alexander V. Zinovev, Jeffrey W. Elam, Anil U. Mane, Qing Peng, and Z. Insepov. Secondary electron yield of emissive materials for large-area micro-channel plate detectors: Surface composition and film thickness dependencies. *Physics Procedia*, 37:740–747, 1 2012.

[27] Thomas F Kelly and David J Larson. Local electrode atom probes. *Materials Characterization*, 44(1-2):59–85, 1 2000.

[28] S. Koelling, A. Li, A. Cavalli, S. Assali, D. Car, S. Gazibegovic, E. P. A. M. Bakkers, and P. M. Koenraad. Atom-by-atom analysis of semiconductor nanowires with parts per million sensitivity. *Nano Letters*, 17(2):599–605, 2 2017.

[29] Joseph Ladislas Wiza. Microchannel plate detectors. *Nuclear Instruments and Methods*, 162(1):587–601, 6 1979.

[30] Bruce N Laprade. The high output technology microchannel plate. In *Image Intensification*, volume 1072, pages 102–110. International Society for Optics and Photonics, 1989.

[31] David J. Larson, Ty J. Prosa, Robert M. Ulfig, Brian P. Geiser, and Thomas F. Kelly. Design and instrumentation. In *Local Electrode Atom Probe Tomography*, pages 55–77. Springer New York, New York, NY, 2013. DOI: 10.1007/978-1-4614-8721-0.

[32] C. Martin, P. Jelinsky, M. Lampton, R. F. Malina, and H. O. Anger. Wedge-and-strip anodes for centroid-finding position-sensitive photon and particle detectors. *Review of Scientific Instruments*, 52(7):1067–1074, 7 1981.

[33] Frederick Meisenkothen, Eric B. Steel, Ty J. Prosa, Karen T. Henry, and R. Prakash Kolli. Effects of detector dead-time on quantitative analyses involving boron and multi-hit detection events in atom probe tomography. *Ultramicroscopy*, 159:101–111, 12 2015.

[34] M. K. Miller. Concepts in atom probe designs. *Surface Science*, 246(1):428–433, 4 1991.

[35] M. K. Miller. Implementation of the optical atom probe. *Surface Science*, 266(1):494–500, 4 1992.

[36] M K Miller. Atom probe field ion microscopy. *Vacuum*, 45(6):13, 1994.

[37] M. K. Miller and G. D. W. Smith. An atom probe study of the anomalous field evaporation of alloys containing silicon. *Journal of Vacuum Science and Technology*, 19(1):57–62, 5 1981.

[38] Michael K. Miller and Richard G. Forbes. *Atom-Probe Tomography*. Springer US, Boston, MA, 2014. DOI: 10.1007/978-1-4899-7430-3.

[39] Erwin W. Müller. Study of atomic structure of metal surfaces in the field ion microscope. *Journal of Applied Physics*, 28(1):1–6, 1 1957.

[40] Erwin W. Müller and Kanwar Bahadur. Field ionization of gases at a metal surface and the resolution of the field ion microscope. *Physical Review*, 102(3):624–631, 5 1956.

[41] Erwin W. Müller, John A. Panitz, and S. Brooks McLane. The atom-probe field ion microscope. *Review of Scientific Instruments*, 39(1):83–86, 1 1968.

[42] Christian Oberdorfer and Guido Schmitz. On the field evaporation behavior of dielectric materials in three-dimensional atom probe: A numeric simulation. *Microscopy and Microanalysis*, 17(1):15–25, 2 2011.

[43] J. A. Panitz. The 10 cm atom probe. *Review of Scientific Instruments*, 44(8):1034–1038, 8 1973.

[44] Zirong Peng, Francois Vurpillot, Pyuck-Pa Choi, Yujiao Li, Dierk Raabe, and Baptiste Gault. On the detection of multiple events in atom probe tomography. *Ultramicroscopy*, 189:54–60, 6 2018.

[45] FHM F. Rahman, John A. Notte, Richard H. Livengood, and Shida Tan. Observation of synchronized atomic motions in the field ion microscope. *Ultramicroscopy*, 126:10–18, 3 2013.

[46] Brian Ralph and D. G. Brandon. A field ion microscope study of some tungsten-rhenium alloys. *The Philosophical Magazine: A Journal of Theoretical Experimental and Applied Physics*, 8(90):919–934, 6 1963.

[47] L Renaud, G Da Costa, M Bouet, and B Deconihout. Design of a fast multi-hit position sensitive detector based on a ccd camera. *Nuclear Instruments and Methods in Physics Research Section A: Accelerators, Spectrometers, Detectors and Associated Equipment*, 477(1):150–154, 1 2002.

[48] Liang Shen, Xiaobing Feng, Yuan Zhang, Min Shi, Dengming Zhu, and Zhaoqi Wang. Stroboscope based synchronization of full frame ccd sensors. *Sensors*, 17(4):799, 4 2017.

[49] H. C. Straub, M. A. Mangan, B. G. Lindsay, K. A. Smith, and R. F. Stebbings. Absolute detection efficiency of a microchannel plate detector for kilo-electron volt energy ions. *Review of Scientific Instruments*, 70(11):4238–4240, 11 1999.

[50] A. S. Tremsin and O. H. W. Siegmund. Spatial distribution of electron cloud footprints from microchannel plates: Measurements and modeling. *Review of Scientific Instruments*, 70(8):3282–3288, 8 1999.

[51] P. J. Turner, P. Cartwright, M. J. Southon, van A. Oostrom, and B. W. Manley. Use of a channelled image intensifier in the field-ion microscope. *Journal of Physics E: Scientific Instruments*, 2(8):731–733, 8 1969.

[52] F. Vurpillot. Field ion emission mechanisms. In *Atom Probe Tomography*, pages 17–72. Elsevier, 2016. DOI: 10.1016/B978-0-12-804647-0.00002-4.

[53] Alfred Wagner, Thomas M. Hall, and David N. Seidman. An atom-probe field-ion microscope for the study of the interaction of impurity atoms

or alloying elements with defects. *Journal of Nuclear Materials*, 69-70:413–423, 2 1978.

[54] L. Yao, B. Gault, J.M. Cairney, and S.P. Ringer. On the multiplicity of field evaporation events in atom probe: A new dimension to the analysis of mass spectra. *Philosophical Magazine Letters*, 90(2):121–129, 2 2010.

[55] Bingli Zhu, Yonglin Bai, Fanpu Lei, Xiaohong Bai, Bo Wang, Junjun Qin, Weiwei Cao, and Yongsheng Gou. Two-dimensional photon counting imaging detector based on pcb delay line anode. In *Selected Papers of the Chinese Society for Optical Engineering Conferences held July 2016*, volume 10141, page 101411A. International Society for Optics and Photonics, 2016.

Chapter II

Spatial and Compositional biases introduced by Position-Sensitive Detection Systems in APT

In order to understand the origin of spatial and compositional biases caused by the detection system during multi-hit events, a simulation tool has been developed for reproducing the detection of multi-hits; from the evaporation of atoms to the time measurements performed on the MCP-DLD detection system.
This simulation tool has been divided into two parts. The first part is aimed at creating a reference list of ion impacts, generated from a material model and a selected APT geometry, and a second part is aimed at simulating the APT detection process (see Chapter I). The comparison between the list of detected ions with the list of theoretical ion impacts, has the advantage of getting indicators about the impact of the detection system on material analyses.

II.1 Model of correlated evaporation

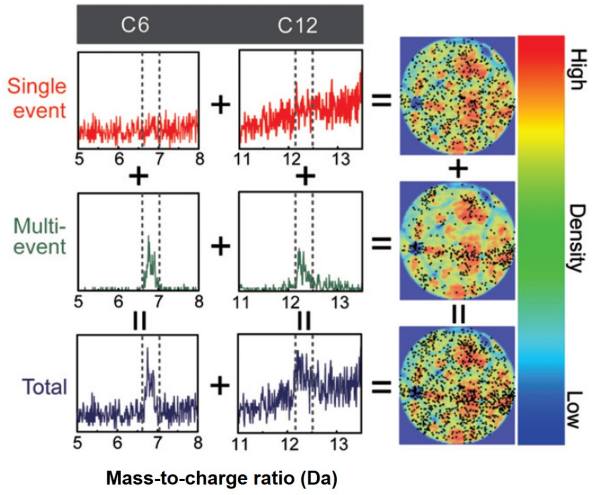

Figure II.1: Analysis of a microalloyed CASTRIP® steel from L. Yao et al. [28]. The figure introduces C^{2+}, C^{+}, $C_2{}^{2+}$ signals from single and multiple hits and their corresponding distribution on density maps. The map corresponding to multi-hit events consistently exhibit a distribution of C that depends on local crystallography.

In order to simulate virtual ion impacts on the detector, it is necessary to reproduce the evaporation mechanism (see Chapter I), and more specifically the evaporation of atoms correlated both in time and space, involving multi-hit events. Looking back to the evaporation mechanism, it has been assumed that analyzed materials are shaped as a sharp needle tip, until the apex forms a hemispherical shape. However, it has to be known that the shape of the tip apex is not really hemispherical at the local scale [2, 11, 15]. Due to local protrusions on the tip surface, it can be deduced that the induced electric field on the tip surface cannot be totally homogenous [20, 23, 27]. Furthermore, the chemical structure of the analyzed material can introduce different binding forces between elements that can also lead to heterogeneous electric field on the tip surface [9,18]. Local protrusions coupled with different binding forces between elements may lead to evaporation of more than one ion during a same pulse event, also known as multi-hit events [8, 29]. The probability to evaporate more than one ion is then higher experimentally than with a simple spherical model of the tip apex. Those different factors show that the evaporation process cannot be easily simulated due to the amount of parameters to take into account to reproduce the shape and chemical

properties of the specimen. Thus, as a first approach it has been chosen to simplify the study by only taking into account different evaporation rates as a function of elements that tend to field evaporate more or less than others during multi-hit events. In addition, with the aim of generalizing this study to all types of material, the effect of local protrusions introduced by crystallographic poles will not be considered. Therefore, following simulation results will represent minimized effects of the detection system on APT analyses, but will give a clearer idea about mechanisms inducing spatial and compositional biases.

II.1.1 Simulation of an evaporation sequence

The main goal of the first part of the simulation tool is to generate an evaporation sequence relying on two input models; the composition of the analyzed material and a theoretical multi-hit distribution on the detection surface (Figure II.2).

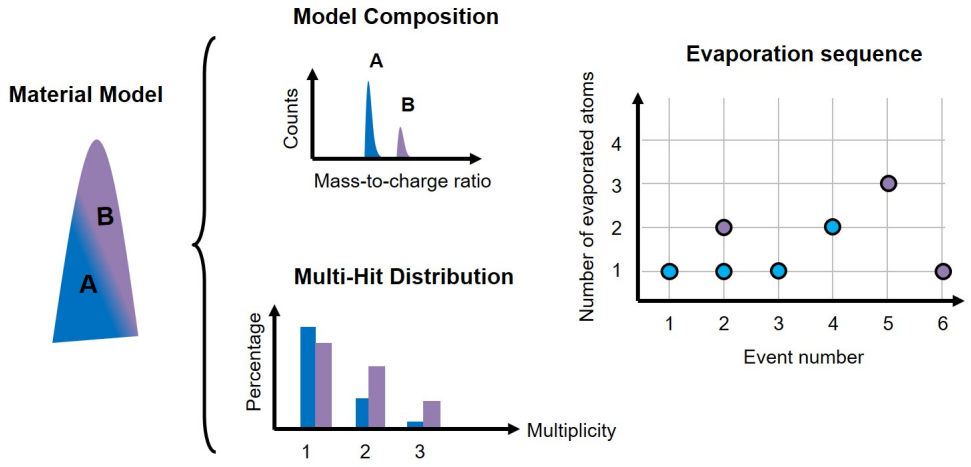

Figure II.2: Schematic of the evaporation sequence through a material model on the simulation tool. The field evaporation mechanism is simulated through a model of composition and a model of multi-hit distribution representing the susceptibility of some elements to be evaporated during multi-hit events. According to these combined models, an evaporation sequence is generated.

The composition of the analyzed material is represented by a mass spectrum having two main parameters; the fraction of each element in the material and the mass resolving power (MRP) for a specific mass peak in the spectrum. The interest in applying a mass spread to each mass peak is to reproduce the time delay caused by the mismatch between the pulse event

and the evaporation event [12].
Depending on the chemical structure of the analyzed material, it is possible to have some elements that tend to field evaporate more than others during pulse events. Consequently, individual evaporation rates may be distinguished as a function of the material composition. By keeping the global evaporation rate intentionally low (less than 1% atom per pulse), the probability P_k to evaporate more than one atom should follow a Poisson law [10];

$$P_k = \mathrm{e}^{-\lambda}\frac{\lambda^k}{k!} \tag{II.1}$$

Where λ is the average multiplicity of an elemental nature detected during an event, and the parameter k corresponds to a specific multiplicity on which the probability P_k must be determined. Thus, in the simulation tool, different average multiplicities have been arbitrary assigned to each element in order to simulate the tendency of some elements to be evaporated with high or low multiplicities (Figure II.2). The different values of λ have been chosen by taking into account some tendencies from experimental results, such as the tendency of boron to field evaporate in multi-hit events more than the silicon during the analysis of B-implanted in silicon materials.

II.1.2 Simulation of a spatial distribution on the detector

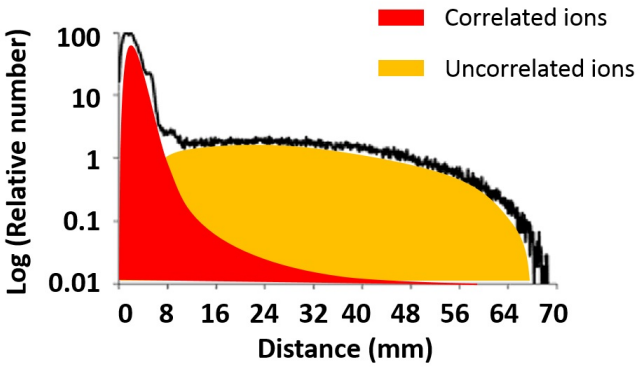

Figure II.3: Distribution of inter-Impact distances on the detector during multiple events from an analysis on a LaWATAP instrument. The red area represents inter-impact distances between correlated ions. The orange area represents inter-impact distances between uncorrelated ions.

The other aspect to take into account is the spatial correlation between evaporated atoms during multi-hit events. From APT experiments, it has been shown that the distribution of inter-impact distances, on the detector surface, is mainly composed of two overlapped spatial distributions [8, 10]; one related to ions coming from a same emission site (correlated ions), and another one related to the stochastic evaporation process on the whole tip surface (uncorrelated ions). Noting that some APT analyses may also introduce specific spatial distributions, that are related to the dissociation of molecular ions all along their flight towards the detector [3, 26, 29], but that will not be addressed for this study.
With the aim of including a model of spatial distribution for multi-hit events, two theoretical models have been respectively taken into account (Figure II.3); a Rayleigh distribution for correlated ions and a uniform random distribution for uncorrelated ions.

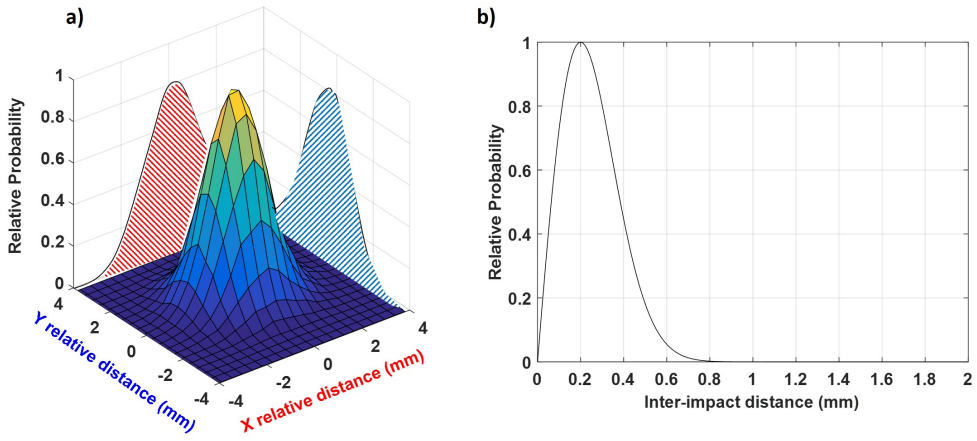

Figure II.4: Models used for defining the inter-impact distances between correlated ions during multi-hit events; a) Two-dimensional Gaussian distribution representing the spatial probability distribution of the relative distance between secondary ion hits and first ion hits; b) Resulting Rayleigh distribution representing the probability of secondary ion hits to be separated by first ion hits at a certain distance.

$$P_X = \frac{1}{\sigma\sqrt{2\pi}} \mathrm{e}^{-\frac{1}{2}\left(\frac{X}{\sigma}\right)^2} \tag{II.2}$$

$$P_Y = \frac{1}{\sigma\sqrt{2\pi}} \mathrm{e}^{-\frac{1}{2}\left(\frac{Y}{\sigma}\right)^2} \tag{II.3}$$

$$P_R = \frac{r}{\sigma^2} \mathrm{e}^{-\frac{1}{2}\left(\frac{r}{\sigma}\right)^2} \tag{II.4}$$

On one side, the Rayleigh distribution is a probability distribution which considers that X and Y relative distances between multi-hits respectively rely on two independent and identical Gaussian distributions (Figure II.4a). Equations (II.4) and (II.5) show that those two Gaussian distributions share the same standard deviation σ. By considering those two probability distributions, a resulting probability distribution can be calculated for finding the relative distance r between ion pairs (Equation (II.6)). This resulting distribution, also called Rayleigh distribution [22], is in part characterized by its mode representing the most probable inter-impact distance. The mode of the Rayleigh distribution is equal to the standard deviation σ originating from the two previous Gaussian distributions.

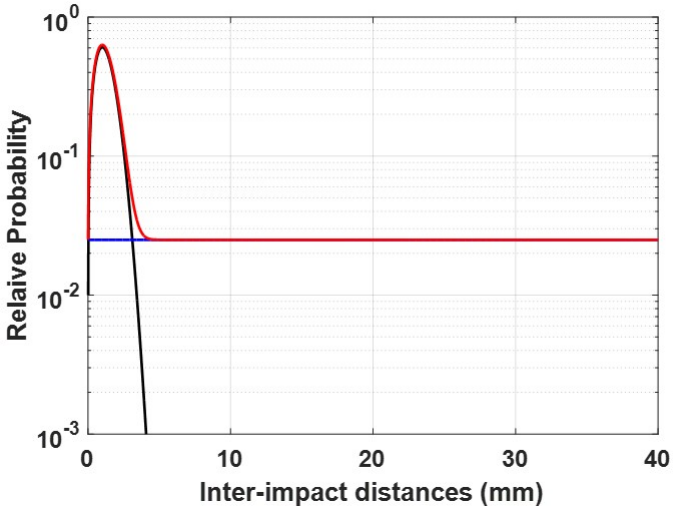

Figure II.5: Model of distribution of inter-impact distances (red curve) generated from a Rayleigh distribution (black curve) with $\sigma = 1$ mm combined with a uniform distribution (blue line).

On the other side, a uniform random distribution, representing the probability of secondary ion hits to be separated by first ion hits at a random distance, is appended to the Rayleigh distribution (Figure II.5). It should be recalled that this uniform random distribution is a representation of the stochastic evaporation process conducted by the electric field perceived on the entire tip surface (see Chapter I).
By referring to the experimental distribution of inter-impact distances on Figure II.3, one can note that the part that should represent the uniform

random distribution is not really uniform but introduces a bowl shape. This is simply due to the restriction of the uniform distribution inside the circle shape of the detection area [5, 21]. This assumption can be simply demonstrated by performing a Monte-Carlo simulation generating pairs of X and Y coordinates, uniformly distributed on a very large area, and separated by distances uniformly distributed between 0 mm and 80 mm, the supposed the diameter D of the detection surface. Figure II.6 clearly shows the transformation of the uniform distribution into a non-uniform distribution through a disk area selection. It has to be known that this non-uniform distribution can also be mathematically explained in the same manner as the Buffon's needle problem[1] [25], and can be expressed by the following equation (from [5, 21]);

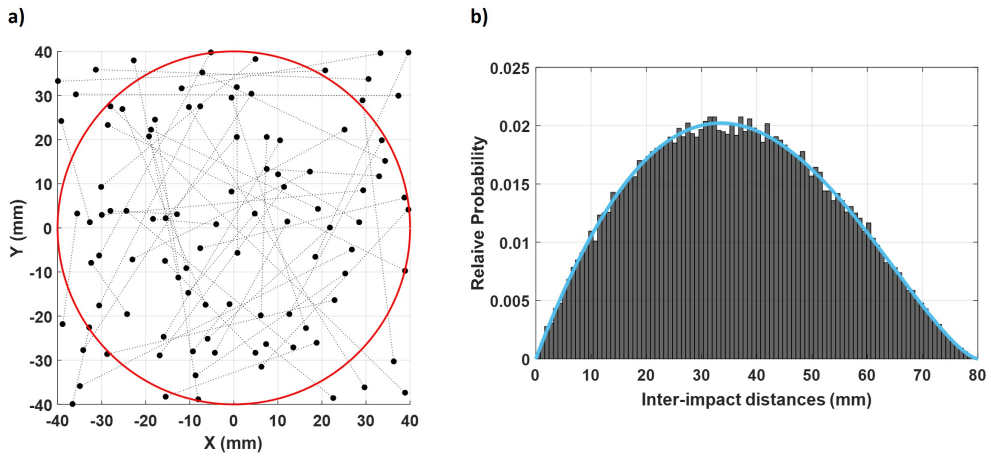

Figure II.6: Monte-Carlo simulation on the calculation of the distribution of inter-impact distances from the evaporation of uncorrelated ions; a) 2D map of uniformly distributed pairs of ion impacts bounded by circle shape of the detection area in red; b) Probability distribution of inter-impact distances resulting from the simulation. The blue line, following the shape of the histogram represents the theoretical probability density function of inter-impact distances inside the disk area (Equation (II.7)).

[1]The Buffon's needle problem is a probability experiment, proposed by Georges-Louis Leclerc de Buffon in 1733, allowing the computation of the number π through a geometrical method. The goal of the experiment is to throw several times a needle on a plane surface composed of parallel strips, having the same width. By counting the number of times the needle crosses a separation line between two strips, related to the total number of throws, it is possible to get an approximation of π.

$$P_{NC} = \frac{8r\left(\cos^{-1}\left(\frac{r}{D}\right) - \frac{r\sqrt{1-\frac{r^2}{D^2}}}{D}\right)}{\pi D} \tag{II.5}$$

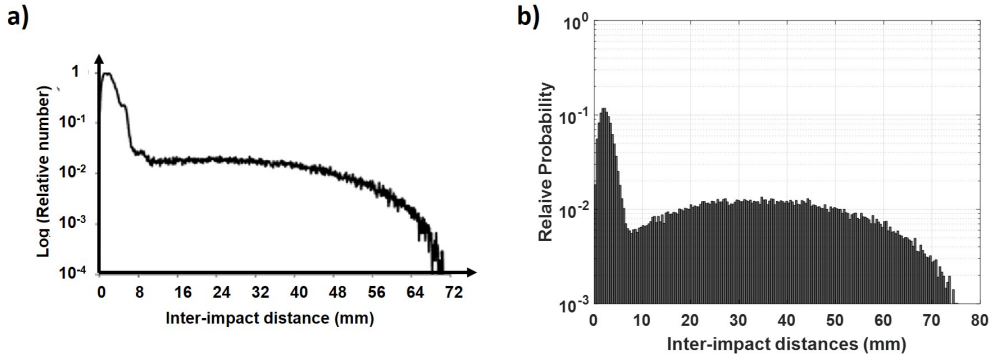

Figure II.7: Comparison between experimental and simulated distribution of inter-impact distances; a) Distribution from an analysis on a LaWATAP instrument; b) Distribution obtained after simulating multi-hits on a detection surface of 80 mm diameter.

Figure II.7 shows that the application of the model of distribution of inter-impact distances on a circular detection surface has a similar shape as in APT experiments. As a consequence, this first mathematical approach on the generation of virtual ion impacts makes it possible to partly reproduce experimental conditions from APT experiments.

II.2 Creation of a list of theoretical ion impacts

From the generated evaporation sequence (Figure II.2) and the theoretical distribution of inter-impact distances (Figure II.5), it is then possible to perform a random sampling that determines the theoretical position and elemental nature of each simulated ion. Given that the purpose of the simulation tool is, as a first step, only focused on the APT detection process, no consideration has been given to the quasi-stereographic projection of materials introducing crystallographic patterns. Therefore, concerning single-hit events, it has been first decided to position every single impact position through a uniform random distribution on the detection surface. Then, in order to ensure compliance with the model of inter-impact distances for multi-hit events (Figure II.5), it has been decided to apply an iterative position random sampling through the following algorithm;

1. Drawing of the first impact position through a uniform random distribution on the detection surface.

2. A relative distance between the first impact position and the second one is drawn through the theoretical distribution of inter-impact distances (Figure II.5).

3. The second ion impact is positioned around the first ion impact at the drawn inter-impact distance.

4. In case of multi-hit events introducing more than two impacts, another drawing is performed in the theoretical distribution of inter-impact distances.

5. The third ion impact is positioned around the barycenter of the two first impacts, in order to not bias the theoretical distribution of inter-impact distances.

6. Steps 4 and 5 are successively applied for any other successive ion impact.

At this point, a first list of ion impacts, composed of mass-to-charge ratios and position coordinates, is available. That list will allow to determine the theoretical signal chronograms representing output signals from the MCP assembly and the DLD.

II.3 Generation of output signals

Regarding the physical and electrical properties given to the detector (see Chapter I), every virtual ion impact has to be associated to a TOF and four (or six) time-stamps originating from DLD outputs. Theoretically, those times can be calculated by taking into account the mass-to-charge ratio and the position of each virtual ion, as well as the APT instrument geometry used (Equations (II.8) to (II.12)).

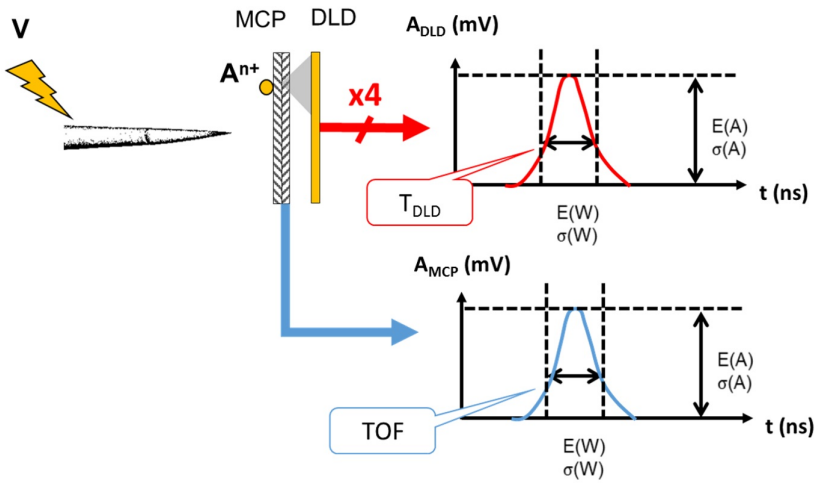

Figure II.8: Schematic of the generation of signals from detector outputs. Output signals from the detector have been reproduced in accordance with the most realistic shape [7], their amplitude distribution and their width distribution.

$$TOF = \sqrt{X^2 + Y^2 + {L_0}^2}\sqrt{\frac{m}{2neV}} \tag{II.6}$$

$$T_{X1} = \left(\frac{1}{2} - \frac{X}{l_X}\right) TPX + TOF \tag{II.7}$$

$$T_{X2} = \left(\frac{1}{2} + \frac{X}{l_X}\right) TPX + TOF \tag{II.8}$$

$$T_{Y1} = \left(\frac{1}{2} - \frac{Y}{l_Y}\right) TPY + TOF \tag{II.9}$$

$$T_{Y2} = \left(\frac{1}{2} + \frac{Y}{l_Y}\right) TPY + TOF \tag{II.10}$$

Where l_X and l_Y are the transversal length of the delay lines from the X and Y axes; L_0 is the distance between the tip and the detector; TPX and TPY are the total propagation times of electric signals on X and Y axes; and V is the evaporation potential of each ion.
As a reminder, two types of MCP-DLD output configurations can be found in current APT instruments; a particle detection operated with the MCP output and four outputs coming from two delay lines, and a particle detection which does not take into account the MCP output, but which resolves ambiguous

particle detections with a third superimposed delay line, either oriented at 45° related to the two firsts orthogonally oriented delay lines [16], or three delay lines oriented at 60° from each other [13]. The first configuration has been adopted by the LaWATAP instrument [4], and the second one by the LEAP series [14]. As a consequence, in addition to the previous description of the theoretical time stamps that could be obtained from a LaWATAP instrument, the simulation can also take into account the Z axis from the third delay of a LEAP detector, oriented at 45° oriented related to the two firsts orthogonally oriented delay lines.

$$Z = \sqrt{X^2 + Y^2} \cos\left(\tan^{-1}\left(\frac{Y}{X}\right) - \frac{\pi}{4}\right) \tag{II.11}$$

$$T_{Z1} = \left(\frac{1}{2} - \frac{Z}{l_Z}\right) TPZ + TOF \tag{II.12}$$

$$T_{Z1} = \left(\frac{1}{2} + \frac{Z}{l_Z}\right) TPZ + TOF \tag{II.13}$$

Where l_Z is the transversal length of the delay line from the Z axis, and TPZ is the total propagation time of electric signals on the Z axis.
With the aim of representing as well as possible the working process of the APT detector, output signals are hooked to those theoretical times (Figure II.8). By referring to signals acquired experimentally on APT detectors, it has been found that their width and rise time are approximately constant whatever their amplitude [7].

II.4 Model of the APT detection system

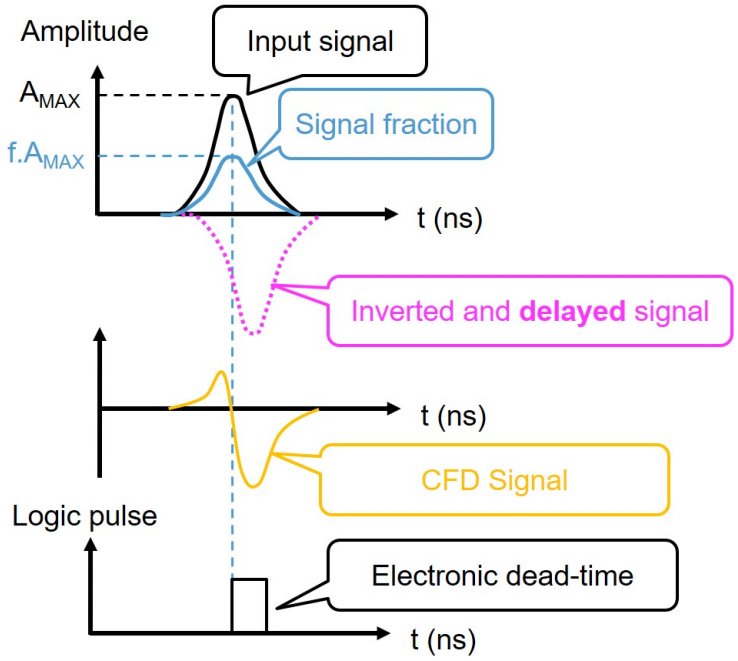

Figure II.9: Schematic of the operating process of the CFD. The addition between a replica of the output signal, shifted by a fraction of the rise time $f.t_R$ and inverted (purple curve), and another replica whose amplitude is attenuated by the same fraction f, gives a resulting signal (yellow curve) on which the zero crossing point is used for triggering a timing measurement.

As mentioned in Chapter I, one of the best approaches to perform time measurements on signals having homothetic shapes, is the use of CFD systems. Conversely to simple discriminators, which rely on the detection of electric signals exceeding an amplitude threshold, CFDs rely on time thresholds defined by a fraction of signals rise time (Figure II.9). Thus, in accordance with the homothetic behaviour of output signals, time measurements with CFDs can ensure a high timing precision. That involves both high precision for mass-to-charge measurements and high spatial precision for the DLD.
Moreover, it has to be known that every time measurement from a CFD system is always followed by a logic signal with a duration between 3 and 5 ns [1,17]. This time duration represents the dead-time (DT) of the detection system (see Chapter I).

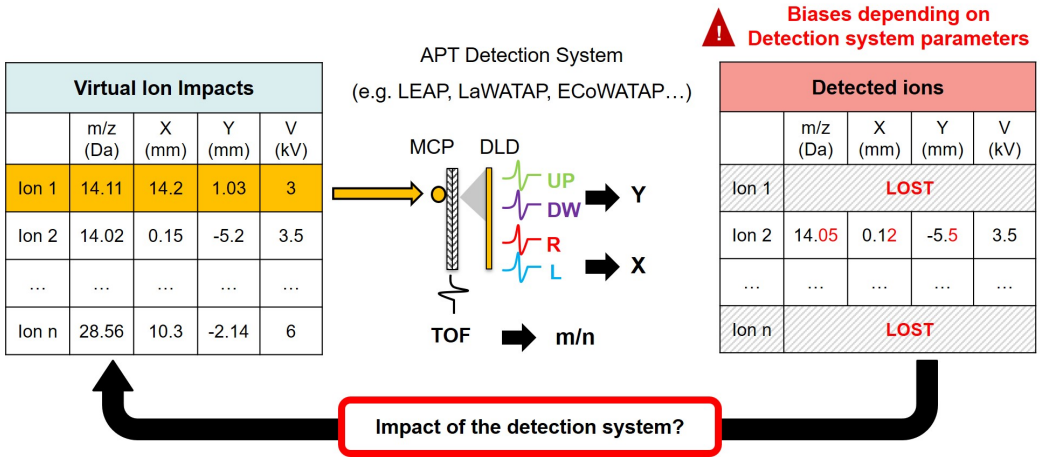

Figure II.10: Schematic of the simulation of the APT detection process.

II.5 Hit Finding Algorithm

At this point, it can be assumed that a simulation of the APT detection process can be performed through this last description of the APT detection system. Therefore, a list of detected ions can be determined from the different simulated time measurements (Figure II.10).

$$\frac{m}{n} = 2eV\frac{TOF^2}{X^2 + Y^2 + {L_0}^2} \tag{II.14}$$

$$X = \frac{T_{X1} - T_{X2}}{2TPX} l_X \tag{II.15}$$

$$Y = \frac{T_{Y1} - T_{Y2}}{2TPY} l_Y \tag{II.16}$$

$$Z = \frac{T_{Z1} - T_{Z2}}{2TPZ} l_Z \tag{II.17}$$

From Equations (II.14) to (II.17), it is then possible to predict the mass-to-charge ratio and the position that would be detected for each ion impact. However, it has to be known that positions and mass-to-charge ratios cannot be directly determined when multi-hits occur. Indeed, it must be understood that there are some cases of multi-hit events where DLD time-stamps cannot be ordered as a function of their arrival. As illustrated on Figure II.11, as long as DLD electric signals generated from a first ion impact, are still not transmitted to each ending, it is totally possible to receive upstream signals from successive ion impacts. In other words, first time-stamps arriving at DLD ending are not necessarily related to first

ion hits. Therefore, it is necessary to develop an algorithm that is able to automatically attribute a specific index to each time-stamps, and then determining the resulting mass-to-charge ratio and position from each impact coming from multi-hit events.

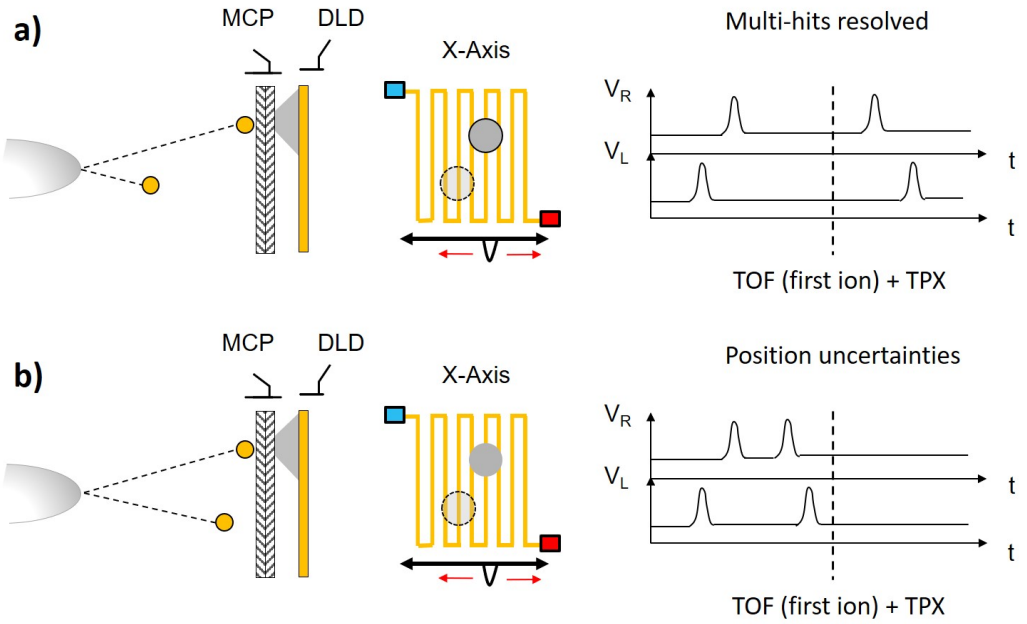

Figure II.11: Illustration of the main scenarios that can occur during multi-hit events on a single DLD axis. The temporal separation of the two ion hits in a) makes it possible to clearly resolve each ion position contrary to the situation b). Given that propagation times of electric signals on delay lines cannot exceed the total propagation times (TPX and TPY), it can be deduced that multi-hits can be resolved if their associated DLD signals are temporally separated at least by the total propagation times.

For those specific cases of multi-hit events, where DLD time-stamps could be mixed-up, Figure II.12 also shows that the number of position possibilities could reach n^2 in worst cases, with n the number of ion impacts. For example, with three ion impacts, two set of three time-stamps can be recorded respectively on X and Y DLD axes, which represents 9 potential positions. This issue represents one of the main causes of spatial biases induced by DLD detectors [13]. However, no concrete studies on this topic have been submitted until now. Algorithms used for resolving those spatial uncertainties are known as "Hit-Finding Algorithms", and the most widely used today is embedded in the LEAP series [14]. But this algorithm is not currently available for APT users. As a consequence, for the next studies,

a simple hit-finding algorithm has been implemented to the instrument model, and the following results will be only based on a LaWATAP detector configuration (MCP output and four DLD endings).

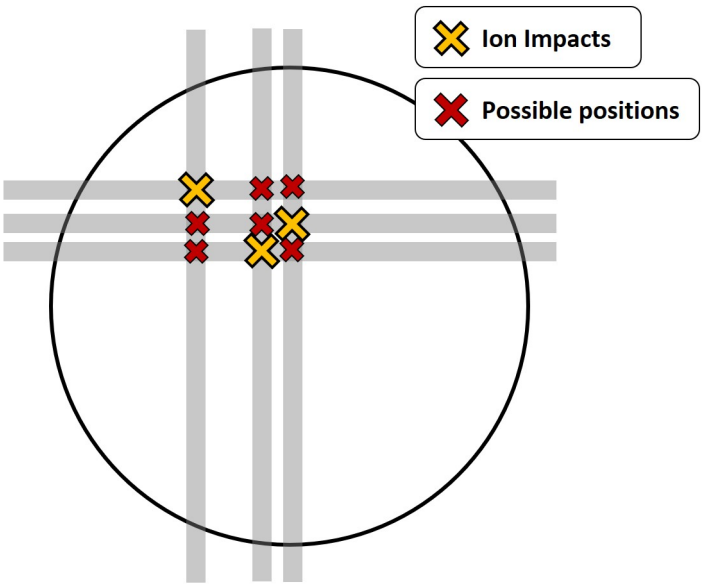

Figure II.12: Schematic representation of 3 ion impacts on the detection surface during a multi-hit event. Grey areas represent all axes detected from time measurements on the DLD. Crossing areas between detected axes create different position possibilities.

The hit finding algorithm used for this study is based on the comparison of all TOF directly measured from the MCP output with all TOF calculated from DLD time measurements, during a multi-hit event (Equations (II.7) to (II.10)). If two (or more) signals are separated by less than the instrument DT, information will be lost. To avoid artifacts in this situation, the number of atoms that can be treated is limited to the minimum number of time-stamps extracted among the four ends of the X and Y anodes. The only exception is when a single ending has only one time less than the others. In this case, the time left can be recovered from Equations (II.6) to (II.10).

II.6 Simulation of material analyses

APT Instrument simulated					
DT	MCP Detection Efficiency	Tip to Detector Flight Path	APT Geometry	Acquisition System	Rayleigh distribution mode
5 ns	80%	10 cm	Straight Flight Path	CFD/TDC	2.1mm

Table II.1: Main parameters of the APT Instrument simulated.

By means of the simulation tool, two critical cases in APT have been studied. The first one is the analysis of boron implanted in silicon, characterized by the high probability of the boron to be evaporated in multi-hit events [8,17]. The second one is the analysis of an AlMgSi alloy, that introduces more complex evaporation mechanisms because of the presence of precipitates in the material [10]. Both of them have been modeled to be analyzed with the simulation tool. Table II.1 introduces the APT instrument modeled for analyzing those material models.
It has to be noted that only one distribution model of inter-Impact distances has been taken into account for this study (Table II.1).

II.6.1 Analysis of a B-implanted Si material

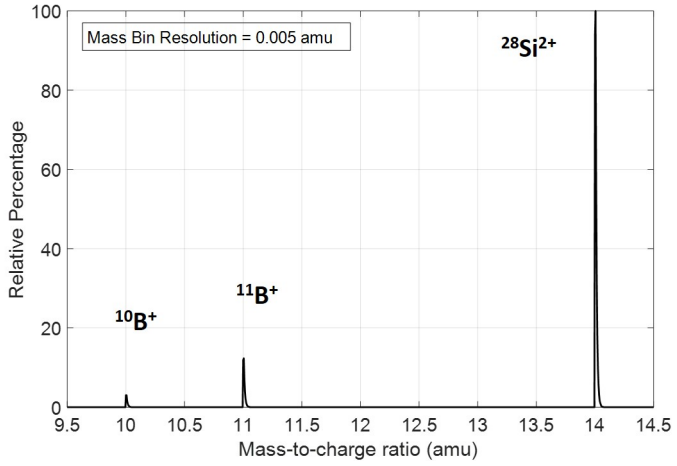

Figure II.13: Mass spectrum used for modeling the composition of the B-implanted Si material.

	Input Composition	Output Composition	Average Multiplicity λ	Multi-Hit Efficiency	Total Efficiency
^{10}B	2.6%	2.1%	1.5	68.7%	55%
^{11}B	10.8%	8.4%	1.53	69.3%	55.4%
^{28}Si	86.6%	89.1%	1.26	90.9%	72.7%

Table II.2: Compositional biases induced by the APT detection system on a B-implanted in Si material model. The total efficiency is calculated from the combination of the multi-hit efficiency and the MCP efficiency (80% on the simulated instrument).

In the case of the B-implanted in Si material , the two boron isotopes, ^{10}B and ^{11}B, were included in the material model in order to monitor any change in their natural abundances (Figure II.13). As agreed previously, each element has its own average multiplicity in order to underscore the difference between their evaporation behaviors (Table II.2). Table II.2 illustrates how the combination of the multi-hit capacity of the instrument and the variability of the evaporation mechanism, plays an important role in the correct estimation of the material composition. Given that the detector is subject to a geometrical transmission originating from the MCP assembly, the total detection efficiency of the detection system can be defined by the combination of the MCP efficiency (80% on the detector model) and the multi-hit efficiencies from respective elements. Noting that the computed multi-hit efficiencies are determined through the counting of the number of ions detected, originating from multi-hit events. As expected from APT experiments [8, 17], Table II.2 indicates that the boron is clearly under-estimated compared to its original fraction in the material.

II.6.2 Analysis of an AlMgSi alloy

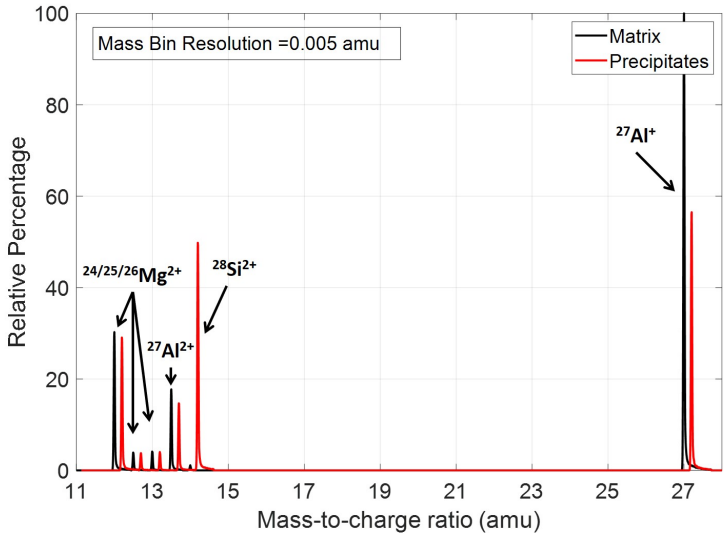

Figure II.14: Mass spectrum used for modeling the composition of the AlMgSi material. The two spectra have been shifted by 0.2 amu for better visibility.

		Input Composition	Output Composition	Average Multiplicity λ	Multi-Hit Efficiency	Total Efficiency
Matrix	Al	60.5%	64.8%	1.17	85%	68%
	Si	0.67%	0.61%	1.4	71.2%	57%
Precipitates	Al	34.2%	37.3%	1.45	63.3%	50.6%
	Si	30.4%	24.1%	2.18	46.6%	37.3%

Table II.3: Compositional biases induced by the APT detection system on an AlMgSi alloy model. The total efficiency is calculated from the combination of the multi-hit efficiency and the MCP efficiency (80% on the simulated instrument).

More complex examples can be found in mixed materials, where not only multiplicities between elements are unequal but also multiplicities between phases. This is the case for the AlMgSi alloy (Figure II.14 and table II.3).

In addition to selective losses between elements, one can see that a same element, in this case Si or Al, does not have the same detection efficiency depending on the phase encountered. As a consequence, more complex compositional biases may arise when one has to cope with mixed materials.

II.7 Investigation on losses due to the "Dead-Region"

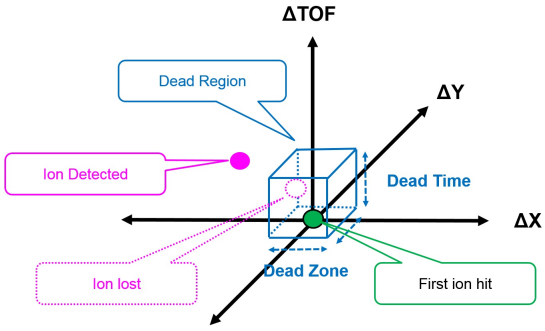

Figure II.15: Schematic representation of the DR around each first ion hit as defined in the literature [6, 19]. Any other ions arriving inside the DR are considered to be lost.

	Efficiencies in double events	
	Expected Efficiencies	**Efficiencies from simulation output data**
$Si_{1-x}B_x$	65%	59.4%
AlMgSi (Matrix)	71.8%	67.2%
AlMgSi (Precipitates)	64.9%	57.2%

Table II.4: Efficiencies (in double events) expected from the literature ([6, 19]) and obtained with the simulation tool.

As mentioned in Chapter I, the main assumption about losses during multi-hit events is based on the theoretical "Dead-Region" (DR) around each first ion hit (Figure II.15), where it is expected to lose any other ions arriving inside. From this assumption, expected losses can be then calculated by selecting secondary ion arrivals, from virtual ion impacts, that are inside

the theoretical DR. It is then proposed to compare those expected losses with the amount of ions lost during the simulation of the detection process. This comparison has only been focused on losses from double-hit events (Figure II.4). In Table 4, it can be seen that differences between expected and detected efficiencies fluctuate between 5% and 8%. As a consequence, a new definition of the DR has to be found in order to correctly identify the origin of losses during multi-hit events.

II.8 Origin of losses during multi-hit events

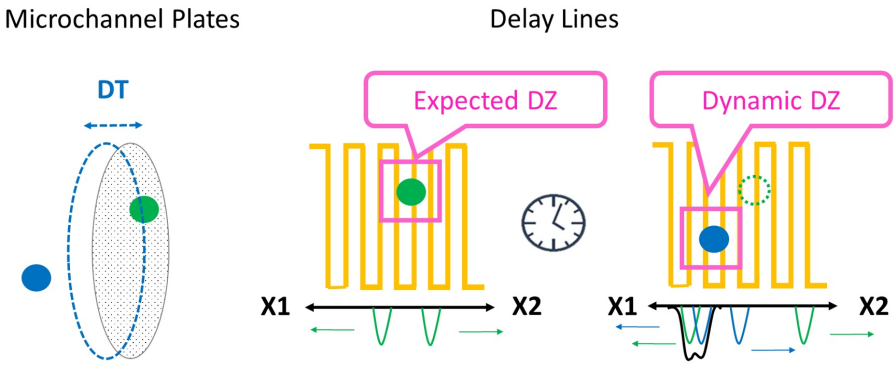

Figure II.16: Signal loss mechanism on a single delay line that can happen beyond the DZ around the first point of impact. A signal that propagates along the delay line remains subjected to the DT during all its propagation on the line.

As a reminder, the dead-time (DT) of the APT detection system is by definition, the inability of the electronic system to record successive time-stamps after a first time measurement. That means that, if the time offset between successive signals is under the DT, only a single time-stamp can be recorded. As illustrated on Figure II.16, by taking into account a single delay line, one can deduce that a signal that propagates along the delay line remains subjected to the DT during all its propagation on the line. The arrival of a first ion on the delay line generates two electric signals that propagate in opposite directions. During a double-hit event, a second ion will generate in turn two other electric signals. In the case where one of them merges with one of the first two signals, timing information can be lost outside the theoretical DR [6, 19]. From this assumption it can be inferred

that the signal loss mechanism is not only dedicated to ion pairs with very close TOF and very close relative distances, but also effective for separated TOF and longer relative distance on the detector.

$$\Delta TOF + DT \geq \frac{2\Delta X}{v_X} \geq \Delta TOF - DT \tag{II.18}$$

$$\Delta TOF + DT \geq \frac{2\Delta Y}{v_Y} \geq \Delta TOF - DT \tag{II.19}$$

This phenomenon can be put into two simple equations (Equations (II.18) and (II.19)) defining a new vision of the DR, ruled by dynamic "Dead-Zones" (DZ) around each signal that propagate along the delay lines; where ΔTOF is the TOF difference between ion pairs, v_X and v_Y are the transversal propagation velocities of electric signals respectively on X and Y delay line, ΔX and ΔY are respectively the distance between points of impact on X and Y anodes.

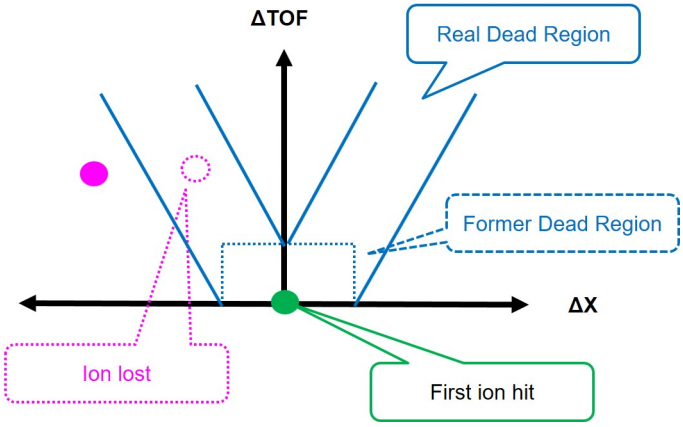

Figure II.17: Graphical representation of the new definition of the DR (Equation (II.18)). The arrival of a first ion on the delay line generates two electric signals that propagate in opposite directions. During multi-hit events, successive ions arriving with TOF differences ΔTOF, will generate in turn other pairs of electric signals. In the case where one of them merges with one of the two first signals, timing information can be lost.

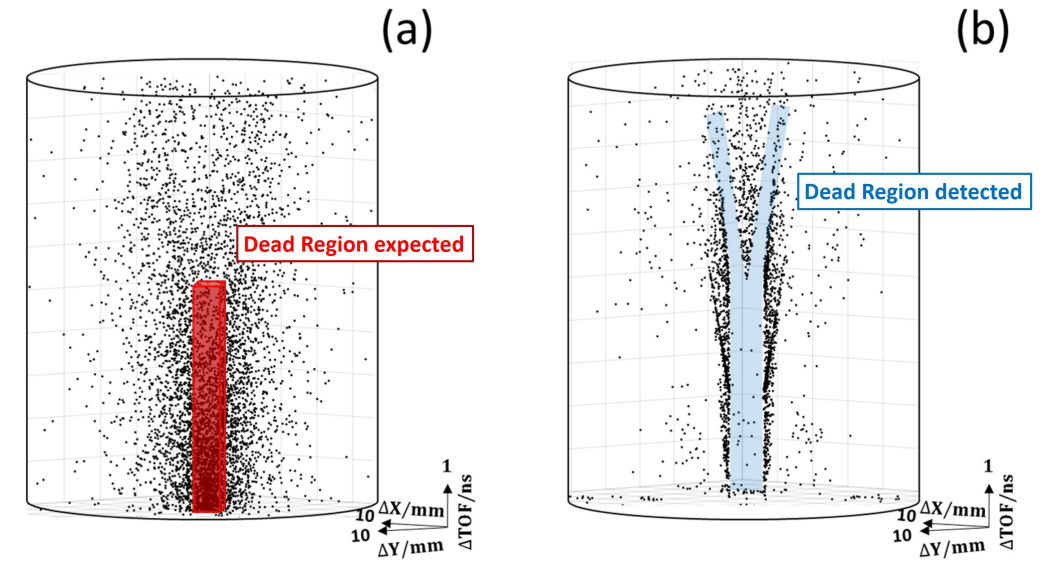

Figure II.18: 3D correlation maps on the analysis of the boron-silicon alloy. (a) Simulation input data (virtual ion impacts before being treated by the detection system); (b) Simulation output data (Ions detected by the detection system model).

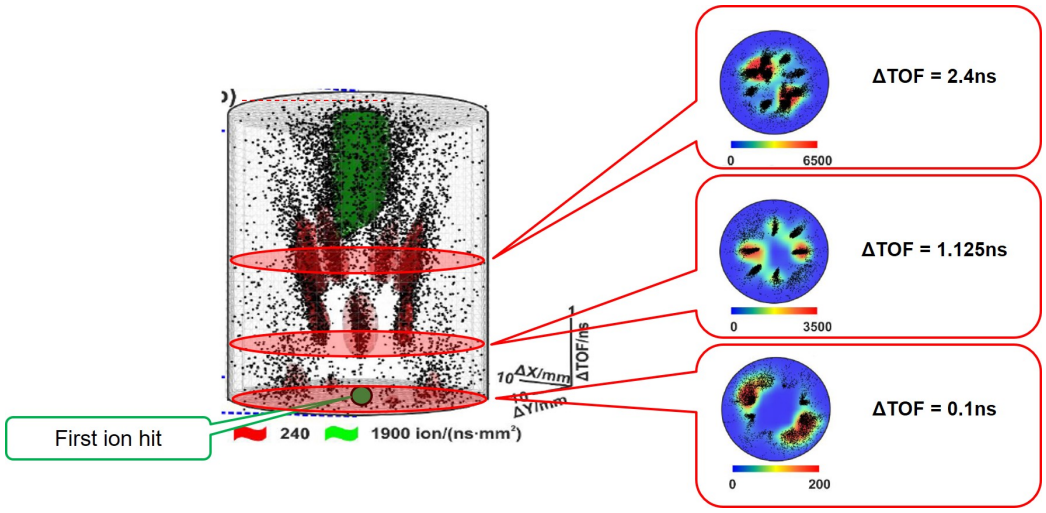

Figure II.19: Multi-hit 3D correlation map from the analysis of a tungsten carbide sample on a LEAP 5000 XS [24]. This 3D map reveals the relative position and TOF differences between ion pairs during multi-hit events.

This new definition of the DR could explain experimental results

introduced by Peng et al. on the analysis of a tungsten carbide (Figure II.19), where it has been found that the depleted region observed in the 3D correlation map exceed the boundaries of the theoretical DR [6, 19]. As illustrated in Figure II.18, simulation results, from the previous analysis of a Boron-Silicon alloy, also support the shape of this new theoretical DR (Figure II.17).

II.9 Reduction of the instrument DT through a simulation approach

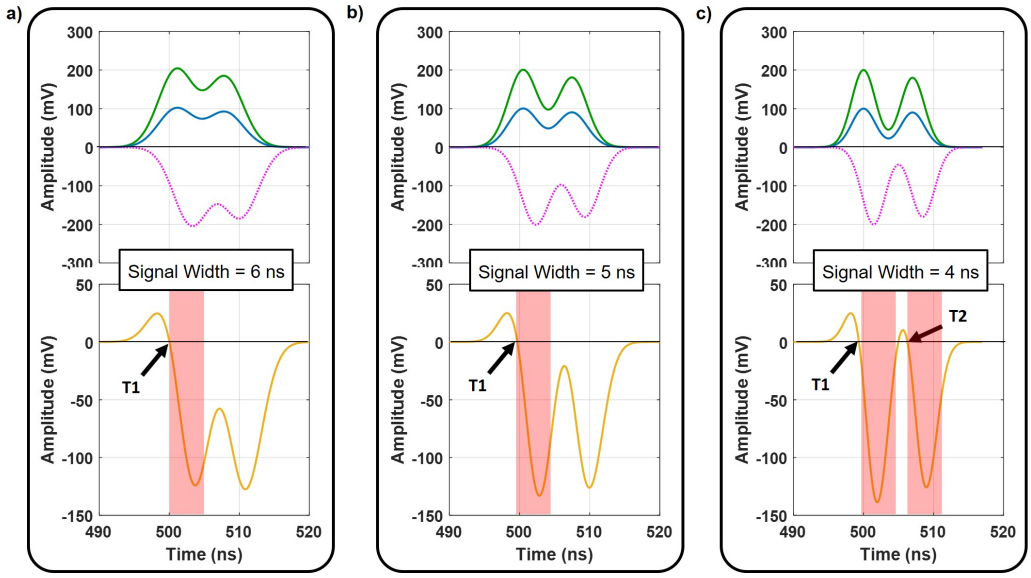

Figure II.20: Signal loss mechanism from CFD systems. The different signals from a), b) and c), use the same colour scheme as in Figure II.9; The green curve represents the input signal, the blue one represents the input replica whose amplitude is attenuated by a fraction f, the purple one represents the input replica shifted by a fraction of the rise time $f.t_R$ and inverted, and the yellow curve represents the resulting signal on which the zero crossing point is used for triggering timing measurements. From cases a), b) and c), the overlapped input signals are separated by 7 ns, and the timing detection is characterized by a DT of 5 ns (red zones). Only signals widths (at FWHM) differ between a), b) and c).

Regarding the impact of the DR on APT analyses, one question may arise; is it possible to increase the multi-hit capacity of the APT detector by

reducing the instrument DT? By looking back to the operating process of the CFD system (Figure II.9), it can be recalled that output signals are triggered through the detection of zero crossing points at the CFD output signal. Taking this into account, one can note that some cases of loss do not always depend on the DT. Indeed, by referring to Figure II.20, it can be observed that despite a time difference between two successive signals, exceeding the instrument DT, signal losses may occur. Figure II.20a and Figure II.20b clearly show that those signal losses are not related to the instrument DT, but are related to the inability of the CFD system to provide as many zero crossing points as the number of successive signals generated. For those specific cases, reducing the DT will not have the effect of improving the multi-hit capacity of the APT detection system. It is clear that, reducing the DT must be coupled with the reduction of output signal widths to enable the emergence of zero crossing points at the CFD signal output (Figure II.20c).

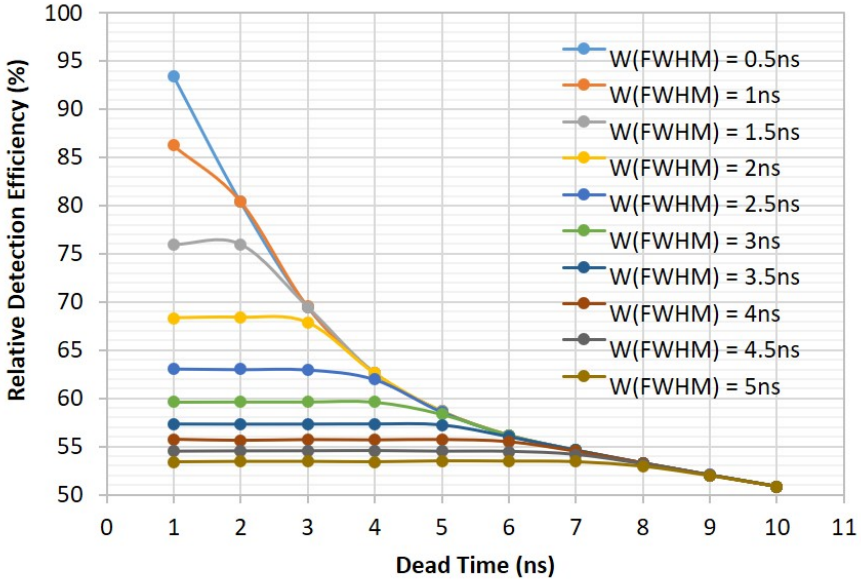

Figure II.21: Relative Detection Efficiency in double-hit events (from the previous simulation of the analysis of B-implanted in Si material) as a function of the instrument DT and the width of output signals.

In order to get a clear idea of the impact of both the instrument DT and the width of output signals on APT analyses, parametric simulations have been performed with the previous simulation of the analysis of Boron-silicon alloy. In this study only double-hit events have been taken into account. Specifying that the detection efficiency of double-hit events does not refer

to the number of ion impacts detected, but referred to the number of detected double-hit events. As illustrated in Figure II.21, it can be observed that output signals reach a limit in terms of detection efficiency when it is attempted to reduce the instrument DT. As a consequence, instruments promoting a reduction of the instrument DT cannot claim the improvement of their multi-hit capacity as long as the width of their output signals is not reduced at the same time.

II.10 Conclusion

This work has introduced a systematic study of the impact of APT detection system on material analysis. For this purpose, a simulation tool has been developed to simulate the detection process; from atoms that are field ion emitted to TOF and delay line time measurements, but also signals generation on detector outputs.
In accordance with studies on APT compositional biases [7, 9, 17, 18], it has been observed that the APT detection efficiency does not only depend on the instrument DT, but also on the evaporation mechanism of the material analyzed. In a same material, different elements that tend to field evaporate in multi-hit events more than others, can be under-estimated. This phenomenon is in part responsible for compositional biases during APT experiments. The two material models introduced in this study (B-implanted in Si and AlMgSi alloys) are part of the critical cases in APT experiments [8–10, 17]. Thus, it must be expected to get higher efficiencies and less selective losses for non-critical materials.
Moreover, by trying to understand the origin of losses in APT experiments, a new definition of the DR has been found. It turns out that this DR is not only restricted to the space and time volume around each ion impact as defined in the literature [6, 19]. Simulations proved that in some cases, it possible to trigger signal losses with ion pairs having TOF differences that are higher than the instrument DT.
From those simulation results, one can deduce that, in order to avoid both compositional and spatial biases, an additional step has to be taken for reducing the instrument DT. This step has already been initiated by a system called the Advanced Delay Line Detector (aDLD). However, the reliability of this promising detection system has been put into question. The next chapter will be aimed at introducing the aDLD system and will be aimed at getting back its credibility through simulations, and also through the development of a new design of DLD detector that is able to outperform current DLDs using the aDLD system.

Bibliography

[1] Mohamed Serraj Andaloussi, Mounir Boukadoum, and El-Mostapha Aboulhamid. A novel time-to-digital converter with 150 ps time resolution and 2.5 ns pulse-pair resolution. In *The 14th International Conference on Microelectronics,*, pages 123–126. IEEE, 2002.

[2] Jie Bao, Zhijie Xu, Robert Colby, Suntharampillai Thevuthasan, and Arun Devaraj. Level set method for tip shape evolution simulation for atom probe tomography. *Microscopy and Microanalysis*, 21(S3):841–842, 8 2015.

[3] Ivan Blum, Lorenzo Rigutti, François Vurpillot, Angela Vella, Aurore Gaillard, and Bernard Deconihout. Dissociation dynamics of molecular ions in high dc electric field. *The Journal of Physical Chemistry A*, 120(20):3654–3662, 2016.

[4] Joseph H Bunton, Jesse D Olson, Daniel R Lenz, and Thomas F Kelly. Advances in pulsed-laser atom probe: Instrument and specimen design for optimum performance. *Microscopy and Microanalysis*, 13(6):418, 2007.

[5] Joel E. Cohen and Daniel Courgeau. Modeling distances between humans using taylor's law and geometric probability. *Mathematical Population Studies*, 24(4):197–218, 10 2017.

[6] G. Da Costa. Atom probe tomography. In *Atom Probe Tomography*, pages 155–181. Elsevier, 2016. DOI: 10.1016/B978-0-12-804647-0.00006-1.

[7] G. Da Costa, F. Vurpillot, A. Bostel, M. Bouet, and B. Deconihout. Design of a delay-line position-sensitive detector with improved performance. *Review of Scientific Instruments*, 76(1):013304, 1 2005.

[8] G. Da Costa, H. Wang, S. Duguay, A. Bostel, D. Blavette, and B. Deconihout. Advance in multi-hit detection and quantization in atom probe tomography. *Review of Scientific Instruments*, 83(12):123709, 12 2012.

[9] F Danoix, M.K Miller, and A Bigot. Analysis conditions of an industrial al–mg–si alloy by conventional and 3d atom probes. *Ultramicroscopy*, 89(1-3):177–188, 10 2001.

[10] Frédéric De Geuser, Baptiste Gault, Alain Bostel, and François Vurpillot. Correlated field evaporation as seen by atom probe tomography. *Surface science*, 601(2):536–543, 2007.

[11] Claudia Fleischmann, Kristof Paredis, Davit Melkonyan, and Wilfried Vandervorst. Revealing the 3-dimensional shape of atom probe tips by atomic force microscopy. *Ultramicroscopy*, 194:221–226, 11 2018.

[12] Baptiste Gault, Michael P Moody, Julie M Cairney, and Simon P Ringer. *Atom probe microscopy*, volume 160. Springer Science & Business Media, 2012.

[13] O Jagutzki, V Mergel, K Ullmann-Pfleger, L Spielberger, U Spillmann, R Dörner, and H Schmidt-Böcking. A broad-application microchannel-plate detector system for advanced particle or photon detection tasks: large area imaging, precise multi-hit timing information and high detection rate. *Nuclear Instruments and Methods in Physics Research Section A: Accelerators, Spectrometers, Detectors and Associated Equipment*, 477(1-3):244–249, 2002.

[14] Thomas F Kelly and David J Larson. Local electrode atom probes. *Materials Characterization*, 44(1-2):59–85, 2000.

[15] S. Koelling, N. Innocenti, A. Schulze, M. Gilbert, A. K. Kambham, and W. Vandervorst. In-situ observation of non-hemispherical tip shape formation during laser-assisted atom probe tomography. *Journal of Applied Physics*, 109(10):104909, 5 2011.

[16] David J Larson, TyJ Prosa, Robert M Ulfig, Brian P Geiser, and Thomas F Kelly. Local electrode atom probe tomography. *New York, US: Springer Science*, 2, 2013.

[17] Frederick Meisenkothen, Eric B. Steel, Ty J. Prosa, Karen T. Henry, and R. Prakash Kolli. Effects of detector dead-time on quantitative analyses involving boron and multi-hit detection events in atom probe tomography. *Ultramicroscopy*, 159:101–111, 12 2015.

[18] M. K. Miller and G. D. W. Smith. An atom probe study of the anomalous field evaporation of alloys containing silicon. *Journal of Vacuum Science and Technology*, 19(1):57–62, 5 1981.

[19] Michael K. Miller and Richard G. Forbes. *Atom-Probe Tomography*. Springer US, Boston, MA, 2014. DOI: 10.1007/978-1-4899-7430-3.

[20] M.K. Miller and M.G. Hetherington. Local magnification effects in the atom probe. *Surface Science*, 246(1-3):442–449, 4 1991.

[21] D. Moltchanov. Distance distributions in random networks. *Ad Hoc Networks*, 10(6):1146–1166, 8 2012.

[22] A. Papoulis and H. Saunders. Probability, Random Variables and Stochastic Processes (2nd Edition). *Journal of Vibration, Acoustics, Stress, and Reliability in Design*, 111(1):123–125, 01 1989.

[23] S Parviainen, F Djurabekova, S P Fitzgerald, A Ruzibaev, and K Nordlund. Atomistic simulations of field assisted evaporation in atom probe tomography. *Journal of Physics D: Applied Physics*, 49(4):045302, 2 2016.

[24] Zirong Peng, Francois Vurpillot, Pyuck-Pa Choi, Yujiao Li, Dierk Raabe, and Baptiste Gault. On the detection of multiple events in atom probe tomography. *Ultramicroscopy*, 189:54–60, 6 2018.

[25] J. F. Ramaley. Buffon's noodle problem. *The American Mathematical Monthly*, 76(8):916, 10 1969.

[26] DW Saxey. Correlated ion analysis and the interpretation of atom probe mass spectra. *Ultramicroscopy*, 111(6):473–479, 2011.

[27] F. Vurpillot, A. Bostel, and D. Blavette. Trajectory overlaps and local magnification in three-dimensional atom probe. *Applied Physics Letters*, 76(21):3127–3129, 5 2000.

[28] L. Yao, B. Gault, J.M. Cairney, and S.P. Ringer. On the multiplicity of field evaporation events in atom probe: A new dimension to the analysis of mass spectra. *Philosophical Magazine Letters*, 90(2):121–129, 2 2010.

[29] Min Zhu, Oana Cojocaru-Mirédin, Antonio M Mio, Jens Keutgen, Michael Küpers, Yuan Yu, Ju-Young Cho, Richard Dronskowski, and Matthias Wuttig. Unique bond breaking in crystalline phase change materials and the quest for metavalent bonding. *Advanced Materials*, 30(18):1706735, 2018.

Chapter III

Towards the democratization of the Advanced Delay Line Detector

In the previous chapter, it has been demonstrated that reducing the electronic dead-time (DT) of APT detection systems, composed of constant fraction discriminators (CFDs) and Time-to-Digital Convertors (TDCs), will not systematically reduce the compositional and spatial biases associated to the detection system. Technological efforts on the reduction of the DT have to be coupled with the reduction of output signal widths. It turns out that none of current TDC/CFD technologies allow improvements on both parameters; the DT of TDC systems has reached its limit since 2002 with 2.5 ns [2], and despite the efforts made to shorten output signal widths from MCPs [11, 12], the electronic processing chain used for exploiting MCP and DLD output signals is still limited in bandwidth introducing minimum signal widths around 5 ns (FWHM) [4,5]. Regarding the difficulty to improve those two parameters, current APT instruments may be subject to a significant limit of detection.

III.1 The Advanced Delay Line Detector

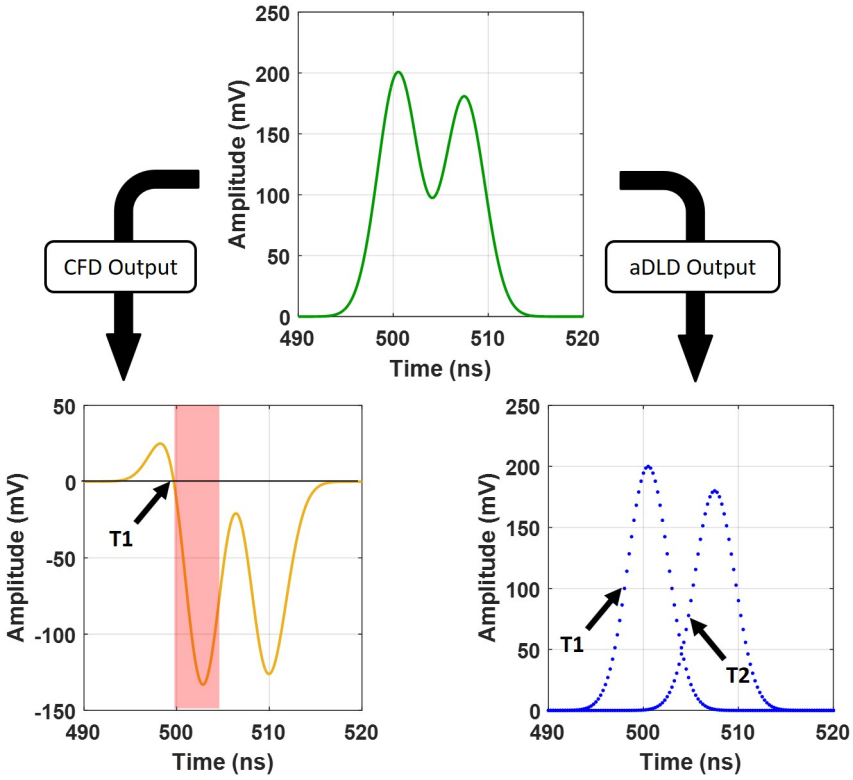

Figure III.1: Comparison between CFD and aDLD signal processing. The green curve representing an output signal from the APT detector composed of two overlapped signals, both 5 ns wide (FWHM) and separated by 7 ns, is both submitted to a CFD and aDLD system. Contrary to the CFD, the aDLD system is able to decompose overlapped signals and extract successive time-stamps that cannot be resolved in conventional APT detection systems [7].

In 2005, another type of detection system, called the Advanced Delay Line Detector (aDLD), emerged and promised an improvement of the multi-hit capacity (MHC) of APT detectors [4]. With the help of fast digitizers, the aDLD has the ability to decompose output signals, potentially overlapped during multi-hit events, into individual signals (Figure III.1). Hence, it has been demonstrated that the DT of conventional APT detection systems could be outperformed.

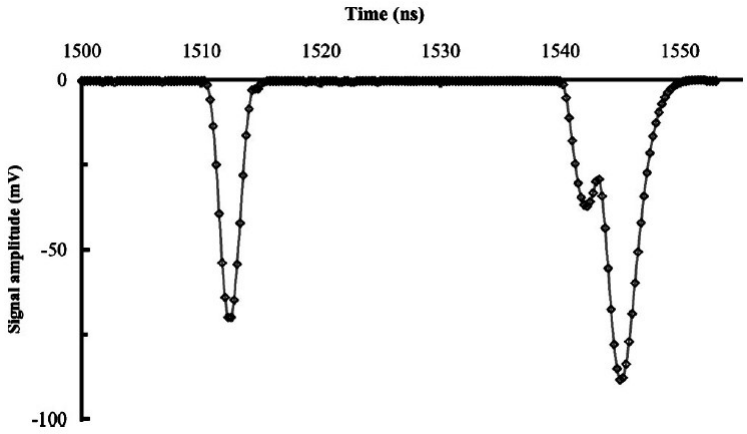

Figure III.2: Example of digitized output signals from an MCP assembly with a 4 GHz digitizer board (from [4])

The idea behind the aDLD process is to use a signal shape recognition algorithm in order to decompose step by step output signals potentially made of overlapped signals (Figure III.3). By assuming that individual output signals follow homothetic shapes (Figure III.2), as mentioned in the literature [4], it can be deduced that overlapped output signals, originating from multi-hit events, could be resolved through a matching algorithm using individual reference signals. Those reference signals can be determined through the mean shape of acquired signals which are most likely originating from single-hit events. As a result, the following key steps are then applied to resolve most of signal detection cases;

1. Output signals are sampled by a fast digitizers,
2. Slopes from acquired signals are chosen to be compared with slopes from reference signals,
3. Slopes from reference signals are then used for recovering individual signals through a fitting between the envelope of acquired signals and the reference signals.
4. Each time a recovered signal is built, a time-stamp is extracted on its rising edge at a fraction of its amplitude.
5. To determine the envelope of the next potentially overlapped signals, the previous recovered signal is subtracted from the envelope of the acquired signal.

6. The process is repeated from step 2 to step 5 until the width of the residual signal envelope is considered too small to be a valuable signal.

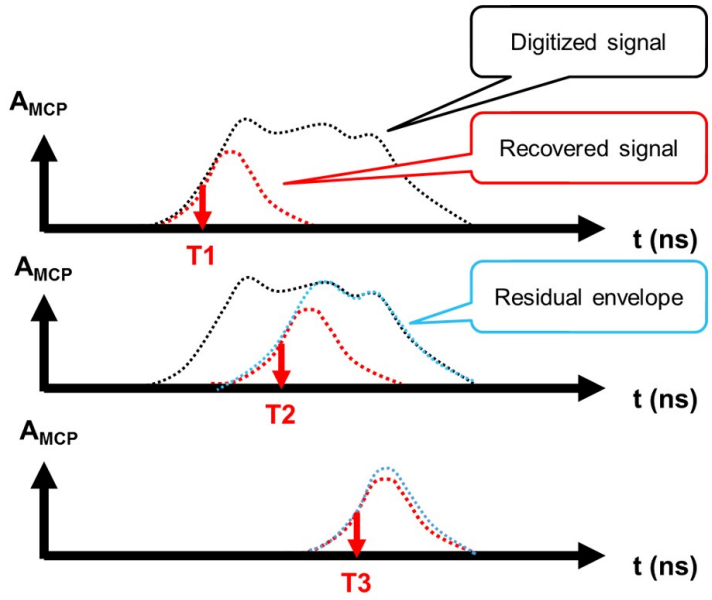

Figure III.3: aDLD operating process. With the help of a reference signal, the envelope of an acquired signal made of overlapped signals can be decomposed into individual signals.

As a consequence, with the help of fast digitizers, the aDLD system is able to decompose output signals into individual signals that could be potentially overlapped, and then outperform the limited DT introduced by conventional CFD systems.
Regarding the operating process of the aDLD, it can be assumed that the restricted DT imposed by CFD systems can be significantly outperformed. However, despite the clear benefits that the aDLD can provide for APT instruments, very few studies has been achieved for determining quantitative results on the contribution of the aDLD compared to CFD systems [4, 5], and none of them have been able to strictly compare their performances in terms of material analyses. That is why the following studies are aimed at estimating the impact of the aDLD system on APT experiments. Moreover, to strictly compare CFD and aDLD systems, it should be required to analyze a same material, under the same analysis conditions. However, due to the technical difficulty to perform this type of analysis, it would be difficult to get reliable comparisons. Therefore, the only way to strictly compare CFD to aDLD systems, under the same conditions, is to perform simulation studies.

III.2 Performances of the aDLD detection process

One of the mean chosen for estimating the theoretical performances of the aDLD detection system is the simulation of pairs of overlapped signals from a single output, by applying variations on their amplitude and their time separation (Figure III.4). Those parameters try to mimic the main variations observed in APT experiments.

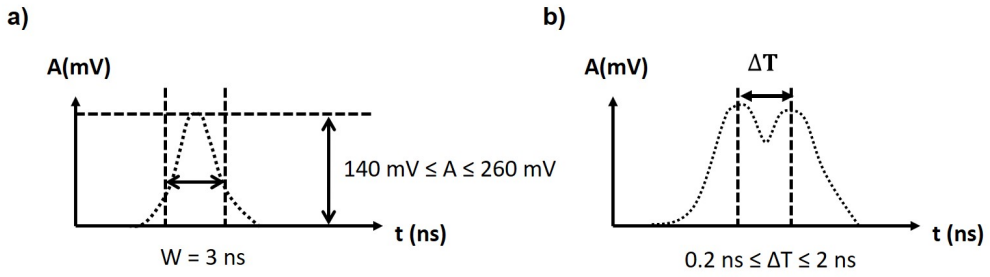

Figure III.4: Signal parameters taken into account for the first estimation of the theoretical performances of the aDLD detection system; a) Simulated signals introduce a Gaussian shape with 3 ns width (FWHM) and a uniform variation of their amplitude between 140 mV and 260 mV; b) The time separation between successive signals varies between 0.2 ns to 2 ns.

ΔT (ns)	Detection Efficiency
0.2	53.80%
0.4	50.00%
0.6	50.00%
0.8	65.40%
1	88.50%
1.2	100.00%
1.4	100.00%
1.6	100.00%
1.8	100.00%
2	100.00%

Table III.1: Detection efficiency of the aDLD system from a single output on the APT detector. Results obtained originate from the detection of signals described in Figure III.4.

By applying the aDLD operating process previously described, two main evaluation criteria have been studied; the detection efficiency and the timing

error from a single output ending. Table III.1 shows that, with the model of signals previously described, no signal loss appear above a time separation of 1.2 ns between two successive output signals. In addition to being in accordance with experimental results from Da Costa et al. [4], this result also bring the first theoretical evidence that the aDLD system clearly outperform the DT of CFD systems.
Concerning the timing errors induced by the aDLD system, Table III.2a and Table III.2b show that for signals with a fixed width (3 ns in this case), timing errors do not exceed 1 ns, and are the highest for every second signals recovered. From those results, it can also be observed that there is a complex relation between timing errors, amplitude ratios and the time separation between successive signals.

a)

Timing Error on Signal 1 (ps)		Amplitude Ratios (A1/A2)												
		0.7	0.75	0.8	0.85	0.9	0.95	1	1.05	1.1	1.15	1.2	1.25	1.3
ΔT (ns)	0.2	0	0	0	0	0	0	0	0	0	0	0	0	0
	0.4	0	148.6	155.2	161.5	167.5	173.2	178.6	183.8	188.7	193.5	198	202.3	206.5
	0.6	202.8	212.9	221.2	228.4	234.1	238.6	242.5	245.1	247.5	248.7	249.8	250	250
	0.8	232.7	238.7	242.6	246.2	248	249.6	250	250	250	250	250	250	250
	1	238.4	242.8	246	247.9	249.8	250	250	250	250	250	250	250	250
	1.2	236.4	240.9	244.5	246.5	248.4	250	250	250	250	250	250	250	250
	1.4	0	234.5	238.8	242.7	244.6	246.5	248.3	250	250	250	250	250	250
	1.6	34.51	229.1	232.5	235.6	238.8	240.3	242.6	244.2	245.8	247.4	249	250	250
	1.8	34.51	34.51	34.51	34.51	34.51	231.2	233.8	236.5	239.1	241.7	242.9	244	245.1
	2	34.51	34.51	34.51	34.51	34.51	34.51	34.51	34.51	34.51	34.51	34.51	34.51	235.2

b)

Timing Error on Signal 2 (ps)		Amplitude Ratios (A1/A2)												
		0.7	0.75	0.8	0.85	0.9	0.95	1	1.05	1.1	1.15	1.2	1.25	1.3
ΔT (ns)	0.2	NaN	NaN	NaN	NaN	NaN	NaN	NaN	NaN	NaN	NaN	NaN	NaN	800
	0.4	NaN	NaN	NaN	NaN	NaN	NaN	NaN	NaN	NaN	NaN	NaN	NaN	NaN
	0.6	NaN	NaN	NaN	NaN	NaN	NaN	NaN	NaN	NaN	NaN	NaN	NaN	NaN
	0.8	NaN	NaN	NaN	NaN	NaN	NaN	NaN	NaN	NaN	968.5	950	950	890.2
	1	NaN	NaN	NaN	1010	1000	1000	922.3	916.3	916.3	858.1	854.5	851.4	848.6
	1.2	1050	1050	966.3	879.1	848.9	893.9	792	766.9	744.2	813.6	702.6	690.8	678.9
	1.4	246.4	850	811.3	787.5	775.8	766.3	723.2	712.1	709	706.2	703.8	653.2	649
	1.6	285.5	816.3	731.5	750.1	746.9	744.1	641.7	679.5	674.8	670.7	667	561.7	552.1
	1.8	256.8	256.8	256.8	256.8	256.8	595.9	584.5	574.9	565.5	563.6	527.5	518.8	515.3
	2	107.6	107.6	107.6	107.6	107.6	107.6	107.6	107.6	107.6	165.5	165.5	165.5	529.2

Table III.2: Timing errors from time measurements applied on signals described in Figure III.4; a) Timing errors from all first recovered signals; b) Timing errors from all second recovered signals. "NaN" values in b) indicate that no signal has been detected for those cases.

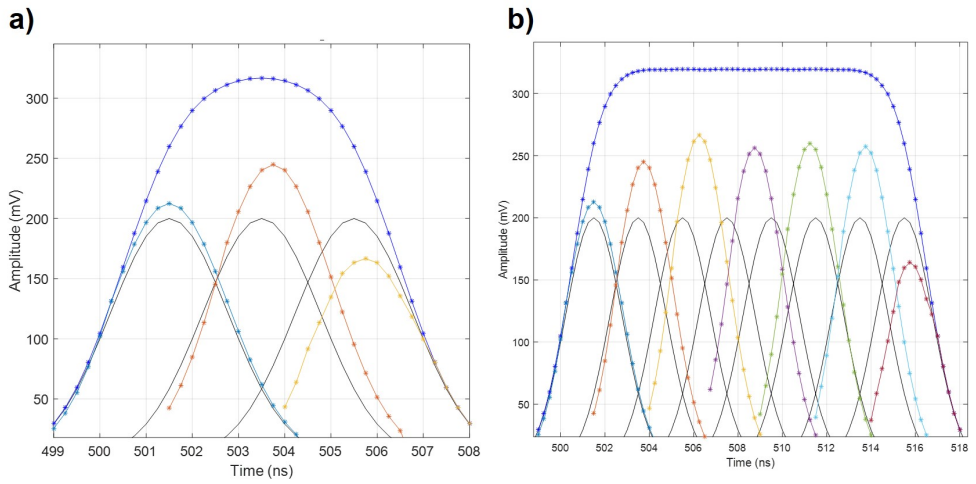

Figure III.5: Example of signal decomposition with the aDLD detection system. Dark blue signal envelopes in a) and b) represent the acquired output signals, which are originate from the sum of individual signals (black curves), all having a signal width of 3 ns and an amplitude of 200 mV. The other colored curves represent the recovered signals built from the aDLD detection process.

In order to get a deeper knowledge of the aDLD operating process, another study was aimed at modeling the detection of more than two successive signals on a single output ending. Results from Figure III.5, based on the detection of 3 and 8 successive signals, clearly shows that despite the advantage of reducing the instrument DT, the application of the aDLD signal processing on overlapped signals may both increase the timing errors, and mislead on the real shape of each signal component of acquired signals. Indeed, it can be observed that the shape recognition algorithm, previously described, reaches its limits when it has to cope with several overlapped signals.

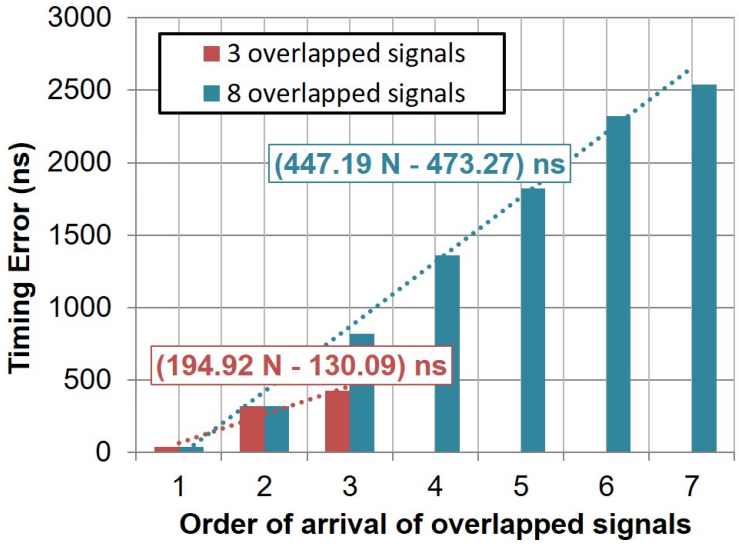

Figure III.6: Timing errors from timing measurements performed on simulated signals from Figure III.5. The red and blue histograms represent the evolution of the timing errors as a function of the order of arrival of overlapped output signals, respectively for 3 and 8 overlapped signals (Figure III.5). Red and blue dotted lines represent the linear trends of those two histograms.

III.3 Comparison between aDLD and CFD systems

With the aim of comparing performances of the aDLD system with the CFD systems, the simulation tool, previously described in Chapter II (Table III.3), used for reproducing the APT detection system, has been configured for sampling output signals and applying the aDLD detection process.

APT Instrument simulated				
DT	MCP Detection Efficiency	Tip to Detector Flight Path	APT Geometry	Rayleigh distribution mode
5 ns	80%	10 cm	Straight Flight Path	2.1mm

Table III.3: Main parameters of the APT Instrument simulated.

	Material Composition	Average Multiplicity λ
^{10}B	2.6%	1.5
^{11}B	10.8%	1.53
^{28}Si	86.6%	1.26

Table III.4: $Si_{1-X}B_X$ alloy model used for comparing simulation results between aDLD and CFD systems. As a reminder, In the case of the $Si_{1-X}B_X$ alloy, the two boron isotopes, ^{10}B and ^{11}B, were included in the material model in order to monitor any change in their natural abundances. As agreed previously, each element has its own average multiplicity in order to underscore the difference between their evaporation behaviors.

The model used for reproducing the aDLD system is based on the configuration of the most prominent APT instrument using the aDLD system; the LaWATAP [3,5]. The detection system of the LaWATAP is based on fast digitizers sampling MCP output signals at 4 Gs/s and DLD output signals at 1 Gs/s. In addition, an oversampling process on DLD output signals allows treating every signal as if they were sampled at 4 Gs/s [5]. That is why, every signal generated on the simulation tool has been sampled at 4 Gs/s.
Based on the parametric simulations performed on the $Si_{1-X}B_X$ model in Chapter II, and in the same analysis conditions (Table III.4), results from the aDLD system have been compared to the previous results obtained with the CFD system.

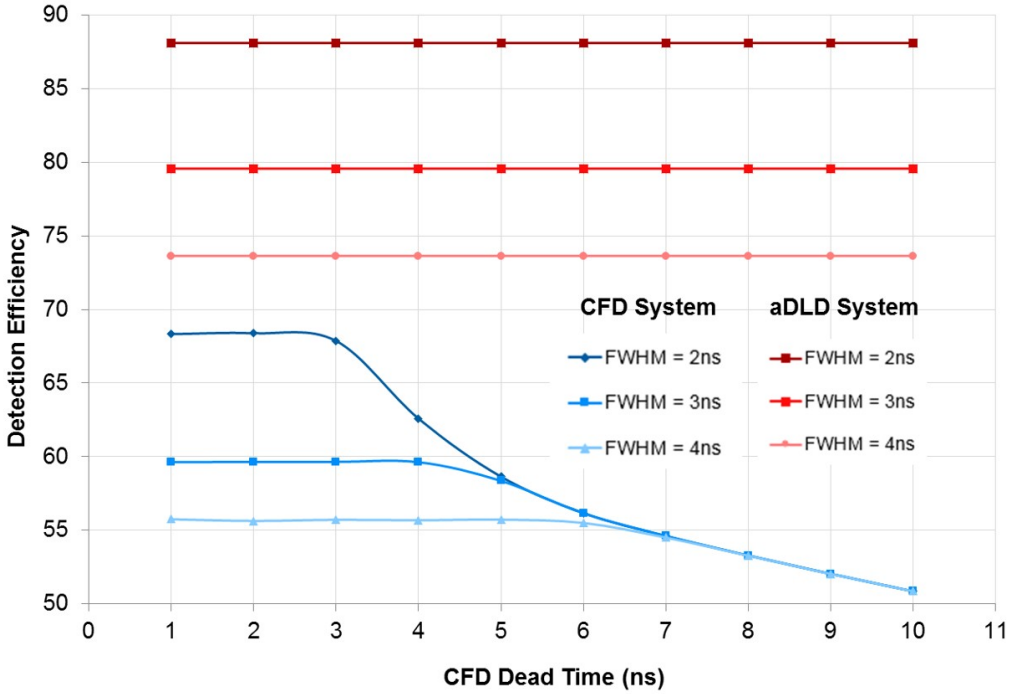

Figure III.7: Comparison of the detection efficiencies between aDLD and CFD systems on double-hit events, through different output signal widths. Specifying that the detection efficiency of double-hit events does not refer to the number of detected ion impacts, but refers to the number detected double-hit events.

As illustrated in Figure III.7, the strict comparisons of the two different detection systems confirm the assumptions on the superiority of the aDLD system on CFD systems, in terms of detection efficiency. In this specific case, it is demonstrated that the detection efficiency of double-hit events for the aDLD system is around 20% higher than the CFD system. Specifying that the detection efficiency of double-hit events does not refer to the number of detected ion impacts, but refers to the number of detected double-hit events. To support this quantitative improvement, it is also necessary to evaluate the quality of those results by determining the time and space errors generated during those two different detection processes. To do so, time and space information from detected ion impacts have to be compared with time and space references from virtual ion impacts. Thus, from those comparisons, position and TOF errors have been computed for being gathered in two-dimensional histograms (Figure III.8). Those results clearly show that the aDLD system can offer higher timing and spatial precisions

than the CFD system. This means that the additional detected ions collected with the aDLD system has little chance to be artifacts.

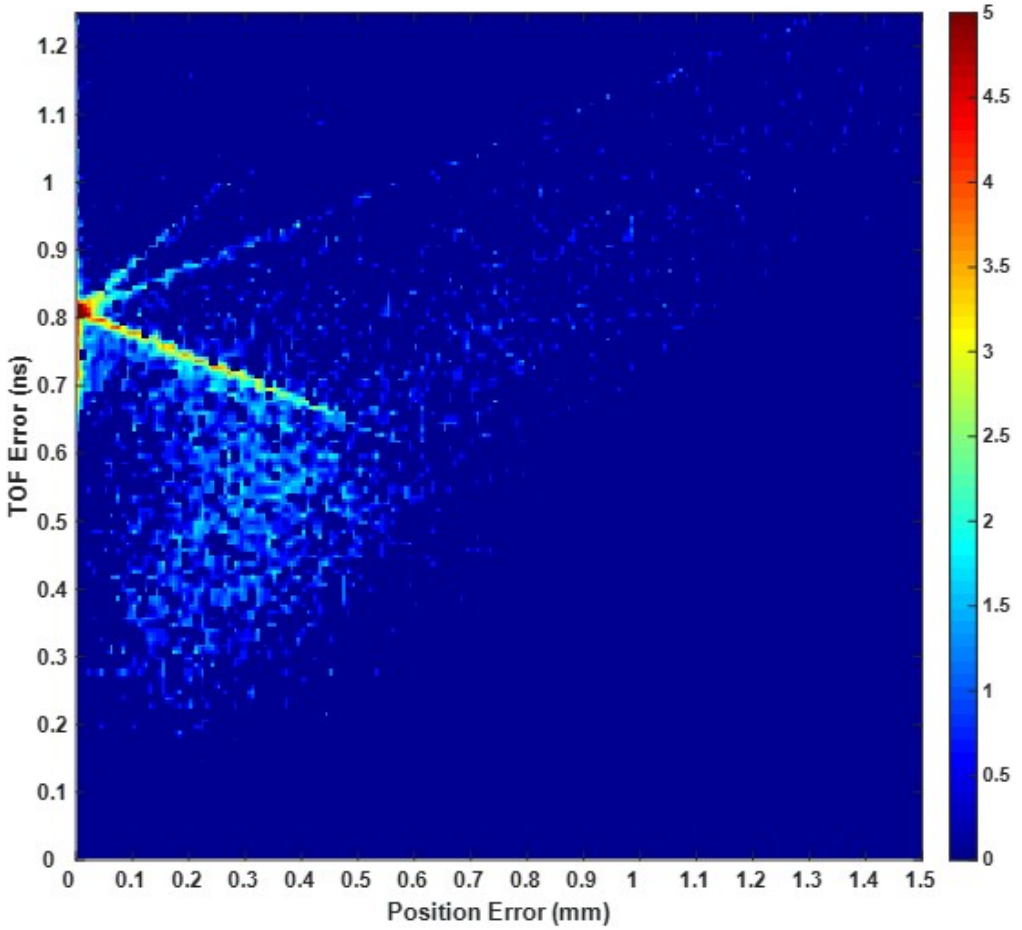

Figure III.8: Time and space errors from the simulated analysis of the B-implanted in Si material model (Table III.4) performed with a CFD system acquiring output signals introduced in Figure III.4.

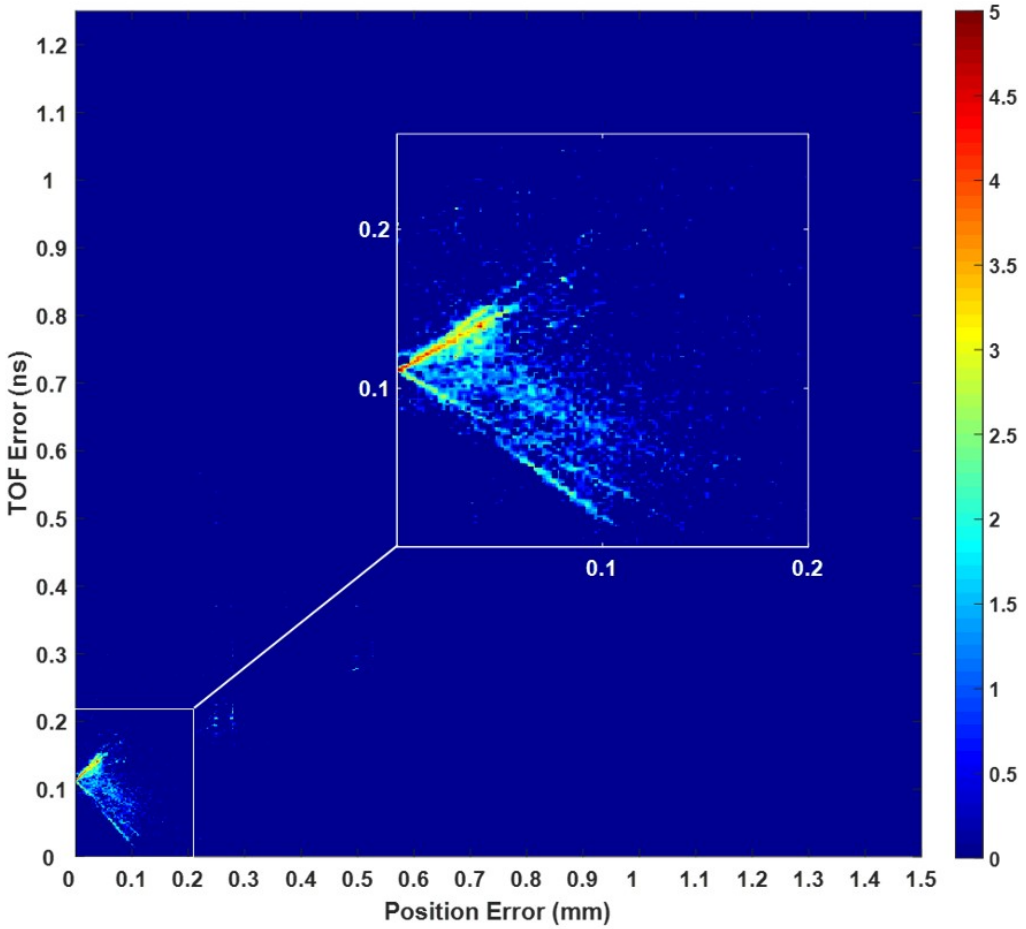

Figure III.9: Time and space errors from the simulated analysis of the B-implanted in Si material model (Table III.4) performed with an aDLD system acquiring output signals introduced in Figure III.4.

III.4 Drawbacks of aDLD systems

Regarding those last results, it can be deduced that the reliability of APT analyses can be improved by replacing CFD systems by aDLD systems. However, according to some studies, the benefits of the aDLD could be questioned. So far, the aDLD system has not been generalized to all APT instruments for two main reasons. Firstly, it has to be known that current aDLD systems embedded to the LaWATAP are subject to a dwell time after each acquisition. When an event is detected (single-hit or multi-hit), output signals are digitized during 3 μs, and are then transferred to memory buffers. Then, the dumping and the reading of data last about 500 μs.

During this dwell time, no other start pulse can be processed. This has the effect of decreasing the detection rate, and thus, increasing the analysis time. The second reason is the lack of reliability of the signal decomposition process. As previously described, reference signals are used to determine the composition of acquired signals. Thus, the accuracy of timing measurements highly depends on the consistency of output signals shape. Unfortunately, it turns out that current instruments using the aDLD system are subject to signal distortions, having the effect of degrading the performances of those instruments.
Regarding those two main limitations, the following studies are aimed at finding appropriate solutions to give more credibility to the democratization of the aDLD system in APT instruments.

III.4.1 aDLD data processing

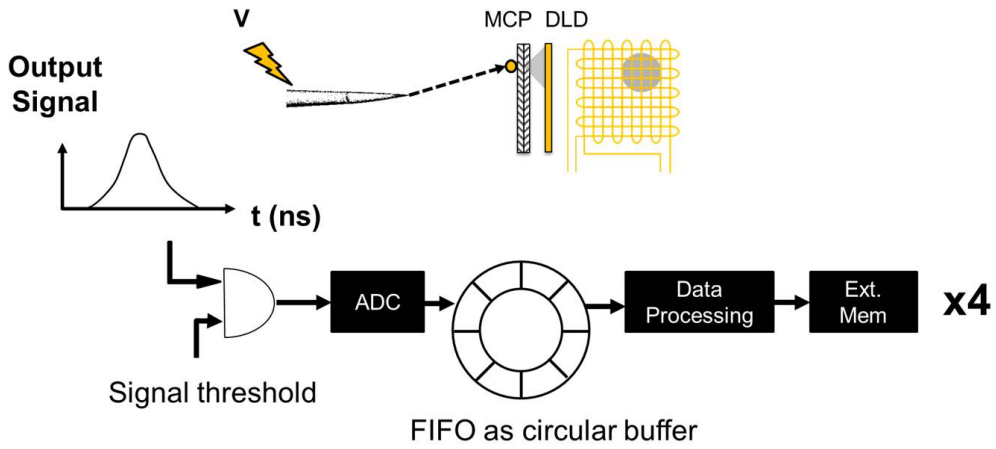

Figure III.10: Schematic of the future aDLD data processing. Instead of acquiring output signals over a whole pulse period, this new configuration allows selecting only usable signals. Moreover, free-running analyses can be possible through the use of circular buffers.

To avoid the limitation caused by the dwell time after each acquisition, a more appropriate processing scheme has to be applied. Figure III.10 illustrates a possible processing scheme that could allow continuous high data rates without dwell time after each acquisition. In this case, only signal amplitudes exceeding specific thresholds will be processed in order to limit the amount of data to only useful signals. This has the effect of reducing the time to dump and read the data to transfer. Moreover, to ensure the

detection of successive ion impacts during the processing time, the idea is to employ the use of several memory buffers which alternate in a circular way between reading and writing processing. As a consequence, conversely to the aDLD implanted in the LaWATAP, this processing scheme has the advantage of performing APT analyses in free-running. This processing scheme is currently under test in the instrumentation team of the GPM lab. To get an idea of the potential enhancement brought by this setup, Figure III.11 introduces a comparison between the two detection systems in term of acquisition speed.

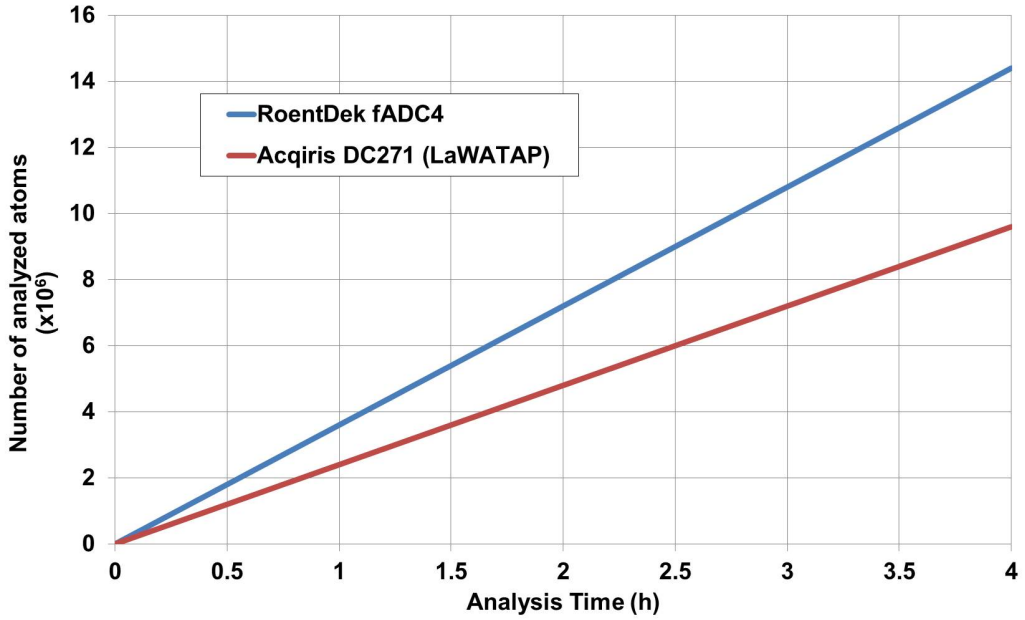

Figure III.11: Theoretical acquisition speed comparison between two aDLD detection systems. Both curves represent the potential acquisition speed of the aDLD under an evaporation rate of 0.01 atoms/pulse and through a pulse frequency of 100 kHz. On one side, the acquisition system of the LaWATAP (Acqiris DC271) introduces a dwell time of 500 μs at each acquisition, whereas on the other side, the new processing scheme, composed of the fADC4 (from RoentDek) can operate in free-running. Those two acquisition systems have respectively an acquisition speed of 3.6 Mat/h for the fADC4, and 2.4 Mat/h for the DC271.

III.4.2 Biases from DLD signal distortions

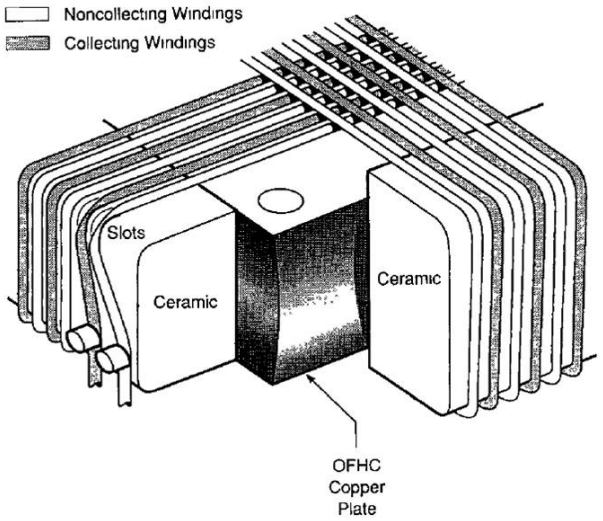

Figure III.12: Representation of the HDL structure [9]. Conductive wires wounded around an insulating frame ensure the collection of electron clouds. Two differential pairs are superimposed and orthogonally oriented on one another, for determining the X and Y coordinates of ion impacts.

Concerning the doubts about the consistency of DLD output signals, it has to be known that most of APT instruments using aDLD systems are equipped with Helical Delay Line (HDL) detectors. HDL detectors are composed of copper-beryllium wires, running in differential pairs and wounded around an insulating frame (Figure III.12). It has been reported that due to the mechanical strength applied on the wounded lines, HDL structures can be highly subject to variations on their electrical properties [6]. Indeed, because the electrical resistance of a conductive wire is proportional to its length and inversely proportional to its cross sectional area, any mechanical stresses applied on the wires may involve local resistance variations and then involve impedance mismatches [10]. However, until now, no concrete results have been reported about signal distortions on HDL detectors. To get to the bottom of this, HDL detectors from LaWATAP instruments have been experimentally studied for determining the potential distortions on output signals. Two parameters have been studied for characterizing the shape of output signals; the rise time and the signal width (FWHM).

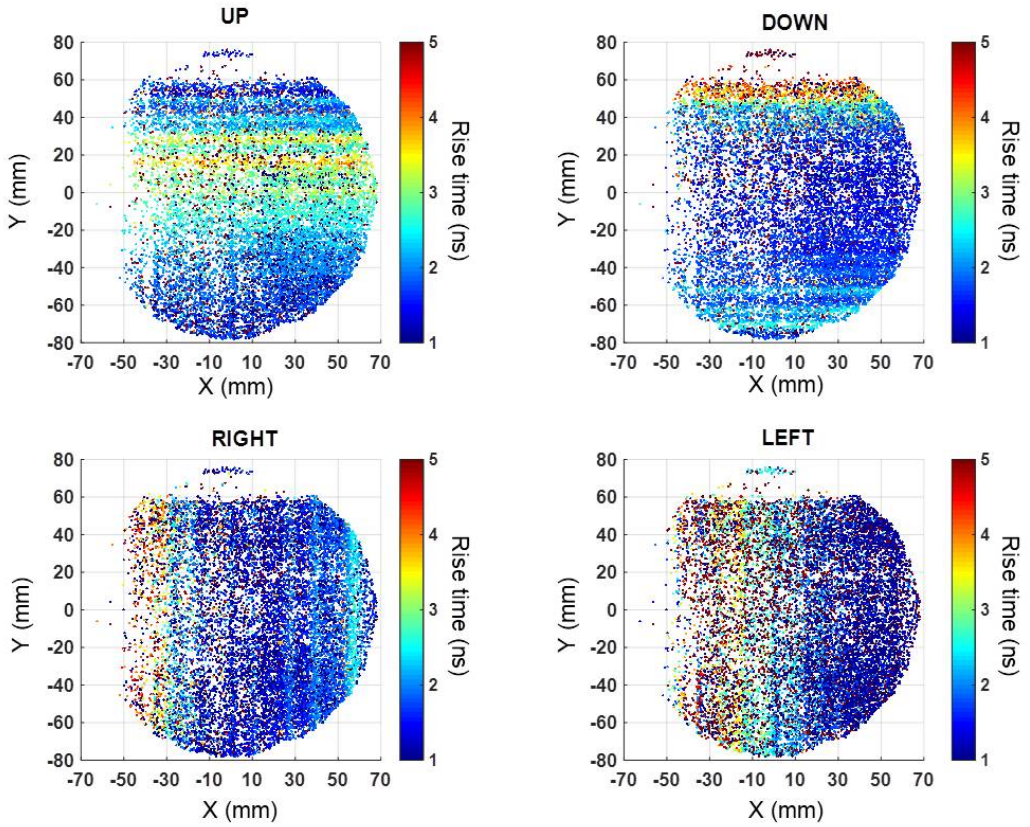

Figure III.13: Spatially resolved rise time distributions from output signals on a HDL detector, from an analysis performed on the LaWATAP.

According to the 2D maps in Figures III.13 and III.14, it can be observed that signal distortions are truly introduced on the whole detection surface. In other words, it sounds like conclusions on the theoretical aDLD timing and spatial precision (Figure III.9) may be put under question due to the mismatch between the acquired signals from the HDL detector, and the reference signals used for the signal shape recognition.

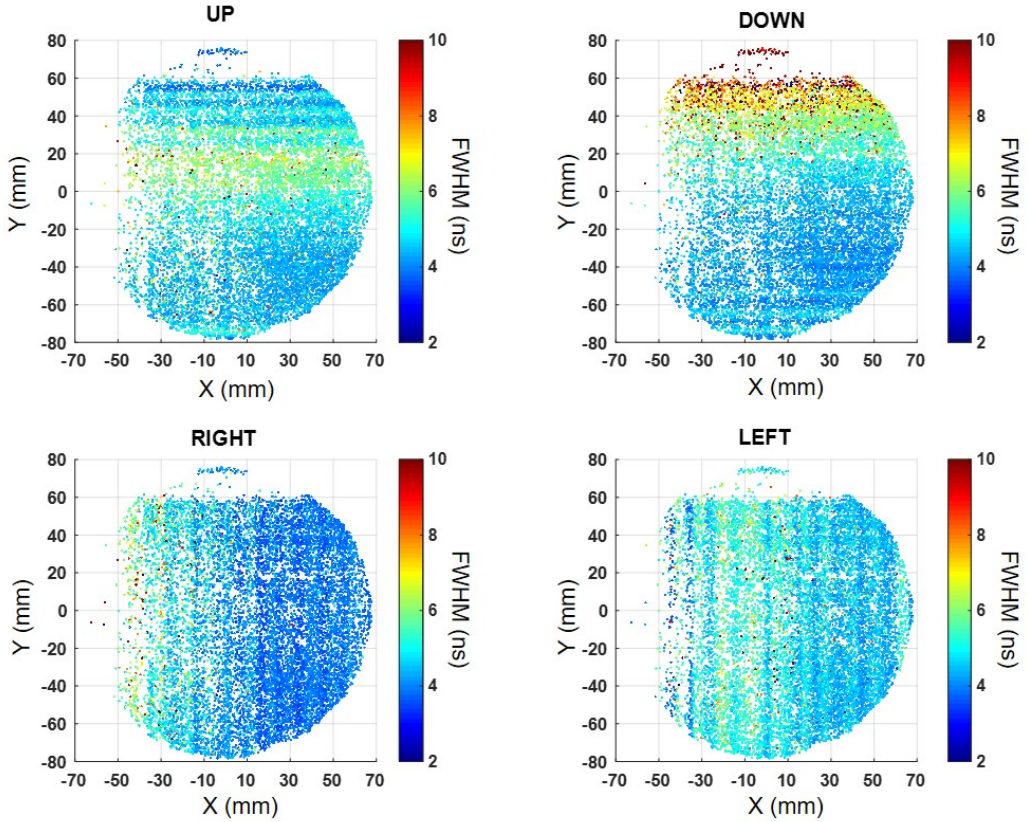

Figure III.14: Spatially resolved signal width (FWHM) distributions from output signals on a HDL detector, from an analysis performed on the LaWATAP.

The impact of those signal distortions can also be emphasized through the monitoring of normally invariant parameters of the detector, such as the total propagation time of electric signals all along the delay lines (see Chapter I). The multimodal distribution of the propagation time in Figure III.15 can be observed on most of HDL detectors. This can affirm that time and space information extracted from aDLD systems may be subject to biases during the detection process.

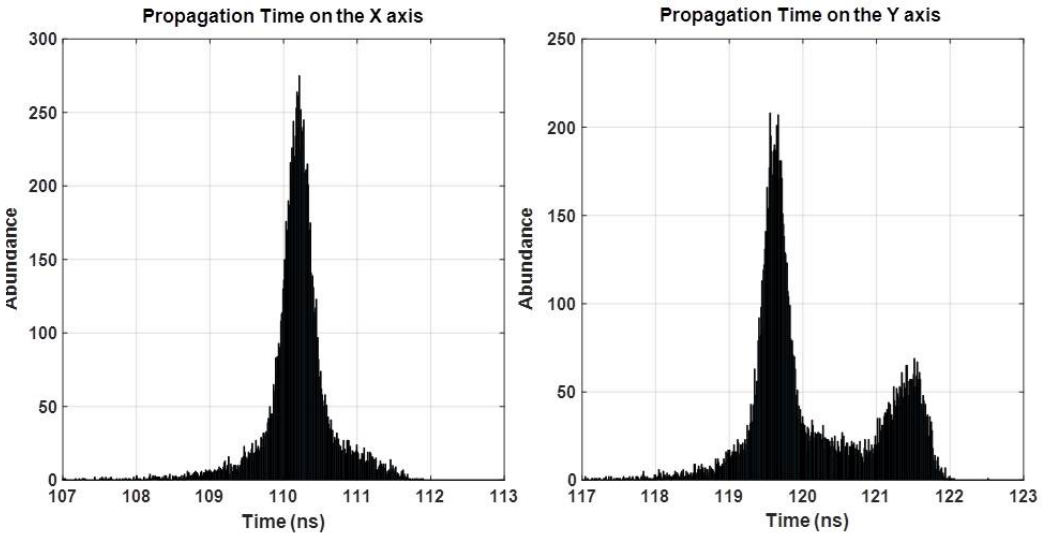

Figure III.15: Signal propagation time distributions on X and Y axes from the HDL detector on a LaWATAP instrument.

III.5 Development of a Serpentine Delay Line Detector

To outperform the limitations caused by HDL detectors, it is necessary to find a design of DLD introducing a rigid structure for controlling the consistency of the resistance all along the delay lines. This specific property may be found in the design of a multi-layer printed-circuit board (PCB) on which delay lines are represented by etched planar transmission lines (Figure III.16). Compared to wounded wires (Figure III.12), planar transmission lines have the benefit of being perfectly controllable in impedance and mechanically robust. This type of DLD was first developed more than 20 years ago [6] and has been called "Serpentine Delay Line" (SDL) detectors. However, since their development, SDL detectors have not been fully studied, specifically in terms of signal distortions on their whole detection surface. Therefore, the following study is aimed at introducing the development of a new design of SDL detector for resolving signal distortions observed on aDLD systems.

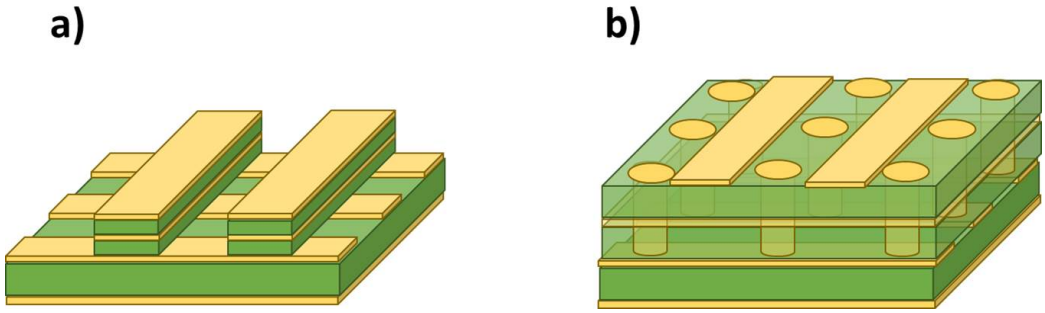

Figure III.16: a) SDL design manufactured by laser ablation machining, b) SDL design manufactured with via connections.

Contrary to the HDL design, letting the electron clouds, coming from the MCP assembly, passing through the two superimposed delay lines, the structure of a PCB design introduces non-conductive substrate layers between each conductive copper layers which can potentially block the access to the lower delay line stage. Therefore, the most difficult in the manufacture of SDL detectors is the stacking of two independent delay lines which both collect enough electrons for generating useable output signals. With the aim of accessing the lower delay line stage, two different manufacturing options have been achieved up until now (Figure III.16); the laser ablation machining [1, 6] (Figure III.16a) and the use of vertical interconnect access, also known as via [8, 13] (Figure III.16b). It appears that the laser ablation machining is both an expensive and complex technique compared to the use of vias, whose the manufacturing process has the benefit of being both very cheap and electrically reliable. That is why, it has been decided to design an SDL detector through the use of vias.
In the framework of this study, three different SDL detectors have been designed. Each of those circuits has successively introduced improvements on the quality of output signals. In the interest of complete confidentiality on the innovative aspect of third and the last development, only the two first SDL designs will be described.

III.5.1 First Prototype of SDL

The first developed SDL prototype has been inspired from existing SDL designs [8, 13]. The requirements for this first development were: 50 Ω impedance-match transmission lines, low cost circuit through the use of a standard etching class, circuit dimensions that must fit on a CF200 flange, and the use of dielectric layers that can be maintained under high vacuum

conditions by respecting the ASTM E595 standard (www.astm.org).

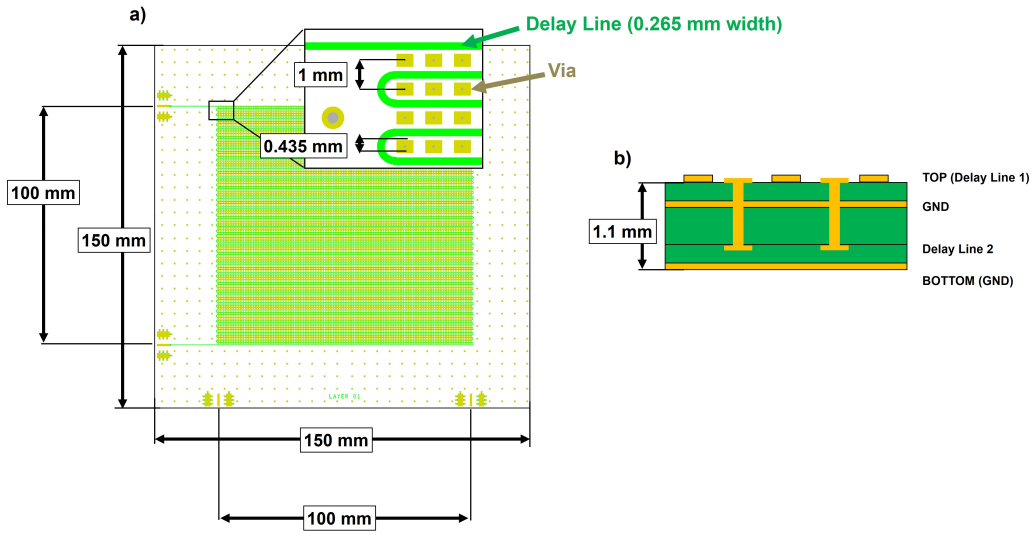

Figure III.17: First SDL prototype developed; (b) The PCB design is based on a 4-stack configuration, with two delay line layers (TOP and 3^{rd} layers), and two ground planes (2^{nd} and BOTTOM layers). (a) Top view layer of the SDL design, introducing a single transmission line with around ∼100 delay line meanders, with a total length of 10.6 m, and covering a transversal length of 10 cm on the X axis. Electron clouds coming from the MCP assembly access to the internal delay line through vias from the TOP layer. The inner layer delay line introduces the same 2D dimensions as the TOP layer delay line.

From those requirements emerged the SDL design illustrated on Figure III.17, which is based on four stacked layers. The delay line meanders on the top layer are surrounded by vias that give an access to an inner layer hosting the second axis delay line. Ground planes have been interleaved after each delay line layer in order to prevent any cross talks between the two delay line layers.
After setting up the SDL detector to a dedicated APT detector workbench, it has been observed that the internal delay line (Delay Line 2 in Figure III.17) was too resistive to correctly acquire output signals. Therefore, only output signals from the top layer have been studied (Delay Line 1 in Figure III.17). Moreover, the analysis of output signals coming from the top layer delay line revealed the presence of high interferences which did not allow any APT analyses (Figure III.18). Figure III.18 shows that the correspondence of some amplitude in the noise level of the two endings reveals the presence

of a common-mode noise coming from an external source. During the analysis of those output signals, it has been assumed that the source of this common-mode noise comes from the MCP output signal, reflecting its image on the delay lines.

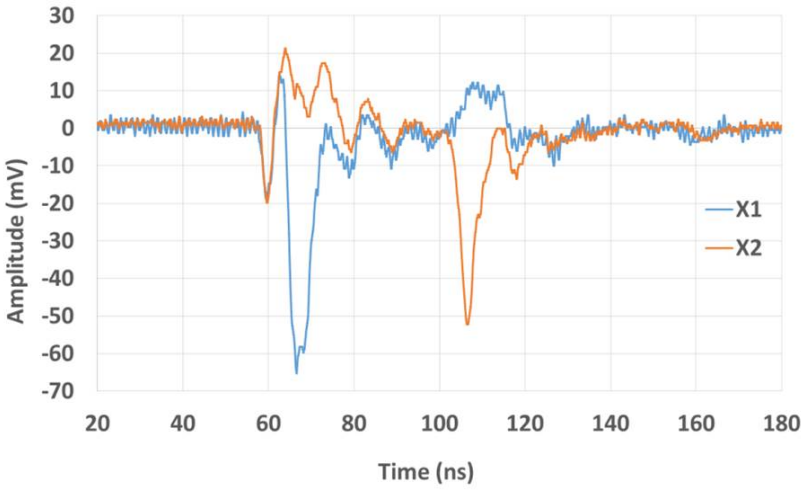

Figure III.18: Output signals from the top layer delay line of the first SDL prototype (Figure III.17).

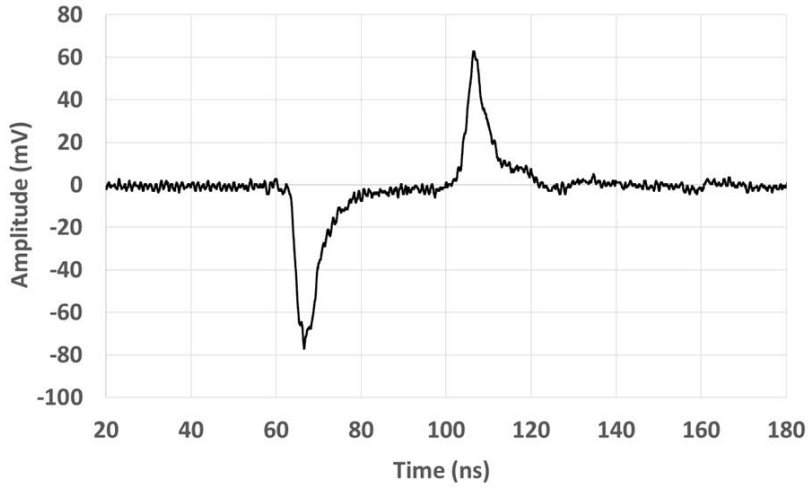

Figure III.19: Subtraction of the two output signals from Figure III.18. The increase of the signal-to-noise ratio related to the two previous signals supports the idea that a common-mode noise from the MCP is intercepted by the delay lines.

This assumption has been supported by the subtraction of the two output signals from Figure III.18, giving a resulting signal composed of two distinct signals introducing a higher signal-to-noise ratio related to the original output signals (Figure III.19).

III.5.2 Second prototype of SDL detector

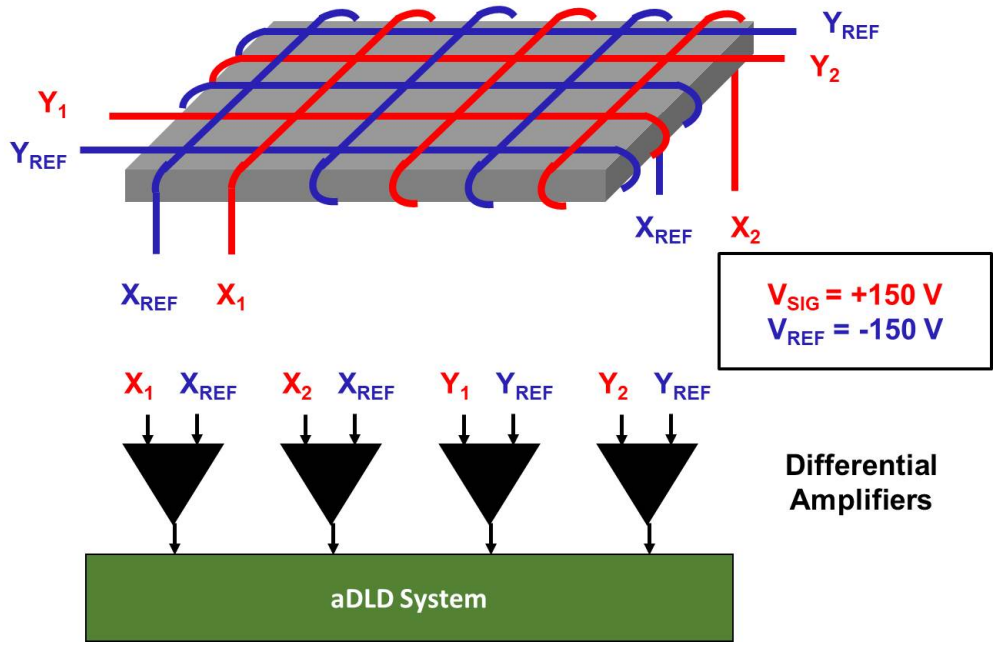

Figure III.20: Schematic of the HDL operating process coupled with the aDLD system in the LaWATAP intrument. Each differential wire pair, from X and Y axes, is formed by a collection wire and a reference wire. A potential difference of 300 V between signal and reference wire ensures that the electron cloud emerging from the MCP output is mainly collected on the signal wires. The following differential amplifiers allow the subtraction of any common-mode noise shared in each differential pair.

Thereafter, it was decided to develop a second SDL design for resolving those two last limitations; the high resistance on the inner layer delay line, and the common-mode noise from the MCP output, that interfere with SDL output signals. By referring to the design of HDL operating process (Figure III.20), it has to be noted that the removal of common-mode noise is ensured by the use of differential pairs coupled with differential amplifiers. For each delay line dimension, a differential wire pair is formed by a collection

wire and a reference wire. A potential difference of 300 V between signal and reference wire (on the LaWATAP) ensures that the electron cloud emerging from the MCP output is mainly collected on the signal wires. The differential signals from the two pairs allow a significant reduction of the common-mode noise from the MCP assembly. Thus, another design of SDL detector with differential pairs has been developed for avoiding biases from the first design and keeping the advantage from the HDL design (Figure III.21). At the same time, it has been decided to increase the cross section area of the delay lines tracks to reduce their electric resistance, while keeping a control of an impedance matching of 50 Ω.

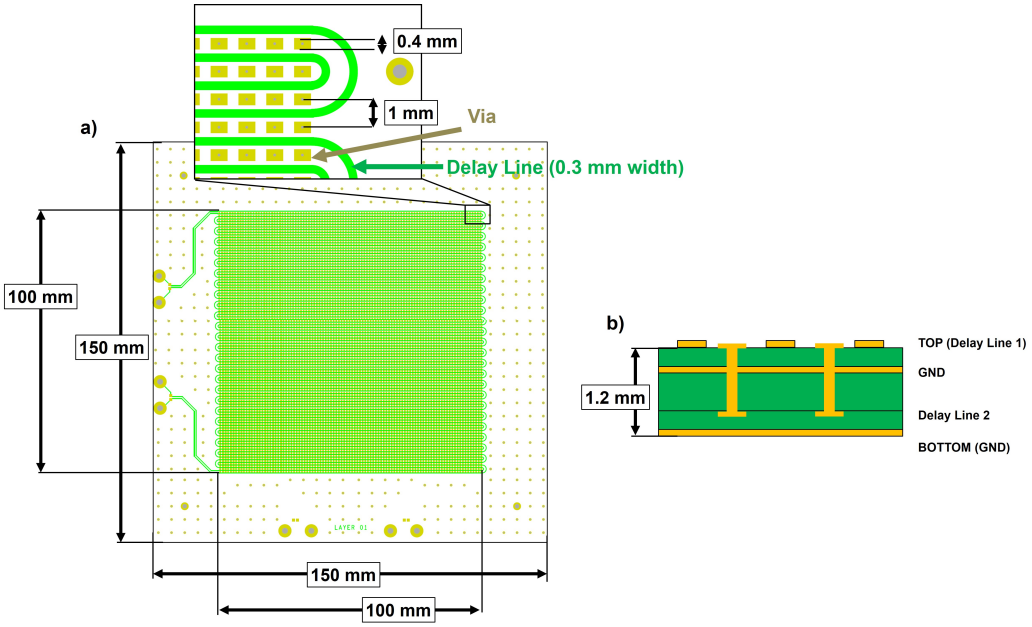

Figure III.21: Second SDL prototype developed; (b) The PCB design is based on a 4-stack configuration, with two delay line layers (TOP and 3^{rd} layers), and two ground planes (2^{nd} and BOTTOM layers). (a) Top view layer of the SDL design, introducing a differential pair transmission line with around ∼50 delay line meanders, with a total length of 5.2 m, and covering a transversal length of 10 cm on the X axis. Electron clouds coming from the MCP assembly access to the internal delay line through vias from the TOP layer. The inner layer delay line introduces the same 2D dimensions as the TOP layer delay line.

III.5.3 Performances of the SDL design

As made for the previous HDL detector from the LaWATAP, the consistency of the shape of output signals has to be analyzed for evaluating the compatibility of the SDL detector with the aDLD system. With the aim of getting a visual comparison between SDL and HDL detectors, color bars in Figures III.22 and III.23 have been set to the same scale as in Figures III.13 and III.14. Those last results clearly show that output signals, originating from the second developed SDL detector, introduce far less distortions compared to the HDL design (Figures III.13 to III.15). It can be affirmed that the use of delay lines on a rigid structure can reduce distortions on DLD output signals.

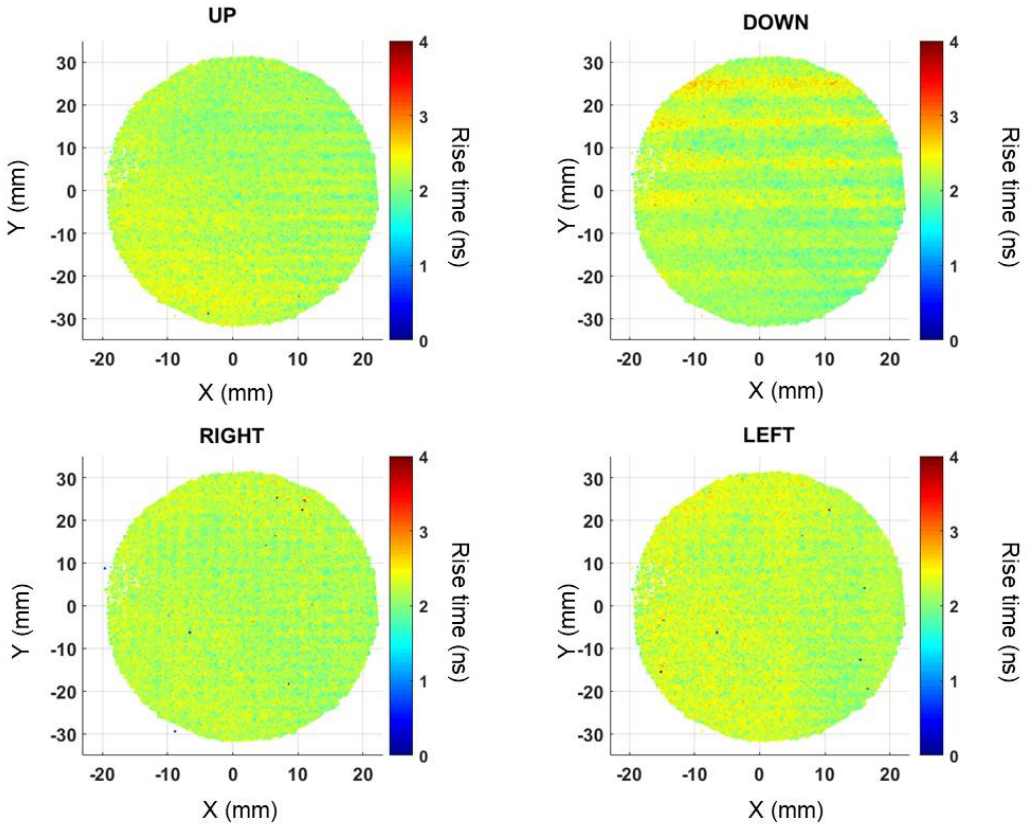

Figure III.22: Spatially resolved rise time distributions from output signals extracted from the second SDL prototype (Figure III.17).

Similarly to the study of the HDL detector, the impact of output signals from the SDL detector can also be emphasized through the monitoring of normally invariant parameters of the detector, such as the total propagation

time of electric signals all along the delay lines (Figure III.15). This time, the absence of multimodal distribution on propagation time distributions (Figure III.24) also confirms that time and space information extracted from aDLD systems can be exempted from biases caused by any signal distortion.

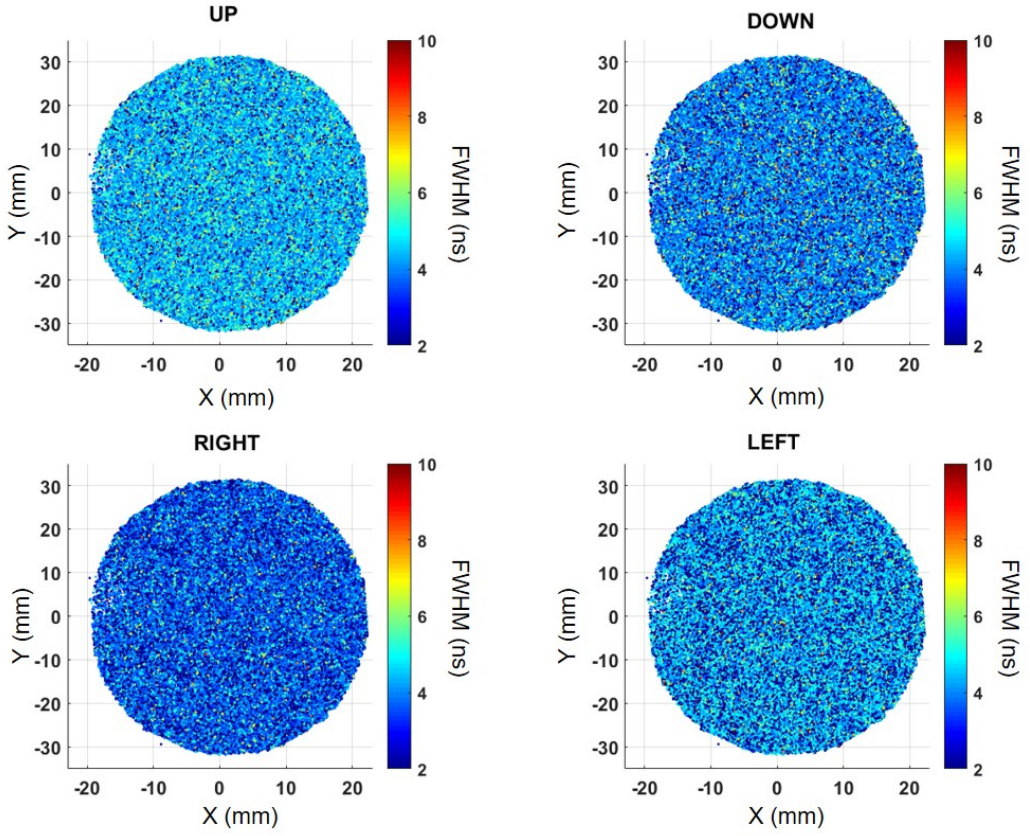

Figure III.23: Spatially resolved signal width (FWHM) distributions from output signals extracted from the second SDL prototype (Figure III.17).

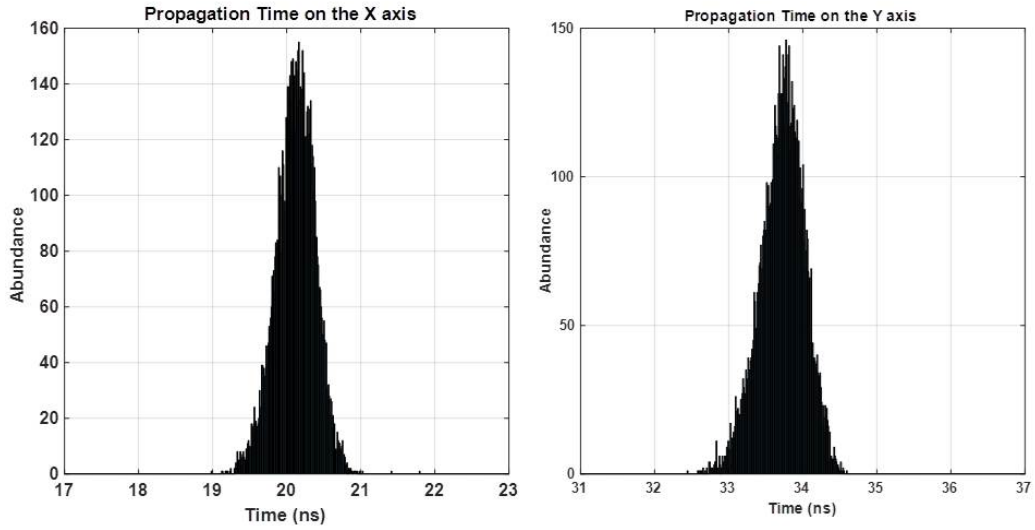

Figure III.24: Signal propagation time distributions on X and Y axes from the second SDL prototype (Figure III.17).

In order to get a complete comparison of the SDL design related to the HDL design, one might be interested in comparing their respective spatial precision, to finally get an estimation of their spatial resolution (see Section I.2.1). In Chapter I, it has been demonstrated that, due time-to-position conversion performed by DLD detectors, the width at half maximum of timing distribution resulting from the calculation of the signal propagation times TPX and TPY, represents the image of the DLD spatial resolution (Equations (III.1) and (III.2) and fig. III.25).

$$\Delta X = \frac{\Delta TPX}{2.TPX} l_X \tag{III.1}$$

$$\Delta Y = \frac{\Delta TPY}{2.TPY} l_Y \tag{III.2}$$

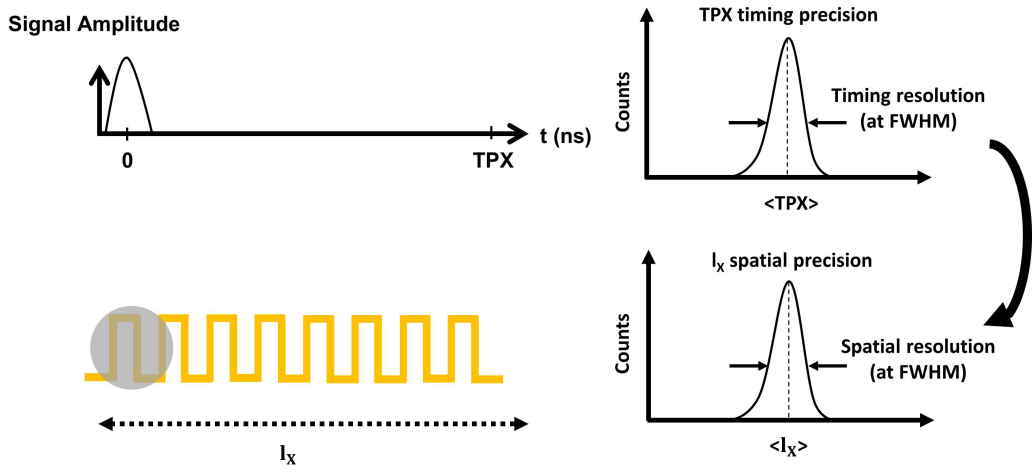

Figure III.25: Representation of the direct relation between the timing precision and the spatial precision on the X-axis delay line. The spatial resolution of the DLD can be determined by considering the width at half maximum of the statistical position spread.

From Table III.5, it can be observed that, despite the lower values of calculated timing resolution from the SDL design, the calculated spatial resolutions from the SDL are around 4 times higher than those from the HDL design. This can be simply explained through Equations (III.1) and (III.2), describing the statistical position spread of ion impact, where it can be observed that two DLDs having the same dimensions can have different spatial resolutions if their signal propagation times are different. This is case for the two DLDs compared in Table III.5; despite the poorer timing resolution of the HDL design, its longer signal propagation times allow to take an advantage on the SDL design in terms of spatial resolution.
In addition to this last drawback, it has also been observed that hit maps from the second SDL design introduce heterogeneous and periodic patterns in both X and Y axes (Figure III.26). Regarding the meander structure of the differential pairs on the SDL design, one can realize that the electron clouds, coming from the MCP output, cannot be spread equally across the entire detection surface (Figure III.27). Indeed, through the Figure III.27, it can be deduced that the direction of the electric field lines, directing the electrons originating from the MCP output, appears reversed at each successive branch of the delay lines. This has the effect of creating heterogeneous collection zones across the entire detection surface (Figure III.26b and Figure III.26c). As a consequence, further investigations have to be conducted for achieving SDL designs with better spatial resolution and without hit map distortions

caused by the structure of the delay lines. Studies on a third SDL design has been recently initiated to outperform those limitations, but will not be introduced in this manuscript (patent pending).

	HDL	SDL
<TPX> (ns)	110.21	20.09
<TPY> (ns)	119.65	33.77
Timing resolution on the X axis (ps)	835.5	557.74
Timing resolution on the Y axis (ps)	837.5	648.5
Spatial resolution on the X axis (µm)	303.24	1388.10
Spatial resolution on the Y axis (µm)	279.98	960.17

Table III.5: Comparison of the spatial resolutions between HDL (from the LaWATAP) and SDL (second prototype). Time and space information allowing the calculation of the spatial resolution are detailed.

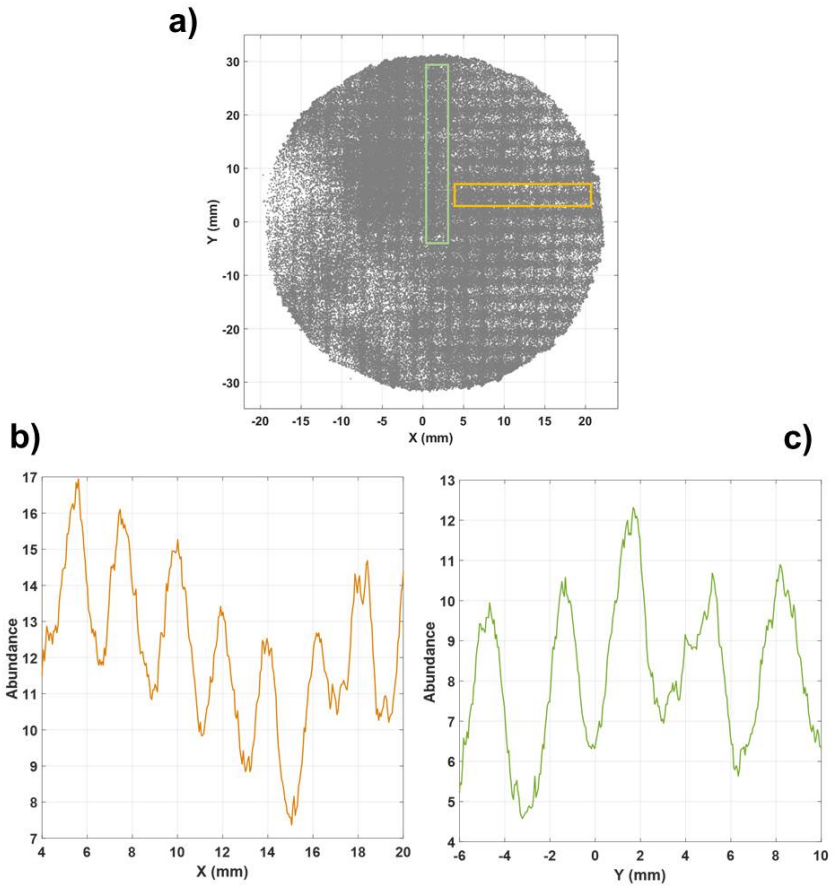

Figure III.26: a) Hit map from an analysis performed with the second SDL prototype; b) Density profile from impacts detected inside the orange zone on the hit map (representative to the density profile along the X axis); b) Density profile from impacts detected inside the green zone on the hit map (representative to the density profile along the Y axis).

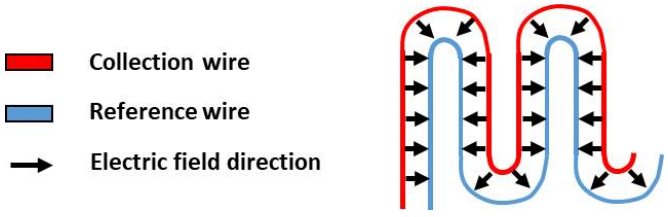

Figure III.27: Representation of the electric field distribution around a delay line differential pair. Heterogeneous collection zones might appear due to the meander structure of the differential pair.

III.6 Conclusion

It must be recalled that the first issue of this chapter relates to finding a mean to both reduce the instrument DT and reduce the width of output signals, with the aim of reducing the impact of the APT detection system on spatial and compositional biases. However, it has been demonstrated that technologies used in common APT instruments have reached their limits and cannot ensure those improvements.
In 2005, Da Costa et al. [4] proposed a digital processing detection system, called the aDLD, to drastically reduce the instrument DT. Consequently, by reducing the instrument DT, aDLD systems allow the reduction of selective losses caused by the variability of the evaporation mechanism during APT experiments. Despite the fact that the aDLD can significantly reduce losses in APT experiments, no studies have been conducted to get a concrete comparison between aDLD and conventional detection systems. Therefore, this chapter has first introduced simulations for qualifying and quantifying the contribution of aDLD systems on APT analyses related to conventional APT detection systems.
It has to be known that, up until now, one of the reasons why aDLD systems have not been generalized to all APT instruments, is the fact that doubts remain about the probable spatial and compositional biases induced by the physical properties of the DLD. Therefore, this chapter has also highlighted the development of a new design of DLD to provide the required elements necessary to democratize the aDLD detection system in APT instruments.

Bibliography

[1] Aos Alwaidh, Martin Sharp, and Paul French. Laser processing of rigid and flexible pcbs. *Optics and Lasers in Engineering*, 58:109–113, 7 2014.

[2] Mohamed Serraj Andaloussi, Mounir Boukadoum, and El-Mostapha Aboulhamid. A novel time-to-digital converter with 150 ps time resolution and 2.5 ns pulse-pair resolution. In *The 14th International Conference on Microelectronics,*, pages 123–126. IEEE, 2002.

[3] Didier Blavette, Talaat Al Kassab, Emanuel Cadel, Alexander Mackel, François Vurpillot, Mathieu Gilbert, Oana Cojocaru, and Bernard Deconihout. Laser-assisted atom probe tomography and nanosciences. *International journal of materials research*, 99(5):454–460, 2008.

[4] G. Da Costa, F. Vurpillot, A. Bostel, M. Bouet, and B. Deconihout. Design of a delay-line position-sensitive detector with improved performance. *Review of Scientific Instruments*, 76(1):013304, 1 2005.

[5] G. Da Costa, H. Wang, S. Duguay, A. Bostel, D. Blavette, and B. Deconihout. Advance in multi-hit detection and quantization in atom probe tomography. *Review of Scientific Instruments*, 83(12):123709, 12 2012.

[6] Peter G. Friedman, Raúl A. Cuza, Judith R. Fleischman, Christopher Martin, David Schiminovich, and Dale J. Doyle. Multilayer anode with crossed serpentine delay lines for high spatial resolution readout of microchannel plate detectors. *Review of Scientific Instruments*, 67(2):596–608, 2 1996.

[7] Thomas F Kelly and David J Larson. Local electrode atom probes. *Materials Characterization*, 44(1-2):59–85, 1 2000.

[8] M. Lampton and M. Marckwordt. Stacked orthogonal serpentine delay lines with vias for two-dimensional microchannel plate readout. *Review of Scientific Instruments*, 71(12):4611, 2000.

[9] M.K. Miller and M.G. Hetherington. Local magnification effects in the atom probe. *Surface Science*, 246(1-3):442–449, 4 1991.

[10] George S. Pine. Change of electrical resistance in wires by stretching. *Proceedings of the American Academy of Arts and Sciences*, 11:303, 1875.

[11] Andreas Riedo, Marek Tulej, Urs Rohner, and Peter Wurz. High-speed microstrip multi-anode multichannel plate detector system. *Review of Scientific Instruments*, 88(4):045114, 4 2017.

[12] Peter Wurz and Lukas Gubler. Fast microchannel plate detector for particles. *Review of Scientific Instruments*, 67(5):1790–1793, 5 1996.

[13] Bingli Zhu, Yonglin Bai, Fanpu Lei, Xiaohong Bai, Bo Wang, Junjun Qin, Weiwei Cao, and Yongsheng Gou. Two-dimensional photon counting imaging detector based on pcb delay line anode. In *Selected Papers of the Chinese Society for Optical Engineering Conferences held July 2016*, volume 10141, page 101411A. International Society for Optics and Photonics, 2016.

Chapter IV

Development of a mass and energy-sensitive detector for the Atom Probe Tomography

Considering the potential improvements on the APT detection system, previously described (see Chapter III), one can note that, even by pushing the performances of MCP-DLD systems to their utmost limits, another important issue still remains; the overlapping of mass peaks originating from different elements (Figure IV.1).

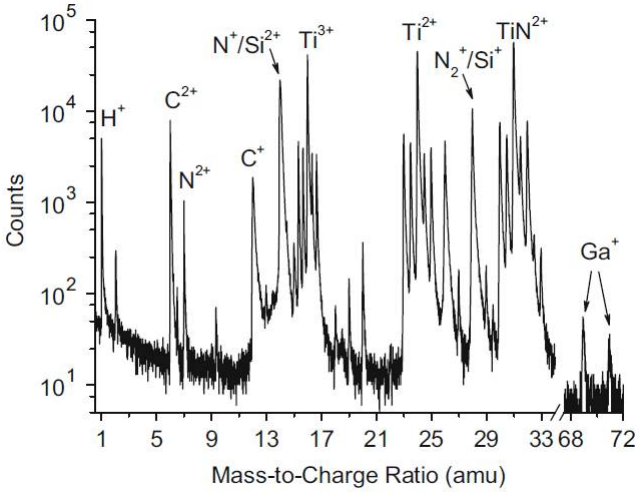

Figure IV.1: Mass spectrum from an analysis of a nanocomposite Ti–Si–N film [57]. Peaks at 14 and 28 Da both result from the combination of silicon and nitrogen isotopes.

Indeed, it can be noticed that the composition of some analyzed materials may involve the evaporation of elements having almost equal mass-to-charge ratios. That is the case, for instance for nitrogen and silicon in TiSiN systems [13, 65] and in fin field-effect transistors [38], or titanium and carbon in cemented carbide materials [60]. The clear identification of each ion, from materials analyzed by APT, reveals all its importance when one has to cope with complex 3D nano-structures containing solutes at very low concentration levels. Figure IV.2 clearly illustrates this issue though images revealing that the presence of mass peak overlaps between silicon and nitrogen prevent the characterization of Si dopants in semiconducting nitride materials, thus leading to a misinterpretation of solutes distribution in analyzed materials.

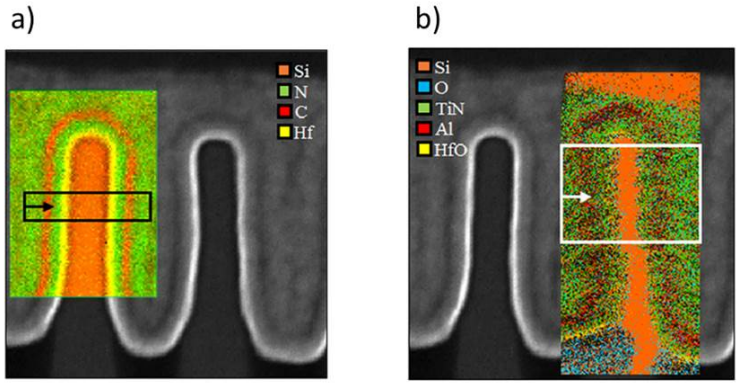

Figure IV.2: (a) Complimentary HAADF STEM and EELS mapping performed across a finFET channel, normal to the plane of the fin [38]; (b) Complimentary APT analysis performed on a nearby device (a few microns away), overlaid on the same HAADF STEM image from (a).

Given that the elemental nature of each ion is determined by a Time-of-Flight Mass Spectrometry technique (see Chapter I), it is likely that different elements from a same material may be mixed up with each other because of the closeness between their respective mass-to-charge ratios. Thus, materials made of different elements having near or equal mass-to-charge ratios may be subject to uncertainties on the estimation of their fraction. Some elements such as nitrogen and iron in nitride steels, or nitrogen and silicon in semiconductor materials, are respectively detected under the same mass peak and cannot be distinguished since their mass-to-charge ratios are very close each other ($^{56}Fe^{2+}$ and $^{28}N_2^+$ at 28 Da and $^{28}Si^{2+}$ and $^{14}N^+$ at 14 Da). To overcome this limitation, it is necessary to couple the TOFMS technique with a new spectroscopy technique that would be able to resolve

mass peak overlaps.

IV.1 Resolving mass peak overlaps through kinetic energy discrimination

It can be noticed that a significant part of mass peak overlaps concerns elements having different charge states [13, 28, 32, 60]. Therefore, it has to be recalled that, during the field evaporation process, projected ions, with a mass m and a velocity v, reach a kinetic energy E_K that tends towards the value of the potential energy E_P generated on the analyzed tip apex, through an equivalent electric potential V;

$$E_K = \frac{mv^2}{2} \tag{IV.1}$$

$$E_P = neV \tag{IV.2}$$

With n the charge state of ion projectiles and e the elementary charge of the electron. As a consequence, it can be deduced that a significant part of ions involved in mass peak overlaps could be resolved through their kinetic energy (Equations (IV.1) and (IV.2)). In the same way as the Mass Resolving Power (MRP) estimates the ability of APT instruments to resolve mass peaks (see Chapter I), the Energy Resolving Power (ERP) would be then the additional indicator for estimating the ability of APT instruments to resolve energy peaks. Similarly, the narrower will be the energy peaks, the better will be the ability to distinguish successive ion charge states.

$$ERP = \frac{E_K}{\Delta E_K} = \frac{1}{\sqrt{(\frac{\Delta V}{V})^2 + (\frac{\Delta n}{n})^2}} \tag{IV.3}$$

Through the propagation of uncertainties on the determination of ions kinetic energy (Equation (IV.3)), it can be seen that the ERP depends on the uncertainties from the electric potential V applied on the tip, and the uncertainties from the estimation of the charge states. However, considering that the set value of V is subjected to very small variations ($\Delta V < 2$ V) related to the high voltage applied on samples [47, 53], it can assumed that the ERP mainly depends on the estimation of the charge states. Generally, the working process of energy-sensitive detectors rely on the conversion of single particle impacts into electric current increasing as a function of the particle kinetic energy. Therefore, when talking about "the estimation of the charge states", it must be understood "the measurement of signal amplitudes

representing the charge states". As a consequence, the ERP can be reduced to the following expression;

$$ERP \approx \frac{A}{\Delta A} \tag{IV.4}$$

With A an amplitude level reached by output signals coming from an energy-sensitive detector, and ΔA the resulting amplitude spread (FWHM) coming from the measurement of A. Noting that, for the calculation of the ERP between two amplitude distributions, the amplitude level A in Equation (IV.4) must be taken at the higher amplitude level.
With the aim of determining the minimum ERP required for discriminating separate ion charge states, it is necessary to know how evolve the measured amplitudes as a function of ions kinetic energy. Indeed, one can note that despite the theoretical proportionality between ions kinetic energy and ions charge state (Equations (IV.1) and (IV.2)), it is possible that the amplitudes measured from an energy-sensitive detector could introduce a non-linear behavior as a function of ions kinetic energy. In other words, successive charge states (n = 1, 2, 3...) would not be necessarily identified through amplitude levels equally separated from each other. To illustrate this point, Figure IV.3 clearly shows that the minimum ERP required cannot be easily determined, since the distances between amplitude levels, reflecting the different charge states, may differ according to the transfer function of the energy-sensitive detector used.

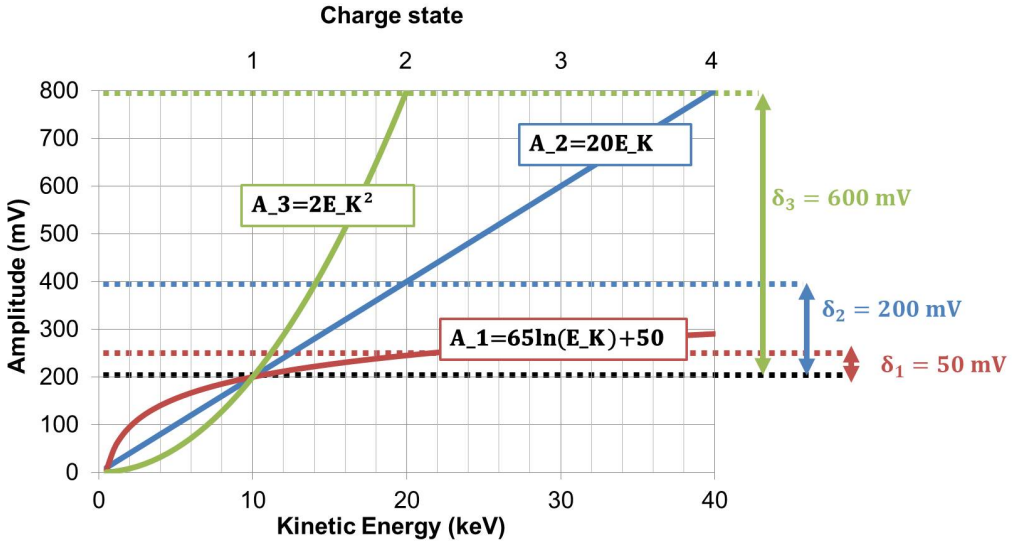

Figure IV.3: Characteristic curve models representing three different transfer functions from three hypothetical energy-sensitive detectors. On those models, it is considered an evaporation potential $V = 10$ kV. As a consequence, δ_1, δ_2 and δ_3 represent the distances between amplitude levels, reflecting the charge states of single and double charged ions, respectively from the three different models.

Assuming that each amplitude level, measured from an energy-sensitive detector, introduces an amplitude spread matching with a normal distribution (Figure IV.4a); it can be assumed that the minimum ERP required for discriminating separated ion charge states will depend on the standard deviation σ of those distributions. In an arbitrary manner, it can be considered that two amplitude distributions can be resolved if their mean values are at least separated by 6σ[1]. Knowing that the full-width at half maximum of a normal distribution is nearly equal to 2.35σ (corresponding to ΔA), it can be deduced that the minimum ERP required for discriminating separated ion charge states could be expressed by only considering the distance δ between two amplitude levels.

$$\delta = 6\sigma \tag{IV.5}$$

[1]For a normal distribution it is known that 99.7% of its data set is covered within the interval $[\mu\text{-}3\sigma\ ;\mu+3\sigma]$; with μ representing the mean value of the normal distribution. That means that two normal distributions with a same standard deviation, separated by 6σ, can be resolved with a confidence level of ~99.7%.

$$ERP_{MIN} = \frac{A}{0.39\delta} \tag{IV.6}$$

δ (mV)	ERP_{MIN}
50	12.82
200	5.13
600	3.42

Table IV.1: Minimum ERP required for discriminating single and double ion charge states as a function of the distance between their reflected amplitude levels extracted from energy-sensitive detectors (Figure IV.3).

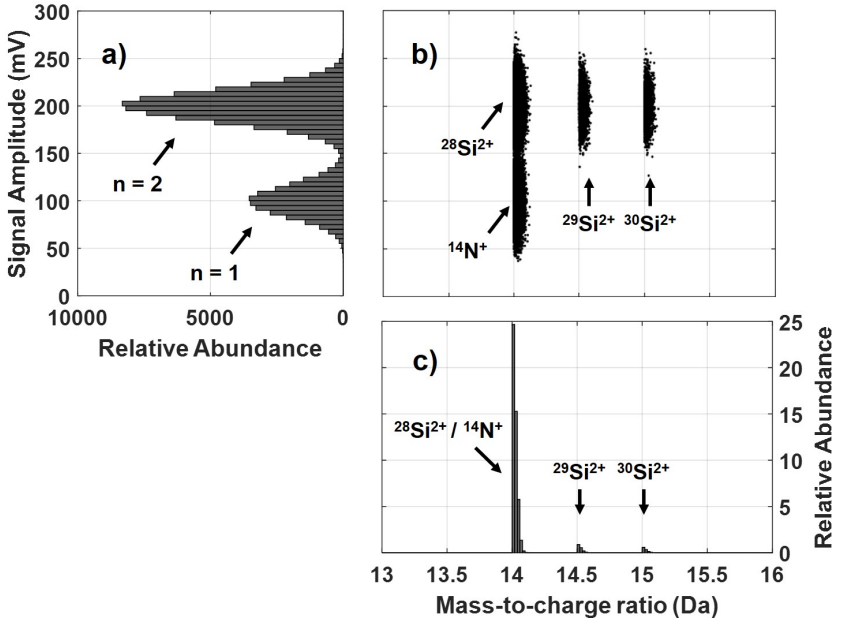

Figure IV.4: Simulated analysis of a material composed of 70% of Si^{2+} (64.55% of $^{28}Si^{2+}$, 3.28% of $^{29}Si^{2+}$, 2.16% of $^{30}Si^{2+}$) and 30% of $^{14}N^{+}$. Considering an APT instrument with an energy-sensitivity, the scatter plot (b) shows how the additional energy dimension allows the resolving of the mass peak overlap between $^{28}Si^{2+}$ and $^{14}N^{+}$ peaks (c). Conditions from Equations (IV.5) and (IV.6) show that an ERP of 5 (at 200 mV) is sufficient for resolving the amplitude distributions in (a).

In accordance with the assumptions illustrated in Figure IV.3, values from Table IV.1 provide a first quantitative insight of the minimum ERP required

for APT experiments, and at the same time, complete the study conducted by T. F. Kelly [26], where only energy-sensitive detectors with linear transfer functions were considered.

IV.2 State-of-the-art on Position-Energy-Sensitive Detectors

The assumption of using kinetic energy discriminations in APT has already been stated few years ago [7, 26], but has never been practically realized. Therefore, it necessary to know if there are some existing energy-sensitive detectors that could be able to maintain the high spatial and compositional performances of current APT instruments, and at the same time, introduce a sufficient ERP for resolving mass peak overlaps. Thus, it is necessary to first focus especially on existing position-energy-sensitive detectors (PESD).

IV.2.1 Solid-State Detectors

The first existing type of PESD is the Solid-State detector (SSD). A SSD, also called semi-conductor radiation detector [35], is a diode-based detector, where ionizing particles produce free charge carriers inside a p-n junction (Figure IV.5), generally based on silicon materials. During the detection of ionizing particles, the electric field applied between the metal electrodes of a diode, turns out to be briefly lowered by the release of free charge carriers in the p-n depleted region. This drift of the electric field allows inducing an electric signal on the metal electrodes that should be proportional to the amount of electron-hole pairs generated during the particle detection. Most of studies on SSDs state that the magnitude of SSD output pulses is a measure of incident particles energy. However, among those studies, it has been observed that the electrical response of SSDs may differ as a function their material composition [44], and also as a function of the energy range and the atomic number of incident particles [19, 20, 33].

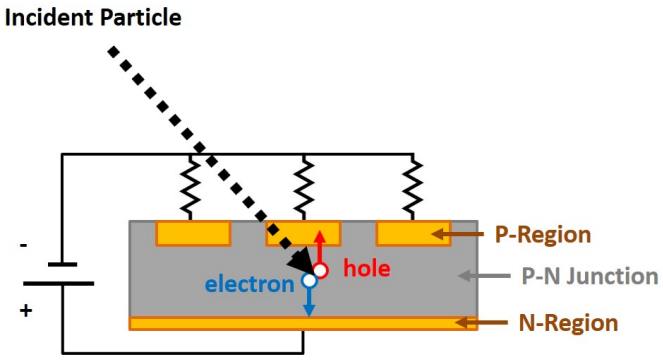

Figure IV.5: Schematic representation of a SSD detector. Through the p-n junction structure of the detector, an energetic incident particle can be detected through a drift of the electric field between the metal electrodes, externally connected to the P and N regions, caused by the generation of electron-hole pairs.

The latest SSD technology providing both the best spatial resolution and the most of results in terms of energy measurement is the Medipix technology [4]. This technology, currently provide a particle tracking pixel detector, called TimePix, introducing a pixel array of 256x256 cells, each measuring 55 μm^2, forming a total detection surface of 14.08 mm x 14.08 mm. It has been reported that the last version of the TimePix is able to simultaneously provide time-of-flight (TOF) and energy measurements on each independent sensitive cell through a continuous stream of data [27], contrary to CCD cameras used in the OAP, OPoSAP and OTAP instruments (see Chapter I). Moreover, experiments on this device have shown that the energy vs. pulse amplitude transfer function appears linear, with an ERP that can exceed a value of 4 (Figure IV.6).

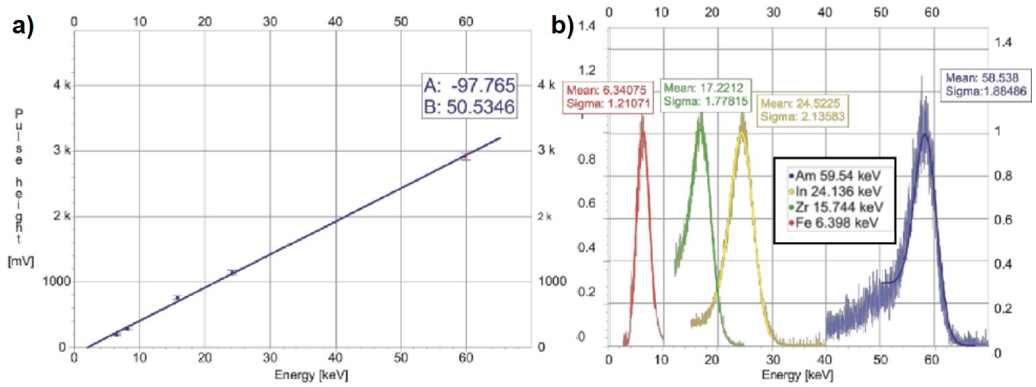

Figure IV.6: Response in energy of the Timepix detector (from [27]). (a) Energy vs. pulse amplitude transfer function of the TimePix detector for low ion kinetic energies. The solid line represents the linear trend of the transfer function ($PH = B.E_K + A$, with PH the output pulse height); (b) Kinetic energy distributions of different ion projectiles at different kinetic energies.

Despite those performances, some drawbacks might prevent the use of this detector in APT instruments. Some studies have shown that the energy measurement of low energy ions (tens to hundreds of keV) in SSDs, might be limited by the small magnitude of generated output pulses, which can approach the intrinsic noise level of SSD cells and their electronics [19]. Therefore, this limitation may have the effect of inducing selective losses in case of APT experiments. An example of this effect is illustrated in Figure IV.7, where it can be observed that the detection of heavy ions may be underestimated related to lighter ions, even for ions with very close mass-to-charge ratios and with different charge states. Furthermore, it has been stated that the typical response time of SSD outputs ranges from tens to hundreds of nanoseconds [34, 44], which cannot ensure the typical APT acquisition rates, introducing only few nanoseconds of output response time (see Chapter I).

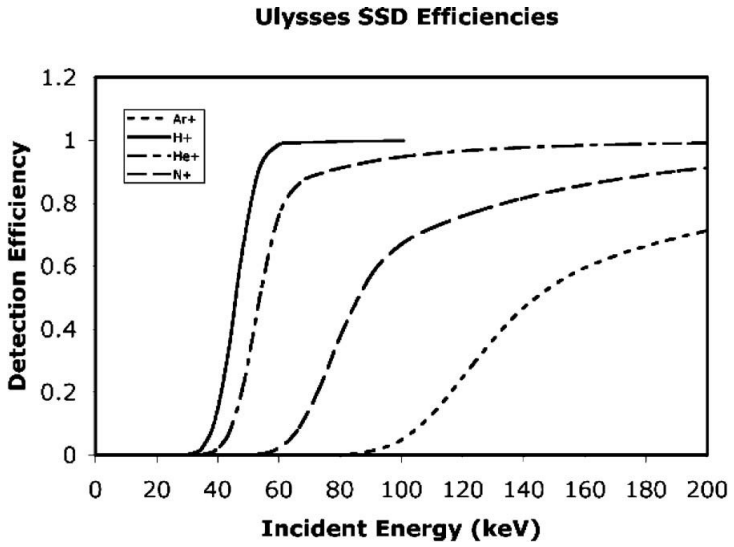

Figure IV.7: Solid-state detector efficiency curves of the Solar Wind Ion Composition Spectrometer on the Ulysses spacecraft. The curves were fitted to laboratory calibration data [33].

IV.2.2 Superconducting Tunnel Junction detectors

Another mean for measuring ions kinetic energy concerns the use of Superconducting Tunnel Junction (STJ) detectors. An STJ cell consists of two superconducting electrodes separated by a thin insulator, and cooled at a cryogenic temperature, typically $\sim$1 K or less [17,22,29] (Figure IV.8). The use of cryogenic temperatures allows the formation of electron pairs, inside the superconducting electrodes, known as Cooper pairs. When a high-energy ion impinges on one of the superconducting layers, millions of Cooper pairs are broken, and a bias voltage between the two superconducting electrodes allows the flow of the liberated electrons, from one electrode to the other, by a tunnelling current through the thin insulating layer. This physical phenomenon is called the Josephson effect [25]. Considering that the amount of energy required to break a Cooper pair is around few meV [29, 68], it can be deduced that STJ cells are sufficiently sensitive to single ion impact event, and can provide sufficient output pulse heights reflecting ions kinetic energy. Up until now, very few studies have been performed for determining the transfer function between the kinetic energy of incoming particles and the pulse height of STJ output signals. However, recent results on this type of detector might suggest a non-linear response of STJ cells, with a trend that is less favorable than a linear trend (Figure IV.9). The mechanism for this deviation is not understood yet, but those recent studies have demonstrated

that the energy spread of STJ cells is low enough to discriminate ion charge states [45, 68]. The performances of STJ detectors allowed confirming the first successful detection of $^{14}N_2{}^{2+}$ and $^{16}O_2{}^{2+}$ ions respectively without the disturbance of the $^{14}N^+$ and $^{16}O^+$ ions, which respectively share the same mass-to-charge ratio [54].

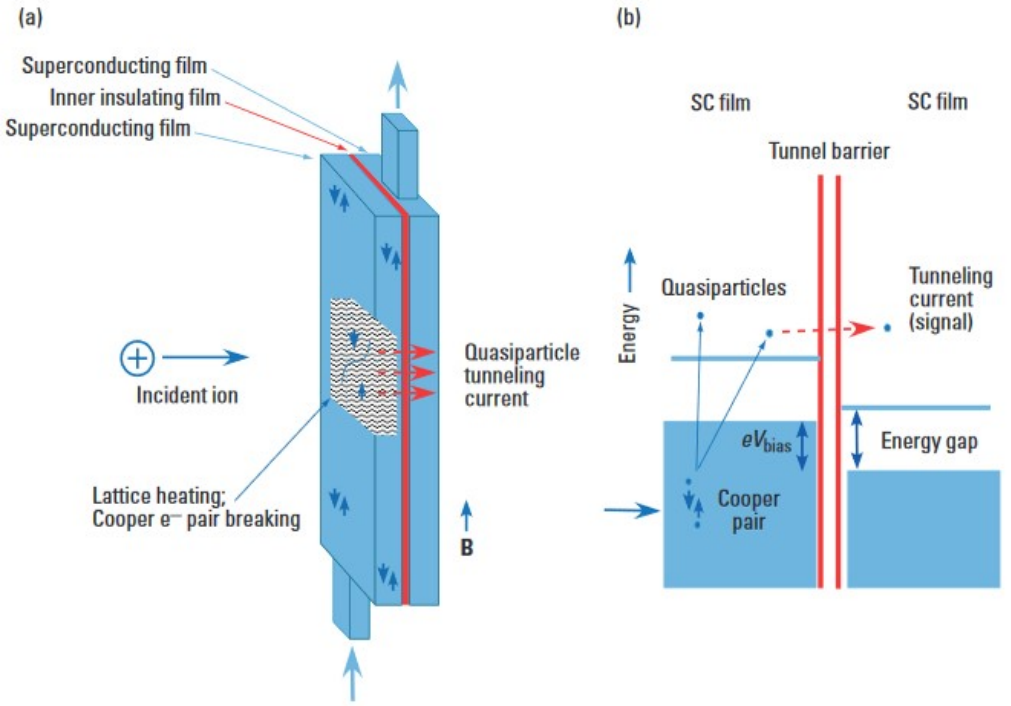

Figure IV.8: Schematic and (b) energy-level diagram of an STJ cryodetector. When a high-energy ion impinges on one of the superconducting layers, millions of Cooper pairs are broken, and a bias voltage between the two superconducting electrodes allows the flow of the liberated electrons, from one electrode to the other, by a tunneling current through the thin insulating layer.

Conversely to SSDs, STJ detectors are only sensitive to the total energy deposited by incident particles and not to their speed. Therefore STJ detectors can guarantee a mass-independent, 100% intrinsic detection efficiency even for slow-moving particles [15, 45].
Concerning the position sensitivity, the largest STJ array detector ever fabricated, introduces an effective detection area of 4 mm^2, with a pixel size of 200×200 μm^2 [63]. Those dimensions clearly shows that one of weakness of current STJ array detectors is their small sensitive area compared with that

of SSDs. The reason to this comes from the observation of the increase of a current leakage as a function of the STJ array size [63], introducing biases during the energy measurement.

As the same way as for SSDs, the other limiting factor of STJ detectors is their slow response time. Several studies have shown that the output pulse shape of STJ cells introduces a rise time of ∼1 us, and a fall time that can vary between 1 and 20 us [17, 54, 56, 63]. Consequently, in the same way as SSDs, or even worse, the slow response of STJ detectors is incompatible with the typical APT acquisition rates, introducing only few nanoseconds of output response time (see Chapter I).

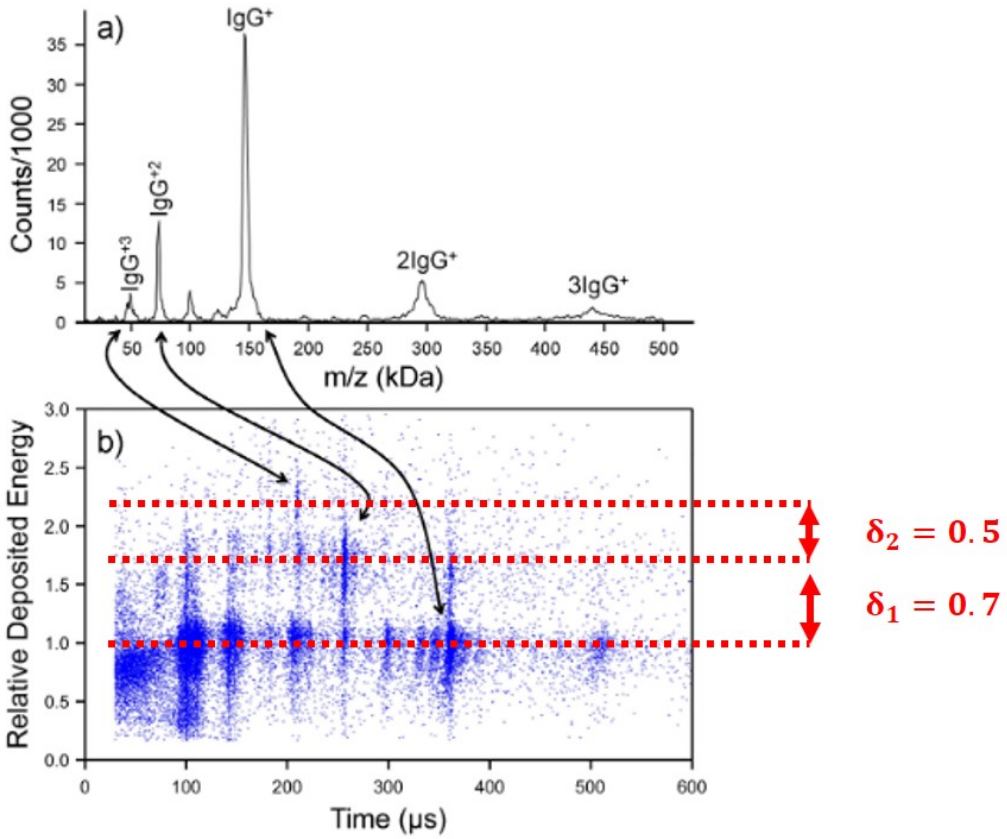

Figure IV.9: Results from the first development of a commercially available STJ cryodetector array [68]. (a) Mass spectrum of immunoglobulin G antibodies measured with the 4x4 STJ array. (b) Scatterplot of individual ion events showing ions TOF vs. ions kinetic energy from the analysis in (a).

IV.2.3 Metallic Magnetic Calorimeters

Among the existing PESDs, there are also the cryogenic calorimeters. Generally, a calorimeter is a device that measures the amount of heat (energy) deposited in a sample of material. Through the use of thermal absorbing materials, cooled at very low temperature < 2 K, a calorimeter cell measures the temperature rise ΔT induced by a deposited particle energy E [29] [16, 62].

$$\Delta T = \frac{E}{C_{tot}(T)} \tag{IV.7}$$

Given that the heat capacity C_{tot} of absorbers, becomes very small at low cryogenic temperatures [62], calorimeters are able to measure very large temperature excursion for a small amount of heat input, which makes them highly sensitive to single particle detection.

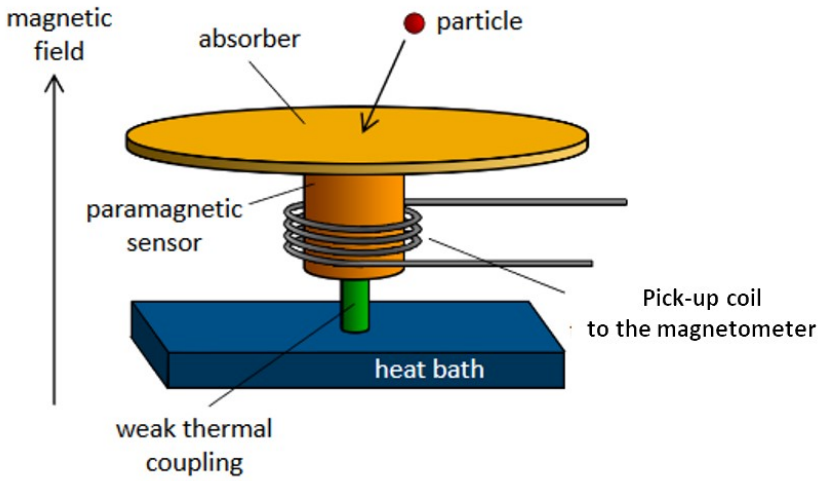

Figure IV.10: Schematic diagram of the MMC setup. The absorption of energy in the calorimeter, composed of a metallic absorber coupled with a paramagnetic sensor, leads to a rise in temperature and a decrease in magnetization, which can be measured accurately using a low noise superconducting magnetometer.

One of the means frequently used for converting the temperature variations ΔT into electric signals, is to couple a calorimeter cell with a magnetic thermometer, forming a high sensitive cell called Metallic Magnetic Calorimeter (MMC). MMC detectors consist of a metallic absorber coupled with a paramagnetic sensor, which are in strong thermal contact with

each other, but have a rather weak coupling to a thermal reservoir, aimed at defining an average temperature in the absence of an energy input (Figure IV.10). The absorption of energy in the calorimeter leads to a rise in temperature and a decrease in magnetization of the magnetic sensor, which can be measured accurately using a low noise superconducting magnetometer (also known as a SQUID) [14].
Through suitable calibrations, it has been claimed that pulse amplitudes extracted from the magnetometer (Figure IV.10) are proportional to incident particle energies [43]. In addition, experiments from Novotny et al. [43] have shown that the energy spreads obtained with MMC detectors are strongly influenced by the energy and the elemental nature of incident ions (Figures IV.11 and IV.12). The higher is the energy of incident ions the higher will be the energy spread. The higher is the mass of ions the higher will be the energy spread. Despite those effects, it can be observed that the ERP of MMC detectors stays above 100, which is totally sufficient for APT experiments (Table IV.1 and fig. IV.4).

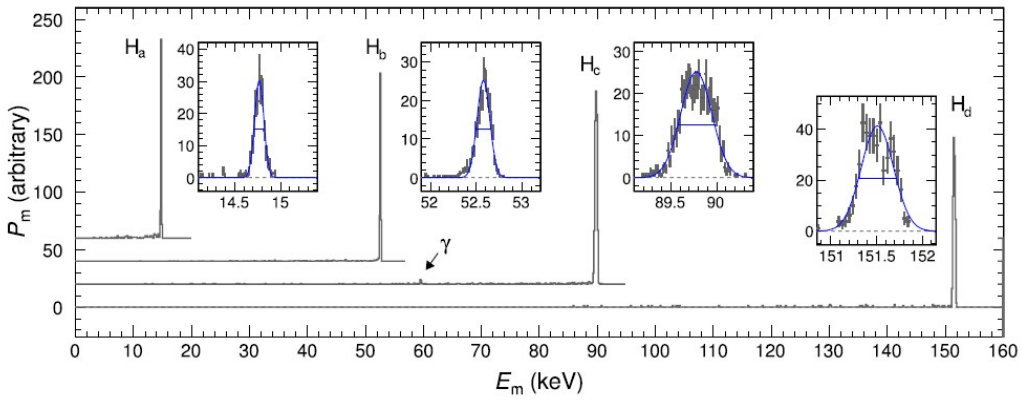

Figure IV.11: (From Novotny et al. [43]) Energy spectra performed with an MMC detector, for proton beams at 14.7, 52.6, 89.9 and 151.5 keV.respectively label as H_a, H_b, H_c and H_d. The relative counts Pm are given on an arbitrary scale. In order to visually separate the spectra, vertical offsets have been added to H_a, H_b and H_c. The statistical uncertainties are given by the vertical error bars in each inset. Gaussian-fit curves of the dominant peak in each spectrum are plotted in blue. The blue horizontal solid lines indicate the respective FWHMs and the dashed lines the baselines.

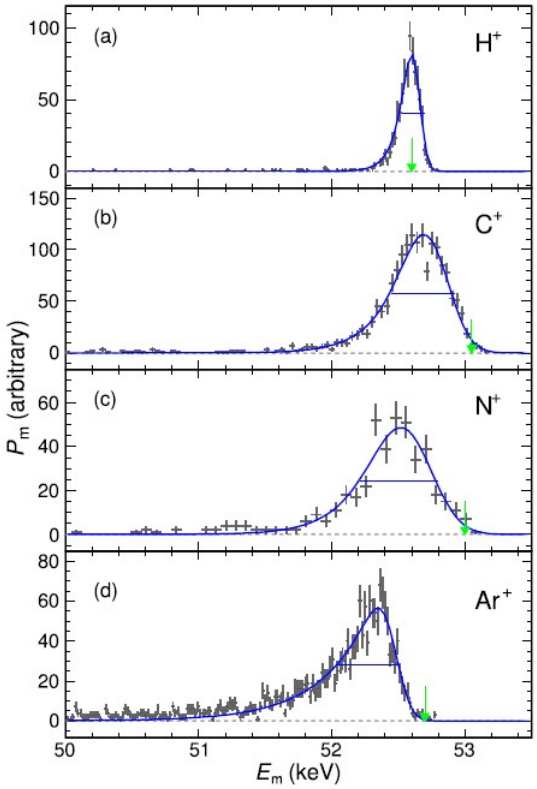

Figure IV.12: (From Novotny et al. [43]) Energy spectra performed with an MMC detector, for H^+, C^+, N^+, and Ar^+ beams at ∼53 keV, repectively in panels (a), (b), (c) and (d). The statistical uncertainties are given by the vertical error bars. Green arrows mark the respective nominal ion beam energies. The asymmetric shape of energy peaks has been fitted with the convolution of a Gaussian function with a left-sided exponential function (plotted in blue). The blue horizontal lines indicate the respective FWHMs.

To date, only the study from Gamer et al. [21] has proposed a design of MMC array for combining the energy-sensitivity of MMC detectors with a position-sensitivity (Figure IV.13). However, no experimental results on this design have been published yet.

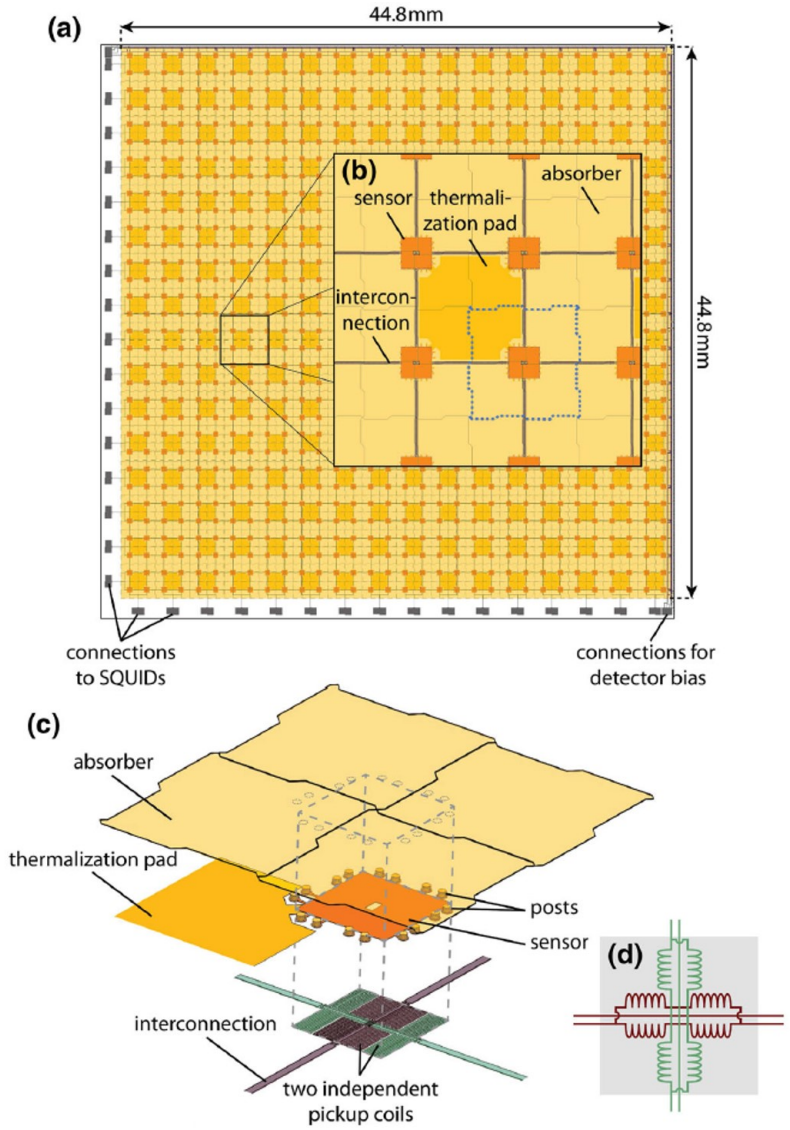

Figure IV.13: Schematic of the MMC array designed by Gamer et al. [21]; (a) Overall array layout showing the connections to the SQUIDs as well as the connections for the detector bias; (b) Magnification of the area that is marked in (a) by the continuous black square. It indicates the arrangement of the temperature sensors, the interconnections as well as the particle absorbers. For clarity, the absorbers are shown in transparent color; (c) Exploded view of the region marked in (b) by a dotted frame. It shows the two independent pickup coils (marked by different colors), their interconnections, the temperature sensor, the posts connecting the sensor and the absorbers as well as a part of the thermalization pad; (d) Schematic of the wiring of the two independent pickup coils, each consisting of two parallel-connected individual coils.

Despite the significant potential of MMC detectors, it has to be pointed that every system using thermal measurements is subjected to thermal equilibrium after each temperature variation, inducing the increase of MMCs response time related to the previous type of energy-sensitive detectors. Therefore, studies on MMCs involving the detection of single particle mostly introduce output signal shapes with rising edges in the range of 4 to 80 us, and falling edges of about 3 ms [21, 43]. As well as for SSD and STJ detectors, the time response of MMC detectors seems to be incompatible with the typical APT acquisition rates.
From those existing PESD, it can be stated how difficult it is to measure single particle energies, while trying to retrieve the high performances of current APT instruments (see Chapters II and III). The main drawbacks of those technologies are their slow response time, limiting the detection rate and the ability to resolve multi-hit events, but also their poor spatial resolution caused by their limited number of energy-sensitive cells.

IV.3 Mass and energy-sensitivity of thin foils

Other devices, that are to date not known or used as PESDs, could bring this lack of energy sensitivity to APT instruments. This applies to the secondary electron emission (SEE) induced by ion impacts on thin foils. It has been known for many decades that the amount of secondary electrons generated from positive ion bombardment on thin foils is a function of both mass and kinetic energy of ion projectiles [4,27,30,34]. The possibility to use thin-foils as energy-sensitive detectors has already been mentioned and encouraged by Š. Šaro et al. [3], but has never been used as such. Until now, one of main practical purposes of thin foils was to be used as electron multipliers for getting start and/or stop signals for TOF spectrometers by being coupled with microchannel plates [17,22,25,68], all this without considering the mass and energy-sensitivity of thin-foils (Figure IV.14). For those last studies, the mass and energy sensitivity of thin foils were only considered for avoiding selective losses caused by the lack of secondary electrons induced by some elements, at certain energies [41].

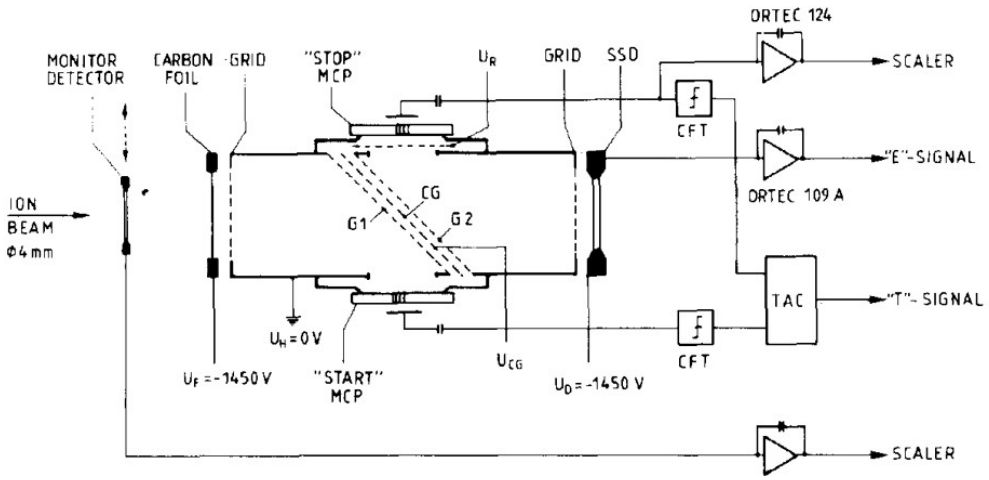

Figure IV.14: Schematic diagram of a satellite-born ion-mass-spectrometer [69]. A thin carbon foil ($\sim$2.5 μg/cm^2) is used as a converted for "START" electrons and "STOP" electrons are released from the surface of a solid state detector serving as an energy spectrometer. Separation of the secondary electrons from incident ions is achieved with an electrostatic dual mirror system deflecting the "START" and "STOP" electrons by 90° but in opposite directions.

Since most of those experiments performed in this field of research were conducted with ion beams rather than through atom-by-atom analyses, it cannot be stated that this phenomenon could be useful for APT experiments. Moreover, a very few number of publications has reported the measurements of secondary electron yield (SEY) induced by ions, having the kinetic energy range of APT experiments (around 5 keV - 40 keV). Therefore, the following study is aimed at conducting experiments that could confirm the mass and energy-sensitivity of thin foils in the energy range of APT experiments, and also aimed at evaluating the potential selective losses related to the energy and the mass of incident ions.

IV.4 The Ion-Induced Secondary Electron Emission phenomenon

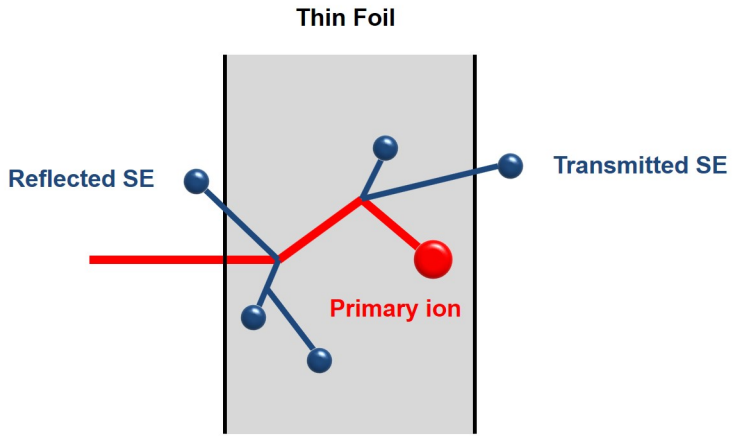

Figure IV.15: Ionization of a thin foil through a primary ion. The penetration of the ion projectile inside the solid induces the generation of secondary electrons, which can be ejected from the entrance or the exit surface of the thin foil, as a function of their energy and their trajectory in the matter.

The secondary electron emission (SEE) induced by ion-matter interactions is generally considered as a three-step process [49] (Figure IV.15). First, the projectile transfers its kinetic energy to target electrons; next, a fraction of these secondary electrons (SE) moves, from the internal structure of the thin foil, towards the entrance and exit surfaces; finally a fraction of those SEs will be ejected from the target, provided that their energy is sufficient to overcome the surface barrier between the target and the vacuum medium. It has been reported that most of these SEs have an initial energy in the range 30 eV - 90 eV [5,39,46,59], then reduced to less than 5 eV for SEs ejected to the vacuum medium [1, 6, 10, 46, 50, 61]. Linked to that, studies have shown that those ranges of energies do not depend on the nature of the projectiles, nor on their kinetic energy, but mainly depend on the target material [6, 24]. Based on those values, and knowing the direct relation between SE energies and their mean free path in solids [51, 58], it can be found in the literature that the mean free path of electrons varies between 5 Å and 20 Å for metals and semiconductors [6, 24], and up to hundreds of Å for insulating materials [3, 6, 24, 64].

IV.5 Selection of the thin-foil material

Regarding the different studies implying SEE from thin foils, there is evidence to suggest that carbon foils (CF) would be the best choice for being used in APT experiments. Indeed, in 1955 Murdock et al. [41] reported that CFs introduce one of the highest SEY compared with most other materials (Table IV.2). Although, there are exceptions such as cesium iodide (CsI) thin foils, introducing much higher SEYs than CFs [9], but with difficulties to manufacture robust and regular thicknesses under 100 μm [8, 67]. In counterpart, P. Maier-Komor [36] reported that CFs can be manufactured one order of magnitude thinner than other foils made with other elements, with thicknesses below 5 nm. This can explain why most of current applications using the SEE phenomenon are using CFs [1].

Target Material	H_1^+	H_2^+	H_3^+
Mo	1.8	-	-
Cu	1.7	3.1	3.77
Au	2.0	4.0	-
Brass 1[a]	3.6	6.8	9.3
Brass 1[b]	2.9	5.5	7.3
$AgMg_3$	4.8	6.3	8.8
Steel (stainless)	2.3	5.0	6.2
Carbon	3.9	6.6	8.2

Table IV.2: Comparison of the total SEY (backward and forward) of various materials with ion energies varying from 126 keV to 131 keV.
(Brass 1^a: Surface covered with carbon from acetylene flam / Brass 1^b: Stock brass with no special surface cleaning)

CFs have already been applied in several detection systems requiring ultra-high vacuum conditions in the same order of magnitude as APT instruments ($< 10^{-9}$ Torr) [12, 31]. Moreover, reports from different space programs allow to calculate that CFs have a sufficient lifetime for performing more than one billion APT analyses without noticing any major difference in its SEE properties [1]. From data originating from Allegrini et al. [1]

(Figure IV.16), it can be calculated that a CF surface of 40 cm^2 (∼7 cm of diameter) would only lose less than 1 nm, by collecting ∼8.10^{16} ions. For APT analyses comprising 100 millions of ions each, this thickness loss would be reached after 800 million analyses.

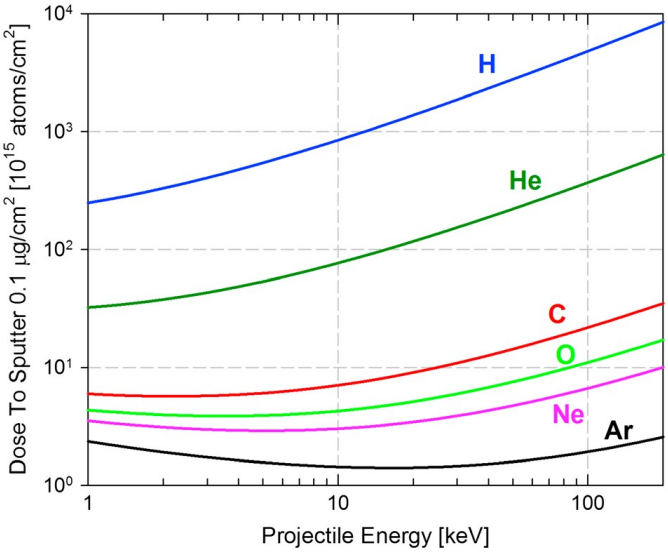

Figure IV.16: Erosion rates of CFs due to sputtering by H, He, C, O, Ne, and Ar projectiles (from [1]).

IV.6 Collection of secondary electrons from CFs

By recalling that SEs can be generated both from the entrance and the exit surfaces of thin foils (Figure IV.15), one can note that those SEs can be collected at the proximity of those two surfaces. For that reason, different collecting techniques have been developed for decades as a function of the different SEE applications (Figure IV.17).
Most of those detection techniques use CFs in combination with MCP assembly for both getting timing pulses (start and stop time measurements), triggered by the SEs, and for determining the original position of ion impacts. In the framework of our study, particular interest has been paid to the configuration using the transitory secondary electron emission (Figure IV.17b), with the aim of keeping a standard APT geometry having a detection surface orthogonal to the probed sample.

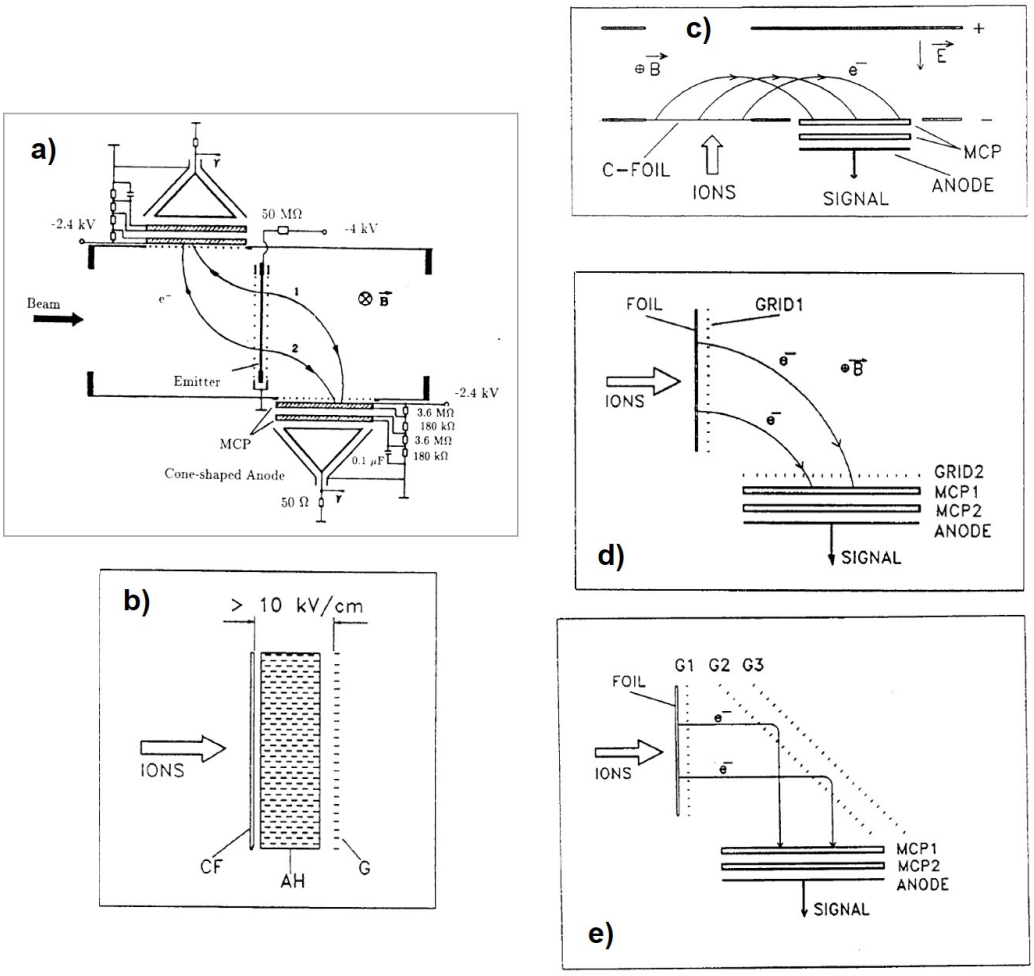

Figure IV.17: Schematics of the main different methods of SE collection (from [3]). Most of those methods use CFs with MCP assemblies for both getting timing pulses triggered by the SE, and for determining the original position of SE. a), c) and d) are configurations using deflecting systems with electro-magnet devices. The configuration in a) stands out from the others by the detection of SE from both sides of the CF; b) and e) are configurations that exclusively use accelerating electric fields.

IV.7 Selection of the foil thickness

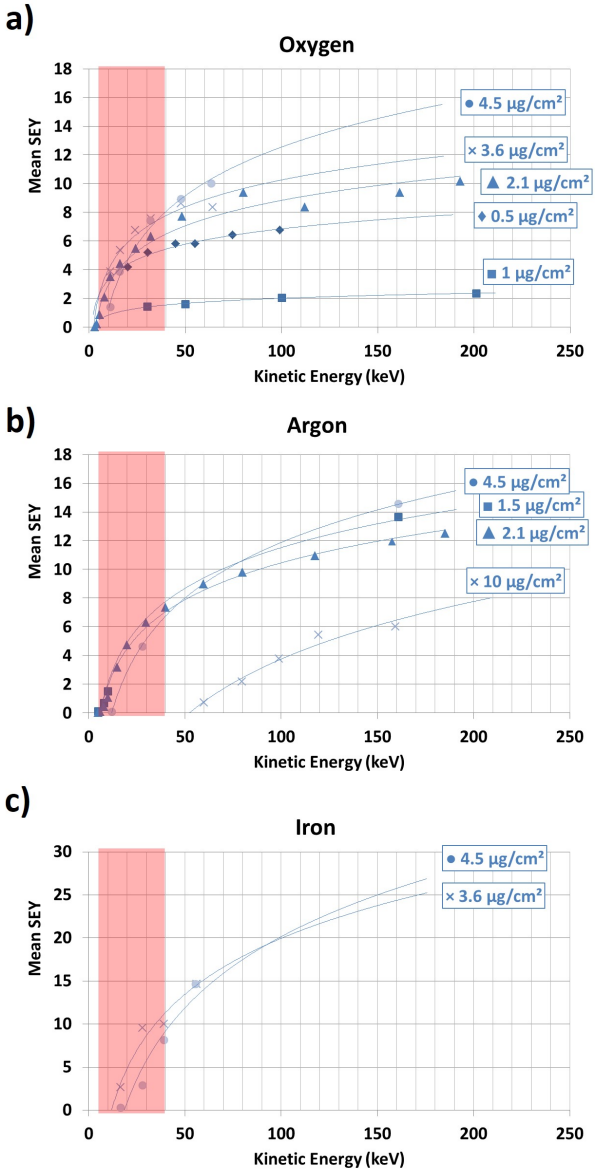

Figure IV.18: Measurements of the SEY in forward direction induced by three different projectiles on CFs, as a function of their kinetic energy (from [2]).Solid lines represent trend log curves highlighting the impact of the different CF thicknesses on the induced SEY. Red areas represent visual aids for identifying the operating range encountered in APT experiments (5 keV – 40 keV).

The only experimental study that can help to choose the best CF thickness, in the energy range of APT analyses (around 5 keV – 40 keV), originates from Allegrini et al. [2], whose compared CF thicknesses from 0.5 $\mu g/cm^2$ to 10 $\mu g/cm^2$ (2.5 nm to 50 nm thick). From this study, it appears that CF thicknesses between 2 and 4 $\mu g/cm^2$ (approximately around 10 nm to 20 nm thick) are the most appropriate for getting the highest SEY in the energy range of APT experiments (Figure IV.18). This range of thicknesses can be theoretically explained through a simple model considering both, the mean distance R_i that primary ions travel before generating SEs, and the mean distance R_{SE} that SEs travel inside the matter (Figure IV.19).

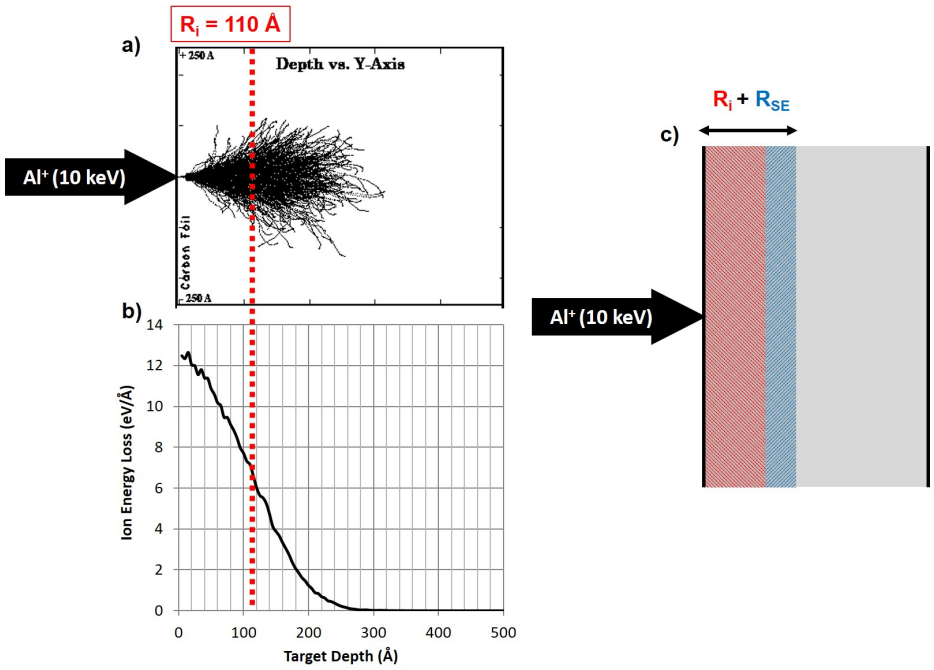

Figure IV.19: Schematic of the process used for determining the mean depth of SEs inside a volume of amorphous carbon. Through a SRIM simulation of ion impacts on a CF (a), the mean distance R_i that primary ions travel before generating SEs is determined through the identification of the mean depth introducing ionization collisions (b). The mean depth of SEs is then calculated through the sum of the mean distance R_i and the mean distance R_{SE} that SEs travel inside the matter (c).

Firstly, it can be recalled that the mean free path of SEs, that is nearly equal to the mean distance R_{SE} [55], does not depend on the nature of the projectiles, nor on their kinetic energy, but mainly depend on the target material [6,24]. Concerning CFs, it has been reported that the mean free path

of SEs varies between 30 Å to 80 Å [18,48]. In the interest of creating a model, an intermediate value of 50 Å has been considered for the value of R_{SE}. Then, concerning the mean distance R_i that primary ions travel before generating SEs, it is possible to estimate its value through the SRIM simulation tool [71,72], which is a Monte Carlo computer program modeling the transport of energetic ions in amorphous targets. Among the available options, SRIM is able to determine the depth at which ionizing collisions occur in the target, as a function of the elemental nature, the kinetic energy and the angle of incidence of ion projectiles. That means that it is possible to determine the mean distance R_i where primary ions travel before generating SEs. As illustrated in Figure IV.19b, the value of R_i is determined by choosing the mean depth at which Al^+ ions loose half of their energy. By summing the mean distances R_i and R_{SE}, it is then possible to get an idea of the optimal range of CF thicknesses that can be used for generating the highest SEY possible, as a function of the elemental nature and the kinetic energy of ion projectiles.

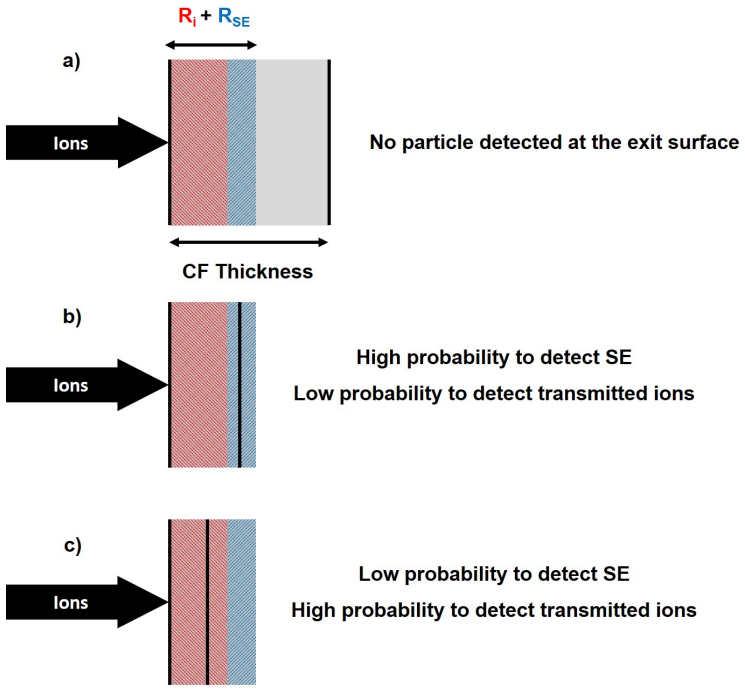

Figure IV.20: Schematic representation of the three main scenarios that may occur during the impact of ions on thin CFs. The most favorable case in APT experiments would be the case b), where only SEs are detected for performing an energy discrimination between elements.

This simple model allows describing the three main scenarios that may occur during the generation of SEs in CFs (Figure IV.20);

a) The thickness of the CF is too wide to bring out SEs. This specific case may occur for heavy ions, having higher probabilities to lose their whole energy at low depth, and thus having higher probabilities to be stopped at low depth.

b) The thickness of the CF is at the same time, higher than the mean distance R_i at which SEs are generated, and lower than the depth at which SEs are stopped in the CF.

c) Projected ions go through the CF before generating any SEs. This specific case may occur for light ions traveling more easily within the density of the CF.

Based on this model, it can be deduced that the CF thickness T must be in accordance with the following conditions;

$$R_i < T < R_i + R_{SE} \tag{IV.8}$$

Considering that R_{SE} is a fixed value, one can note that the choice of T will mainly depend on the value of R_i, which in turn depends on the energy and the elemental nature of ion projectiles (Figure IV.21).

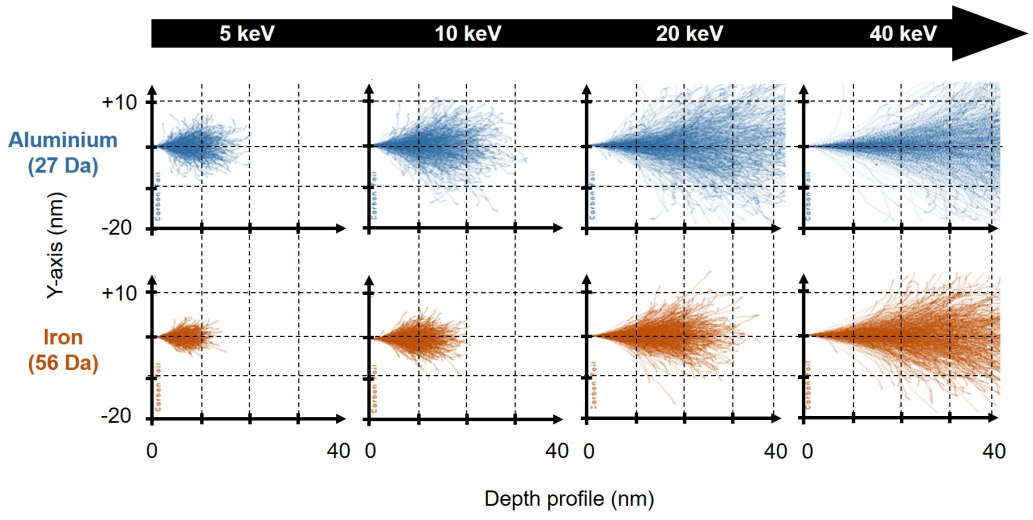

Figure IV.21: SRIM simulations on the projection of Al^+ and Fe^+ ions in a volume of amorphous carbon, as a function of their kinetic energy.

The application of those conditions (Equation (IV.8)) as illustrated on Figure IV.22, shows that for avoiding selective losses (Figure IV.20a and Figure IV.20c) in the application of CFs, it would be necessary to clearly define the elements that will be analyzed, and also the range of their kinetic energy.

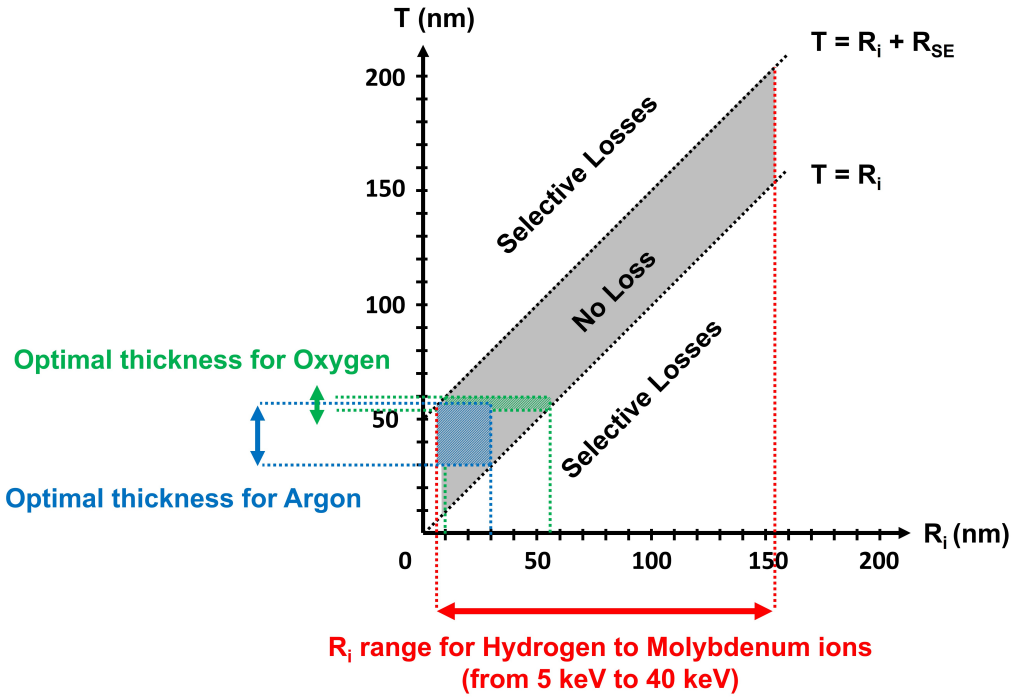

Figure IV.22: Graphical representation of the condition (Equation (IV.3)) that must be applied for avoiding potential selective losses under the impact of ions, with a kinetic energy range between 5 keV and 40 keV, on CFs with a thickness T.

IV.8 Measurement of the SEY from carbon foils

In order to ensure the mass and energy sensitivity of CFs, preliminary studies have been conducted with the help of controlled ion beam sources, also known as Focused Ion Beams (FIB). Through the use of mass separators (also known as Wien filters), consisting of perpendicular electric and magnetic lenses (Figure IV.23), FIB instruments are able to provide mono-isotopic beams with variable energies [66, 70]. As a consequence, through a fine selection of

ion projectiles and kinetic energies, it becomes possible to finely control the input parameters allowing the estimation of the SEY induced from CFs.

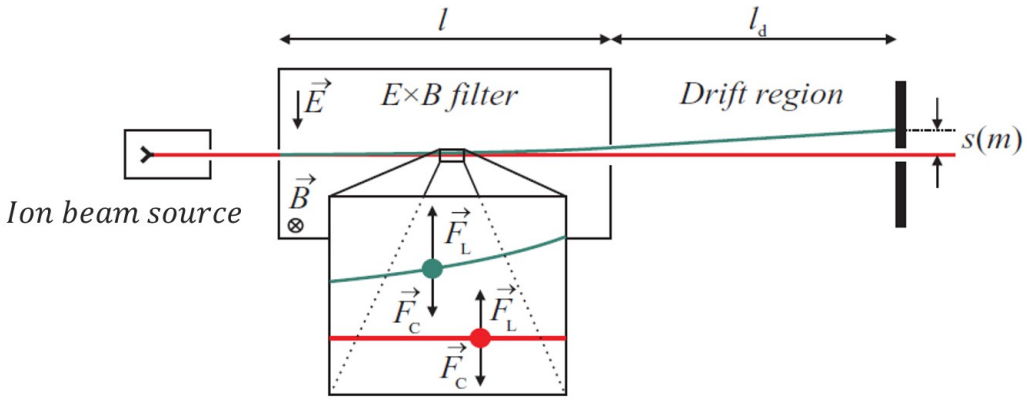

Figure IV.23: Working principle of a mass separator from a FIB instrument [46,70]. The adjustment of the two perpendicular electric and magnetic fields, applied on the ion beam source, allows the selection of ions having specific velocities. The equality between the Lorentz force $\vec{F_L} = qv \times \vec{B}$ and the Coulomb force $\vec{F_C} = q\vec{E}$ for specific velocities allows this selection.

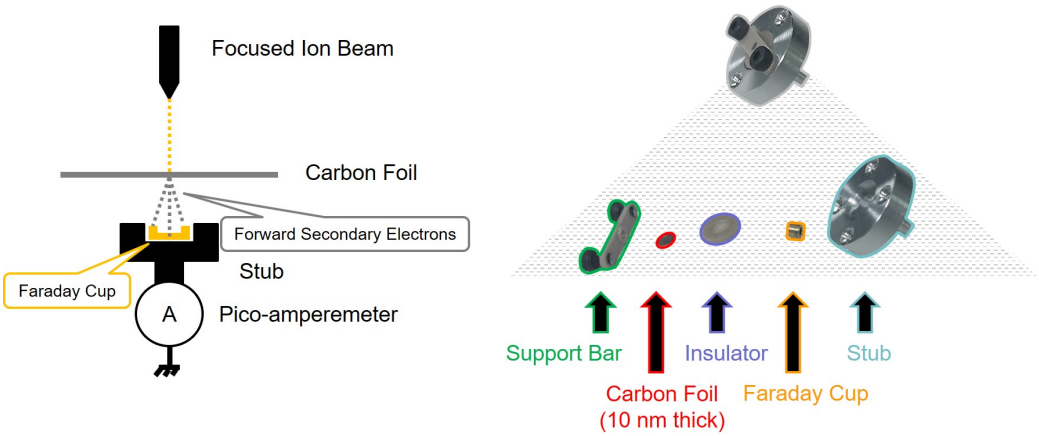

Figure IV.24: Setup specially designed for SEY measurements on FIB instrument.

Figure IV.24 introduces the device specially designed for those measurements. SEY measurements have been performed by collecting

forward SEs emerging from commercially available CFs mounted on TEM grid from EMS (www.emsdiasum.com). The forward SEY has been determined by comparing the ion beam current I_{beam}, originating from the FIB source, to the current induced by forward SEs I_{SE}, measured at the output of the foil. Currents I_{beam} and I_{SE} have been simply measured through the same faraday cup and by means of a pico-ammeter (Figure IV.24).
According to the literature and the previous assessments, it must be recalled that ion projectiles may pass through the foil depending on their energy and their mass [2]. It means that the current I_{pA}, measured on the pico-ammeter, is the combination of a fraction α of incoming ions coming from the FIB source and forward SEs induced by ion impacts. Therefore, in order to get a reliable estimation of the SEY, special attention has been taken in the subtraction of the positive current induced by transmitted ions. In the framework of this this setup, currents induced by transmitted ions have only been statistically determined through the use of SRIM simulation tool [71,72]. The SEY can be then calculated through the following equation;

$$SEY = \left| \frac{I_{pA} - I_{beam} \times \alpha}{I_{beam}} \right| \tag{IV.9}$$

Where α is the transmission coefficient of the foil calculated on SRIM.
It is also necessary to specify that, in order to avoid the electrostatic charging of the foil surface, its front end has been discharged through a tungsten micro-manipulator connected to an external ground.
SEY measurements were performed with two different beam sources, Ga^+ beam from a ZEISS - NVision 40 (www.zeiss.fr), and Xe^+ beam from a Helios G4 PFIB UXe DualBeam (www.thermofisher.com). Given that the respective masses of gallium and xenon are different nearly by a factor two ($\sim$131 Da for xenon and $\sim$70 Da for gallium), it could be possible to reproduce a case of mass peak overlap through the analysis of Xe^+ ions having twice the kinetic energy of Ga^+ ions. With the aim of ensuring high SEY from those heavy ions, CFs with a thickness of 2 $\mu g/cm^2$ (10 nm thick) has been chosen.

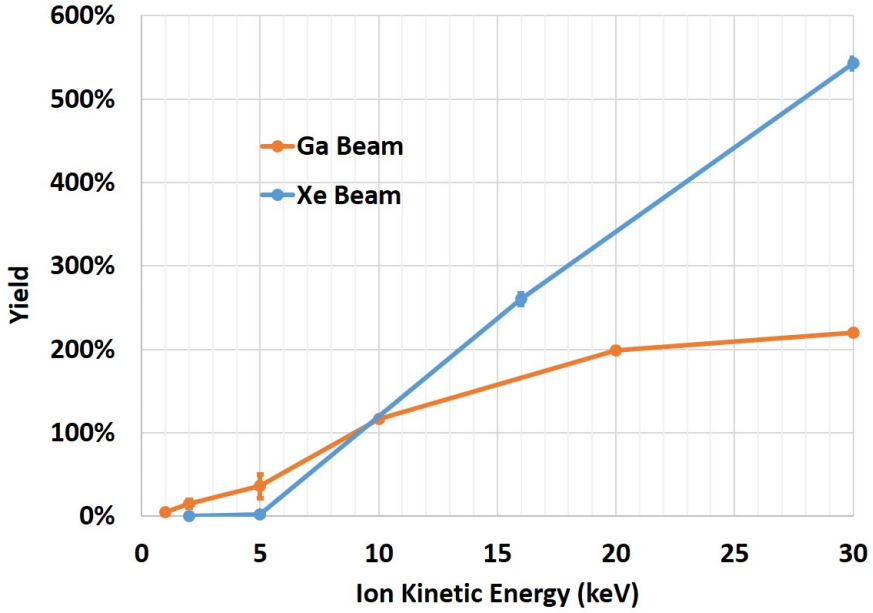

Figure IV.25: SEY measurements from Ga^+ and Xe^+ ion beams.

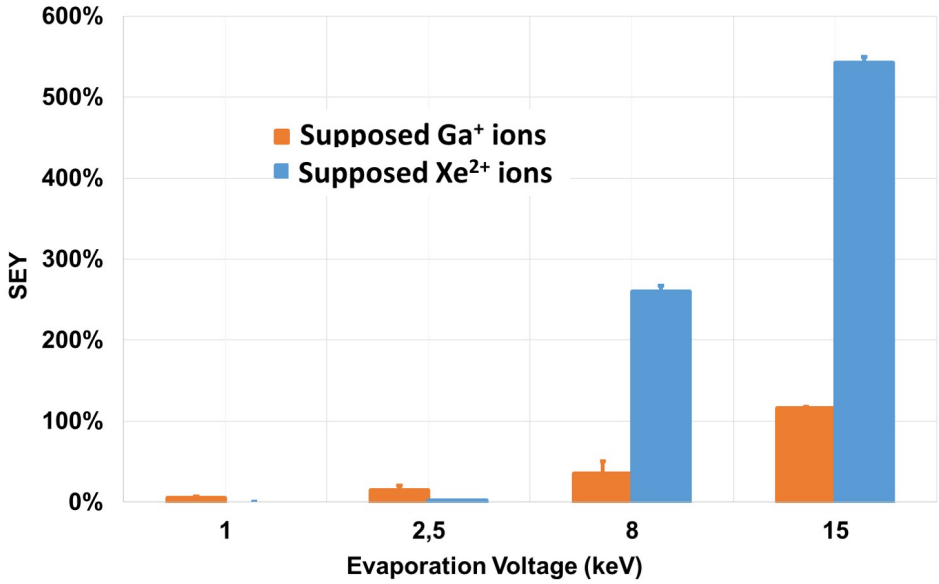

Figure IV.26: Hypothetical SEY induced by Ga^+ and Xe^{2+} ions during an APT experiment. The theoretical proximity of mass-to-charge ratios between Ga^+ and Xe^{2+} ions allows to demonstrate the ability of CFs to distinguish them through their respective induced SEY. The hypothetical evaporation voltage on this graph has been deduced from results in Figure IV.25.

Figure IV.25 clearly shows that SEY measurements from the two different ion beam sources (Ga^+ and Xe^+) provide a first confirmation that the amount of SEs really both depends on the mass and the kinetic energy of incident ions. Moreover, assuming that Xe^+ beam is set with twice the kinetic energy of the Ga^+ beam, it can be assumed that Xe^{2+} and Ga^+ ions, having very close mass-to-charge ratios, could be distinguished through this technique (Figure IV.26). From this last observation, it becomes clear that mass peak overlaps implying elements with different charge states could be resolved through the use of CFs.
On the fact that those results only concern a statistical point of view of the phenomenon, it would be necessary to check if this method can be applied for single particle detection, such as for APT experiments.

IV.9 Experimental setup for the Carbon Foil detector

IV.9.1 CF-MCP-DLD assembly

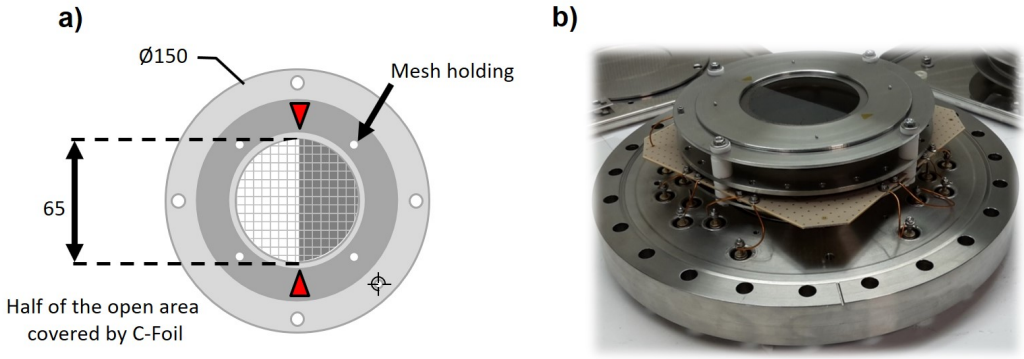

Figure IV.27: Design of the Carbon Foil detector especially designed for this study. (a) Top view of the CF assembly introducing a detection surface half covered by a CF mounted on a 70 lpi Nickel mesh. (b) Photograph of the CF-MCP-DLD assembly mounted on a 200-CF flange.

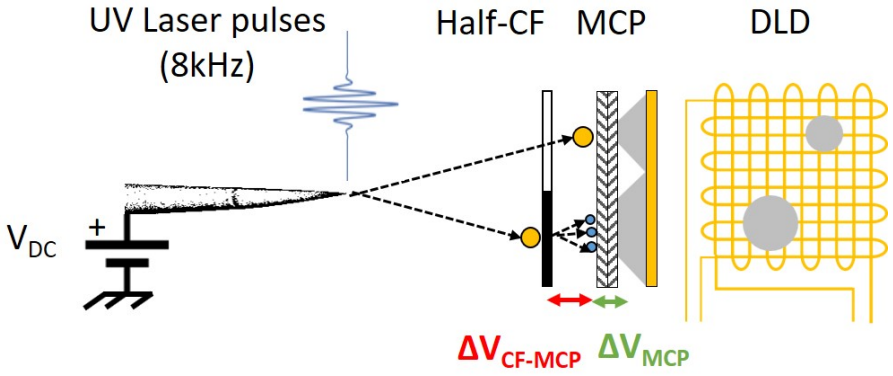

Figure IV.28: Setup of the dedicated CF detector workbench.

With the aim of fully exploiting the benefits of CFs mass and energy-sensitivity, it has been decided to combine a conventional MCP-DLD detector (see Chapter I) with a carbon foil mounting placed on its front-end (Figure IV.27). Amorphous CFs of 2 μg/cm^2 ($\sim$10 nm) thick were provided by Arizona Carbon Foil Company (ACF) in Tucson and the mounting was

designed at the GPM lab. In addition to providing information from the carbon foil detector, a direct comparison with the conventional MCP-DLD detector has been performed by splitting the detection area in two distinct parts (Figures IV.27 and IV.28). The MCP assembly used is characterized by an effective diameter of 77 mm, and an open area ratio of ∼60% (nearly the detection efficiency of the MCP assembly). The DLD used in this setup is the second version of the serpentine delay line (SDL) detector developed during this thesis (see Chapter III).

IV.9.2 Acquisition system of the Carbon Foil detector

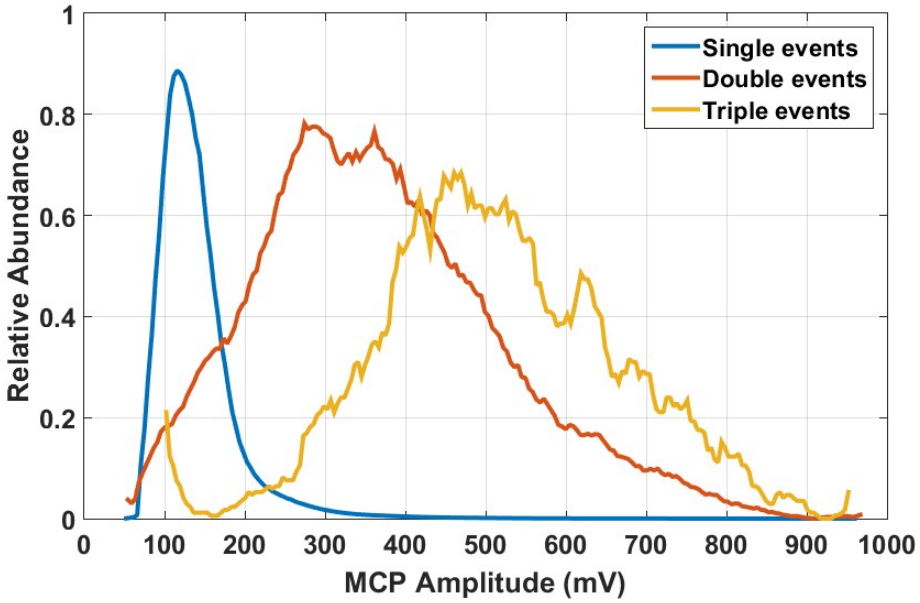

Figure IV.29: Pulse Height Distributions extracted from the LaWATAP instrument for the analysis of a pure aluminum sample. PHDs originating from double (red curve) and triple (yellow curve) events have been selected for events introducing TOF differences that do not exceed 100 ps (arbitrary value).

In order to extract information from ions kinetic energy, it has been decided to use an aDLD detection system (see Chapter III), because of its ability to extract the amplitude of output signals. Given that, in APT instruments, MCP assemblies are used in saturation regime (see Chapter I), which means that every single particle detection induces nearly the same MCP signal amplitude, it can be assumed that the resulting MCP signal

amplitude originating from the collection of simultaneous SE impacts will be proportional to the number of SEs collected. This assumption can be affirmed through the study of pulse height distributions (PHD) coming from conventional APT analyzes performed with the aDLD detection system, where it can be observed that multi-hit events involving very close TOFs introduce well separated distributions as a function of the number of ions detected simultaneously (Figure IV.29). Indeed, Figure IV.29 clearly shows that the study of simultaneous ion impacts in conventional APT analyses allows a close prediction of what will happen during the detection of SE multi-hits in the framework of this study. As a consequence, the study of the MCP pulse height distribution (PHD) can be used as a SEY indicator for all ion impacts. The detection system is based on fast digitizers sampling MCP output signals at 4 Gs/s and DLD output signals at 1 Gs/s.

IV.9.3 Single particle sensitivity of the Carbon Foil detector

According to the literature, it has been observed that the angular distribution of forward SEs exhibits a cosine-dependence [24, 48], suggesting that the distribution of the emitted SEs is isotropic within the target. In that way, it would be highly probable that single ion hits would be transformed into unwanted SE multi-hits spread on the detection surface (Figure IV.30).

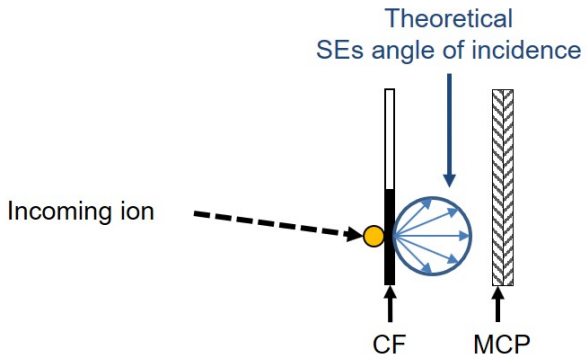

Figure IV.30: Schematic representation of the angle of incidence of forward SEs induced by an ion impact on a CF. Theoretically, the angular distribution of forward SEs exhibits a cosine-dependence [24, 48].

As a consequence, those potential SE multi-hits have to be spatially focused on a small area in order to get a single position and a single TOF for each single ion impact on the CF. To achieve that, it can be recalled

that each impact treated with an MCP-DLD detector is surrounded by a dead-zone (DZ), where no other successive impact can be spatially resolved (see Chapter II). Therefore, SEs coming from a single ion impact on the CF must be focused on a small area that does not exceed this specific DZ. Concretely, for DLDs having X and Y axes, no successive impacts can be resolved within those following conditions (see Chapter II);

$$\Delta TOF + DT \geq \frac{2.\Delta X}{v_X} \geq \Delta TOF - DT \tag{IV.10}$$

$$\Delta TOF + DT \geq \frac{2.\Delta Y}{v_Y} \geq \Delta TOF - DT \tag{IV.11}$$

Where ΔTOF is the TOF difference between ion pairs; v_X and v_Y are the transversal propagation velocities of electric signals respectively on X and Y delay line; ΔX and ΔY are respectively the relative distances between multi-hit impacts on X and Y delay line axes; and DT is the instrument dead-time. Given that ΔTOF is nearly equal to zero for SEs coming from a single ion impact on the CF, it can be deduced that the DZ where they must be confined together is reduced to the following conditions;

$$\Delta X \leq DT\frac{v_X}{2} \tag{IV.12}$$

$$\Delta Y \leq DT\frac{v_Y}{2} \tag{IV.13}$$

Previous studies in Chapter III have shown that successive signals from the aDLD system cannot be resolved if they are temporally separated under approximately 1.2 ns, thus representing the instrument dead-time. Considering the physical and electrical characteristics of the DLD used in this study (Table IV.3), the spatial conditions for converting SE multi-hits into single hits (Equations (IV.12) and (IV.13)) indicate that SEs must be gather in a DZ of less than 2.99 mm $\times$ 1.77 mm. This theoretical DZ can be verified experimentally on the detector workbench through the analysis of the distances between multi-hits having TOF differences that are very close to zero. Experimental results illustrated in Figure IV.31, from the CF detector workbench, introduce an experimental DZ of 3.14 mm $\times$ 2.14 mm, which is clearly near the theoretical DZ calculated. The data points that are present in the DZ are part of the spatial biases brought by the hit finding algorithm of the detection system (see Chapter II).

In order to focus the transmitted SEs on the restricted DZ, it is necessary to apply an electric field between the foil and the MCP front-end, for getting a single TOF and a single position for each single ion collection. To do so, a first electrostatic model has been defined for determining the optimal conditions

Transversal length l_X on the X axis (mm)	100
Transversal length l_Y on the Y axis (mm)	100
Mean propagation time <TPX> on the X axis (ns)	20.09
Mean propagation time <TPY> on the Y axis (ns)	33.77
Transversal propagation velocity v_X on the X axis (mm/ns)	4.98
Transversal propagation velocity v_Y on the Y axis (mm/ns)	2.96

Table IV.3: Physical and electrical characteristics of the DLD used for this study.

for getting the best single particle sensitivity of the CF-MCP-DLD setup (Figure IV.32). This model has been simply determined through Newton's second law. Considering the initial velocity v_0 and the angle of emission θ of forward SEs normal to the CF exit surface, it is possible to compute the electric field F_{CF-MCP} that must be applied between the foil and the MCP front-end, through the following equations;

$$F_{CF-MCP} = \frac{2m_e}{e}\left(D - \frac{d}{2} \times \frac{v_{0x}}{v_{0y}}\right)\left(\frac{v_{0y}}{d}\right)^2 \tag{IV.14}$$

$$v_{0x} = v_0 . \cos\theta \tag{IV.15}$$

$$v_{0y} = v_0 . \sin\theta \tag{IV.16}$$

$$E_0 = \frac{m_e v_0^2}{2} \tag{IV.17}$$

With m_e the mass of the electron, e the elementary charge of the electron, D the distance between the foil and the MCP front-end, d the distance between two SEs having opposite angle of incidence from each other, and E_0 the initial kinetic energy of SEs removed from the CF.

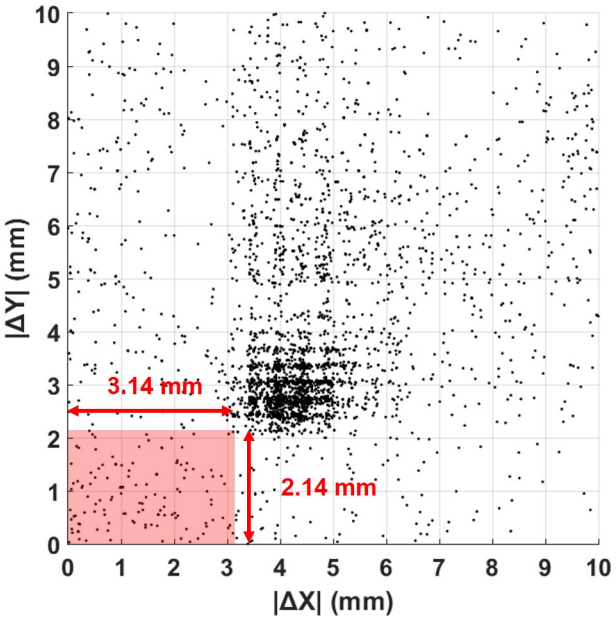

Figure IV.31: Scatter plot of the inter-impact distances on the CF detector workbench, for multi-hit events introducing TOF differences under 100 ps (arbitrary threshold). The red area represents the instrument DZ.

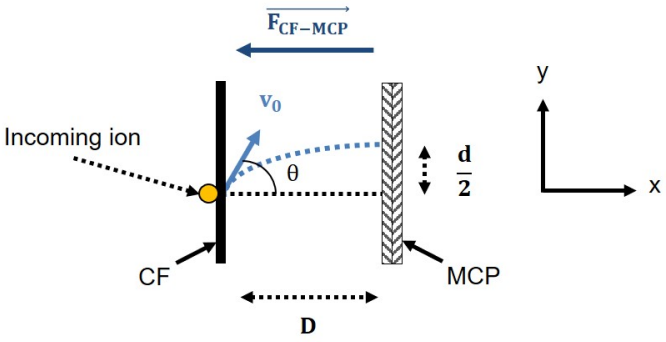

Figure IV.32: Two-dimensional representation of the electrostatic model used for computing the required electric field for focusing SEs on a restricted area on the MCP.

In addition, this model relies on three initial parameters;

1. Due to mechanical constraints, the distance D between the foil and the MCP front-end could not be set under 1 cm. Thus, for maximizing the possibility to focus SEs in very small areas, it has been decided to keep this distance to 1 cm.

2. By considering the cosine dependence of the SEs angular distribution [24, 55], a mean angle of incidence ±60° related to the surface normal of the CF exit surface, has been set for covering half of the maximum probabilities of the angular distribution.

3. The initial kinetic energy of SEs has been set to a mean of 2 eV, in accordance with studies which showed that this order of magnitude does not depend on the kinetic energy or the mass of incoming ions [1, 61].

By putting all those data together, it is then possible to establish a specific model ensuring the monitoring of SEs spatial distribution. The graphical representation of this model in Figure IV.33 shows that the intensity of F_{CF-MCP} must be higher than 123 V/cm for ensuring the focusing of SEs in a same DZ, where the maximum inter-impact distance required is 2.14 mm on this setup.

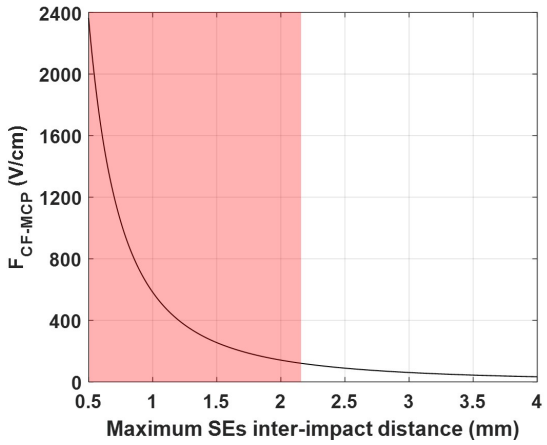

Figure IV.33: Graphical representation of the electrostatic model used for computing the required electric field for focusing SEs on a restricted area on the MCP (Equations (IV.14) to (IV.16)). The red area defines the required electric fields for ensuring the focusing of SEs in a same DZ.

Theoretically, it could be assumed that applying a very high value of FCF-MCP would be favorable for the single sensitivity of the CF detector, but two main limitations from this setup may induce significant losses. First, it should be noted that the saturation regime of the MCP assembly not only implies a limit of output charge from a single microchannel (see Chapter I), but also from the microchannels that are very close to original points of impact [72], [73]. This means that the very high proximity of SEs can trigger the saturation of the MCP around adjacent microchannels. The second main

limitation concerns the restricted electron detection efficiency of MCPs. It has been reported that the highest detection efficiency for electron projectiles can only be reached with energies varying between 200 and 400 eV [23, 40]. Given that the initial kinetic energy of SEs outcoming from CFs is limited to few eV, it can be deduced that, for a distance D between the foil and the MCP front-end of 1 cm, F_{CF-MCP} should be set between 200 V/cm and 400 V/cm.

IV.10 Mass and Energy sensitivity of the CF detector

IV.10.1 Analysis of a Fe40Al alloy

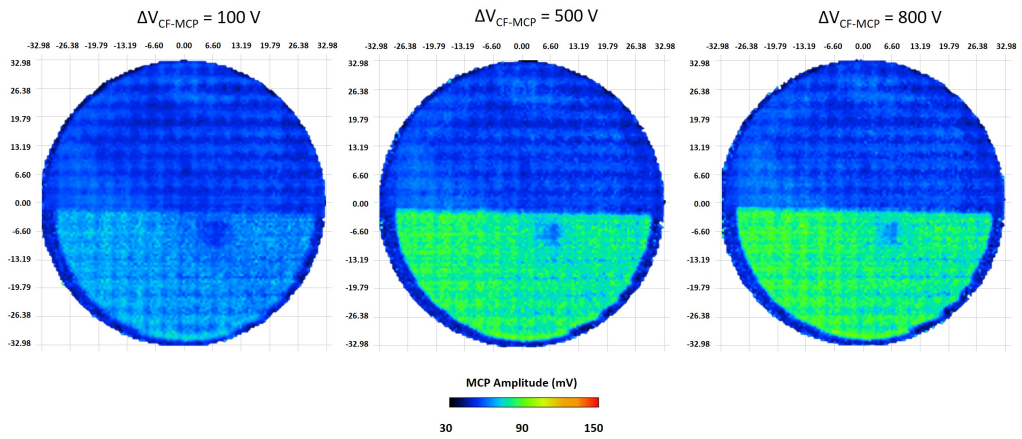

Figure IV.34: 2D distribution of MCP amplitudes on the detector surface. This figure clearly reveals the amplification of MCP signals through the CF detector that is induced by the secondary electron emission for each ion impact on the foil.

With the aim of evaluating the CF detector, a first analysis was performed with a Fe40Al (at. %) alloy for highlighting the mass peak overlap located at 27 Da between the $^{27}Al^{+}$ peak and the $^{54}Fe^{2+}$ peak [37, 52]. In a global aspect, it can be primary observed in Figure IV.35 that the CF properly plays its role of signal amplifier. As discussed earlier, it can be observed that the increase of the electric field between the CF and the MCP has the effect of focusing SEs and creating overlapped electric signals for each ion impact. On the lower part of 2D maps (Figure IV.34), representing the CF area, it

can be observed that MCP amplitudes are nearly twice higher than the upper part, representing the MCP-DLD area (without CF). It has to be specified that the narrow circular band following the edge of the CF area is caused by the absence of SEs, due to the focusing applied by the electric field applied between the CF and the MCP front-end.

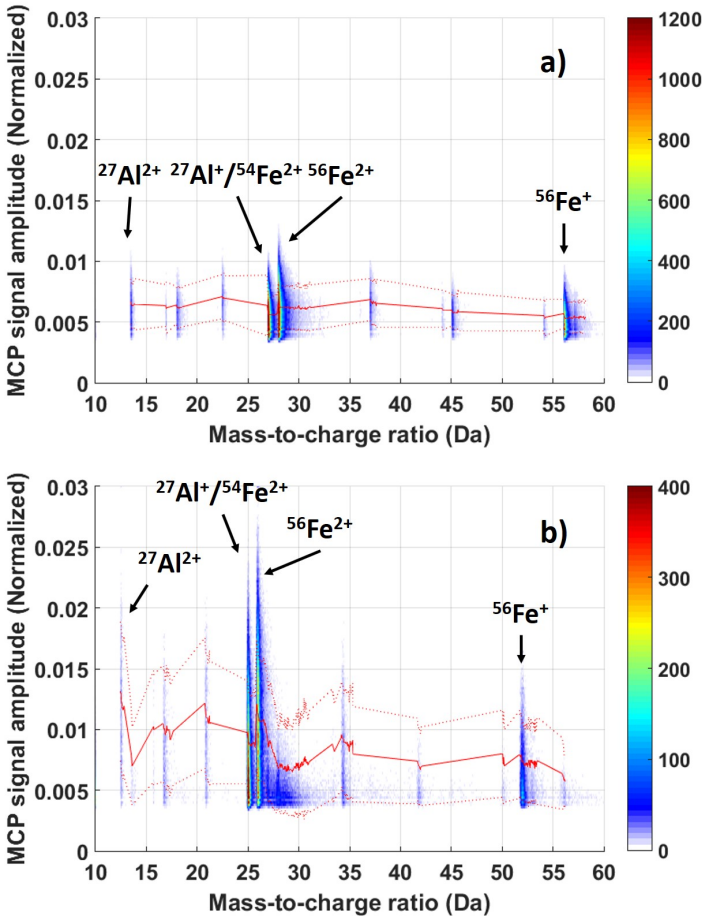

Figure IV.35: MCP amplitude vs. Mass-to-charge ratio spectra that describe how MCP amplitudes are distributed over a certain range of mass-to-charge ratios, respectively for the two areas on the detector: a) "no-foil" area and b) CF area (at $\Delta V_{CF-MCP} = 500$ V). The spectrum b) shows that detected ions with multiple charge state introduce higher amplitudes than ions with single charge state. Red solid lines represent the mean amplitude values for each mass, associated with their standard deviation (red dashed lines). It must be specified that the slight mass offset between spectra a) and b) is due to shorter time-of-flights associated with the ion-to-electron conversion between the carbon foil and the MCP front-end.

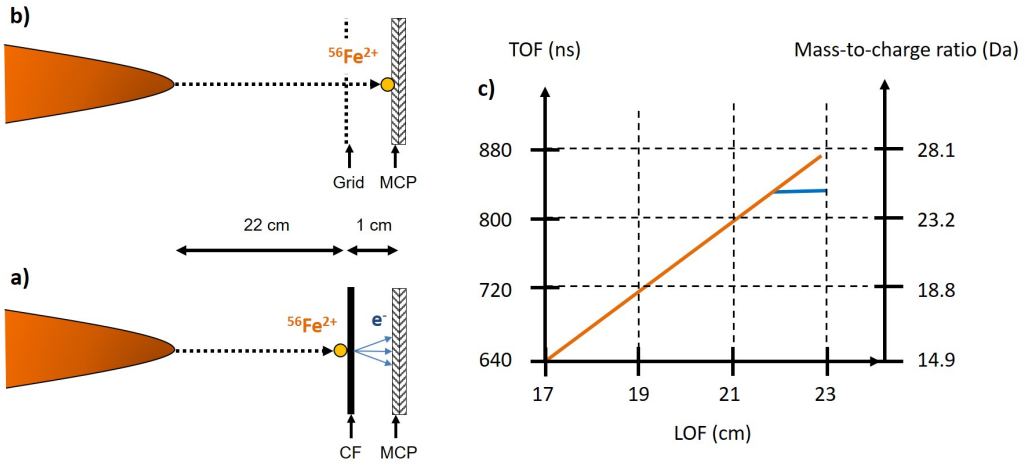

Figure IV.36: Schematic representations in (a) and (b) introduce the detection of a $^{56}Fe^{2+}$ ion on the two different detection setups of this study (CF-MCP-DLD and MCP-DLD). Theoretical results in (c) have been computed for a $^{56}Fe^{2+}$ ion having a kinetic energy of 20 keV (orange curve) and for SEs having a kinetic energy of 500 eV (blue curve). TOFs and mass-to-charge ratios in (c) have been calculated with a length-of-flight (LOF) representing the tip-to-detector distance of detector workbench used for this study (22 cm).

Now concerning the potential mass peak overlap at 27 Da, a comparison between the two areas has been performed through specific spectra representing the MCP amplitudes as a function of the detected mass-to-charge ratios (Figure IV.35). Since there is a theoretical relation between the kinetic energy E_K of ions and the electric potential V applied on the sample (Equations (IV.1) and (IV.2)), MCP amplitudes have been normalized by each corresponding DC potential from each detection event. The spectrum in Figure IV.35b, associated with the CF area in Figure IV.34b, clearly shows that detected ions with multiple charge state introduce higher amplitudes than ions with single charge state. Which confirm again the energy-sensitivity of CFs. It must be specified that the slight mass offset between the two spectra in Figure IV.36 is due to the shorter time-of-flights recorded from the detection of SEs, having higher velocities than ions. For example, Figure IV.36 shows how a $^{56}Fe^{2+}$ ion can be detected under a mass-to-charge ratio lower than 28 Da, because of the TOF shortening, between the CF and the MCP, induced by faster SEs. Considering the tip-to-detector distance of detector workbench used for this study (22 cm), it can be seen that the slight mass offset between the two spectra in Figure IV.35

is identical to the mass offset introduced in Figure IV.36.
At this point, it can be observed that the energy resolving power (ERP) obtained with this setup is not sufficient to totally resolve mass peak overlaps (Figure IV.35b). However, different parameters, such as the CF thickness (Figure IV.22) or the electric field between the CF and the MCP (Figure IV.33), could be tuned to find working points that could improve the ERP. Despite the poor ERP of this setup, the significant difference on MCP amplitudes between ions with different charge states Figure IV.35b) could still allow the spatial identification of elements that was not distinguishable in conventional APT instruments. Unfortunately, the homogenous nature of the analyzed Fe-Al alloy did not allow the clear visualization of the spatial separation between $^{27}Al^{+}$ and $^{54}Fe^{2+}$ ions. Therefore, other materials introducing mass peak overlaps in correlation with heterostructures have to be analyzed for spatially revealing the energy sensitivity of the CF detector.
On the quantitative aspect of this study, one can ask whether the composition of the analyzed material has been altered by the ion-to-electron conversion performed by the CF. Since the design of the detector used in this study both includes a conventional MCP-DLD assembly and a CF-MCP-DLD assembly (Figure IV.25), it is possible to get an estimation of the compositional biases brought by the CF detector, through the use of a reference brought by the conventional MCP-DLD assembly. Through this direct comparison, Table IV.4 shows that the lowest compositional biases are obtained for bias voltages ΔV_{CF-MCP} between 100 V and 800 V. Those results can be partly understood by recalling that the highest MCP detection efficiency for electron projectiles can only be reached with energies varying between 200 and 400 eV [23, 40]. It turns out that, with initial SEs kinetic energies of few eV [1, 61], a bias voltage ΔV_{CF-MCP} of 100 V induces SEs kinetic energies around 100 eV. From those compositional biases originating from the CF detector, a trend can also be observed where most of the singly charged ions are under-estimated, whereas most of doubly charged ions are over-estimated. This observation is in accordance with the literature and the previous results obtained with different ion beams (Figure IV.25), where it has been demonstrated that the amount of SEs released from a CF both depends on the mass and the kinetic energy of incident ions.

	ΔV_{CF-MCP} = 100V					
	No Foil (%)	Foil (%)	Gain/Loss (%)	Fe/Al Fraction (%) (No Foil)	Fe/Al Fraction (%) (Foil)	Gain/Loss (%)
$^{54}Fe^{+}$	1.55	0.56	-0.99	63.75	62.09	-1.66
$^{56}Fe^{+}/^{57}Fe^{+}$	24.75	6.50	-18.25			
$^{56}Fe^{2+}/^{57}Fe^{2+}$	37.45	55.03	17.58			
$^{27}Al^{+}/^{54}Fe^{2+}$	34.62	35.26	0.64	36.25	37.91	1.66
$^{27}Al^{2+}$	1.63	2.66	1.02			

	ΔV_{CF-MCP} = 500V					
	No Foil (%)	Foil (%)	Gain/Loss (%)	Fe/Al Fraction (%) (No Foil)	Fe/Al Fraction (%) (Foil)	Gain/Loss (%)
$^{54}Fe^{+}$	1.26	0.85	-0.41	63.29	62.47	-0.82
$^{56}Fe^{+}/^{57}Fe^{+}$	18.77	8.98	-9.78			
$^{56}Fe^{2+}/^{57}Fe^{2+}$	43.26	52.64	9.37			
$^{27}Al^{+}/^{54}Fe^{2+}$	33.05	33.40	0.35	36.71	37.53	0.82
$^{27}Al^{2+}$	3.66	4.14	0.48			

	ΔV_{CF-MCP} = 800V					
	No Foil (%)	Foil (%)	Gain/Loss (%)	Fe/Al Fraction (%) (No Foil)	Fe/Al Fraction (%) (Foil)	Gain/Loss (%)
$^{54}Fe^{+}$	1.00	0.93	-0.06	63.27	62.32	-0.96
$^{56}Fe^{+}/^{57}Fe^{+}$	16.97	9.80	-7.16			
$^{56}Fe^{2+}/^{57}Fe^{2+}$	45.31	51.58	6.27			
$^{27}Al^{+}/^{54}Fe^{2+}$	32.14	32.73	0.59	36.73	37.68	0.96
$^{27}Al^{2+}$	4.58	4.95	0.37			

Table IV.4: Comparison of the fractions of Al and Fe, in the analyzed Fe-Al alloy, between the MCP-DLD assembly and the CF MCP DLD assembly (Figure IV.25). Results from the different tables have been obtained from the same sample and at different bias voltage between the CF and the MCP front-end.

Assuming that the SEY may exceed more than one secondary electron per incoming ion (Figures IV.25, IV.34 and IV.35), it can be assumed that probabilities to detect ions become higher than for conventional APT detection systems. Therefore, in the same way as the estimation of the compositional biases, it can be assumed that relative detection efficiencies can be obtained by comparing the amount of ions detected with the CF part, related to the conventional MCP-DLD part. Results from Table IV.5 confirm this assumption, where it can be observed that the detection efficiency of some elements can reach an increase of $\sim$20%. It turns out that most of elements concerned by this increase are doubly charged ions; those expected to induce higher SEY related to singly charged ions.

	ΔV_{CF-MCP} = 100V		
	Count (No Foil)	Count (Foil)	Relative Efficiency
$^{54}Fe^{+}$	16919	3040	17.97%
$^{56}Fe^{+}/^{57}Fe^{+}$	269586	35185	13.05%
$^{56}Fe^{2+}/^{57}Fe^{2+}$	407905	298044	73.07%
$^{27}Al^{+}/^{54}Fe^{2+}$	377101	190968	50.64%
$^{27}Al^{2+}$	17780	14383	80.89%
Total	1089291	541620	49.72%

	ΔV_{CF-MCP} = 500V		
	Count (No Foil)	Count (Foil)	Relative Efficiency
$^{54}Fe^{+}$	5947	3651	61.39%
$^{56}Fe^{+}/^{57}Fe^{+}$	88539	38633	43.63%
$^{56}Fe^{2+}/^{57}Fe^{2+}$	204093	226377	110.92%
$^{27}Al^{+}/^{54}Fe^{2+}$	155916	143627	92.12%
$^{27}Al^{2+}$	17265	17785	103.01%
Total	471760	430073	91.16%

	ΔV_{CF-MCP} = 800V		
	Count (No Foil)	Count (Foil)	Relative Efficiency
$^{54}Fe^{+}$	3979	3929	98.74%
$^{56}Fe^{+}/^{57}Fe^{+}$	67673	41277	60.99%
$^{56}Fe^{2+}/^{57}Fe^{2+}$	180702	217178	120.19%
$^{27}Al^{+}/^{54}Fe^{2+}$	128198	137808	107.50%
$^{27}Al^{2+}$	18270	20858	114.17%
Total	398822	421050	105.57%

Table IV.5: Relative detection efficiencies of Al and Fe ions in the analyzed Fe-Al alloy, determined through the comparison between the amount of ions detected with the CF part, related to ions detected on the conventional MCP-DLD part (Figure IV.25). Results from the different tables have been obtained from the same sample and at different bias voltage between the CF and the MCP front-end.

IV.10.2 Analysis of an $ZnO/Mg_xZn_{1-x}O$ multi-quantum well system

For this next study, it has been decided to analyze a $ZnO/Mg_xZn_{1-x}O$ quantum well (QW) system, for specifically resolving the potential mass peak overlap located at 32 Da between $^{64}Zn^{2+}$ and $O_2{}^+$ peaks [9, 58, 64] (Figure IV.37b). The quantum well system is characterized by a heterostructure made from semiconducting barriers, with large band-gaps, surrounding nanometric layers, also known as quantum wells, with smaller band-gaps (Figure IV.37a). Through this structure, both electrons and holes can be confined in the central quantum well region, having lower conduction band energy, in order to operate in different applications such as, lasers, photodetectors, modulators, or switches [42]. Apart from the exitonic properties of this material, it has to be known that the different stoichiometries from the ZnO QWs and the MgZnO barriers will allow monitoring the spatial distribution of $^{64}Zn^{2+}$ and $O_2{}^+$ under the CF detector, which cannot be distinguished in conventional APT instruments.

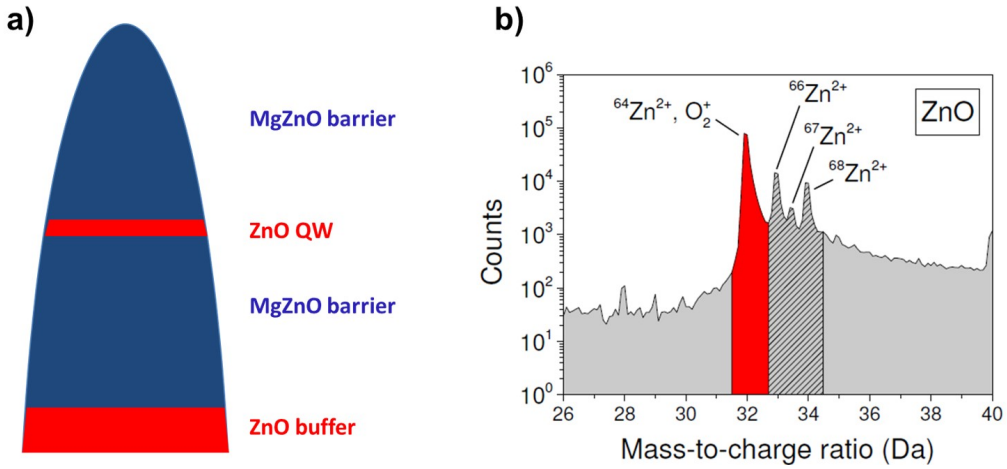

Figure IV.37: a) Scheme of a tip sample extracted from a $ZnO/Mg_xZn_{1-x}O$ system; b) Partial mass spectrum around the potential mass peak overlap between $^{64}Zn^{2+}$ and $O_2{}^+$ peaks [11]

In the same manner as what has been done for the previous analysis of Fe-Al alloy, two specific spectra of MCP amplitudes vs. mass-charge ratios have been respectively extracted from the two areas of the detection surface (with and without CF).

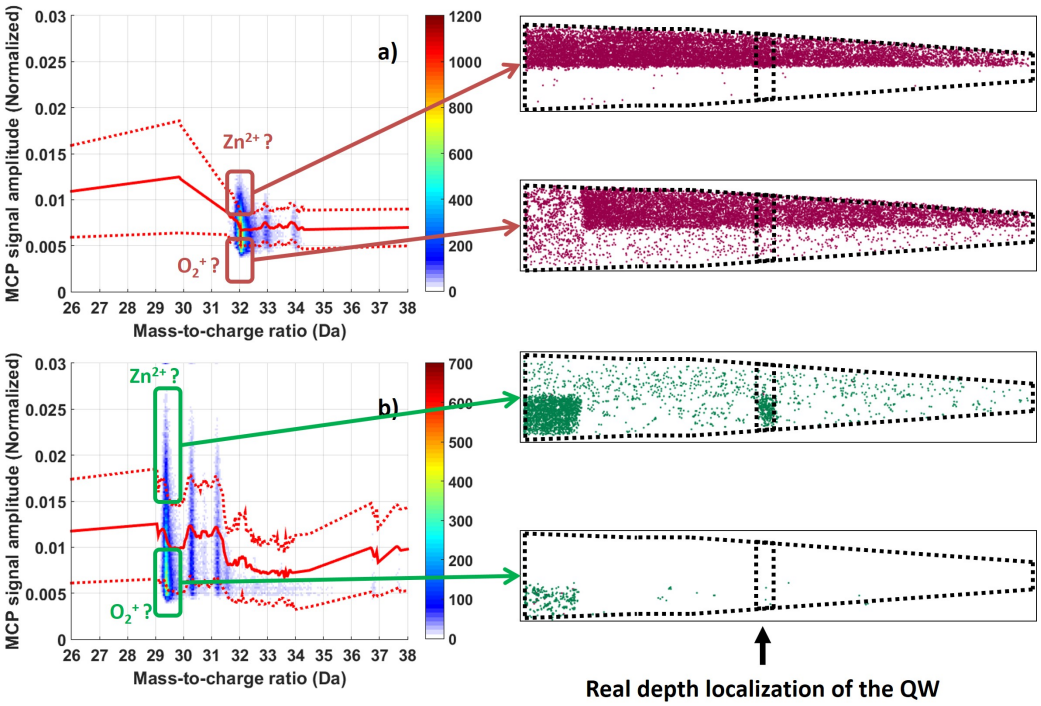

Figure IV.38: MCP amplitude vs. Mass-to-charge ratio spectra associated with their respective 3D reconstructions. a) Spectrum from the detection surface without CF; b) Spectrum from the detection surface with CF. Red solid lines represent the mean amplitude values for each mass, associated with their standard deviation (red dashed lines). It must be specified that the slight mass offset between spectra a) and b) is due to shorter time-of-flights associated with the ion-to-electron conversion between the carbon foil and the MCP front-end.

As illustrated in Figure IV.38, and as mentioned in the previous study, it can be observed that MCP amplitudes from the CF area are nearly twice higher than MCP amplitudes from the area without CF. Moreover, it can be stated again that that the *ERP* on the CF spectrum (Figure IV.38b) is too poor for getting a strict discrimination between $^{64}Zn^{2+}$ and $O_2{}^+$ peaks. However, by arbitrary filtering high and low amplitudes from the CF area, clear differences on 3D reconstructions can be now observed between the conventional MCP-DLD detector (Figure IV.38a) and the CF detector (Figure IV.38b). Contrary to the lack of energy sensitivity from the MCP-DLD detector (Figure IV.38a), the CF detector introduces a high density at the location of the QWs for higher MCP amplitudes in relation to the 32 Da mass peak (Figure IV.38b). By keeping the main hypothesis on

the behavior of CFs, saying that the SEY must increase as a function of the mass and the kinetic energy of ion projectiles, it can be deduced that the high density revealed in Figure IV.38b, at the level of the QW, represents the contribution of $^{64}Zn^{2+}$ ions.

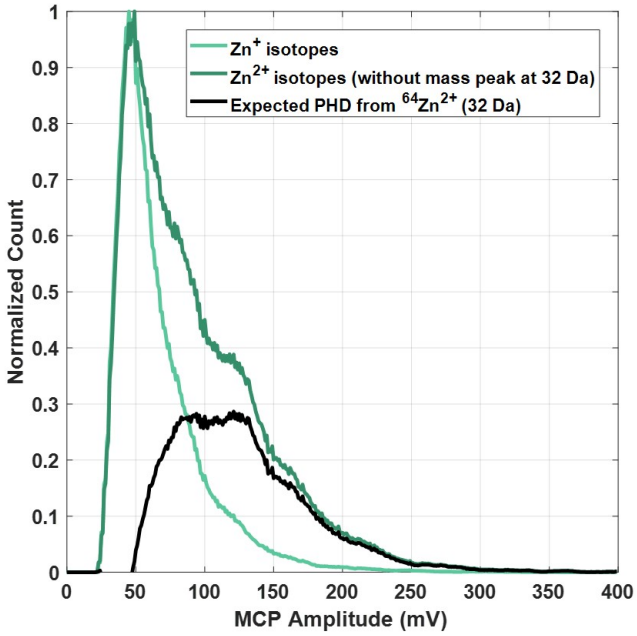

Figure IV.39: Pulse Height Distributions extracted from the CF part of the developed detector. The subtraction of MCP amplitude distribution from Zn^{2+} detection (non-overlapped isotopes) to the distribution from Zn^{+} detection allows the visualization of the MCP amplitude range that only concern Zn^{2+} ions. As a consequence, the range of amplitudes covered by the black curve allows applying a qualitative discrimination between $^{64}Zn^{2+}$ and $O_2{}^{+}$ ions.

The analysis of this material through the CF detector shows that two different MCP amplitude distributions can also be extracted both from single and double charged ions. From Figure IV.39, it can be observed that Zn^{2+} ions are spread over higher amplitudes compared with Zn^{+} ions. Which seems to be consistent with the theoretical energy sensitivity of the CF. Furthermore, it can be assumed the mass peak overlap at 32 Da (Figure IV.37b), between $^{64}Zn^{2+}$ and $O_2{}^{+}$ ions, could be partly resolved by decomposing the pulse height distribution, attributed the mass peak at 32 Da, with the help of the pulse height distribution of Zn^{+} isotopes

(Figure IV.39).

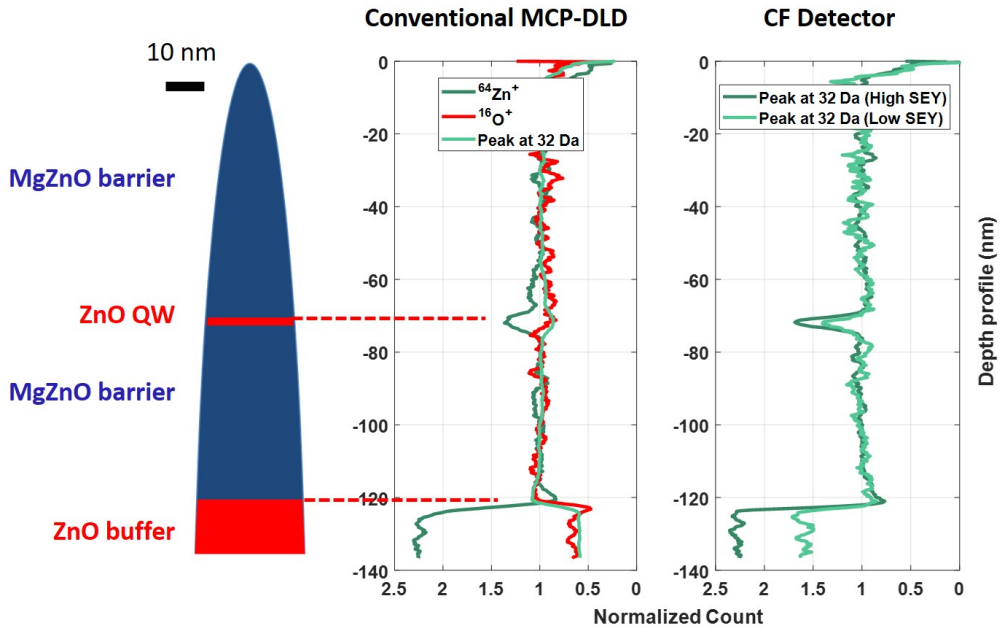

Figure IV.40: Normalized depth profiles comparison from the developed detector. The outburst of $^{64}Zn^{2+}$ that could not be observed at the QW position on the conventional MCP-DLD detector can now be observed through the pseudo-energy sensitivity of the CF detector.

The direct comparison of the depth profiles between the conventional MCP-DLD detector and the CF detector on Figure IV.40, clearly shows that $^{64}Zn^{2+}$ ions, has been partly recovered through the filtering of high MCP amplitudes induced by ions from the mass peak at 32 Da (Figure IV.39). However, it can also be observed that the depth profile of the mass peak at 32 Da, filtered with lower MCP amplitudes (lower SEY), seems to follow the same depth profile as Zn isotopes instead of the O^+ profile. That compositional bias could be explained by a potential selective loss of $O_2{}^+$ ions having not enough kinetic energy to induce secondary electrons.

IV.11 Conclusion

A first proof of concept of position-energy-sensitive detector has been developed for APT instruments in order to deal with some mass peak overlap issues encountered in APT experiments. Through this new type of detector, quantitative and qualitative improvements could be considered for critical materials introducing mass peak overlaps.
This new detector based on a thin carbon foil positioned on the front panel of a conventional MCP-DLD detector is able to generate a number of transmitted secondary electrons that mainly depends on both the kinetic energy and the mass of incident particles. Therefore, this study introduces the first experiments on a potential new generation of APT detectors that would be able to resolve mass peak overlaps through the energy-sensitivity of thin carbon foils.
The observed lack of energy-sensitivity of the CF detector requires future in-depth studies to improve its performances. Given that the MCP assembly used in this study introduce a transparency of $\sim$60%, it is obvious that one of the first improvements to apply concern the increase of this transparency to reduce the uncertainty on the counting of SEs. That means that the use of existing 90% transparent MCP assemblies could be useful for improving the ERP of the CF detector.
The other main improvement could be found in the fine control of the CF thickness, considering that SEs could be generated at different depth, depending on the mass and the energy ranges of analyzed ions. Other future in-depth studies on the Ion Induced Electron Emission phenomenon would be then also necessary to achieve a fine control of this parameter.

Bibliography

[1] F. Allegrini, R. W. Ebert, and H. O. Funsten. Carbon foils for space plasma instrumentation: Carbon foils for space. *Journal of Geophysical Research: Space Physics*, 121(5):3931–3950, 5 2016.

[2] Frédéric Allegrini, Robert F. Wimmer-Schweingruber, Peter Wurz, and Peter Bochsler. Determination of low-energy ion-induced electron yields from thin carbon foils. *Nuclear Instruments and Methods in Physics Research Section B: Beam Interactions with Materials and Atoms*, 211(4):487–494, 12 2003.

[3] Š. Šaro, R. Janik, S. Hofmann, H. Folger, F.P. Heßberger, V. Ninov, H.J. Schött, A.P. Kabachenko, A.G. Popeko, and A.V. Yeremin. Large size foil-microchannel plate timing detectors. *Nuclear Instruments and Methods in Physics Research Section A: Accelerators, Spectrometers, Detectors and Associated Equipment*, 381(2-3):520–526, 11 1996.

[4] Rafael Ballabriga, Michael Campbell, and Xavier Llopart. Asic developments for radiation imaging applications: The medipix and timepix family. *Nuclear Instruments and Methods in Physics Research Section A: Accelerators, Spectrometers, Detectors and Associated Equipment*, 878:10–23, 1 2018.

[5] R. A. Baragiola, E. V. Alonso, and A. Oliva Florio. Electron emission from clean metal surfaces induced by low-energy light ions. *Physical Review B*, 19(1):121–129, 1 1979.

[6] Raúl A. Baragiola. Principles and mechanisms of ion induced electron emission. *Nuclear Instruments and Methods in Physics Research Section B: Beam Interactions with Materials and Atoms*, 78(1-4):223–238, 5 1993.

[7] Scott R. Broderick, Aaron Bryden, Santosh K. Suram, and Krishna Rajan. Data mining for isotope discrimination in atom probe tomography. *Ultramicroscopy*, 132:121–128, 9 2013.

[8] Chih Yuan Chen, Chien Wan Hun, Shih-Fan Chen, Chien Chon Chen, Jin Shyong Lin, Shardai S. Johnson, Niyoyankunze Noel, Niyogushima Juliely, and Zhiping Luo. Fabrication of nanoscale cesium iodide (csi) scintillators for high-energy radiation detection. *Reviews in Nanoscience and Nanotechnology*, 4(1):26–49, 4 2015.

[9] C. Chianelli, P. Ageron, J.P. Bouvet, M. Karolak, S. Martin, and J.P. Robert. Weakly ionizing charged particle detectors with high efficiency using transitory electronic secondary emission of porous csi. *Nuclear Instruments and Methods in Physics Research Section A: Accelerators, Spectrometers, Detectors and Associated Equipment*, 273(1):245–256, 12 1988.

[10] J.R. Dennison, A. Sim, and C.D. Thomson. Evolution of the electron yield curves of insulators as a function of impinging electron fluence and energy. *IEEE Transactions on Plasma Science*, 34(5):2204–2218, 10 2006.

[11] Enrico Di Russo. *Study of the physical mechanisms leading to compositional biases in atom probe tomography of semiconductors*. PhD thesis, Normandie Université, 2018.

[12] C. G. Drexler and R. D. DuBois. Energy- and angle-differential yields of electron emission from thin carbon foils after fast proton impact. *Physical Review A*, 53(3):1630–1637, 3 1996.

[13] David L.J. Engberg, Lars J.S. Johnson, Jens Jensen, Mattias Thuvander, and Lars Hultman. Resolving mass spectral overlaps in atom probe tomography by isotopic substitutions – case of tisi15n. *Ultramicroscopy*, 184:51–60, 1 2018.

[14] C. Enss, A. Fleischmann, K. Horst, J. Schönefeld, J. Sollner, J. S. Adams, Y. H. Huang, Y. H. Kim, and G. M. Seidel. Metallic magnetic calorimeters for particle detection. *Journal of Low Temperature Physics*, 121(3/4):137–176, 2000.

[15] E. Esposito, M. Ejrnaes, S. Pagano, D. Perez de Lara, and R. Cristiano. Josephson device for simultaneous time and energy detection. *Applied Physics Letters*, 82(13):2109–2111, 3 2003.

[16] Matthias Frank. Mass spectrometry with cryogenic detectors. *Nuclear Instruments and Methods in Physics Research Section A: Accelerators, Spectrometers, Detectors and Associated Equipment*, 444(1-2):375–384, 2000.

[17] S Friedrich, CA Mears, B Nideröst, LJ Hiller, Matthias Frank, SE Labov, AT Barfknecht, and SP Cramer. Superconducting tunnel junction array development for high-resolution energy-dispersive x-ray spectroscopy. *Microscopy and Microanalysis*, 4:616–621, 1998.

[18] H. J. Frischkorn, P. Koschar, R. Latz, J. Schader, M. Burkhard, D. Hofmann, and K. O. Groeneveld. Total yield and escape depth of electrons from heavy ion solid interactions. *IEEE Transactions on Nuclear Science*, 30(2):931–933, 4 1983.

[19] H. Funsten, S. Ritzau, R. Harper, J. Borovsky, and R. Johnson. Energy loss by kev ions in silicon. *Physical Review Letters*, 92(21):213201, 5 2004.

[20] HO Funsten, SM Ritzau, RW Harper, and R Korde. Fundamental limits to detection of low-energy ions using silicon solid-state detectors. *Applied physics letters*, 84(18):3552–3554, 2004.

[21] L. Gamer, D. Schulz, C. Enss, A. Fleischmann, L. Gastaldo, S. Kempf, C. Krantz, O. Novotný, D. Schwalm, and A. Wolf. Mocca: A 4k-pixel molecule camera for the position- and energy-resolving detection of neutral molecule fragments at csr. *Journal of Low Temperature Physics*, 184(3-4):839–844, 8 2016.

[22] I Giaever, HR Hart Jr, and K Megerle. Tunneling into superconductors at temperatures below 1 k. *Physical Review*, 126(3):941, 1962.

[23] RR Goruganthu and WG Wilson. Relative electron detection efficiency of microchannel plates from 0–3 kev. *Review of scientific instruments*, 55(12):2030–2033, 1984.

[24] D. Hasselkamp. Kinetic electron emission from solid surfaces under ion bombardment. In Dietmar Hasselkamp, Hermann Rothard, Karl-Ontjes Groeneveld, Jürgen Kemmler, Peter Varga, and Hannspeter Winter, editors, *Particle Induced Electron Emission II*, volume 123, pages 1–95. Springer Berlin Heidelberg, Berlin, Heidelberg, 1992. collection-title: Springer Tracts in Modern Physics DOI: 10.1007/BFb0038298.

[25] B. D. Josephson. The discovery of tunnelling supercurrents. *Reviews of Modern Physics*, 46(2):251–254, 4 1974.

[26] Thomas F. Kelly. Kinetic-energy discrimination for atom probe tomography: Review article. *Microscopy and Microanalysis*, 17(1):1–14, 2 2011.

[27] Mohamad Khalil, Erik Schou Dreier, Jan Kehres, Jan Jakubek, and Ulrik Lund Olsen. Subpixel resolution in cdte timepix3 pixel detectors. *Journal of synchrotron radiation*, 25(6):1650–1657, 2018.

[28] Rita Kirchhofer, David R. Diercks, Brian P. Gorman, Jon F. Ihlefeld, Paul G. Kotula, Christopher T. Shelton, and Geoff L. Brennecka. Quantifying compositional homogeneity in pb(zr,ti)o $_3$ using atom probe tomography. *Journal of the American Ceramic Society*, 97(9):2677–2697, 9 2014.

[29] Hans Kraus. Cryogenic detectors and their application to mass spectrometry. *International Journal of Mass Spectrometry*, 215(1-3):45–58, 2002.

[30] M Kroupa, J Jakubek, and P Soukup. Optimization of the spectroscopic response of the timepix detector. *Journal of Instrumentation*, 7(02):C02058, 2012.

[31] A.V. Kuznetsov, E.J. Veldhuizen, L. Westerberg, V.G. Lyapin, K. Aleklett, W. Loveland, J. Bondorf, B. Jakobsson, H.J. Whitlow, and M. El Bouanani. A compact ultra-high vacuum (uhv) compatible instrument for time of flight–energy measurements of slow heavy reaction products. *Nuclear Instruments and Methods in Physics Research Section A: Accelerators, Spectrometers, Detectors and Associated Equipment*, 452(3):525–532, 10 2000.

[32] Alexandre La Fontaine, Alexander Zavgorodniy, Howgwei Liu, Rongkun Zheng, Michael Swain, and Julie Cairney. Atomic-scale compositional mapping reveals mg-rich amorphous calcium phosphate in human dental enamel. *Science Advances*, 2(9):e1601145, 9 2016.

[33] ST Lepri, Shouleh Nikzad, T Jones, J Blacksberg, and TH Zurbuchen. Response of a delta-doped charge-coupled device to low energy protons and nitrogen ions. *Review of scientific instruments*, 77(5):053301, 2006.

[34] Xavier Llopart, Rafael Ballabriga, Michael Campbell, Lukas Tlustos, and Winnie Wong. Timepix, a 65k programmable pixel readout chip for arrival time, energy and/or photon counting measurements. *Nuclear Instruments and Methods in Physics Research Section A: Accelerators, Spectrometers, Detectors and Associated Equipment*, 581(1-2):485–494, 2007.

[35] Gerhard Lutz. *Semiconductor Radiation Detectors*. Springer Berlin Heidelberg, Berlin, Heidelberg, 2007. DOI: 10.1007/978-3-540-71679-2.

[36] P. Maier-Komor. Carbon foils for nuclear accelerator experiments. *Nuclear Instruments and Methods in Physics Research Section B: Beam Interactions with Materials and Atoms*, 79(1-4):841–844, 6 1993.

[37] R. K. W. Marceau, A. V. Ceguerra, A. J. Breen, D. Raabe, and S. P. Ringer. Quantitative chemical-structure evaluation using atom probe tomography: Short-range order analysis of fe–al. *Ultramicroscopy*, 157:12–20, 10 2015.

[38] Andrew J. Martin, Yong Wei, and Andreas Scholze. Analyzing the channel dopant profile in next-generation finfets via atom probe tomography. *Ultramicroscopy*, 186:104–111, 3 2018.

[39] W Mechbach, G Braunstein, and N Arista. Secondary-electron emission in the backward and forward directions from thin carbon foils traversed by 25-250 kev proton beams. *Journal of Physics B: Atomic and Molecular Physics*, 8(14):L344–L349, 10 1975.

[40] A Müller, N Djurić, GH Dunn, and DS Belić. Absolute detection efficiencies of microchannel plates for 0.1–2.3 kev electrons and 2.1–4.4 kev mg+ ions. *Review of scientific instruments*, 57(3):349–353, 1986.

[41] John W Murdock and Glenn H Miller. *Secondary electron emission due to positive ion bombardment*, volume 652. United States Atomic Energy Commission, Technical Information Service, 1955.

[42] Biswaranjan R Nag. *Physics of quantum well devices*, volume 7. Springer Science & Business Media, 2001.

[43] O. Novotný, S. Allgeier, C. Enss, A. Fleischmann, L. Gamer, D. Hengstler, S. Kempf, C. Krantz, A. Pabinger, C. Pies, D. W. Savin, D. Schwalm, and A. Wolf. Cryogenic micro-calorimeters for mass spectrometric identification of neutral molecules and molecular fragments. *Journal of Applied Physics*, 118(10):104503, 9 2015.

[44] K. Ogasawara, S. A. Livi, F. Allegrini, T. W. Broiles, M. A. Dayeh, M. I. Desai, R. W. Ebert, K. Llera, S. K. Vines, and D. J. McComas. Next-generation solid-state detectors for charged particle spectroscopy: Next-generation solid-state detectors. *Journal of Geophysical Research: Space Physics*, 121(7):6075–6091, 7 2016.

[45] Masataka Ohkubo, Shiki Shigetomo, Masahiro Ukibe, Go Fujii, and Nobuyuki Matsubayashi. Superconducting tunnel junction detectors for analytical sciences. *IEEE Transactions on Applied Superconductivity*, 24(4):1–8, 8 2014.

[46] P. W. Palmberg. Secondary emission studies on ge and na-covered ge. *Journal of Applied Physics*, 38(5):2137–2147, 4 1967.

[47] C. Pareige, W. Lefebvre-Ulrikson, F. Vurpillot, and X. Sauvage. Time-of-flight mass spectrometry and composition measurements. In *Atom Probe Tomography*, pages 123–154. Elsevier, 2016. DOI: 10.1016/B978-0-12-804647-0.00005-X.

[48] S. M. Ritzau and R. A. Baragiola. Electron emission from carbon foils induced by kev ions. *Physical Review B*, 58(5):2529–2538, 8 1998.

[49] Hermann Rothard, Christophe Caraby, Amine Cassimi, Benoit Gervais, Jean-Pierre Grandin, Pascal Jardin, Matthias Jung, Annick Billebaud, Michel Chevallier, Karl-Ontjes Groeneveld, and Robert Maier. Target-thickness-dependent electron emission from carbon foils bombarded with swift highly charged heavy ions. *Physical Review A*, 51(4):3066–3078, 4 1995.

[50] R. A. Rymzhanov, N. A. Medvedev, and A. E. Volkov. Electron emission from silicon and germanium after swift heavy ion impact: Electron emission from si and ge after swift heavy ion impact. *physica status solidi (b)*, 252(1):159–164, 1 2015.

[51] M. P. Seah and W. A. Dench. Quantitative electron spectroscopy of surfaces: A standard data base for electron inelastic mean free paths in solids. *Surface and Interface Analysis*, 1(1):2–11, 2 1979.

[52] Jae-Bok Seol, Dierk Raabe, P. Choi, Hyung-Seok Park, J. H. Kwak, and Chan-Gyung Park. Direct evidence for the formation of ordered carbides in a ferrite-based low-density fe–mn–al–c alloy studied by transmission electron microscopy and atom probe tomography. *Scripta Materialia*, 68(6):348–353, 3 2013.

[53] N Sévelin-Radiguet, L Arnoldi, F Vurpillot, Antoine Normand, B Deconihout, and A Vella. Ion energy spread in laser-assisted atom probe tomography. *EPL (Europhysics Letters)*, 109(3):37009, 2015.

[54] Shigetomo Shiki, Masahiro Ukibe, Yuki Sato, Shigeo Tomita, Shigeo Hayakawa, and Masataka Ohkubo. Kinetic-energy-sensitive mass spectrometry for separation of different ions with the same m/z value. *Journal of mass spectrometry*, 43(12):1686–1691, 2008.

[55] Peter Sigmund and Sven Tougaard. Electron emission from solids during ion bombardment. theoretical aspects. In *Inelastic Particle-surface collisions*, pages 2–37. Springer, 1981.

[56] K Suzuki, M Ohkubo, M Ukibe, K Chiba-Kamoshida, S Shiki, S Miki, and Z Wang. Charge-state-derivation ion detection using a super-conducting nanostructure device for mass spectrometry. *Rapid Communications in Mass Spectrometry*, 24(22):3290–3296, 2010.

[57] Fengzai Tang, Baptiste Gault, Simon P. Ringer, and Julie M. Cairney. Optimization of pulsed laser atom probe (plap) for the analysis of nanocomposite ti–si–n films. *Ultramicroscopy*, 110(7):836–843, 6 2010.

[58] S. Tanuma, T. Shiratori, T. Kimura, K. Goto, S. Ichimura, and C. J. Powell. Experimental determination of electron inelastic mean free paths in 13 elemental solids in the 50 to 5000 ev energy range by elastic-peak electron spectroscopy. *Surface and Interface Analysis*, 37(11):833–845, 11 2005.

[59] K. Töglhofer, F. Aumayr, and H.P. Winter. Ion-induced electron emission from metal surfaces — insights from the emission statistics. *Surface Science*, 281(1-2):143–152, 1 1993.

[60] M. Thuvander, J. Weidow, J. Angseryd, L.K.L. Falk, F. Liu, M. Sonestedt, K. Stiller, and H.-O. Andrén. Quantitative atom probe analysis of carbides. *Ultramicroscopy*, 111(6):604–608, 5 2011.

[61] S. Tomita, S. Yoda, R. Uchiyama, S. Ishii, K. Sasa, T. Kaneko, and H. Kudo. Nonadditivity of convoy- and secondary-electron yields in the forward-electron emission from thin carbon foils under irradiation of fast carbon-cluster ions. *Physical Review A*, 73(6):060901, 6 2006.

[62] Damian Twerenbold. Cryogenic particle detectors. *Reports on Progress in Physics*, 59(3):349–426, 3 1996.

[63] M. Ukibe, Y. Chen, Y. Shimizugawa, Y. Kobayashi, A. Kurokawa, and M. Ohkubo. Anomaly in fabrication processes for large-scale array detectors of superconducting tunnel junctions. *Journal of Low Temperature Physics*, 151(1-2):316–321, 4 2008.

[64] Demetrios Voreades. Secondary electron emission from thin carbon films. *Surface Science*, 60(2):325–348, 11 1976.

[65] Francois Vurpillot, Constantinos Hatzoglou, Bertrand Radiguet, Gerald Da Costa, Fabien Delaroche, and Frederic Danoix. Enhancing element identification by expectation–maximization method in atom probe tomography. *Microscopy and Microanalysis*, 25(2):367–377, 4 2019.

[66] BW Ward, DC Shaver, and ML Ward. Repair of photomasks with focussed ion beams. In *Electron-Beam, X-Ray, and Ion-Beam Techniques for Submicrometer Lithographies IV*, volume 537, pages 110–116. International Society for Optics and Photonics, 1985.

[67] L.W. Weathers and M.B. Tsang. Fabrication of thin scintillator foils. *Nuclear Instruments and Methods in Physics Research Section A: Accelerators, Spectrometers, Detectors and Associated Equipment*, 381(2-3):567–568, 11 1996.

[68] Ryan J. Wenzel, Urs Matter, Lothar Schultheis, and Renato Zenobi. Analysis of megadalton ions using cryodetection maldi time-of-flight mass spectrometry. *Analytical Chemistry*, 77(14):4329–4337, 7 2005.

[69] B. Wilken and W. Stüdemann. A compact time-of-flight mass-spectrometer with electrostatic mirrors. *Nuclear Instruments and Methods in Physics Research*, 222(3):587–600, 5 1984.

[70] Martin Wortmann, Arne Ludwig, Jan Meijer, Dirk Reuter, and Andreas D. Wieck. High-resolution mass spectrometer for liquid metal ion sources. *Review of Scientific Instruments*, 84(9):093305, 9 2013.

[71] James F Ziegler and Jochen P Biersack. The stopping and range of ions in matter. In *Treatise on heavy-ion science*, pages 93–129. Springer, 1985.

[72] James F. Ziegler, M.D. Ziegler, and J.P. Biersack. Srim – the stopping and range of ions in matter (2010). *Nuclear Instruments and Methods in Physics Research Section B: Beam Interactions with Materials and Atoms*, 268(11-12):1818–1823, 6 2010.

Conclusion

As previously stated, the design of innovative materials must be partly done through both the localization and the identification of individual atoms, not only from samples surface, but also from internal atomic layers. That makes the APT instrument one of the most powerful analytical tool in material sciences.
However, it has been demonstrated that performances of APT instruments can be put into question because of some limitations that do not sufficiently promote their democratization in material sciences. Among these limitations, some of them concern the spatial and compositional biases caused by the APT detection system. The majority of those limitations have already been discussed through the three-last generation of Position Sensitive Detectors (PSD); charge detectors (WSA, TAP detectors), optical detectors (OAP, OPoSAP and OTAP detectors) and Delay Line Detectors (DLD).
Despite the significant improvements brought by the last generation of PSD, based on DLDs, it has been first pointed out that potential selective losses may occur when APT detection systems are stressed by simultaneous or quasi-simultaneous multi-hit impacts. It has long been known that this mainly concerns the inability of the detector to correctly treat high amount of hits in a short period of time, also called the dead-time (DT). However, the true mechanism behind those selective losses remained unresolved. Therefore, the first study of this thesis was aimed at understanding the origin of spatial and compositional biases caused by the detection system during multi-hit events. This is through the development of a simulation tool, aimed at reproducing the APT detection process, that is has been demonstrated that significant losses may occur for materials introducing different elements that tend to field evaporate in multi-hit events more than others. Moreover, by trying to understand the origin of those losses, it has been found that signal losses, on the APT detector, may occur for ion pairs having TOF differences that are larger than the instrument DT, conversely to what has been reported in the literature. Given that the instrument DT still have a leading role in the potential biases on APT analyses, it is clear that an additional step has

to be taken for reducing its influence. This step has already been initiated by a system called the Advanced Delay Line Detector (aDLD). However, the reliability of this promising detection system has been put into question.
The next logical study of this thesis was then focused on both the study and the improvement of the aDLD system. As a reminder, the aDLD is a detection system based on fast digitizers that help to decompose MCP and DLD output signals, potentially overlapped during multi-hit events, into individual signals. APT instruments equipped with an aDLD system, such as the LaWATAP, has demonstrated that the DT of conventional APT detection systems could be outperformed through this data processing scheme. Consequently, by reducing the instrument DT, aDLD systems allow the reduction of selective losses caused by the variability of the evaporation mechanism during APT experiments. However, despite the fact that the aDLD can significantly reduce losses in APT experiments, no studies have been conducted yet to get a concrete comparison between aDLD and conventional APT detection systems. Therefore, it has been decided to use the simulation tool developed during this thesis for getting a concreate comparison by excluding any other parameters originating from outside the APT detection system. Unsurprisingly, simulation results confirmed that APT instruments equipped with aDLD system introduce far less selective losses compared to conventional APT detection system, for critical materials introducing high amounts of multi-hit events.
Despite this significant benefit, aDLD systems have not been generalized to all APT instruments for two main reasons. Firstly, current aDLD systems are subjected to a significant dwell time after each acquisition, which has the effect of decreasing the detection rate, and thus, increasing the analysis time. The second reason concerns the lack of reliability of the signal decomposition process applied by the aDLD, which may cause spatial distortions during the detection process. Therefore, the other step of this study was aimed at resolving those limitations for reconsidering the use of the aDLD detection system on future APT instruments. Concerning the enhancement of the aDLD acquisition speed, a new acquisition scheme, based on the reduction of the transferred data packages, has been introduced and shows that free-running analyses can be this time correctly performed. On the other side, it has been demonstrated that the potential spatial distortion in APT instruments equipped with aDLD system is not really linked to the electronic detection system itself, but linked to the type of DLD used. It turns out that the only commercial APT instrument using the aDLD system (LaWATAP) is equipped with a Helical Delay Line (HDL) detector. Some experiments during this thesis have shown that this type of DLD, made of copper-beryllium wires, running in differential pairs and wounded around

an insulating frame, is subjected to local resistance variations, having the effect of involving impedance mismatches. Based on those results, it has been decided to develop another type of DLD, called Serpentine Delay Line (SDL), that theoretically promises to reduce those local resistance variations, and thus promises to avoid spatial distortions. This study of research and development gave rise of a new design of DLD whose first results clearly show the potential improvement of APT instruments equipped with aDLD system.
Among the current limitations of APT detection systems, only one of them has still not been resolved since the first generation of PSDs; the mass peak overlaps. As a reminder, mass peak overlaps are interferences between mass peaks originating from different elements. This type of limitation is part of the potential compositional biases caused by the APT detection system.
Given that most of mass peak overlaps concern elements with different charge states, it has been assumed that it would be theoretically possible to resolve them through an indirect measurement based on the kinetic energy of collected ions. Knowing that current APT detectors are not able to provide this type of information, it becomes clear that a new generation of APT detectors has to be developed. Therefore, the last part of this thesis was aimed at resolving those mass peak overlaps through the development of a Position-Energy-Sensitive Detector (PESD).
Studies on existing PESDs have already shown that mass peak overlaps can be resolved through a kinetic energy discrimination. However, it has been stated that those existing PESDs introduce very slow time responses related to what is required in APT experiments. It has also been stated that their effective area is limited to less than 4 cm^2 against 50 cm^2 for an MCP surface. Besides those existing PESDs, this thesis was focused on the study of a physical phenomenon that is known for providing information about the kinetic energy of ion projectiles, but which has never been used as a mean for resolving mass peak overlaps. This physical phenomenon is known as the Ion Induced Electron Emission (IIEE). The IIEE consists of the generation of secondary electrons (SE) induced by the impact of energetic ions on a solid sample. Previous studies on this phenomenon have demonstrated that the number of SEs generated is a function of the mass and the energy of incident ions. In this thesis, particular interest has been focused on the generation of transmitted (forward) SEs induced through thin carbon foils (CF). Independently from the mass and energy sensitivity of thin CF, other studies have also shown that it is possible to maintain a high spatial resolution by collecting the forward SEs through an MCP assembly facing the foil. Thus, those independent studies allowed to constitute hard-hitting arguments for initiating the development of a PESD based on CF.
With the aim of stating the possibility of CF detectors to resolve mass peak

overlaps, two distinct studies have been conducted. Firstly, a theoretical approach has been conducted for demonstrating the single particle sensitivity of a CF-MCP-DLD setup. This study has shown that it is theoretically possible to maintain a detection efficiency and a spatial resolution that are comparable to conventional APT detectors. Secondly, a new detector based on a thin CF has been developed for experimentally determining the ability of this supposed PESD to resolve mass peak overlaps. First experiments performed with this new detector have clearly shown that qualitative kinetic energy discriminations are possible for nano-features introducing mass peak overlaps. Therefore, this study introduces the first experiments on a potential new generation of APT detectors that would be able to resolve mass peak overlaps through the energy-sensitivity of thin CF.

In addition to the mass and energy sensitivity of the carbon foil, it has been demonstrated that this type of detector could also be used as a mean for improving the APT detection efficiency. However, it has also been observed that significant losses may occur for massive and low in energy ions, due to their low associated secondary electron yield. Future in-depth studies on the Ion Induced Electron Emission phenomenon would be necessary to achieve a fine control of this parameter.

Résumé

La Sonde Atomique Tomographique (SAT) est un outil d'analyse qui permet de déterminer la structure et la composition locale de matériaux à l'échelle atomique. Afin d'obtenir ce type d'analyse, la SAT utilise une technique destructive appelée « évaporation par effet de champ », permettant d'extraire et de collecter un certain volume d'atomes provenant d'un échantillon de matériau. Pour ce faire, il est nécessaire, dans un premier temps, d'usiner le matériau à analyser sous la forme d'une pointe très fine. Puis, dans un second temps, d'appliquer un potentiel électrique très élevé au niveau de cette pointe, afin de d'ioniser et expulser les atomes de surface. Ces atomes de surface sont alors projetés vers un détecteur sensible en position, couche après couche, afin d'obtenir une tomographie à l'échelle atomique du volume analysé. Afin d'être chimiquement identifié, chaque atome détecté est associé à une mesure de temps de vol, qui s'effectue entre une impulsion électrique (ou laser) appliqué sur la pointe, et un signal d'arrivé sur le détecteur. Connaissant le potentiel électrique total appliqué à la pointe, ainsi que la vitesse des ions projetés vers le détecteur, il est alors possible de déterminer un rapport masse sur charge (m/n) de chaque ion collecté.

Au vu de cette dernière description, la SAT peut apparaitre comme l'un des meilleurs outils d'analyse permettant de caractériser des matériaux à une échelle atomique. Cependant, l'utilisation de cet instrument reste encore restreinte en science des matériaux. L'une des principales raisons à cela concerne les biais apportés par le système de détection de la SAT. En effet, il a été constaté que des pertes d'information pouvaient se produire lorsque le détecteur était soumis à des impacts d'ions multiples sur de très courtes périodes de temps. Ceci peut se traduire par des pertes sélectives dans le cas où certains éléments auraient tendance à s'évaporer par groupe de plusieurs ions sur une même impulsion de départ sur la pointe. D'autre biais ont aussi été constatés au niveau de l'identification chimique des ions détectés. Étant donné que cette identification s'effectue par spectrométrie de masse à temps de vol, on peut s'apercevoir que certains éléments d'un même matériau peuvent se regrouper sous des rapport m/n extrêmement proches. Ce qui a pour effet de créer des interférences entre pics de masses provenant d'éléments différents, et donc de créer de potentiels biais de compositions.

Sur la base de ces différentes limites, cette thèse a pour but de répondre à la problématique suivante : Comment peut-on surpasser les limites des différents systèmes de détection de SAT ? Pour y répondre, des études, à la fois théoriques et expérimentales, ont été effectuées pour traiter l'ensemble de ces derniers biais, jusqu'à l'aboutissement de nouveaux modèles théoriques et de nouveaux prototypes de détecteurs pour la SAT.

Keywords: Sonde Atomique Tomographique, Détecteur sensible en position, Outil de simulation, Lignes à retard, Recouvrement de spectre

Abstract

The Atom Probe Tomography (APT) is an analysis technique allowing the visualization of the atomic structure and the determination of the elemental nature of each atom originating from material samples. In order to get this type of analysis, the APT uses a destructive technique, called the Field Evaporation, allowing the extraction and the detection of atoms constituting the analyzed material. To do so, it is necessary, in a first step, to shape the material sample in the form of a very sharp needle. Then, in a second step, to apply a high electric potential on the tip for ionizing and expelling the atoms from the surface of the tip apex. Surface atoms are then projected towards a position-sensitive detector (PSD), with the aim of reconstructing the internal three-dimensional shape of the analyzed material, layer-by-layer. Concerning the spectrometric aspect of this technique, each detected atom is associated to a time-of-flight (TOF) measurement. Those TOFs are measured between electric (or laser) pulses applied on the tip, and arrival times on the detector. Knowing the resulting electric potential applied on the tip and the projection speed of ions, it is possible to get the mass-to-charge ratio of each collected ion.

Regarding the working process of this technique, it may be thought that APT instruments could be the best mean for analyzing materials at the atomic scale. However, since the invention of this technique, more than 30 years ago, APT instruments are still relatively confidential in the panel of high-resolution microscopes used in material sciences. One of the main reasons to this concerns the potential biases brought by the APT detection system. Some of those biases concern the inability of the detector to correctly treat high amounts of ion arrivals in a short period of time. In the case where some elements tend field evaporate in bundles of more than one ion, it is then possible to suffer from selective losses during APT experiments. Secondly, given that the elemental nature of collected ions is determined through time-of-flight mass spectrometry, material analyses may be intrinsically subjected to compositional biases. This is due to interferences between mass peaks originating from different elements, sharing very close mass-to-charge ratios.

Based on the foregoing, this thesis is intended to answer to the following issue: How to outperform the limitations of APT detection systems? To do so, theoretical and experimental studies have been conducted for resolving those biases, and finally led to the development of new theoretical models and new type of detectors for APT instruments.

Keywords: Atom Probe Tomography, Position-Sensitive Detector, Simulation Tool, Delay-Line Detector, Mass Peak Overlaps